frontiers | Research Topics

Nuclear physics and astrophysics in plasma traps

Edited by
David Mascali, Sara Palmerini, Giuseppe Torrisi, Giacomo De Angelis, Domenico Santonocito and Karl-Ludwig Kratz

Published in
Frontiers in Physics
Frontiers in Astronomy and Space Sciences

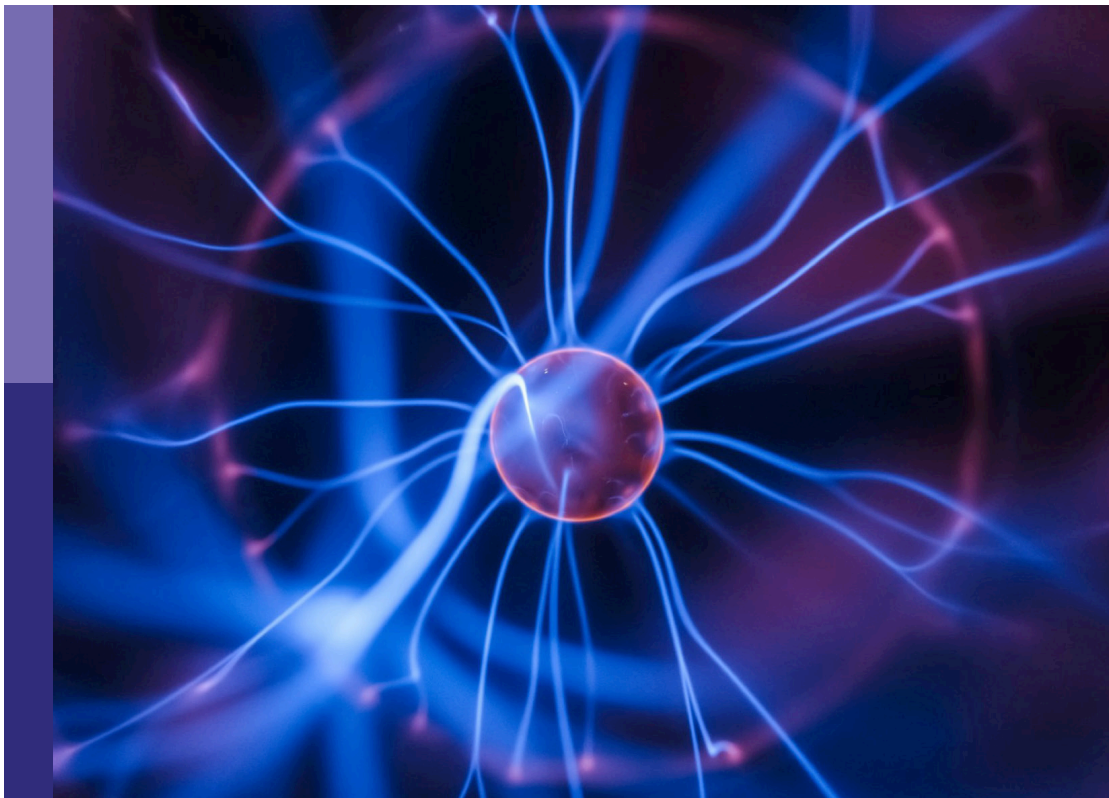

ISSN 1664-8714
ISBN 978-2-83251-062-9
DOI 10.3389/978-2-83251-062-9

About Frontiers

Frontiers is more than just an open access publisher of scholarly articles: it is a pioneering approach to the world of academia, radically improving the way scholarly research is managed. The grand vision of Frontiers is a world where all people have an equal opportunity to seek, share and generate knowledge. Frontiers provides immediate and permanent online open access to all its publications, but this alone is not enough to realize our grand goals.

Frontiers journal series

The Frontiers journal series is a multi-tier and interdisciplinary set of open-access, online journals, promising a paradigm shift from the current review, selection and dissemination processes in academic publishing. All Frontiers journals are driven by researchers for researchers; therefore, they constitute a service to the scholarly community. At the same time, the *Frontiers journal series* operates on a revolutionary invention, the tiered publishing system, initially addressing specific communities of scholars, and gradually climbing up to broader public understanding, thus serving the interests of the lay society, too.

Dedication to quality

Each Frontiers article is a landmark of the highest quality, thanks to genuinely collaborative interactions between authors and review editors, who include some of the world's best academicians. Research must be certified by peers before entering a stream of knowledge that may eventually reach the public - and shape society; therefore, Frontiers only applies the most rigorous and unbiased reviews. Frontiers revolutionizes research publishing by freely delivering the most outstanding research, evaluated with no bias from both the academic and social point of view. By applying the most advanced information technologies, Frontiers is catapulting scholarly publishing into a new generation.

What are Frontiers Research Topics?

Frontiers Research Topics are very popular trademarks of the *Frontiers journals series*: they are collections of at least ten articles, all centered on a particular subject. With their unique mix of varied contributions from Original Research to Review Articles, Frontiers Research Topics unify the most influential researchers, the latest key findings and historical advances in a hot research area.

Find out more on how to host your own Frontiers Research Topic or contribute to one as an author by contacting the Frontiers editorial office: frontiersin.org/about/contact

Nuclear physics and astrophysics in plasma traps

Topic editors

David Mascali — Laboratori Nazionali del Sud (INFN), Italy
Sara Palmerini — University of Perugia, Italy
Giuseppe Torrisi — Laboratori Nazionali del Sud (INFN), Italy
Giacomo De Angelis — Legnaro National Laboratories (INFN), Italy
Domenico Santonocito — Laboratori Nazionali del Sud (INFN), Italy
Karl-Ludwig Kratz — Johannes Gutenberg University Mainz, Germany

Citation

Mascali, D., Palmerini, S., Torrisi, G., De Angelis, G., Santonocito, D., Kratz, K.-L., eds. (2023). *Nuclear physics and astrophysics in plasma traps*. Lausanne: Frontiers Media SA. doi: 10.3389/978-2-83251-062-9

Table of contents

frontiers | Frontiers in Astronomy and Space Sciences

TYPE Editorial
PUBLISHED 01 December 2022
DOI 10.3389/fspas.2022.1087543

OPEN ACCESS

EDITED AND REVIEWED BY
Jie Meng,
Peking University, China

*CORRESPONDENCE
David Mascali,
davidmascali@lns.infn.it

SPECIALTY SECTION
This article was submitted to Nuclear Physics,
a section of the journal
Frontiers in Astronomy and Space Sciences

RECEIVED 02 November 2022
ACCEPTED 09 November 2022
PUBLISHED 01 December 2022

CITATION
Mascali D, Santonocito D, de Angelis G, Kratz K-L, Palmerini S and Torrisi G (2022), Editorial: Nuclear physics and astrophysics in plasma traps.
Front. Astron. Space Sci. 9:1087543.
doi: 10.3389/fspas.2022.1087543

Editorial: Nuclear physics and astrophysics in plasma traps

David Mascali[1]*, Domenico Santonocito[1], Giacomo de Angelis[2], Karl-Ludwig Kratz[3], Sara Palmerini[4,5] and Giuseppe Torrisi[1]

[1]Laboratori Nazionali Del Sud (INFN), Catania, Italy, [2]Legnaro National Laboratories (INFN), Legnaro, Italy, [3]Johannes Gutenberg University Mainz, Mainz, Germany, [4]University of Perugia, Perugia, Italy, [5]INFN, Sezione di Perugia, Perugia, Italy

KEYWORDS

Beta-decay of highly charged ions, plasma, nucleosynthesis—stars: abundances, s-process nucleosynthesis, r-process, gamma detection, plasma diagnostic measurement

Editorial on the Research Topic
Nuclear physics and astrophysics in plasma traps

β-decay rates are a fundamental ingredient of stellar nucleosynthesis. In particular, elements heavier than iron are produced by a subtle interplay between neutron captures and β-decays, being r-, i- and s-processes mechanisms driving the synthesis of neutron rich nuclei up to the limits imposed by nuclear stability. Therefore, any attempt to reproduce the observed abundances of heavy elements in the Universe calls for an accurate knowledge of neutron capture cross-sections and β-decay rates in a stellar environment as well as the comprehension of any possible mechanism affecting isotope times of life. Even though the β-decay constant has been measured for a wide range of nuclei, a major difference exists between laboratory and stellar conditions. Indeed, temperatures and densities may have very different values, ranging over several orders of magnitude, in the different nucleosynthesis environments. Therefore, stellar plasmas, where nucleosynthesis occurs, are not always fully ionized and when thermodynamical conditions affect the ionization degree of the involved atoms the β-decay process of their nuclei can be strongly modified too. This is particularly true for those nuclei whose β-decay Q value is small or slightly negative in the laboratory. In those cases, half-lives ($t_{1/2}$) in stellar and terrestrial conditions are predicted to be different for a fixed type of transition at temperatures above a few keV. Such an effect was first shown in the seminal work by Takahashi and Yokoi published in 1987 (Takahashi and Yokoi, 1983; Takahashi and Yokoi, 1987), which investigated the in-plasma effects due to the temperature and the electron density on β-decay rates. Despite the pivotal importance of these data, the cited paper is so far the only one reporting the high temperature β-decay rate of several nuclei and after 35 years the Takashi and Yokoi values are still the most used in calculations of stellar and primordial nucleosynthesis.

The first experimental evidence of the effect on β-decay of the high degree of ionization of atoms was found in Storage Rings (Litvinov and Bosch, 2011), which opened up the possibility of measuring β-decay rates in fully ionized atoms. Among the

most impressive results, the fully stripped $^{187}Re^{75+}$ ions were found to decay nine orders of magnitude faster than neutral ^{187}Re ones, which have a half-life of 42 Gyr. The reason for this striking variation is rooted in a new decay mechanism called "bound-state β-decay", typically forbidden in neutral atoms, in which the electron emitted in the decay process is captured in one of the inner shells of the atom.

Storage ring studies can only investigate one charge state at a time, meaning they do not enable the simulation of specific stellar like conditions where ions with broad charge distribution are present, due to the high values and gradients of the temperature of the environment. This limits the comparison of experimental data with model predictions, which typically take into account the average effect due to the ion charge distribution.

A new approach is needed to overcome such limitations and elucidate the possible effects of the charge state distribution (CSD) on the β-decay rate. In the very near future, controlled laboratory plasmas will allow us to investigate the β-decay properties of radioactive nuclei emulating the ionic charge state distributions of several nucleosynthesis environments. This is the main goal of the PANDORA facility (Mascali et al., 2017; Mascali et al., 2022). This approach will shed light on challenging open questions about primordial nucleosynthesis, s-, r- and i-processing (Palmerini et al., 2021), the Solar System formation and its early pollutions with radioactive nuclei, the cosmo-chronometer "calibrations", *etc.* At the same time, the plasmas created in laboratory are suited for opacity measurements that are relevant for Kilonovae scenarios, to support and address issues in observations of r-process abundances hours or days after the event. Such attractive opportunities require us to develop suitable theoretical and experimental procedures and methodologies, which are the subject of this Research Topic.

State-of-the-art studies of nucleosynthesis that are beyond Sr for both the s-process and r-process are discussed in contributions by Busso et al. and Spartà et al., respectively. By using up-to-date nuclear inputs, the implications disclosed by a proper knowledge of β-decay rates and neutron cross-sections are discussed in the two papers. New measurements of half-lives in ionized plasmas are suggested to improve the knowledge of both nucleosynthesis scenarios. To achieve this task a trap confining the plasma at temperatures up to about 30 keV and electron densities of 10^{11}–10^{13} cm^{-3} is needed. The design and the realization of the plasma trap are complex because some lines of sight have to be created to give access to the diagnostics and the gamma detection system needed to tag the decay events. This setup is described in detail by Mauro et al. The peculiarity of the approach is based on the possibility of operating with magneto-hydrodynamically stable plasmas, whose main features (density, temperature, and ion charge distribution) can be monitored online by a multi-diagnostics system.

The potentialities of some dedicated diagnostics tools to measure electron properties in plasma are discussed by Tsikata et al. and Torrisi et al. While their measurement is fundamental to establishing the thermodynamical condition of the plasma, *a priori* calculations of plasma electron density and energy distribution in a 3D space are mandatory to predict ion creations and their spatial distribution following plasma neutrality conditions. These arguments are discussed by Galatà et al. who indicate that information coming from the diagnostic system is fundamental to mapping the evolution of the β-decay rates as a function of the plasma thermodynamical conditions. However, the ion distribution in the trap is neither homogeneous nor isotropic and therefore one has to evaluate its implication in the decay rate measurements as well as the non-local thermodynamic equilibrium nature of the system, joining plasma kinetic equations with the expected β-decay rates in ionized and excited ions, a challenging task debated in another contribution to this Research Topic by Mishra et al. The gamma array used to tag the β-decay events will be made of HPGe detectors that work in rather harsh conditions, due to the high background rate coming from the plasma self-emission. Dedicated electronics have been developed to cope with such extreme conditions, making the measurement feasible without any important losses in the array performance. The design of the array, its efficiency, and the simulation of the measurability of a few physic cases are discussed in Naselli et al. while the development of the dedicated electronics and the tests of their performances are presented in the article by Goasduff et al. Finally, the possibility of applying the same experimental setup to an additional physics case is presented in the work of Pidatella et al., which examines the intriguing perspective of measuring the plasma opacities relevant to investigating Kilonovae and multi-messenger astronomy scenarios.

Author contributions

All authors listed have made a substantial, direct, and intellectual contribution to the work and approved it for publication.

Conflict of interest

The authors declare that the research was conducted in the absence of any commercial or financial relationships that could be construed as a potential conflict of interest.

Publisher's note

References

Litvinov, Y. A., and Bosch, F. (2011). Beta decay of highly charged ions. *Rep. Prog. Phys.* 74, 016301. doi:10.1088/0034-4885/74/1/016301

Mascali, D., Musumarra, A., Leone, F., Romano, F. P., Galata, A., Gammino, S., et al. (2017). PANDORA, a new facility for interdisciplinary in-plasma physics. *Eur. Phys. J. A* 53 (7), 145. doi:10.1140/epja/i2017-12335-1

Mascali, D., Santonocito, D., Amaducci, S., Ando, L., Antonuccio, V., Biri, S., et al. (2022). A novel approach to β-decay: PANDORA, a new experimental setup for future in-plasma measurements. *Universe* 8, 80. doi:10.3390/universe8020080

Palmerini, S., Busso, M., Vescovi, D., Naselli, E., Pidatella, A., Mucciola, R., et al. (2021). Presolar grain isotopic ratios as constraints to nuclear and stellar parameters of asymptotic giant branch star nucleosynthesis. *Astrophys. J.* 921 (1), 7. doi:10.3847/1538-4357/ac1786

Takahashi, K., and Yokoi, K. (1987). Beta-decay rates of highly ionized heavy atoms in stellar interiors. *Atomic Data Nucl. Data Tables* 36 (3), 375–409. doi:10.1016/0092-640X(87)90010-6

Takahashi, K., and Yokoi, K. (1983). Nuclear β-decays of highly ionized heavy atoms in stellar interiors. *Nucl. Phys. A* 404 (3), 578–598. doi:10.1016/0375-9474(83)90277-4

frontiers | Frontiers in Physics

REVIEW
published: 26 May 2022
doi: 10.3389/fphy.2022.896011

Neutron-Driven Nucleosynthesis in Stellar Plasma

R. Spartà[1], M. La Cognata[1], G. L. Guardo[1,2], S. Palmerini[3,4], M. L. Sergi[1,2], G. D'Agata[1,2], L. Lamia[1,2,5], D. Lattuada[1,6], A. A. Oliva[1,2], R. G. Pizzone[1], G. G. Rapisarda[1,2], S. Romano[1,2,5] and A. Tumino[1,6]*

[1]*Laboratori Nazionali del Sud, INFN, Catania, Italy,* [2]*Dipartimento Fisica e Astronomia "Ettore Majorana", Università degli Studi di Catania, Catania, Italy,* [3]*Dipartimento di Fisica e Geologia, Università degli Studi di Perugia, Perugia, Italy,* [4]*INFN sezione di Perugia, Perugia, Italy,* [5]*Centro Siciliano di Fisica Nucleare e Struttra della Materia, CSFNSM, Catania, Italy,* [6]*Facoltà di Ingegneria e Architettura, Università degli Studi di Enna "Kore", Enna, Italy*

A large uncertainty for the slow neutron capture nucleosynthesis (s-process) models is caused by the amount of neutrons available to the process itself. This quantity is strongly affected by the $^{13}C(\alpha,n)^{16}O$, and $^{22}Ne(\alpha,n)^{25}Mg$ reaction cross sections, whose measurements at energies corresponding to the s-process thermal conditions (~ 10^2 keV) are mainly hampered by the Coulomb barrier. For this reason, indirect approaches could offer a complementary way of investigation and, among these, the Trojan Horse Method (THM) has been applied to determine these cross sections overcoming the Coulomb barrier. With this approach, a low-energy binary reaction cross section can be obtained selecting the quasi-free contribution from a suitable three-body reaction cross section, taking advantage of the cluster structure of proper nuclei.

Keywords: neutron induced reactions, stellar evolution, nucleosynthesis, indirect process, s-process

OPEN ACCESS

Edited by:
Paul Denis Stevenson,
University of Surrey, United Kingdom

Reviewed by:
Pierre Descouvemont,
Université libre de Bruxelles, Belgium
Giuseppe Verde,
Universities and Research, Italy

****Correspondence:***
R. Spartà
rsparta@lns.infn.it

Specialty section:
This article was submitted to Nuclear Physics, a section of the journal Frontiers in Physics

Received: *14 March 2022*
Accepted: *22 April 2022*
Published: *26 May 2022*

Citation:
Spartà R, La Cognata M, Guardo GL, Palmerini S, Sergi ML, D'Agata G, Lamia L, Lattuada D, Oliva AA, Pizzone RG, Rapisarda GG, Romano S and Tumino A (2022) Neutron-Driven Nucleosynthesis in Stellar Plasma. Front. Phys. 10:896011. doi: 10.3389/fphy.2022.896011

1 INTRODUCTION

Neutron capture nucleosynthesis is the main responsible for the production of elements heavier than Fe. Such a process can be rapid (r-process) or slow (s-process), according with the comparison between the neutron capture reaction (n,γ) rates of the involved nuclei and their half-lives [1], but anyway they are a series of subsequent neutron captures, separated by β − decays. Therefore, the rapidity of the process is determined by the intensity flux of neutron available in the stellar environment in which occurs.

In recent years, nuclear astrophysicists focused their attention to the s-process relevant cross sections, also considering that r-process abundances can be obtained by the s-process ones [2]. The s-process nucleosynthesis follows a path that wanders along the valley of β-stability close to the strongly bound isotopes of a given atomic weight (or mass number) A. The main site of the slow neutron captures is the final Asymptotic Giant Branch (hereafter AGB) phase of low- and intermediate-mass stars. Stars with mass up to 3 $M_\odot$ are actually responsible for the production of the main component of the s-process (i.e., nuclei from Sr to Bi) and the main neutron source is known to be the $^{13}C(\alpha,n)^{16}O$ reaction [3]. It operates at typical energies of 8 keV in radiative conditions and provides a neutron density of about 10^6–10^7 n/cm^3 [4,5]. The $^{22}Ne(\alpha,n)^{25}Mg$ reaction is the second neutron source in AGB stars and it is activated only marginally during the *thermal pulses* (periodic episodes of He-convective burning) in low mass stars. Only red giants more massive than 3 $M_\odot$ (the intermediate mass stars) burn ^{22}Ne efficiently, at maximum temperatures of 3–3.2 · 10^8 K. Even stars with larger masses, terminating their evolution as core-collapse Supernovae, are sites of s-process nucleosynthesis, and in particular they are responsible of the so-called weak component, namely that devoted to the production of nuclei with A ≤ 85 [6].

The s-process is considered as being a rather well-known nucleosynthesis mechanism because 1) its main component occurs in common astrophysical objects and 2) neutron capture reactions are not hampered by the Coulomb barrier. This fact makes the most of (n,γ) reactions relatively easy to be studied experimentally. However, there are still theoretical problems to be understood ([7]), as like as the ^{19}F abundance in AGB stars [8]. Thus, some nuclear reactions cross sections need to be measured with high precision in the energy range of AGB star nucleosynthesis, where objective experimental difficulties are present. Among them, we appoint:

1. Reactions delivering the neutrons for the s process, in particular ^{13}C(α,n)^{16}O (**Section 3**) and ^{22}Ne(α,n)^{25}Mg (**Section 4**), whose cross section determination is affected by the well-known problems in measuring the reactions between charged particles at low energy [9,10];
2. Neutron capture reactions on unstable nuclei, whose half-lives are characterised by time-scales close to those corresponding to neutron capture rates and thus might constitute branching points of the s-nucleosynthesis path;
3. Neutron capture reactions on the so-called poisons of the s-process, i.e. those relatively light nuclei that, having a very large neutron capture cross section, can absorb the neutrons delivered by the ^{13}C(α,n)^{16}O and the ^{22}Ne(α,n)^{25}Mg reactions, subtracting them to the s-nucleosynthesis. Among the poisons of the s-process we recall the ^{14}N, the $^{16-17}$O and the $^{25-26}$Mg. For reactions like ^{14}N (n,p)^{14}C or ^{17}O(n,α)^{14}C (**Section 5**), a precision study of these reactions is very hard to perform, owing to the non-existence of a pure-neutron target and to the current unavailability of a neutron beam facility with sufficient energy precision.
4. β − decays of the nuclei involved in the s process in stellar plasma conditions are estimated only by theoretical calculations. A crucial contribution in this field will be provided by future experiments such as those planned at the PANDORA project [11,12], for which we refer to the specific paper in this volume.

Thanks to the indirect Trojan Horse Method (THM), described in the following section, one can extract the cross sections at the ultra-low energies of astrophysical interest for charged particle induced reactions, where this is made almost impossible by the Coulomb barrier presence. In more recent years, the method has been largely tested and applied with success to shed light on different problems, such as the different levels contributions to the cross sections [13,14], for neutron induced reactions [15–21] and for reactions induced by unstable beams [22,23], thus helping in solving the experimental difficulties of points 1 to 3.

2 THE TROJAN HORSE METHOD

The idea at the base of THM is to obtain the binary reaction cross section of interest for astrophysics $a + x \rightarrow c + C$, by measuring the reaction cross section of a given $A+ a \rightarrow c + C + s$ quasi-free (QF) break-up reaction.

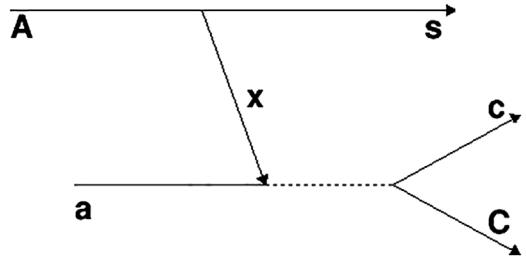

FIGURE 1 | Sketch of the polar diagram representing the TH process.

This is possible if we use a suitable nucleus A (called TH nucleus) that has a high probability to be found in a x-s cluster configuration, so that $A = x \oplus s$. The QF break-up of A occurs if, in the interaction between A and a, in the exit channel s keeps the same momentum distribution before its break-up. In this case s is the *spectator* to the virtual process $a + x \rightarrow c + C$ [24]. It has been experimentally demonstrated that changes in the Trojan Horse nucleus are not impacting the applicability of the THM, despite the change in the spectator cluster for example from a charged to a neutral particle [25,26]. **Figure 1** represents a sketch of the TH process, where it is possible to apply the polar approximation [27] only for small spectator momenta p_s respecting the relation in [28].

The possibility to reach ultra-low energies is given by the binding energy E_B of x inside A, which compensates for the beam energy [29–31]. One of the advantages of the THM is that, using only one beam energy, the variation of the spectator momentum values inside the limit in [28] makes it possible to scan almost the entire energy range of interest.

Once the QF break-up data have been selected from all other reaction mechanisms with the same final state, in the Plane Wave Impulse Approximation (PWIA) the three-body cross section can be factorized as:

$$\frac{d^3\sigma}{d\Omega_c d\Omega_C dE_C} \propto KF|\phi(p_s)|^2 \left(\frac{d\sigma}{d\Omega}\right)_{Cc}^{HOES} \quad (1)$$

where the phase space is taken into account by the kinematical factor KF and $|\phi(p_s)|^2$ is the squared Fourier transform of the radial wave function describing the intercluster motion inside the TH nucleus. The factor KF $\cdot|\phi(p_s)|^2$ is calculated by means of a Montecarlo simulation where the momentum distribution has a width fixed to the value measured experimentally, to account for the distortion effects arising at low transferred momenta [32,33].

The extracted $(d\sigma/d\Omega)^{HOES}$ obtained inverting **Eq. (1)** is denoted half-off-energy-shell (HOES), being x virtual and then the entrance channel off-shell, while the exit channel in on-shell (OES). This cross section has to be corrected for the penetration factor, that in case of n-induced reaction is only relative to the centrifugal barrier, and then it has to be normalized to direct data at energies higher than the Coulomb barrier, where the HOES and OES cross sections are proportional.

Details and reviews of the THM can be found in [34,35].

3 THE $^{13}C(\alpha,n)^{16}O$ NEUTRON SOURCE FOR THE MAIN COMPONENT

The main s-process neutron source has been singled out in AGB stars where, following the injection of protons from the outer layers into the carbon- and helium-rich shell, they are captured by carbon nuclei, leading to the formation of a ^{13}C pocket [36]. Then, at typical temperature range between 0.8×10^8 K and 1×10^8 K [3], ^{13}C is burnt through the $^{13}C(\alpha, n)^{16}O$ reaction producing neutrons. Such temperatures correspond to $^{13}C - \alpha$ center-of-mass energies of about $E_{13C-\alpha} \sim 140–230$ keV. A recent review can be found in Xu et al. [37] and besides, theoretical evaluations are available, using microscopic cluster approach, leading to results in good agreement with the experimental data in [38] and in [39]. It is worth noting that the crucial role of the $\frac{1}{2}+$ subthreshold state was already foreseen in [38] despite of the absence of very low energy data at the time.

Owing to its astrophysical importance, the $^{13}C(\alpha, n)^{16}O$ reaction has been the subject of many direct and indirect studies. Indirect methods are mandatory since direct measurements could not span so far the energy window of astrophysical interest, which lies between 150 and 230 keV. For instance, the most recent direct measurement [40] could only reach about 230 keV in the center of mass system. Extrapolations to even lower energies are then necessary to establish the trend of the $^{13}C(\alpha, n)^{16}O$ astrophysical factor inside the Gamow window. However, the understanding of the astrophysical region of the S-factor is complicated by the interplay between the rise due to the ^{17}O 6.356 MeV $1/2^+$ level and the enhancement due to the electron screening effect (see e.g. La Cognata et al. [41] and references therein). The latter introduces a correction of about 20% at the lowest-energy data point of Drotleff et al. [42] at 279 keV, growing up exponentially approaching the energy region of astrophysical interest. Yet, larger uncertainties are introduced by the occurrence of the 6.356 MeV broad resonance in ^{17}O. Indeed, until 2015 [43], it was commonly assumed that the aforementioned $1/2^+$ ^{17}O state was lying −3 keV below the $^{17}O \rightarrow ^{13}C + \alpha$ dissociation threshold [44]. Precision spectroscopy studies [43] have shown that the location of such near-threshold resonance should be 4.7 keV above the $^{17}O \rightarrow ^{13}C + \alpha$ dissociation energy.

An additional challenge for direct measurements is the determination of the absolute value of the $^{13}C(\alpha, n)^{16}O$ astrophysical factor, since neutron detectors are often used to measure the cross section. Already in Heil et al. [45], the scatter of the absolute normalizations of existing data was evident and as large as a factor two. This spread was realistically attributed to systematic errors affecting neutron detection efficiency as a function of its energy. This is the reason that lead Heil et al. [45] to measure the experimental detection efficiency using a setup identical to the one used for the study of the $^{13}C(\alpha, n)^{16}O$ reaction and to cross check the results using a GEANT4 simulation. Then, the obtained astrophysical factor was used to scale existing $^{13}C(\alpha, n)^{16}O$ data sets. Earlier THM studies of this reaction used the Heil et al. [45] astrophysical factor for normalization.

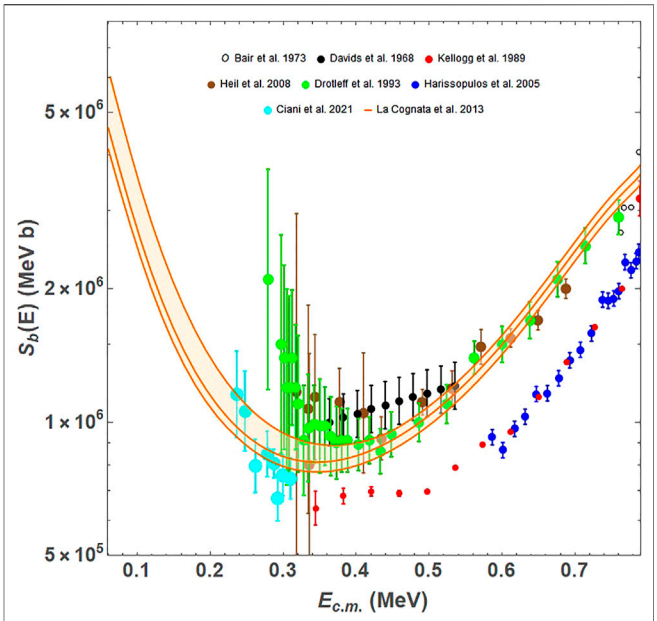

FIGURE 2 | Comparison of S(E)-factor obtained in Trippella and La Cognata [48] (orange band) with direct measurements: cyan solid circles are from Ciani et al. [40], black from Davids [58], open circles from Bair and Haas [59], red from Kellogg et al. [60], green from Drotleff et al. [42], blue from Harissopulos et al. [61], brown from Heil et al. [45].

In the THM framework, the $^{13}C(\alpha, n)^{16}O$ S-factor was extracted from the $^{13}C(^6Li, n^{16}O)^2H$ QF cross section, measured at 8 MeV beam energy. With this method, neither Coulomb nor centrifugal barriers quell the cross section and electron screening does not shield the $^{13}C - ^4He$ interaction. However, astrophysical energies could be reached thanks to the energy spent to break ^6Li into to the $\alpha - d$ system as well as to their relative motion. Details on the THM measurement can be found in La Cognata et al. [46,47]. A drawback of the THM is the need of normalization to existing direct data. In those works, the $E_{13C-\alpha}$ energy region between ~ 0.6 − 1.2 MeV was selected, namely a region where the contribution of the threshold state is negligible.

While a THM S-factor in good agreement with the direct ones scaled to match the Heil et al. [45] absolute value was found, a Coulomb modified Asymptotic Normalization Coefficient (ANC) [47] for the $1/2^+$ ^{17}O threshold state equal to $7.7 \pm 0.3_{stat}{}^{+1.6}_{-1.5\ norm}$ was determined, contradicting the existing independent assessments of the Coulomb modified ANCs, whose weighted average is 3.9 ± 0.5 fm^{-1}. This may be attributed to the systematic errors affecting direct data absolute normalization. This fact triggered further studies, which ended up in the work of Trippella and La Cognata [48]. Indeed, to unequivocally size the contribution of the ^{17}O threshold state to the reaction rate, many coherent measurements of its ANC were carried out [49–52].

The ANC method is another powerful indirect method meant to extract the direct radiative part of the cross section for reactions of importance for astrophysics: with this technique, in principle, it is in fact possible to study (p,γ), (n,γ) and (α, γ) reactions of

astrophysical importance using p-, n- or α-transfer. Such transfer, at low energies, must show a mostly peripheral character, and such a condition must be verified experimentally. The difference between ANC and THM lies in which kind of reaction can be studied–direct and resonant capture, respectively–and in the reaction products: the ANC method, in fact, can be applied just for reactions that have γ-rays in the exit channel (see also [53] for a recent review on the ANC and, particularly [54], for proton [55], for neutron and [56] for alpha captures at low energies from suitable transfer reactions, also using mirror nuclei [57]).

Therefore, a change in the paradigm usually adopted in the THM application was implemented and the THM S-factor was normalized to the ANC of 6.356 MeV state. This approach lead to a concordance scenario for the ^{13}C (α, n)^{16}O S-factor, where both direct (some data sets with a more appropriate normalization) and indirect data (both ANC and THM) accurately agree.

With the normalization of Trippella and La Cognata [48], the astrophysical factor in **Figure 2** (shown as an orange band upper, where middle and lower orange lines are used for recommended + 1σ, recommended and recommended − 1σ THM S-factor) was deduced. An ANC of 3.6 ± 0.7 fm^{-1} has been determined, in perfect agreement with the weighted average of the results in the literature. The corresponding THM S-factor at $E_{c.m.}$ = 140 keV was found to be $1.80^{+0.50}_{-0.17} \times 10^6$ MeVb, to be compared with the astrophysical factor in Heil et al. [45] $S(140\,\text{keV}) = 2.2^{+1.1}_{-0.8} \times 10^6$ MeVb. More details can be found in Trippella and La Cognata [48]; a recent direct measurement reported in Ciani et al. [40] has confirmed such results, as it is clearly demonstrated in **Figure 2**, where other direct measurements with their original normalizations are shown.

4 THE ^{22}NE(α,N)^{25}MG NEUTRON SOURCE FOR THE WEAK COMPONENT

A key role in the s-process is played by the ^{22}Ne(α,n)^{25}Mg reaction, the major neutron producer for its weak component (60 < A < 0) in massive stars, influencing all the late evolution of stars, until their death. Despite of the importance of this reaction, in the energy region of astrophysical interest (E_{cm} = 600 ± 300 keV) three orders of magnitude discrepancies in the cross section of data available in literature are still present, making those data essentially not useful for astrophysical needs [62].

The trend of the excitation function measured so far shows a steep drop in the yield which makes it possible to provide only upper limits to the cross section already at center-of-mass energies of the order of 800 keV, that is at the edge of the region of interest. A clear picture of the status of the art can be found in [63]. Indeed, direct measurements at such low energies are very challenging due to the exponential Coulomb damping (Coulomb barrier is located at 3.5 MeV) of the cross section to values less than 1 μb, pushing the signal-to-noise ratio essentially to zero.

Indirect measurements, such as capture and transfer reactions [63], at low energy are thus needed to supply resonance parameters, such as spectroscopic factors, to be used in the calculation of the reaction rate. In this regard, a recent paper [10] recalculated the reaction rates of ^{22}Ne(α,n)^{25}Mg and its competitor ^{22}Ne(α,γ)^{26}Mg, updating energies and spin-parities of all the ^{26}Mg levels, particularly focusing on the results in [64], obtained with ^{22}Ne(^{6}Li,d)^{26}Mg, and ^{22}Ne (^{7}Li,t)^{26}Mg transfer reactions. The authors find that, excluding the results in [64], s-process nucleosynthesis will not substantially change, but including them leads to a better agreement of Ba and Zr isotopic ratios with the data from presolar SiC grains. However, the results reported in [10,64] suggest the need for further measurements, particularly focusing on the excitation function trend, to include also levels interference in the reaction rate evaluation.

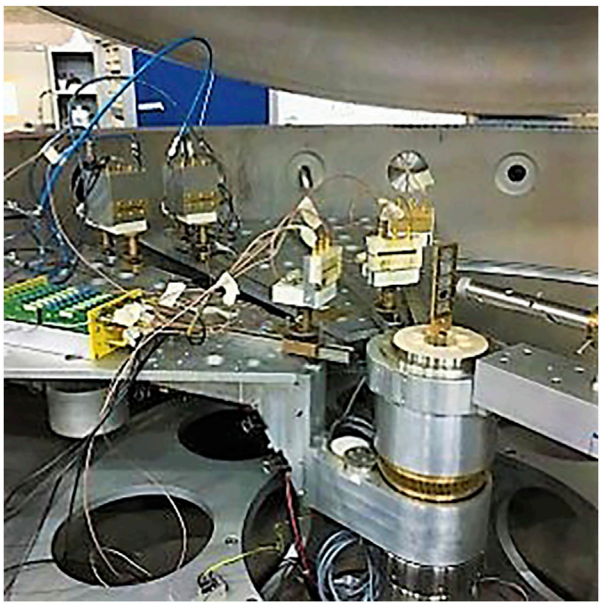

FIGURE 3 | Setup of one of the experimental runs of the Magn-a experiment in Catania, at LNS, aimed to perform the ^{2}H(^{25}Mg,αp)^{22}Ne reaction to extract the ^{22}Ne(α,n)^{25}Mg cross section with the THM and the detailed balance principle.

To try to deal with this issue, a new measurement was performed at INFN-LNS of Catania (Italy), aimed at bypassing the challenges that prevented to obtain the result until now. To avoid problems related to the poor efficiency in neutron detection, the idea was to obtain the desired cross section applying the detailed balance principle to the inverse reaction: ^{25}Mg(n,α)^{22}Ne. Then, to avoid the use of neutron beam (and the consequent worsening of the energy resolution) the THM was used, exploiting the well-known p-n structure of the deuteron, used as neutron virtual source. The experiment to measure the 3-body ^{2}H(^{25}Mg,αp)^{22}Ne cross section was performed in the Camera2000 scattering chamber, because of its 1 m radius that allowed to put detectors as far as it was needed to keep a good angular resolution to apply the THM. In **Figure 3** is evident how the use of THM also helped to bypass complex setups. Moreover, THM allowed the use of thin CD_2 targets, to minimize the beam energy spread on the target. The

first ^{25}Mg beam of LNS was accelerated with the Tandem accelerator for this experiment.

This measurement was performed with two different experimental approaches, and thus setups. At first, coincidences between α particles and the spectator proton, using Position Sensitive Detectors (PSD), were detected, reconstructing the ^{22}Ne kinematics offline, identifying the desired ions with ΔE-E technique using thin PSD (35 μm thickness) as ΔE stage. Dealing with the very low energy of the spectator proton below 1 MeV, forced to reduce the acquisition system threshold to its minimum. The second approach tried was to detect ^{22}Ne and α particles in coincidence, reconstructing the proton kinematics offline. This has implied to change beam energy to stay focused on the region where QF kinematics is most probable, as required by THM, from $^{(7+)25}$Mg at 74 MeV to $^{(6+)25}$Mg at 50 MeV. The ΔE stage PSDs were substituted with two Ionization Chambers (5 cm deep), filled with isobutane (p = 65 mb) to detect and separate ^{22}Ne. The analysis of these data is still ongoing and additional validity tests are mandatory in order to safely apply THM to this specific case.

It is worth noting that many other possibilities of indirect measurements can be considered. The possible extension of the THM to p-wave intercluster motion nuclei could open the doors to the use of ^{23}Ne as TH nucleus for its ^{22}Ne + p configuration, and another good candidate TH nucleus can be the ^{26}Mg as ^{22}Ne+α in s-wave. In any case, the possibility of new highly ^{4}He-enriched solid targets obtained with NESTOR [65], the new ECR ion source at LNS, will be pivotal for these measurements.

5 NEUTRON POISONS REACTIONS

The presence of certain nuclei lighter than Fe produced in the previous stages of stellar evolution, causes the capture of a large fraction of the neutrons produced by the ^{13}C(α,n)^{16}O and ^{22}Ne(α,n)^{25}Mg reactions. These neutron poisons reactions significantly constrain the *s*-process efficiency [1]. As an example, due to the large abundances of ^{12}C and ^{16}O, the ^{12}C(n,γ)^{13}C and ^{16}O(n,γ)^{17}O reactions are serious neutrons consumer, removing a non-negligible fraction of the produced neutrons [5].

5.1 The ^{17}O(n,α)^{14}C

In massive stars (with initial mass M > M$_\odot$), due to the high abundance of oxygen from CNO cycle, one of the most important neutron poison reaction is the ^{16}O(n,γ)^{17}O [66]. The ^{17}O produced by the ignition of this reaction can undergo the ^{17}O(α,n)^{20}Ne reaction, that represents a recycling channel for neutrons, or the ^{17}O(n,α)^{14}C reaction that is another neutron-absorbing reaction [67]. Thus, in order to establish the total neutron flux available for the so-called weak s-process pathway, it is of fundamental importance to ascertain the ratio between the cross sections of the aforementioned reactions. For this reason, the ^{17}O(n,α)^{14}C reaction has triggered several measurements with direct experiments and by applying the detailed balance principle to the inverse reaction [68–72]. The population of two excited

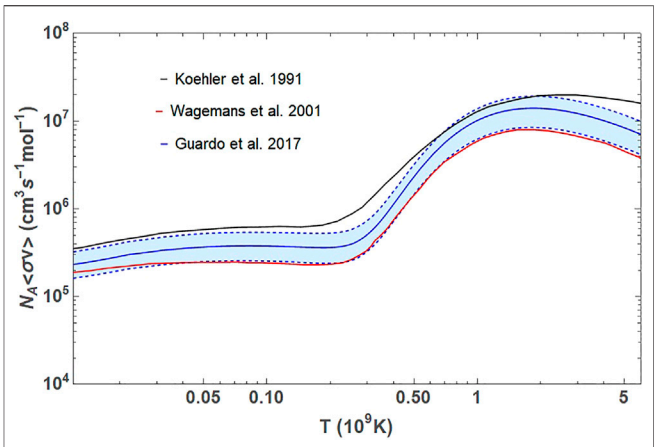

FIGURE 4 | THM reaction rate for the ^{17}O (n,α)^{14}C reaction (blue line) in comparison with the ones available in literature (see text for details).

states at 8,213 keV and 8,282 keV and the contribution of a sub-threshold level at 8,038 keV are present in the available data, while no evidence for the 8,125 keV level is shown [73]. Indeed, the contribution of this resonance is suppressed by the centrifugal barrier, since this resonance is populated in *f*-wave. In addiction, in the astrophysically relevant temperature region, the reaction rate calculated from measurements available in literature, is affected by a difference of about a factor of 2.5–3, due to disagreement present in the different data sets [71].

For such a reason, two THM measurements were performed at different laboratories, namely at LNS-INFN in Catania (Italy) and at ISNAP (Institute for Structure and Nuclear Astrophysics) in Notre Dame (IN—United States). The experiments were devoted to the measurement of the cross section of the ^{2}H (^{17}O,α^{14}C)p three-body reaction to cover the energy range from zero up to a few hundred keV in the binary reaction center-of-mass energy [74,75]. A ^{17}O beam of 41 (43.5) MeV was delivered onto a CD_2 target in the LNS (ISNAP) experiment.

In order to probe the presence of the QF reaction process, the procedure described in [74,75] was followed, finally extracting the HOES cross section of the ^{17}O (n,α)^{14}C reaction.

The experimental data of the two data sets, weighted over the respective errors and summed in order to improve the statistical precision, were then normalized to the available direct measurements [71], integrated to the angular distribution and fitted following the modified R-matrix approach [76] in order to calculate the reduced γ-widths of the excited levels. Thus, the calculated reaction rate is shown in **Figure 4** with a blue line, while the blue band highlights the region allowed by uncertainties (statistical and normalization). In comparison, reaction rates from [69] (black line) and [71] (red line) are reported.

In this measurement, it was possible to excite the sub-threshold level centered at −7 keV in the center-of-mass system corresponding to the 8.039 MeV level of ^{18}O, which is important to determine the ^{17}O(n,α)^{14}C reaction rate. In addiction, it was found that the resonance corresponding to the 8.213 MeV level is better reproduced by adopting an angular momentum l = 2 instead of l = 0, as assumed in the

past [68]. This result triggered the need of a new experiment with an improved detection setup and a wider angular coverage, whose analysis is still ongoing [77]. Finally, the use of deuteron as source of virtual neutrons allows us to populate the level centered at 75 keV in the ^{17}O-n center-of-mass system, corresponding to the 8.121 MeV level of ^{18}O. Due to its 5^- J^π assignment, the population of such level is suppressed in direct measurements because of its $l = 3$ angular momentum. The application of the modified R-matrix approach made it possible to measure the neutron and α partial widths that are in agreement with the ones available in the literature, while these partial widths were extracted for the first time in the case of the 8.125 MeV level. Therefore, extensive calculations are ongoing in order to understand the precise impact of the present results on astrophysics.

5.2 The ^{14}N(n,p)^{14}C

^{14}N is very abundant in stars, due to its production during the stage prior to the *s*-process, namely the hydrogen-burning in the CNO cycle. Thus, with its relatively high cross section, this reaction represents a strong neutron poison, especially in low-mass AGB stars [78]—thus for the main component elements production. Moreover, ^{14}N is of crucial importance in the nucleosynthetic origin of fluorine and the He-burning shell in AGB stars is thought to be the most likely site for this synthesis, mainly through the nuclear chain ^{14}N(α,γ)^{18}F(β^+) ^{18}O(p,α) ^{15}N(α, γ)^{19}F. In this sense, the ^{14}N(n,p)^{14}C reaction plays a key role because of its double effect of removing neutrons and producing protons. In addition, the protons can trigger the ^{18}O(p,α)^{15}N or the ^{13}C(p,γ)^{14}N reactions, being the last one in competition with the ^{13}C(α,n)^{16}O reaction [5].

The first direct measurement of the stellar ^{14}N (n,p)^{14}C cross section was done by [79]. Their result for the reaction rate was about a factor three smaller than the rate used in most of the previous s-process calculations, but it was also 2–3 times smaller than rates estimated from the inverse reaction and extrapolations from the thermal cross section, for which an evaluated value of 1.83 b was adopted. Indeed, measurements performed from thermal neutron energy up to 35 keV [80,81] found clear evidence for a 1/v behavior of the ^{14}N(n,p)^{14}C reaction cross section up to approximately 30 keV and also their results for the stellar reaction rate at $kT = 525$ keV are about a factor of 3 higher than reported by [79]. Measurements with quasimonoenergetic neutrons at 25 keV from [82] are in fair agreement with the results from [80,81] and with the estimates from the inverse reaction, since again the same thermal value was used for the normalization. Another direct measurement of the ^{14}N (n,p)^{14}C stellar cross section at kT = 525 keV was done by [83]. The authors found a value approximately a factor of 2 higher than [79] and a rather good agreement with the other results. In 1999 a new measurement at neutron energies of 35.8 and 67.1 keV by [84] supports the previous measurements but have rather large (20 and 12%, respectively) uncertainties. In 2000 [85] determined at the high flux reactor of the ILL in Grenoble an accurate value of (1.93 ± 0.05) b for the ^{14}N($n_{thermal}$,p)^{14}C cross section, that is in good agreement with some results present in literature but differs by 10% with the lower extreme value.

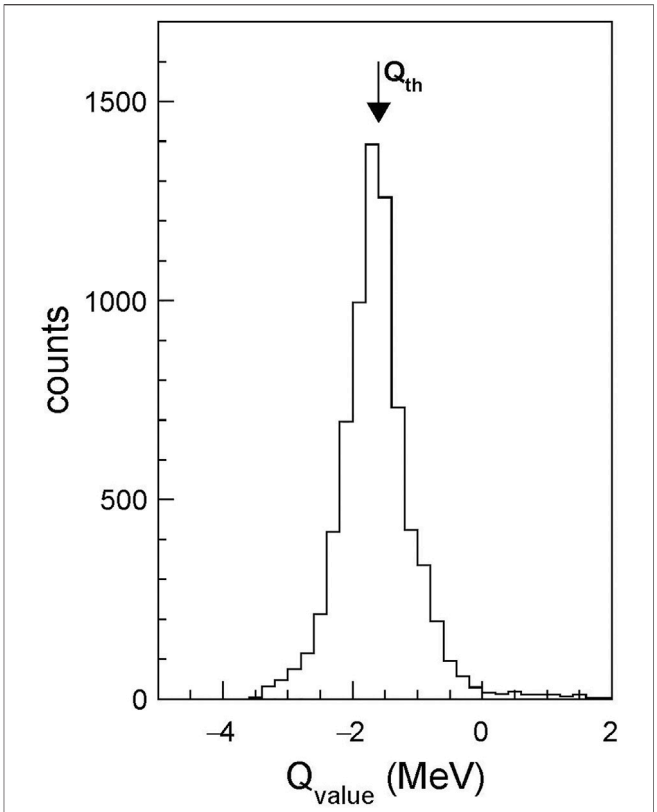

FIGURE 5 | The experimental Q-value for the selected ^{2}H(^{14}N,p ^{14}C)p events. The black arrow correspond to the theoretical Q value, Q_{th} = -1.6 MeV.

For this reason, a careful new evaluation is needed and the THM was applied to determine the cross section of the ^{14}N (n,p) ^{14}C reaction by selecting the QF contribution to the ^{2}H(^{14}N,p ^{14}C)p reaction. The experiment was performed at INFN-LNS where the SMP Tandem accelerator provided a 40 MeV ^{14}N beam on deuterated polyethylene target (CD_2) of about 150 μg/cm^2 was placed at 90°with respect to the beam axis. The reaction channel selection has been performed *via* the prior selection of the Z = 6 locus in the ΔE-E telescope and the full kinematic reconstruction of the selected events with the hypothesis of an unitary mass for the third undetected particle.

The experimental Q-value spectrum has been reconstructed and the result is shown in **Figure 5**. The spectrum is centered at −1.61 MeV, showing a FWHM of about 130 keV, reflecting the energy loss of the incoming beam in the 150 μg/cm^2 CD_2 thick target. The experimental value nicely overlaps the expected one of −1.599 MeV, thus showing the correct selection of the reaction channel. Further studies on these data, presently under way and beyond the scope of this article, will be published in near future.

6 CONCLUSION

The use of THM is helping in achieving neutron producers and poisons reaction cross sections at energies relevant for the

s-process in stars, where they are otherwise unreachable, because of the Coulomb barrier presence or the struggling with the neutron detection.

For $^{13}C(\alpha,n)^{16}O$ the results obtained with THM has already moved forward our knowledge in this sense, as it summarized in Trippella and La Cognata [48]. On the contrary, much work remains to be done for $^{22}Ne(\alpha,n)^{25}Mg$, where the results of an ongoing analysis of a TH measurement can boost our knowledge on its reaction rate. This has not been found out yet, despite of recent indirect measurements clarifying the role of crucial levels in ^{26}Mg. The same holds for the neutron poisons reactions, which affect the neutron flux available for the s-process nucleosynthesis, mainly $^{17}O(n,\alpha)^{14}C$ and $^{14}N(n,p)^{14}C$. Also in these cases, ongoing analysis on TH measurements will help in completing the picture of our understanding of the neutron involving reactions in the stellar plasma.

Thus, the overall s-process nucleosynthesis understanding can be strongly constrained by the results of these reaction rates, jointly with the measurements of half-lives of radioactive nuclei at the s-process path branching points.

AUTHOR CONTRIBUTIONS

RS, MLC, GLG, SP, and MLS wrote the paper. All the coauthors participated to the experiments described in the paper and revised the paper itself. Experimental data were analyzed by MLC, RS, GLG, and MLS for $^{13}C(\alpha,n)^{16}O$, $^{22}Ne(\alpha,n)^{25}Mg$, $^{17}O(n,\alpha)^{14}C$ and $^{14}N(n,p)^{14}C$, respectively.

ACKNOWLEDGMENTS

The authors acknowledge "Programma ricerca di ateneo UNICT2020-22 linea 2" and "Starting grant 2020" from the University of Catania.

REFERENCES

1. Käppeler F, Gallino R, Bisterzo S, Aoki W. Thesprocess: Nuclear Physics, Stellar Models, and Observations. *Rev Mod Phys* (2011) 83:157–93. doi:10.1103/RevModPhys.83.157
2. Pritychenko B (2020). *Determination of Solar System R-Process Abundances Using endf/b-viii.0 and Tendl-2015 Libraries*. doi:10.2172/1737434
3. Busso M, Gallino R, Wasserburg GJ. Nucleosynthesis in Asymptotic Giant Branch Stars: Relevance for Galactic Enrichment and Solar System Formation. *Annu Rev Astron Astrophys* (1999) 37:239–309. doi:10.1146/annurev.astro.37.1.239
4. Gallino R, Busso M, Picchio G, Raiteri CM, Renzini A. On the Role of Low-Mass Asymptotic Giant Branch Stars in Producing a Solar System Distribution of S-Process Isotopes. *Astrophysical J* (1988) 334:L45. doi:10.1086/185309
5. Iliadis C, Longland R, Champagne AE, Coc A, Fitzgerald R. Charged-particle Thermonuclear Reaction Rates: Ii. Tables and Graphs of Reaction Rates and Probability Density Functions. *Nucl Phys A* (2010) 841:31–250. doi:10.1016/j.nuclphysa.2010.04.009
6. The LS, El Eid MF, Meyer BS. s-Process Nucleosynthesis in Advanced Burning Phases of Massive Stars. *Astrophysical J* (2007) 655:1058–78. doi:10.1086/509753
7. Busso M, Vescovi D, Palmerini S, Cristallo S, Antonuccio-Delogu V. s-Processing in Agb Stars Revisited. Iii. Neutron Captures from Mhd Mixing at Different Metallicities and Observational Constraints. *Astrophysical J* (2021) 908:55. doi:10.3847/1538-4357/abca8e
8. D'Agata G, Pizzone R, La Cognata M, Indelicato I, Spitaleri C, Palmerini S, et al. The 19F (α, P)22Ne Reaction at Energies of Astrophysical Relevance by Means of the Trojan Horse Method and its Implications in Agb Stars. *Astrophysical J* (2018) 860:61.
9. Cristallo S, Cognata ML, Massimi C, Best A, Palmerini S, Straniero O, et al. The Importance of the 13C(α,n)16O Reaction in Asymptotic Giant Branch Stars. *Astrophysical J* (2018) 859:105. doi:10.3847/1538-4357/aac177
10. Adsley P, Battino U, Best A, Caciolli A, Guglielmetti A, Imbriani G, et al. Reevaluation of the Ne22(α,γ)Mg26 and Ne22(α,n)Mg25 Reaction Rates. *Phys Rev C* (2021) 103:015805. doi:10.1103/PhysRevC.103.015805
11. Mascali D, Musumarra A, Leone F, Romano F, Galatà A, Gammino S, et al. Pandora, a New Facility for Interdisciplinary In-Plasma Physics. *The Eur Phys J A* (2017) 53:1–14. doi:10.1140/epja/i2017-12335-1
12. Mascali D, Santonocito D, Amaducci S, Andò L, Antonuccio V, Biri S, et al. A Novel Approach to β-Decay: PANDORA, a New Experimental Setup for Future In-Plasma Measurements. *Universe* (2022) 8:80. doi:10.3390/universe8020080
13. Cvetinović A, Spitaleri C, Spartá R, Rapisarda G, Puglia S, La Cognata M, et al. Trojan Horse Measurement of the $^{10}B(p,\alpha_0)^7Be$ Cross Section in the Energy Range from 3 Kev to 2.2 Mev. *Phys Rev C* (2018) 97:065801.
14. Rapisarda G, Spitaleri C, Cvetinović A, Spartà R, Cherubini S, Guardo G, et al. Study of the $^{10}B(p,\alpha_1)^7Be$ Reaction by Means of the Trojan Horse Method. *Eur Phys J A* (2018) 54:1–12. doi:10.1140/epja/i2018-12622-3
15. Spartà R, Lamia L, La Cognata M, Spitaleri C, Rapisarda G, Guardo G, et al. $^{10}B(n,\alpha_0)^7Li$ and $^{10}B(n,\alpha_1)^7Li$ Reactions Measured via *T*rojan *H*orse *M*ethod. *Eur Phys J A* (2021) 57:1–9.
16. Hayakawa S, La Cognata M, Lamia L, Yamaguchi H, Kahl D, Abe K, et al. Constraining the Primordial Lithium Abundance: New Cross Section Measurement of the 7Be + N Reactions Updates the Total 7Be Destruction Rate. *The Astrophysical JournalL* (2021) 915:L13. doi:10.3847/2041-8213/ac061f
17. Pizzone R, Spampinato C, Spartá R, Couder M, Tan W, Burjan V, et al. Indirect Measurement of the 3He(n, p)3H Reaction Cross Section at Big Bang Energies. *Eur Phys J A* (2020) 56:1–7. doi:10.1140/epja/s10050-020-00212-x
18. Guardo G, Spitaleri C, Lamia L, Spartá R, Carlin N, Cherubini S, et al. The $^{10}B(n,\alpha)^7Li$ Cross Sections at Ultra-low Energy through the Trojan Horse Method Applied to the $^2H(^{10}B,\alpha^7Li)H$. *Eur Phys J A* (2019) 55:1–13. doi:10.1140/epja/i2019-12914-0
19. Gulino M, Spitaleri C, Cherubini S, Crucillà V, Cognata ML, Lamia L, et al. Study of the6Li(n, α)3H Reaction via the2H Quasi-free Break-Up. *J Phys G: Nucl Part Phys* (2010) 37:125105. doi:10.1088/0954-3899/37/12/125105
20. Lamia L, Spitaleri C, Carlin N, Cherubini S, Del Szanto M, Gulino M, et al. Indirect Study of (P, α) and (N, α) Reactions Induced on boron Isotopes. *Il nuovo cimento C* (2008) 31:423–31.
21. Tumino A, Spitaleri C, Bonomo C, Cherubini S, Figuera P, Gulino M, et al. Quasi-free 6Li(n,α)3H Reaction at Low Energy from 2H Break-Up. *Eur Phys J A* (2005) 25:649–50. doi:10.1140/epjad/i2005-06-085-1
22. Lamia L, Mazzocco M, Pizzone RG, Hayakawa S, La Cognata M, Spitaleri C, et al. Cross-section Measurement of the Cosmologically Relevant 7Be(n, α)4He Reaction over a Broad Energy Range in a Single Experiment. *Astrophysical J* (2019) 879:23. doi:10.3847/1538-4357/ab2234
23. Gulino M, Cherubini S, Kubono S, Lamia L, Cognata ML, Pizzone RG, et al. Application of Trojan Horse Method to Radioactive Ion Beams Induced Reactions. *J Phys Conf Ser* (2020) 1610:012005. doi:10.1088/1742-6596/1610/1/012005
24. Satchler G. *Direct Nuclear Reactions, International Series of Monographs on Physics*. Oxford, UK: Oxford University Press (1983).
25. Pizzone R, Spitaleri C, Lamia L, Bertulani C, Mukhamedzhanov A, Blokhintsev L, et al. Trojan Horse Particle Invariance Studied with the $^6Li(d,\alpha)^4He$ and $^7Li(p,\alpha)^4He$ Reactions. *Phys Rev C* (2011) 83:045801.

26. Pizzone R, Spitaleri C, Bertulani C, Mukhamedzhanov A, Blokhintsev L, La Cognata M, et al. Updated Evidence of the Trojan Horse Particle Invariance for the 2H(d, p)3H Reaction. *Phys Rev C* (2013) 87:025805.
27. Baur G. Breakup Reactions as an Indirect Method to Investigate Low-Energy Charged-Particle Reactions Relevant for Nuclear Astrophysics. *Phys Lett B* (1986) 178:135–8. doi:10.1016/0370-2693(86)91483-8
28. Shapiro IS, Kolybasov VM, Augst GR. Treiman-Yang Criterion for Direct Nuclear Reactions. *Nucl Phys* (1965) 61:353–67. doi:10.1016/0029-5582(65)90097-0
29. Spitaleri C. *Proceedings of the Fifth Hadronic Physics winter Seminar*. Folgaria-TN, italy: World Scientific Singapore (1990).
30. Spitaleri C, La Cognata M, Lamia L, Mukhamedzhanov A, Pizzone R. Nuclear Astrophysics and the Trojan Horse Method. *Eur Phys J A* (2016) 52:1–9. doi:10.1140/epja/i2016-16077-2
31. Spitaleri C, La Cognata M, Lamia L, Pizzone R, Tumino A. Astrophysics Studies with the Trojan Horse Method. *Eur Phys J A* (2019) 55:1–29. doi:10.1140/epja/i2019-12833-0
32. Pizzone R, Spitaleri C, Mukhamedzhanov A, Blokhintsev L, Bertulani C, Irgaziev B, et al. Effects of Distortion of the Intercluster Motion in ^{2}H, ^{3}He, ^{3}H, ^{6}Li, and ^{9}Be on Trojan Horse Applications. *Phys Rev C* (2009) 80:025807.
33. Pizzone R, Bertulani C, Lamia L, Cognata ML, Sergi M, Spartá R, et al. Clusters and Their Fundamental Role for Trojan Horse Method. *Eur Phys J A* (2020) 56:1–11. doi:10.1140/epja/s10050-020-00285-8
34. Tribble R, Bertulani C, La Cognata M, Mukhamedzhanov A, Spitaleri C. Indirect Techniques in Nuclear Astrophysics: a Review. *Rep Prog Phys* (2014) 77:106901. doi:10.1088/0034-4885/77/10/106901
35. Tumino A, Bertulani CA, La Cognata M, Lamia L, Pizzone RG, Romano S, et al. The Trojan Horse Method: A Nuclear Physics Tool for Astrophysics. *Annu Rev Nucl Part Sci* (2021) 71:345–76. doi:10.1146/annurev-nucl-102419-033642
36. Gallino R, Arlandini C, Busso M, Lugaro M, Travaglio C, Straniero O, et al. Evolution and Nucleosynthesis in Low-Mass Asymptotic Giant Branch Stars. II. Neutron Capture and thes-Process. *Astrophysical J* (1998) 497:388–403. doi:10.1086/305437
37. Xu Y, Takahashi K, Goriely S, Arnould M, Ohta M, Utsunomiya H. NACRE II: an Update of the NACRE Compilation of Charged-Particle-Induced Thermonuclear Reaction Rates for Nuclei with Mass Number A<16. *Nucl Phys A* (2013) 918:61–169. doi:10.1016/j.nuclphysa.2013.09.007
38. Descouvemont P. Microscopic Analysis of the 13C(α, n) ^{16}O and 13C(α,α)^{13}C Reactions. *Phys Rev C* (1987) 36:2206–11. doi:10.1103/PhysRevC.36.2206^{13}
39. Dufour M, Descouvemont P. Multichannel Study of the 13C(α, n)16O and 16O(n,γ)17O Reactions. *Phys Rev C* (2005) 72:015801. doi:10.1103/PhysRevC.72.015801
40. Ciani GF, Csedreki L, Rapagnani D, Aliotta M, Balibrea-Correa J, Barile F, et al. Direct Measurement of the ^{13}C(α,n)^{16}O Cross Section into the S-Process Gamow Peak. *Phys Rev Lett* (2021) 127:152701. doi:10.1103/PhysRevLett.127.152701
41. La Cognata M, Spitaleri C, Tumino A, Typel S, Cherubini S, Lamia L, et al. Bare-nucleus Astrophysical Factor of the 3He(d, p)4He Reaction via the "Trojan Horse" Method. *Phys Rev C* (2005) 72:065802. doi:10.1103/PhysRevC.72.065802
42. Drotleff HW, Denker A, Knee H, Soine M, Wolf G, Hammer JW, et al. Reaction Rates of the S-Process Neutron Sources Ne-22(alpha, n)Mg-25 and C-13(alpha, n)O-16. *Astrophysical J* (1993) 414:735. doi:10.1086/173119
43. Faestermann T, Mohr P, Hertenberger R, Wirth H-F. Broad Levels in O17 and Their Relevance for the Astrophysicalsprocess. *Phys Rev C* (2015) 92:052802. doi:10.1103/PhysRevC.92.052802
44. Tilley DR, Weller HR, Cheves CM. Energy Levels of Light Nuclei A = 16-17. *Nucl Phys A* (1993) 564:1–183. doi:10.1016/0375-9474(93)90073-7
45. Heil M, Detwiler R, Azuma RE, Couture A, Daly J, Görres J, et al. The 13C(α,n) reaction and its Role as a Neutron Source for The sprocess. *Phys Rev C* (2008) 78:025803. doi:10.1103/PhysRevC.78.025803
46. La Cognata M, Spitaleri C, Trippella O, Kiss GG, Rogachev GV, Mukhamedzhanov AM, et al. Measurement of the -3 keV Resonance in the Reaction 13C(α,n)16O of Importance in the S-Process. *Phys Rev Lett* (2012) 109:232701. doi:10.1103/PhysRevLett.109.232701
47. La Cognata M, Spitaleri C, Trippella O, Kiss GG, Rogachev GV, Mukhamedzhanov AM, et al. On the Measurement of the 13C(α, n)16O S-Factor at Negative Energies and its Influence on the S-Process. *Astrophysical J* (2013) 777:143. doi:10.1088/0004-637X/777/2/143
48. Trippella O, Cognata ML. Concurrent Application of ANC and THM to Assess the 13C(α,n)16O Absolute Cross Section at Astrophysical Energies and Possible Consequences for Neutron Production in Low-Mass AGB Stars. *Astrophysical J* (2017) 837:41. doi:10.3847/1538-4357/aa5eb5
49. Pellegriti MG, Hammache F, Roussel P, Audouin L, Beaumel D, Descouvemont P, et al. Indirect Study of the 13C(α, n)16O Reaction via the 13C(7Li, t)17O Transfer Reaction. *Phys Rev C* (2008) 77:042801. doi:10.1103/PhysRevC.77.042801
50. Guo B, Li ZH, Lugaro M, Buntain J, Pang DY, Li YJ, et al. New Determination of the 13C(a, n)16O Reaction Rate and its Influence on the S-Process Nucleosynthesis in AGB Stars. *Astrophysical J* (2012) 756:193. doi:10.1088/0004-637X/756/2/193
51. Avila ML, Rogachev GV, Koshchiy E, Baby LT, Belarge J, Kemper KW, et al. New Measurement of Theαasymptotic Normalization Coefficient of The 1/2+state in O17 at 6.356 MeV that Dominates the C13(α,n)O16 reaction Rate at Temperatures Relevant for Thesprocess. *Phys Rev C* (2015) 91:048801. doi:10.1103/PhysRevC.91.048801
52. Mezhevych SY, Rudchik AT, Rudchik AA, Ponkratenko OA, Keeley N, Kemper KW, et al. Cluster Structure of O17. *Phys Rev C* (2017) 95:034607. doi:10.1103/PhysRevC.95.034607
53. Burjan V, Mrazek J, D'Agata G. Anc from Experimental Perspective. *Front Astron Space Sci* (2020) 2020:71. doi:10.3389/fspas.2020.562466
54. Kiss GG, La Cognata M, Yarmukhamedov R, Tursunmakhatov KI, Wiedenhöver I, Baby LT, et al. Indirect Determination of the Astrophysical S Factor for the Li6 (p,γ)Be7 Reaction Using the Asymptotic Normalization Coefficient Method. *Phys Rev C* (2021) 104:015807. doi:10.1103/PhysRevC.104.015807
55. Burjan V, Hons Z, Kroha V, Mrázek J, Piskoř Š, Mukhamedzhanov AM, et al. The Determination of the Astrophysical S-Factor of the Direct ^{18}O(p,γ)^{19}F Capture by the Anc Method. *Eur Phys J A* (2019) 55:1–10. doi:10.1140/epja/i2019-12801-8
56. Kiss GG, La Cognata M, Spitaleri C, Yarmukhamedov R, Wiedenhöver I, Baby LT, et al. Astrophysical S-Factor for the 3He(α,γ)7Be Reaction via the Asymptotic Normalization Coefficient (ANC) Method. *Phys Lett B* (2020) 807:135606. doi:10.1016/j.physletb.2020.135606
57. D'Agata G, Kilic AI, Burjan V, Mrazek J, Glagolev V, Kroha V, et al. Si26(p,γ) P27 Direct Proton Capture by Means of the Asymptotic Normalization Coefficients Method for Mirror Nuclei. *Phys Rev C* (2021) 103:015806. doi:10.1103/PhysRevC.103.015806
58. Davids CN. A Study of (α, N) Reactions on 9Be and 13C at Low Energies. *Nucl Phys A* (1968) 110:619–36. doi:10.1016/0375-9474(68)90377-1
59. Bair JK, Haas FX. Total Neutron Yield from the Reactions 13C(α, n)16O and 17,18O(α, n)20,21Ne. *Phys Rev C* (1973) 7:1356–64. doi:10.1103/PhysRevC.7.1356
60. Kellogg S, Vogelaar R, Kavanagh R. *Bull Am Phys Soc* (1989) 34:1192.
61. Harissopulos S, Becker HW, Hammer JW, Lagoyannis A, Rolfs C, Strieder F. Cross Section of the C13(α,n)O16 reaction: A Background for the Measurement of Geo-Neutrinos. *Phys Rev C* (2005) 72:062801. doi:10.1103/PhysRevC.72.062801
62. Longland R, Iliadis C, Karakas AI. Reaction Rates for the S-Process Neutron Source ^{22}Ne+ α. *Phys Rev C* (2012) 85:065809. doi:10.1103/physrevc.85.065809
63. Jaeger M, Kunz R, Mayer A, Hammer JW, Staudt G, Kratz KL, et al. N22e(α,n)M25g: The Key Neutron Source in Massive Stars. *Phys Rev Lett* (2001) 87:202501. doi:10.1103/physrevlett.87.202501
64. Jayatissa H, Rogachev GV, Goldberg VZ, Koshchiy E, Christian G, Hooker J, et al. Constraining the 22Ne(α,γ)26Mg and 22Ne(α,n)25Mg Reaction Rates Using Sub-coulomb α-transfer Reactions. *Phys Lett B* (2020) 802:135267. doi:10.1016/j.physletb.2020.135267
65. Mazzaglia M, Amato AS, Battiato G, Calabrese G, Celona L, Dantoni L, et al. Design and First Operations of a ECR Based He^{-} Source at INFN-LNS. In: Proc. of ICIS'21 - International Conference on Ion Sources (IOP Publishing) (2022). accepted for publication.
66. Mohr P, Heinz C, Pignatari M, Dillmann I, Mengoni A, Käppeler F. Re-evaluation of the 16O(N, γ)17O Cross Section at Astrophysical Energies and its

Role as a Neutron Poison in the S-Process. *Astrophysical J* (2016) 827:29. doi:10.3847/0004-637x/827/1/29
67. Pignatari M, Gallino R, Heil M, Wiescher M, Käppeler F, Herwig F, et al. The Weak S-Process in Massive Stars and its Dependence on the Neutron Capture Cross Sections. *Astrophysical J* (2010) 710:1557–77. doi:10.1088/0004-637x/710/2/1557
68. Sanders RM. Study of the 14C(p, n)14N and 14C(α, n)17O Reactions. *Phys Rev* (1956) 104:1434–40. doi:10.1103/PhysRev.104.1434
69. Koehler PE, Graff SM. O17(n,α)14C Cross Section from 25 meV to Approximately 1 MeV. *Phys Rev C* (1991) 44:2788–93. doi:10.1103/PhysRevC.44.2788
70. Schatz H, Kaeppeler F, Koehler PE, Wiescher M, Trautvetter H-P. O-17(n, alpha)C-14 - Closure of a Primordial CNO Bi-cycle? *Astrophysical J* (1993) 413:750. doi:10.1086/173042
71. Wagemans J, Wagemans C, Goeminne G, Serot O, Loiselet M, Gaelens M. The 17O(n,α)14 Creaction from Subthermal up to Approximately 350 keV Neutron Energy. *Phys Rev C* (2002) 65:034614. doi:10.1103/PhysRevC.65.034614
72. Avila ML, Rogachev GV, Goldberg VZ, Johnson ED, Kemper KW, Tchuvil'sky YM, et al. α-Cluster Structure of O18. *Phys Rev C* (2014) 90:024327. doi:10.1103/PhysRevC.90.024327
73. Ajzenberg-Selove F. Energy Levels of Light Nuclei A = 18-20. *Nucl Phys A* (1987) 475:1–198. doi:10.1016/0375-9474(87)90205-3
74. Gulino M, Spitaleri C, Tang XD, Guardo GL, Lamia L, Cherubini S, et al. Suppression of the Centrifugal Barrier Effects in the Off-Energy-Shell neutron+17Ointeraction. *Phys Rev C* (2013) 87:012801. doi:10.1103/PhysRevC.87.012801
75. Guardo GL, Spitaleri C, Lamia L, Gulino M, La Cognata M, Tang X, et al. Assessing the Near Threshold Cross Section of the O17(n,α)C14 reaction by Means of the Trojan Horse Method. *Phys Rev C* (2017) 95:025807. doi:10.1103/PhysRevC.95.025807
76. Cognata ML, Spitaleri C, Mukhamedzhanov A, Banu A, Cherubini S, Coc A, et al. A Novel Approach to Measure the Cross Section of the 18O(p, α)15N Resonant Reaction in the 0-200 keV Energy Range. *Astrophysical J* (2009) 708:796–811. doi:10.1088/0004-637x/708/1/796
77. Oliva A, Guardo G, Lamia L, Cherubini S, Cvetinovic A, D'Agata G, et al. Study of the Neutron-Induced Reaction $^{17}O(n,\alpha)^{14}C$ at Astrophysical Energies via the Trojan Horse Method. *Nuovo Cim.C* (2020) 43:111. doi:10.1393/ncc/i2020-20111-710.1051/epjconf/202022702007
78. Lugaro M, Herwig F, Lattanzio JC, Gallino R, Straniero O. s-Process Nucleosynthesis in Asymptotic Giant Branch Stars: A Test for Stellar Evolution. *Astrophysical J* (2003) 586:1305–19. doi:10.1086/367887
79. Brehm K, Becker HW, Rolfs C, Trautvetter HP, Käppeler F, Ratynski W. The Cross Section of 14N(n, p)14C at Stellar Energies and its Role as a Neutron Poison for S-Process Nucleosynthesis. *Z Physik A - At Nuclei* (1988) 330:167–72. doi:10.1007/bf01293392
80. Koehler PE, O'Brien HA. N14(n,p)14C Cross Section from 61 meV to 34.6 keV and its Astrophysical Implications. *Phys Rev C* (1989) 39:1655–7. doi:10.1103/physrevc.39.1655
81. Koehler PE. N14(n,p)14C Cross Section Near thermal Energy. *Phys Rev C* (1993) 48:439–40. doi:10.1103/PhysRevC.48.439
82. Gledenov YM, Salatski VI, Sedyshev PV, Sedysheva MV, Pshenichnyj VA, Andrzejewski J. Cross Sections of the 14N(n, p)14C Reaction at 24.5, 53.5 and 144 keV. *Z Physik A - Hadrons Nuclei* (1994) 348:199–200. doi:10.1007/bf01291917
83. Sanami T, Baba M, Matsuyama I, Matsuyama S, Kiyosumi T, Nauchi Y, et al. Measurement of 14N(n,p)14C Cross Section for kT = 25.3 keV Maxwellian Neutrons Using Gridded Ionization Chamber. *Nucl Instr Methods Phys Res Section A: Acc Spectrometers, Detectors Associated Equipment* (1997) 394:368–73. doi:10.1016/S0168-9002(97)00698-0
84. Kii T, Shima T, Sato H, Baba T, Nagai Y. Cross Section of the 14N(n,p)14 Creaction from 10 to 100 keV Measured by a Gas Scintillation Drift Chamber. *Phys Rev C* (1999) 59:3397–401. doi:10.1103/PhysRevC.59.3397
85. Wagemans J, Wagemans C, Goeminne G, Geltenbort P. Experimental Determination of the 14N(n,p)14 Creaction Cross Section for thermal Neutrons. *Phys Rev C* (2000) 61:064601. doi:10.1103/PhysRevC.61.064601

Conflict of Interest: The authors declare that the research was conducted in the absence of any commercial or financial relationships that could be construed as a potential conflict of interest.

Publisher's Note: All claims expressed in this article are solely those of the authors and do not necessarily represent those of their affiliated organizations, or those of the publisher, the editors and the reviewers. Any product that may be evaluated in this article, or claim that may be made by its manufacturer, is not guaranteed or endorsed by the publisher.

frontiers | Frontiers in Physics

ORIGINAL RESEARCH
published: 04 July 2022
doi: 10.3389/fphy.2022.931953

An Innovative Superconducting Magnetic Trap for Probing β-decay in Plasmas

Giorgio Sebastiano Mauro[1], Luigi Celona[1], Giuseppe Torrisi[1], Angelo Pidatella[1], Eugenia Naselli[1], Filippo Russo[1], Maria Mazzaglia[1], Alessio Galatà[2], Fabio Maimone[3], Ralf Lang[3], Klaus Tinscher[3], Domenico Santonocito[1] and David Mascali[1]*

[1]Istituto Nazionale di Fisica Nucleare—Laboratori Nazionali del Sud (INFN-LNS), Catania, Italy, [2]Istituto Nazionale di Fisica Nucleare—Laboratori Nazionali di Legnaro (INFN -LNL), Legnaro, Italy, [3]GSI Helmholtzzentrum für Schwerionenforschung GmbH, Darmstadt, Germany

The main aim of Plasmas for Astrophysics Nuclear Decays Observation and Radiation for Archaeometry (PANDORA) project is to build a compact and flexible magnetic plasma trap where plasma reaches a density n_e ~ 10^{11}–10^{13} cm^{-3}, and a temperature, in units of kT, kT_e ~ 0.1–30 keV in order to measure, for the first time, nuclear β-decay rates in stellar-like conditions. One of the most important aspects of an ECR Ion Source (ECRIS) is its magnetic system. In this paper, the numerical design of the PANDORA magnetic system is presented and validated by using the commercial simulators OPERA and CST Studio Suite, showing an excellent agreement between each other in terms of axial and radial field profiles. In conjunction to the magnetic system design, the overall injection system, including the microwave lines for plasma heating and the isotopes injection schemes with a focus on the developments of the oven for solid elements, has been conceived and will be discussed.

Keywords: electron cyclotron resonance ion source, magnetic system, numerical simulations, wave-plasma coupling, isotopes injection systems

OPEN ACCESS

Edited by:
Giuseppe Verde, Universities and Research, Italy

Reviewed by:
Kurt Ernst Stiebing, Goethe University Frankfurt, Germany
Sandor Biri, Institute for Nuclear Research (ATOMKI), Hungary

****Correspondence:***
Giorgio Sebastiano Mauro
mauro@lns.infn.it

Specialty section:
This article was submitted to Nuclear Physics, a section of the journal Frontiers in Physics

Received: *29 April 2022*
Accepted: *13 June 2022*
Published: *04 July 2022*

Citation:
Mauro GS, Celona L, Torrisi G, Pidatella A, Naselli E, Russo F, Mazzaglia M, Galatà A, Maimone F, Lang R, Tinscher K, Santonocito D and Mascali D (2022) An Innovative Superconducting Magnetic Trap for Probing β-decay in Plasmas. Front. Phys. 10:931953. doi: 10.3389/fphy.2022.931953

1 INTRODUCTION

In the last decades, much experimental and theoretical efforts have been dedicated to investigate various possible scenarios which can influence nuclear decays rates. It has been predicted that sizeable variations in the decay properties can be observed in highly ionized nuclides. This would have a strong impact in the stellar nucleosynthesis where a hot plasma is formed and atoms can be found in different ionization states. In particular, β-decay properties of radioactive nuclei can be strongly affected by the high-temperature plasma of stellar environment. Few experimental evidences showing variations in the β decay rates as a function of the atomic ionization state have been collected, up to now, using storage rings. However, the storage ring approach is based on the investigations of a single charge state at a time: while clearly showing the role played by the high ionization state of an atom in the β-decay process, is not able to reproduce stellar-like conditions where, due to the high temperature of the plasma, a Charge State Distribution (CSD) of the ions is established. A totally new and challenging approach, based on the study of decays rates in a plasma whose conditions can mimic the hot stellar environment, has been conceived in the PANDORA (Plasmas for Astrophysics Nuclear Decays Observation and Radiation for Archaeometry) project Mascali et al. [1]. The main idea is to build a compact and flexible magnetic plasma trap (where plasma reaches a density n_e ~ 10^{11}–10^{13} cm^{-3}, and a temperature

$kT_e \sim 0.1$–30 keV) and use it to measure, for the first time, nuclear β-decay rates in stellar-like conditions. The decay rates of the radioactive ions will be measured through the detection of the γ-rays emitted by the β-decaying daughter nuclei, as a function of the charge state distribution of the in-plasma ions by varying plasma conditions. This task will be accomplished by an array of several Hyper-Pure Germanium (HPGe) detectors placed around the trap, in specific positions where holes are made in the cryostat structure to directly look into the plasma through thin aluminium windows. This new approach is expected to have a major impact in the study of nuclear-astrophysics processes and cosmology.

The magnetic field, necessary for plasma confinement, will be produced by employing a superconducting magnetic system (as typical for ECR ion sources), discussed in **Sections 2** and **3**, consisting of six hexapole coils (for radial confinement) nested inside three solenoid coils (for axial confinement), i. e. a SEXT-IN-SOL configuration. This magnetic system configuration is called *minimum-B* and allows the confinement of a plasma located around the plasma chamber axis (z axis in the following), providing magnetohydrodynamical (MHD) equilibrium and stability. In **Section 4** an overview of the microwave injection system that will be used in PANDORA will be given. The source will operate by employing three microwave injection lines: two 18 GHz lines with 2.4 kW maximum output power and one 21 GHz line with 1.5 kW maximum output power. This configuration will allow to exploit the advantages of different injection schemes, such as multiple frequency heating and two-close-frequency heating, in order to increase the production of higher charge states and overall plasma stability. Finally, **Section 5** will discuss about the techniques to inject isotopes inside the magnetic trap and will report a preliminary study of neutral vapour diffusion inside the PANDORA chamber. This is a critical point since PANDORA will employ radioactive isotopes, usually available in limited amount and very expensive, so the injection efficiency needs to be maximized.

2 ECR ION SOURCES MAGNETIC SYSTEM

It is known that, for ECRISs, high charge state ions are primarily produced by sequential impact ionization, which means that the ions must remain in the plasma long enough (up to hundreds of ms) to reach high charge states. Therefore, one of the main parameters determining the performance of an ECRIS is the product of the plasma density, n_e, and ion confinement time τ_i, called quality factor $Q = n_e\tau_i$. In general, source development has followed the semi-empirical scaling laws first proposed by Geller [2], which state that the plasma density scales with the square of the frequency $n_e \simeq \omega_{RF}^2$. As the frequency increases, the magnetic fields have to be scaled accordingly to fulfill the resonant heating condition for the plasma electrons Gammino and Ciavola [3]. As a consequence, the ion confinement time increases: in fact, it is proportional to the value of the so called mirror ratio, i. e. the ratio between the maximum and the minimum magnetic field value for the considered magnetic system. Furthermore, the ion confinement time increases with plasma chamber length (mirror length) and radius, so these two values need to be increased if the objective is to obtain the highest possible charge states Leitner [4]. **Figure 1** shows a typical magnetic field pattern (in module) generated using a minimum-B magnetic configuration. Usually, the performances of a magnetic system in terms of plasma confining capability are expressed by five magnetic field values: the value corresponding to the ECR, B_{ECR}, that depends on the heating frequency f_{RF}; the maxima values at the injection and extraction sides of the trap, B_{inj} and B_{ext} respectively, along the plasma chamber axis; the minimum, B_{min}, usually located at a central position along the plasma chamber axis; the maximum generated by the sextupole at the plasma chamber inner walls, B_{hex}. For a frequency of 28 GHz B_{ECR} is 1 T and its value at other frequencies can be easily calculated from the equation:

$$B_{ECR}\ [T] = \frac{f_{RF}\ [GHz]}{28\ [GHz]} \times 1\,[T] \tag{1}$$

Then, the established field ratios can be calculated as

$$B_{inj}/B_{ECR} = 4 \tag{2}$$

$$B_{rad}/B_{ECR} = 2 \tag{3}$$

$$B_{ext} \simeq 0.9 - 1.2 \times B_{rad} \tag{4}$$

$$0.4 < B_{min}/B_{ECR} < 0.8 \tag{5}$$

Some considerations can be made about the magnetic field values Leitner [4]. The optimum charge state is proportional to the average magnetic field as $q_{opt} \propto B^{3/2}$, so it is of our interest to increase the average confining field. The highest value of the magnetic field will be in correspondence of the injection and/or extraction axial coils inner surface, so during the numerical design of the magnetic system one has to be careful at not exceeding the threshold field values relative to the magnet material. In superconducting traps, special attention must be paid to the minimum field, B_{min}, that should be tuneable within a wide range of values: it has been experimental observed that, in order to obtain the highest electron density and to reach the optimal charge state, one has to have $0.65 < B_{\mathrm{min}}/B_{ECR} < 0.75$ Benitez et al. [5]; Mazzaglia et al. [6]; Neben et al. [7]. If this ratio exceeds the upper value, sudden non linear effects arise, increasing the plasma x-ray emission and thus the heat load on the cryostat.

3 NUMERICAL DESIGN OF THE PANDORA MAGNETIC TRAP

The requirements and considerations discussed in **Section 2** together with the necessity to have enough space for non-invasive diagnostic tools and for the array of γ-ray detectors Naselli et al. [8], allowed us to fix the plasma chamber dimensions (internal radius R_{CH_IN} = 140 mm and axial length L = 700 mm) and RF pumping frequencies (f_{RF1} =

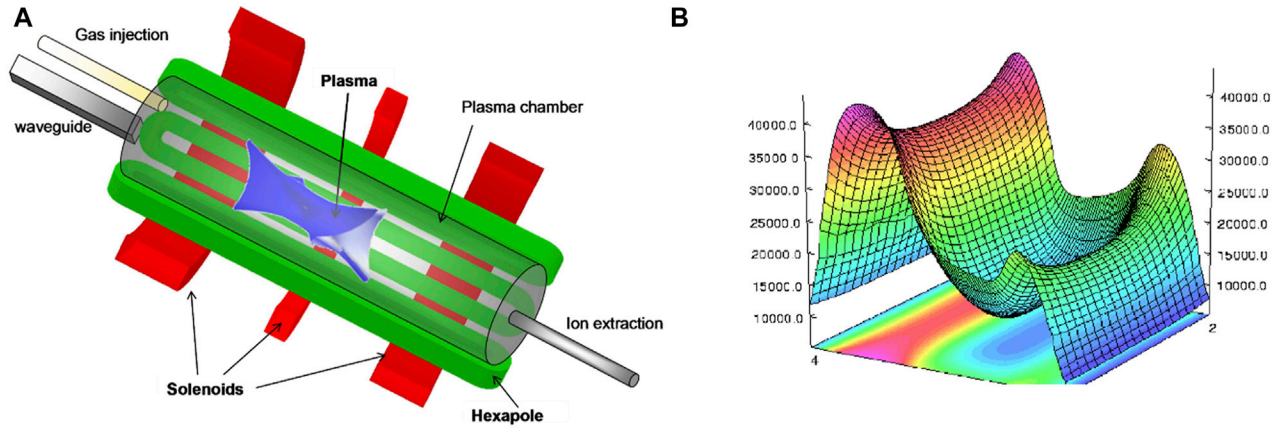

FIGURE 1 | (A) Magnetic system working in minimum-B configuration; **(B)** typical magnetic field generated (field module histogram plot) by a minimum-B configuration.

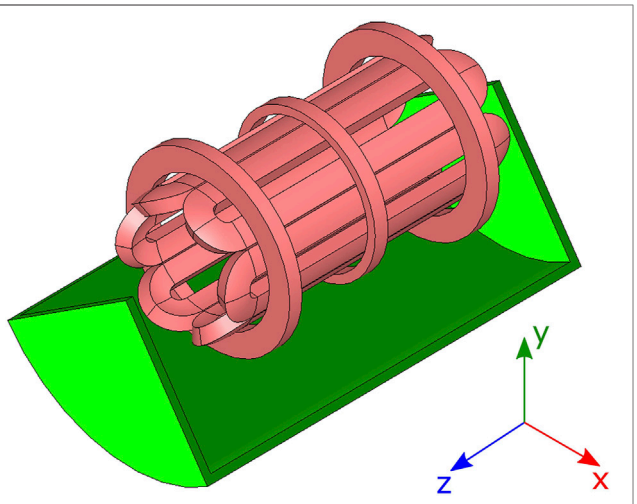

FIGURE 2 | 3D conceptual model of the structure comprehensive of the magnetic system (pale red objects) and the iron yoke (green object, only 1/4 visible).

TABLE 1 | PANDORA magnetic field specifications and operative ranges.

Parameter	Value [T]
B_{inj} max @ z = 350 [mm]	3
B_{inj} operative range	1.7–3
B_{ext} max @ z = −350 [mm]	3
B_{ext} operative range	1.7–3
B_{min} @ z = 0 [mm]	0.4
B_{hex} @ R_{CH_IN}	1.6

18 GHz, f_{RF2} = 21 GHz). Taking into account these values, the PANDORA magnetic system field specifications have been obtained. The superconducting system, whose 3D conceptual model is shown in **Figure 2**, is composed by three axial coils and six radial coils: the field values as well as the operative ranges are reported in **Table 1**. The structure has been simulated with the commercial softwares OPERA® and CST Studio Suite®. The simulated OPERA model and the employed coil dimensions are reported in **Figure 3** and **Table 2**. In the model, the material of the superconducting coils and of the sextupole is Niobium-Titanium alloy (NbTi). The simulated model takes also into account a 25 mm thick iron yoke (ARMCO® iron), distant 20 mm from the injection and extraction coils outer radius, employed to minimize the stray field that could otherwise interfere with the external detectors. The realized superconducting coils assembly will be encased inside a cryostat that will include a central warm bore for plasma chamber insertion.

The axial and radial magnetic field profiles are reported in **Figure 4** and **Figure 5**, scaled for the case f_{RF} = 18 GHz.

Numerical simulations have also been performed to identify the positions of the magnetic branches that need to be avoided when placing the array of γ-ray detectors. In fact, in these positions a rather strong Bremsstrahlung radiation generated on the plasma chamber wall is present due to the intense flux of electrons escaping the magnetic trap, leading to a high background rate on the detectors and thus limiting their performances. The magnetic branches are clearly visible in **Figure 6**, which shows the $|B|$ vector plots (normalized to the value of 2.7 T) in the xy plane at the axial positions z = −100, 0, 100 mm.

By employing the magnetic field profile obtained in the simulations, the distribution of lost electrons on chamber walls due to the magnetic branches has been calculated through the use of a MATLAB particle mover code. **Figure 7** shows the obtained lost electrons mask on chamber walls. The numerical study matches the expected branches position given from CST and at the same time provides a lower boundary thickness of particle loss regions along the branches. These information are relevant for both designing the size of the bias-disk foreseen at the chamber

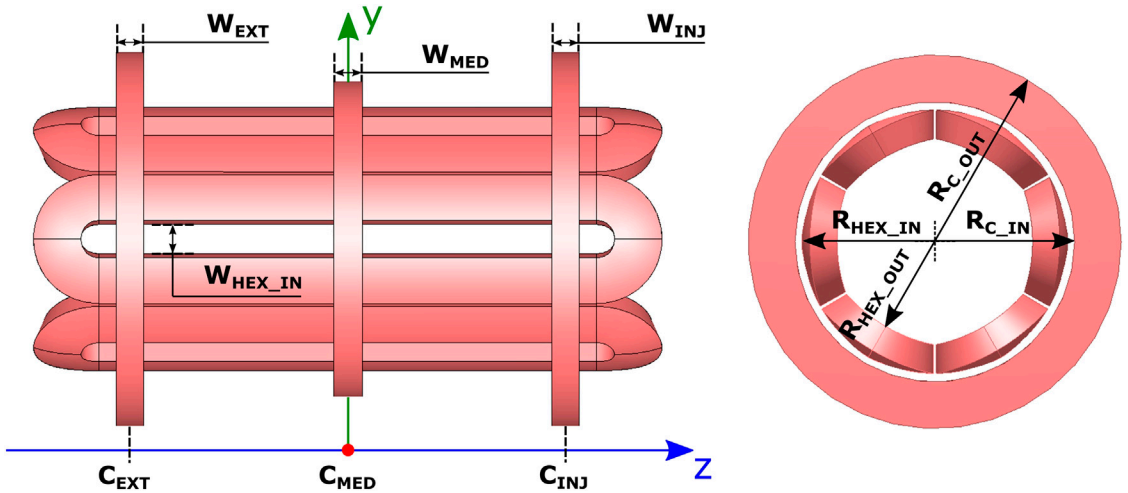

FIGURE 3 | Side and front view of the simulated magnetic system with dimensional parameters. Note: iron yoke does not appear in the picture.

TABLE 2 | Simulated geometrical dimensions of the coils composing the magnetic trap.

Axial Coils		
Parameter	**Description**	**Value [mm]**
R_{C_IN}	Coil inner radius (inj, med, ext)	225/225/225 [mm]
R_{C_OUT}	Coil outer radius (inj, med, ext)	300/253/300 [mm]
$C_{INJ,MED,EXT}$	Coil center (inj, med, ext)	−350/0/350 [mm]
$W_{INJ,MED,EXT}$	Coil width (inj, med, ext)	44/46/44 [mm]
Hexapole		
Parameter	**Description**	**Value [mm]**
R_{HEX_IN}	Hexapole inner radius	165 [mm]
R_{HEX_OUT}	Hexapole outer radius	212 [mm]
W_{HEX_IN}	Hexapole coil inter-space width	78 [mm]

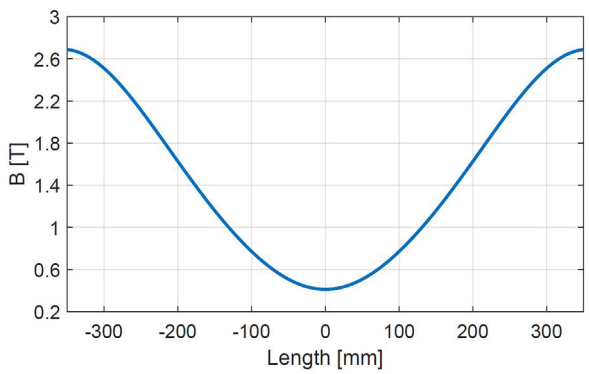

FIGURE 4 | Magnetic field module, $|B|$, along plasma chamber z-axis for pumping frequency f_{RF} = 18 GHz.

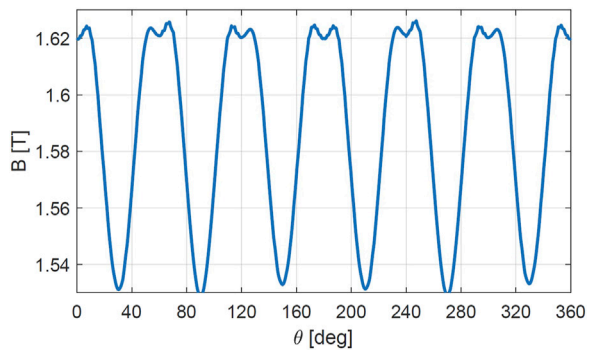

FIGURE 5 | Magnetic field module, $|B|$, along a circumference of radius R_{CH_IN} = 140 mm (plasma chamber inner radius) and axial position z = 0 mm.

injection side, and to find the optimal position for plasma diagnostics, microwave injection waveguides along the injection flange, as well as for the isotope injection systems (e. g., resistive oven), as will be discussed in the next sections.

4 THE MICROWAVE INJECTION SYSTEM

The source performances in terms of charge states and extracted currents has been explained by taking into account the different patterns of the electromagnetic field that are excited into the cavity, for a specific frequency (or set of frequencies) Mascali et al. [9]; Gammino et al. [10]. An improved coupling between microwaves and plasma is a key factor to design more powerful electron cyclotron resonance and microwave ion sources Hitz et al. [11]; Zhao et al. [12]; Xie et al. [13]; Guo et al. [14]; Mauro et al. [15]. As said, the electron density is proportional to the square of the microwave pumping frequency: the higher the frequency the higher the microwave power the source plasma can absorb before the onset of instabilities. However, taking

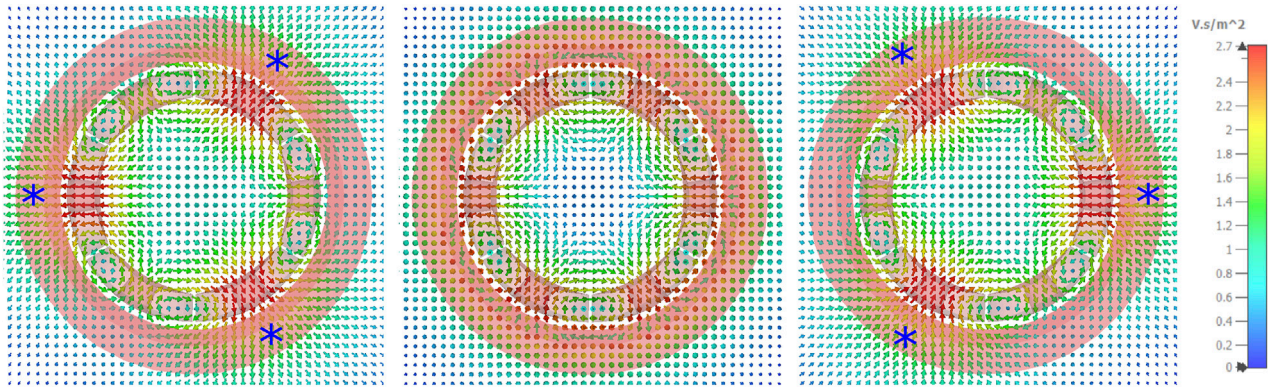

FIGURE 6 | From left to right, $|B|$ vector plot along the xy plane at the positions $z = -100$, 0, 100 mm. The magnetic branches positions are indicated by a blue marker.

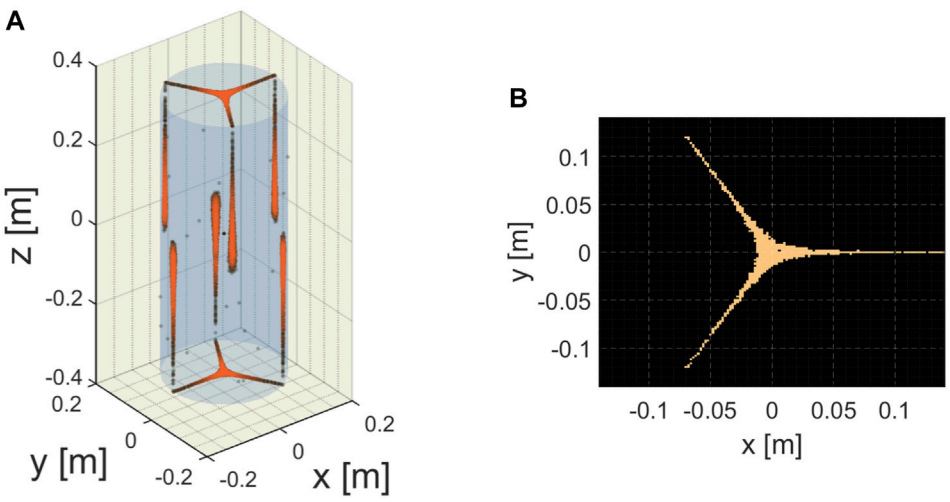

FIGURE 7 | (A) 3D lost electron mask on chamber wall due to PANDORA magnetic branches disposition; **(B)** detail of lost electron mask on the injection end-plate (z = 350 mm, see reference system of **Figure 3**).

into account Geller scaling laws for the magnetic field, a limit arise in terms of magnetic system manufacturability. Multiple frequency heating improves plasma stability and source performance. Historically, this can be considered the first non-conventional method of plasma heating outside the scheme traced by the standard model. Since 1994, the so-called two-frequency heating (TFH) has been used Vondrasek [16] to improve the highly charged ions production by feeding the plasma with two (or more) electromagnetic waves at different frequencies instead of one. From the above considerations and also considering the non conventional PANDORA plasma chamber dimensions with respect to the state of the art ECRISs in the world Leitner [4], it has been decided that the RF injection system will be composed of three lines by employing:

- two Klystrons with 17.3–18.1 GHz operating bandwidth and 2.4 kW maximum output power;
- one Klystron with 21–22 GHz operating bandwidth and 1.5 kW maximum output power.

This configuration will allow to operate with different microwave injection schemes, and in particular: 1) single-frequency mode by employing only one amplifier; 2) two-frequency heating and two-close-frequency heating (TCFH) modes, also with the possibility to vary the power ratio between two microwave amplifiers; 3) three-frequency-heating mode by simultaneously employing the three amplifiers. A final consideration can be made about the selected total microwave power that could be delivered to the PANDORA plasma chamber. Its cooling is an engineering challenge: in all the high performance ECR ion sources operating today, the maximum

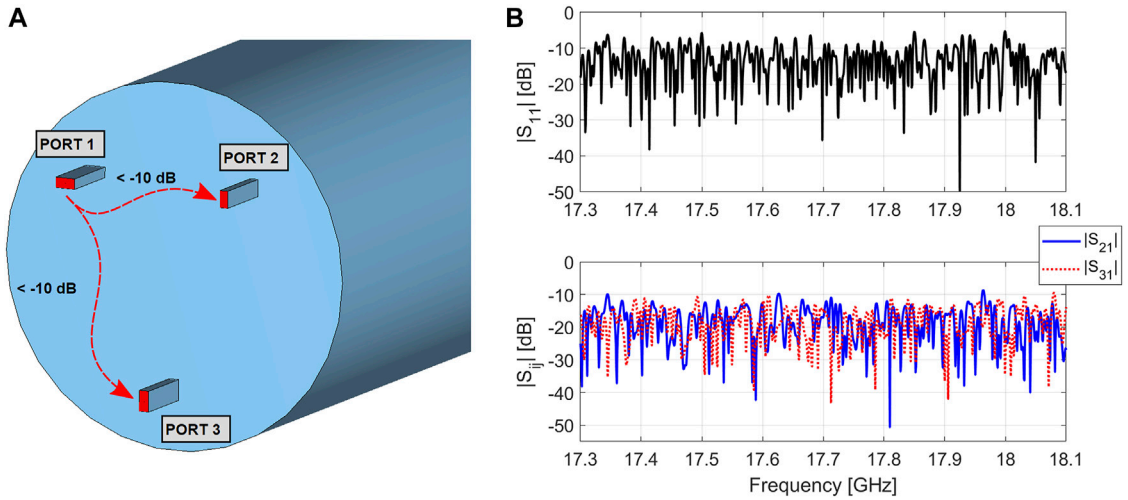

FIGURE 8 | (A) detail of the PANDORA plasma chamber 3D model with its injection waveguides (2 WR62 lines and one WR51 line); **(B)** $|S_{11}|$ and $|S_{ij}|$ parameters obtained considering the vacuum-filled plasma chamber, showing that with the employed waveguide ports disposition the cross-talk is minimized.

microwave power density (referred to plasma chamber volume) that can be coupled into the source is usually between 1.38 kW/L and 2.1 kW/L before a performance plateau is reached Lyneis et al. [17]. Considering a target power density of 1.38 kW/L and considering the PANDORA plasma chamber volume (~ 40 l), an impractical required total microwave power would result in order to obtain the maximum charge state intensity. This issue can be overcomed if we consider 100% of power density coupled to the volume enclosed by the resonance surface (the plasma volume), equal to ~ 3 l in the case of $f_{RF} = 21$ GHz. In this case, a total required microwave power $P_{coupled} \simeq 4$ kW is obtained: this value is compliant with the planned total amount of power delivered by the three klystrons, which is close to 6 kW. Such a power allows to obtain the charge state intensities needed for the experimental program. The PANDORA waveguide injection system has been initially simulated in CST by considering a vacuum-filled cavity in order to choose the correct waveguide positions and reciprocal orientation angle, with the aim at minimizing the cross-talk between each other and to avoid the magnetic branches (i. e. where the plasma hits the chamber injection end-plate, see **Figure 7**). As an example, **Figure 8** shows the waveguides positioning scheme as well as the reflection ($|S_{11}|$) and transmission ($|S_{ij}|$) parameters when only port 1 (WR62 waveguide) is enabled. From the picture it can be seen that, with the proposed configuration, the waveguide ports cross-talk is minimized, that is $|S_{ij}| < -10$ dB. By looking at the $|S_{11}|$ it can also be noticed that a high number of well adapted modes is excited inside the empty cavity.

5 ISOTOPES INJECTION TECHNIQUES

Besides the challenges encountered in the design of the magnetic and microwaves injection systems, a special attention was dedicated to the identification of the techniques to inject the various elements of interest inside the magnetic trap. The experiments carried out within PANDORA will involve, in fact, the use of radioactive isotopes, usually available in limited amount and very expensive: for this reason, it is mandatory to choose the most efficient injection technique, not only in terms of percentage of atoms effectively introduced inside the plasma, but also of ease and speed of preparation, in particular in the case of solid elements (radioactive elements could lead to a dose for the operator during their handling). The techniques will be employed within PANDORA derive directly from the experience made with ECRIS operation with solid elements: in this case, it is necessary to create first a neutral vapour, or an ejection of neutral particles towards the plasma. Neutral vapours of solid elements are usually obtained using small ovens installed just outside the plasma and heated by a DC/AC (resistive) or radiofrequency (RF) current Brown [18]. In general, resistive ovens can be used for elements whose vapor pressure reaches 10^{-2} mbar at a temperature T ≤ 2000 °C. They consist in a crucible with a very thin filament wrapped on it: the crucible is filled with the compound to evaporate and is heated by letting the current flow through the filament. Such kind of ovens are usually very small and are mounted inside the ECR trap, beyond the maximum of the magnetic field at injection. This technique has an efficiency ϵ of around 30%, while the ratio between metallic and buffer gas ions in the plasma is 1÷10%. For the PANDORA trap a dedicated resistive oven based on the Standard Temperature Oven (STO) has been developed at GSI. The STO has been being in operation at GSI for the production of metallic ion beams from the 14.5 GHz CAPRICE-type ECR Ion Source for several years. It can withstand up to 1,550°C to create vapours of metallic elements with high efficiency, low material consumption and longer lifetime Tinschert et al. [19]. However, in order to adapt the STO to the PANDORA Trap, some mechanical components have been modified. The system of three concentric stainless steel tubes for cooling water flow together with the inner insulated rod for the current connection made of alumina have been modified in order to

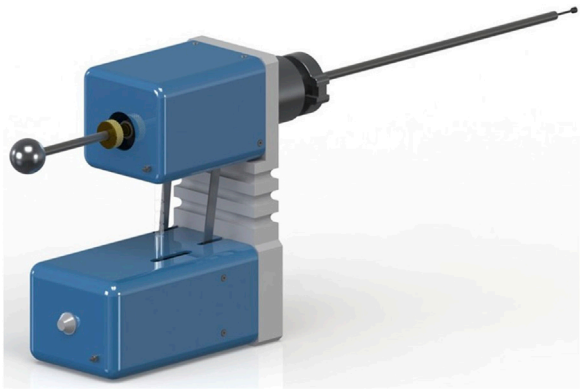

FIGURE 9 | Sputtering system for the PANDORA trap.

get a 360–400 mm longer STO. This assembled part compensates the longer path to the plasma with respect to the plasma chamber of the CAPRICE ECRIS which the oven was designed for. Two complete longer STOs have been assembled and test have been carried out to check the water cooling flow, the vacuum, and the electrical conncections. The items are ready for the shipment to INFN-LNS, where a test campaign has been scheduled with the AISHA ECRIS in order to study for the first time the performance of the STO with a 18 GHz ECRIS. For this purpose the injection flange of the AISHA ECRIS has been modified to match the oven feedthrough with the oven head. Since the STO has been designed and optimized for the CAPRICE-Type 14.5 GHz ECRIS, several evaporation tests will be carried out with metallic elements already produced at GSI, like Zn and Fe. After this feasibility tests, a campaign focused on the evaporation of isotopes like ^{176}Lu and ^{133}Cs will be scheduled. The study of the position and the insertion of the STOs into the PANDORA Trap together with the mechanical constrains is already ongoing. Ejection of neutral particles towards the plasma is obtained by employing the sputtering technique, normally used for refractory elements. A target of the material to be sputtered is prepared, mounted on a rod inside the magnetic trap and polarized negatively at some hundreds of V with respect to the plasma (sputtering voltage). The sputtering voltage accelerates ions naturally leaking from the core of the plasma to the target, causing the emission of neutral particles from it. Such neutral particles can be captured by the plasma but with a lower efficiency compared to the oven ($\epsilon \leq$ 10%), due to the fact that they are ejected at an energy of several eVs. Normally, the ratio between sputtered ions and buffer gas ions is around 1%. The PANDORA trap will be equipped with a sputtering system built by the Pantechnik company PK [20] and shown in **Figure 9**: a rod with the sample to be sputtered is mounted inside a position adjuster allowing its movement under vacuum, in order to find the best operating position with respect to the plasma. The translation is transmitted to the rod through an insulated belt: this will allow connecting the sputtering system to the magnetic trap put at high voltage, while keeping its control at ground potential.

Among all the possible elements to be tested in PANDORA, three have been selected as first day experiments: they are listed in **Table 3**, together with the necessary activity, the consumption for a single experiments and the technique will be employed to inject them into the plasma. Considering that the variation of the half life will be measured from the signal coming form the γ ray accompaining the β decay and that its detection should be distinguished by the background normally emitted by the plasma, the activity and the following consumption has been derived from the expected counting rate and measurement time necessary for the signal to overcome the 3σ noise level coming from the background.

TABLE 3 | List of elements selected for the first day experiments.

Isotope	Activity [GBq]	Consumption [mg]	Technique
^{176}Lu	4.246	2.00E+3	Oven
^{134}Cs	0.022	5.54E-10	Oven
^{94}Nb	0.173	2.46E-5	Sputtering

^{176}Lu is commercially available with an enrichment of around 70%, but in oxide form. For this reason, before loading it inside the oven, reduction to metallic form will have to be applied. Test on the efficiency and cleanliness of the reduction process will be carried out on natural abundance Lu, in collaboration with the target Laboratory of INFN-LNL. ^{134}Cs is commercially available as well, but in liquid solution of CsCl in HCl: for this reason, before loading it into the oven, a specific technique will be applied, currently adopted to produce ^{133}Cs ion beams in the framework of the SPES project Galatà et al. [21]. The solution will be dried and the remaining compound will be loaded inside the resistive oven: heated under vacuum inside the trap at moderate temperatures ($<$ 500 °C), the compound will sublimate and cesium dissociate, making it available for ionization by plasma electrons. ^{94}Nb is available from several suppliers, as well as a product of nuclear reactors and the sputtering targets will be prepared using the technique employed with the negative ion sources for Tandem accelerators: a powder or small pieces of the material will be pressed in a metallic holder, that will then be screwed on the sputtering rod shown in **Figure 9**.

5.1 Numerical Simulations of Vapour Diffusion

In view of the aforementioned experimental campaign, we make some progress on the study of neutral vapour diffusion inside the PANDORA chamber. This aspect is relevant both for the optimization of the amount of material which turns into plasma state over the totality of the sample evaporated, and for studying the impact of deposited neutrals on the HpGe detection efficiency. The numerical study has been performed by means of COMSOL Multiphysics® with the purpose to study the diffusion of ^{134}Cs neutral atoms in the cylindrical trap. First, we have checked under which fluid dynamic regime to study the problem. The Knudsen number,

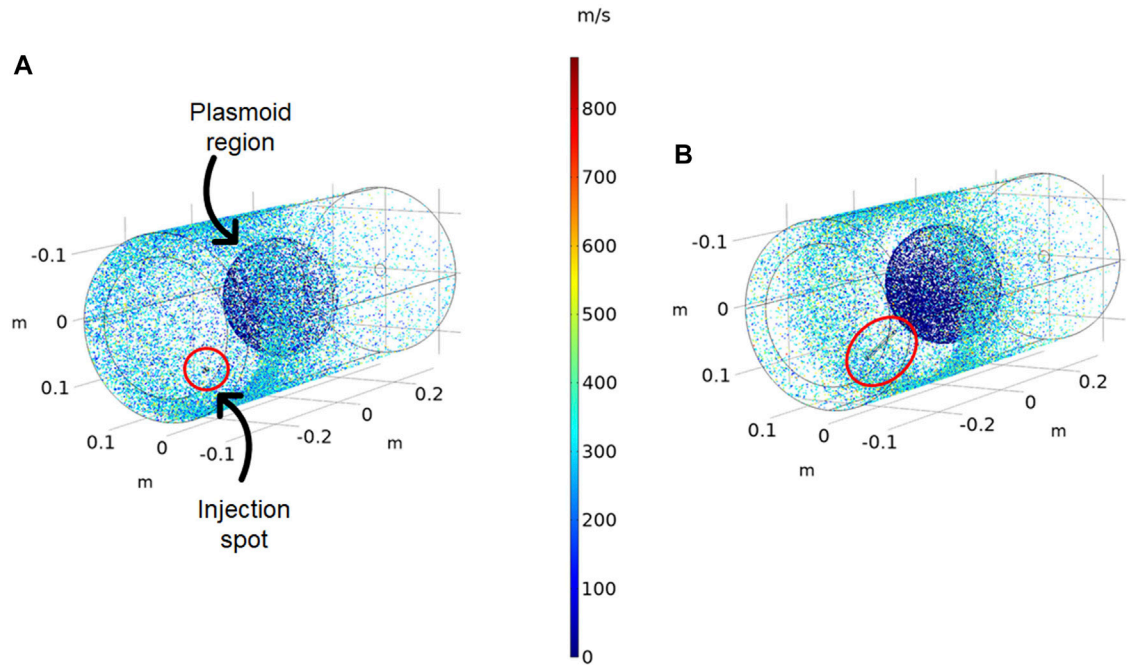

FIGURE 10 | Numerical simulation of particle diffusion of ^{134}Cs neutral vapours for the PANDORA trap performed using COMSOL Multiphysics®. **(A)** 10 mm long STO, and **(B)** 120 mm long STO, cases. STOs are indicated inside the red circles. Particles' speed [m/s] is indicated in the color bar.

$Kn = \lambda/L$, can help in this sense. It is defined as the ratio of the species mean-free path length, λ, to a representative physical length scale, such as the chamber length L, which determines whether statistical mechanics or the continuum mechanics formulation of fluid dynamics should be used in the model. Considering some Cs neutral vapour parameters, in particular: pressure $p \sim 10^{-5}$ mbar, temperature T_g = 417 K, and the Cs particle diameter $d_g \sim 6 \cdot 10^{-10}$ m, as well as a chamber length L = 700 mm, the Knudsen number is around $Kn \approx 7$. Thus, the problem can be modelled in the *free molecular regime*, where collisions between gas molecules as they traverse the interior of the system can be ignored.

As mentioned before, the STO head position can be longitudinally adjusted by using a rod that allows to expose it outside of the injection flange, towards the center of the plasma chamber. Two STOs of, respectively, 10 and 120 mm length have been employed for the neutral vapour tracing simulations: results are visible in **Figure 10A** for the 10 mm-long STO and in **Figure 10B** for the 120 mm-long STO. The not-axisymmetric position of STOs is required to avoid the magnetic branches location on the injection plate, as shown in **Figure 6**. The STOs are also tilted with respect to the chamber axis in order to maximize the injection direction towards the center of the plasma chamber. Vapours have starting velocity conditions according to a Maxwellian distribution with an initial temperature $T = T_g$, and the particles' speed is indicated in the color bar in the figure. The emitting surface radius of the STO is 2.5 mm. Modelled particles' trajectory drifts according to the initial conditions, until they hit the chamber walls or the modelled plasmoid surface (in middle of the chamber). Particles hitting the wall surface have non zero probability to be re-emitted since the surface temperature is close to T_g. This was assumed trying to simulate the effects of an internal liner on the surface. Moreover, particles hitting the plasmoid surface have about 6% probability to pass through, and hence about 94% probability to stick on the surface. These numbers arises from mean-free path calculations of neutral atoms going into ionization, at a given average electron density and ionization cross section. Particles sticking on the plasmoid are assumed to go into plasmization. As can be evinced, depositions of **Figure 10B** compared to that of **Figure 10A** is different. Because of the closer position of STO emitting surface of the former, a greater neutral deposition in the central region of the chamber is achieved, which is closer to the plasmoid; conversely, a more broadened deposition is shown in the latter case, where most of neutrals end close to the injection position. Therefore, the longer STO seems to provide a better chance for the neutrals to interact with the plasma, hence more likely being ionized by the warm electron population, and to a less waste of evaporated material. The calculated ratio of particle deposited on the plasmoid over the total amount of particles (i. e., deposited both on the plasmoid and on the chamber wall) is 17 and 30% for **Figures 10A,B**, respectively. Further investigations on the problem are planned, including space-dependent plasma parameters in the neutral atoms ionization mechanism, which we expect to impact on the deposition map of remaining neutrals. These preliminary results have been used to study the HPGe detectors efficiency as a function of vapour deposition Naselli et al. [8].

6 CONCLUSION

In this work the numerical design of the PANDORA magnetic system, for plasma confinement, has been presented. The design, whose scaling is based on the employment of 18 and 21 GHz pumping frequencies, has been carried out by using the commercial simulators OPERA and CST, whose results are in agreement between each other. By employing the obtained magnetic field profiles, the positions of the magnetic branches have been identified. These positions, along the plasma chamber side walls, are critical due to generated strong Bremsstralhung radiation and need to be avoided when placing the array of γ-ray detectors. Furthermore, the lost electron maps on the plasma chamber end plates have been calculated through the magnetic field profile: this information will be relevant both for the design of the bias-disk (at the injection end-plate) and for the correct placement of the plasma chamber diagnostics. The second part of the work has been dedicated to the numerical simulation of the microwave injection system: it will be composed by two 2.4 kW WR62 waveguides (f_{RF} = 18 GHz) and one 1.5 kW WR51 waveguide (f_{RF} = 21 GHz), for a total of 6 kW total available power. First in-vacuum simulations show that, with the proposed configuration, the waveguide ports cross-talk is minimized ($|S_{ij}| <$ − 10 dB) and a high number of well adapted modes is excited inside the empty cavity, that is desirable to exploit the frequency tuning effect in order to improve source performances. The last part of the work deals about the techniques to inject the elements of interest inside the magnetic trap. Because PANDORA experiments will employ radioactive isotopes, available in limited amount and at a high cost, efficient injection techniques, in terms of atoms percentage and speed of preparation, need to be implemented and are discussed. Finally, preliminary COMSOL simulations have been performed to study the neutral vapour diffusion inside the plasma chamber: this is relevant both for the optimization of the amount of material which turns into plasma state over the totality of the sample evaporated, and for studying the impact of deposited neutrals on the HPGe detection efficiency.

DATA AVAILABILITY STATEMENT

The original contributions presented in the study are included in the article/Supplementary material, further inquiries can be directed to the corresponding author.

AUTHOR CONTRIBUTIONS

Conceptualization, GM, LC, DM, and GT, Numerical simulations, GM, GT, AP, AG, EN, MM, and FR, Isotopes injection studies, AG, FM, RL, and KT, Funding acquisition, DM and DS, Writing—original draft, GM, Writing—review and editing, GM, GT, AP, AG, FM, and DM. All authors have read and agreed to the published version of the manuscript.

ACKNOWLEDGMENTS

The authors wish to thank INFN for the support through the project PANDORA Gr3 funded by 3rd Nat. Sci. Comm., and to thank the whole PANDORA collaboration.

REFERENCES

1. Mascali D, Santonocito D, Amaducci S, Andò L, Antonuccio V, Biri S, et al. A Novel Approach to β-Decay: PANDORA, a New Experimental Setup for Future In-Plasma Measurements. *Universe* (2022) 8:80. doi:10.3390/universe8020080
2. Geller R. *Electron Cyclotron Resonance Ion Sources and ECR Plasmas*. London, UK: Institute of Physics (1996).
3. Gammino S, Ciavola G. The Role of Microwave Frequency on the High Charge States Buildup in the ECR Ion Sources. *Plasma Sourc Sci. Technol.* (1996) 5: 19–27. doi:10.1088/0963-0252/5/1/002
4. Leitner D. High Performance ECR Sources for Next-Generation Nuclear Science Facilities. In: 10th International Particle Accelerator Conference. WEXPLS1 (2019). doi:10.18429/JACoW-IPAC2019-WEXPLS1
5. Benitez J, Lyneis C, Phair L, Todd D, Xie D. Dependence of the Bremsstrahlung Spectral Temperature in Minimum-B Electron Cyclotron Resonance Ion Sources. *IEEE Trans Plasma Sci* (2017) 45:1746–54. doi:10.1109/tps.2017.2706718
6. Mazzaglia M, Castro G, Mascali D, Miracoli R, Briefi S, Fantz U, et al. Study of the Influence of Magnetic Field Profile on Plasma Parameters in a Simple Mirror Trap. In: Proc. 23rd International Workshop on ECR Ion Sources (ECRIS'18); 10-14 September 2018; Catania, Italy. Geneva, Switzerland: JACoW Publishing (2019). p. 144–7. no. 23 in International Workshop on ECR Ion Sources. doi:10.18429/JACoW-ECRIS2018-TUP25
7. Neben D, Fogleman J, Isherwood B, Leitner D, Machicoane G, Renteria S, et al. X-ray Investigation on the Superconducting Source for Ions (SuSI). *J Inst* (2019) 14:C02008. doi:10.1088/1748-0221/14/02/c02008
8. Naselli E, Santonocito D, Amaducci S, Galatà A, Goasduff A, Mauro GS, et al. Design Study of a HPGe Detectors Array for β-decays Investigation in Laboratory ECR Plasmas. *Front Phys* (2022). Research Topics: Nuclear Physics and Astrophysics in Plasma Traps (forthcoming).
9. Mascali D, Neri L, Gammino S, Celona L, Ciavola G, Gambino N, et al. Plasma Ion Dynamics and Beam Formation in Electron Cyclotron Resonance Ion Sources. *Rev Scientific Instr* (2010) 81:02A334. doi:10.1063/1.3292932
10. Gammino S, Ciavola G, Celona LG, Mascali D, Maimone F. Numerical Simulations of the Ecr Heating with Waves of Different Frequency in Electron Cyclotron Resonance Ion Sources. *IEEE Trans Plasma Sci* (2008) 36:1552–68. doi:10.1109/tps.2008.927288
11. Hitz D, Girard A, Melin G, Gammino S, Ciavola G, Celona L. Results and Interpretation of High Frequency Experiments at 28 Ghz in Ecr Ion Sources, Future Prospects. *Rev Scientific Instr* (2002) 73:509–12. doi:10.1063/1.1429313
12. Zhao HW, Sun LT, Guo JW, Lu W, Xie DZ, Hitz D, et al. Intense Highly Charged Ion Beam Production and Operation with a Superconducting Electron Cyclotron Resonance Ion Source. *Phys Rev Accel Beams* (2017) 20: 094801. doi:10.1103/PhysRevAccelBeams.20.094801
13. Xie D, Benitez J, Lu W, Lyneis C, Todd D. Recent Production of Intense High Charge Ion Beams with VENUS. In: 22nd International Workshop on ECR Ion Sources. THAO01 (2017). doi:10.18429/JACoW-ECRIS2016-THAO01
14. Guo JW, Sun L, Lu W, Zhang WH, Feng YC, Shen Z, et al. A New Microwave Coupling Scheme for High Intensity Highly Charged Ion Beam Production by High Power 24-28 GHz SECRAL Ion Source. *Rev Scientific Instr* (2020) 91: 013322. doi:10.1063/1.5131101
15. Mauro GS, Torrisi G, Leonardi O, Pidatella A, Sorbello G, Mascali D. Design and Analysis of Slotted Waveguide Antenna Radiating in a "Plasma-Shaped"

Cavity of an ECR Ion Source. *Telecom* (2021) 2:42–51. doi:10.3390/telecom2010004
16. Vondrasek R. Diagnostics for Multiple Frequency Heating and Investigation of Underlying Processes. *Rev Scientific Instr* (2022) 93:031501. doi:10.1063/5.0076265
17. Lyneis CM, Leitner D, Todd DS, Sabbi G, Prestemon S, Caspi S, et al. Fourth Generation Electron Cyclotron Resonance Ion Sources (Invited). *Rev Sci Instrum* (2008) 79:02A321. doi:10.1063/1.2816793
18. Brown IG. *The Physics and Technology of Ion Sources, 2nd, Revised and Extended Edition*. Hoboken, NJ, USA: Wiley (2004).
19. Tinschert K, Lang R, Mäder J, Maimone F, Roßbach J. Metal Ion Beam Production with Improved Evaporation Ovens. In: Proceedings of the 20th International Workshop on ECR IonSources; September 25–28 (2012). p. 140–2.
20. [Dataset] Pantechnik. *Pantechnik* (2022). Available from: www.pantechnik.com (Accessed June 20, 22).
21. Galatà A, Roncolato C, Bisoffi G, Francescon P, Bellan L, Bermudez J, et al. Towards the First Beams from the ADIGE Injector for the SPES Project. *J Phys Conf Ser* (2019) 1350:012090. doi:10.1088/1742-6596/1350/1/012090

Conflict of Interest: The authors declare that the research was conducted in the absence of any commercial or financial relationships that could be construed as a potential conflict of interest.

frontiers | Frontiers in Physics

TYPE Original Research
PUBLISHED 03 August 2022
DOI 10.3389/fphy.2022.935728

OPEN ACCESS

EDITED BY
Giuseppe Verde,
Ministry of Education, Universities and Research, Italy

REVIEWED BY
Mengoni Daniele,
National Institute of Nuclear Physics of Padova, Italy
Federico Ferraro,
University of Milan, Italy

*CORRESPONDENCE
Eugenia Naselli,
eugenia.naselli@lns.infn.it

SPECIALTY SECTION
This article was submitted to Nuclear Physics, a section of the journal Frontiers in Physics

RECEIVED 04 May 2022
ACCEPTED 04 July 2022
PUBLISHED 03 August 2022

CITATION
Naselli E, Santonocito D, Amaducci S, Celona L, Galatà A, Goasduff A, Mauro GS, Mazzaglia M, Mishra B, Napoli DR, Pidatella A, Torrisi G and Mascali D (2022), Design study of a HPGe detector array for β-decay investigation in laboratory ECR plasmas. *Front. Phys.* 10:935728. doi: 10.3389/fphy.2022.935728

Design study of a HPGe detector array for β-decay investigation in laboratory ECR plasmas

Eugenia Naselli[1]*, Domenico Santonocito[1], Simone Amaducci[1], Luigi Celona[1], Alessio Galatà[2], Alain Goasduff[2], Giorgio Sebastiano Mauro[1], Maria Mazzaglia[1], Bharat Mishra[1], Daniel R. Napoli[2], Angelo Pidatella[1], Giuseppe Torrisi[1] and David Mascali[1]

[1]Laboratori Nazionali Del Sud, Istituto Nazionale di Fisica Nucleare, Catania, Italy, [2]Laboratori Nazionali di Legnaro, Istituto Nazionale di Fisica Nucleare, Legnaro, Italy

In the frame of the PANDORA project, a new experimental approach aims at measuring in-plasma β-decay rate as a function of thermodynamical conditions of the environment, namely a laboratory magnetized plasma able to mimic some stellar-like conditions. The decay rates (expected to change dramatically as a function of the ionization state) will be measured as a function of the charge state distribution of the in-plasma ions. The new experimental approach aims at correlating the plasma environment and the decay rate. This can be performed by simultaneously identifying and discriminating—through an innovative multi-diagnostic system working synergically with a γ-ray detection system —the photons emitted by the plasma and γ-rays emitted after the isotope β-decay. In this study, the numerical simulations supporting the design of the γ-ray detector array, including a statistical significance study to check the feasibility of measuring the in-plasma decay rates, are presented. Geant4 simulations focused on the design of the array of γ-ray detectors and the evaluation of total efficiency depending on the detector type and the optimal displacement of detectors around the trap (including collimation systems and shielding). The simulation results showed that, due to technical limitations in the number of apertures that can be created in the magnetic trap, the best compromise is to use 14 HPGe (70% of relative efficiency) detectors surrounding the magnetic trap. The HPGe detectors were chosen for their excellent energy resolution (0.2% @ 1 MeV), since the harsh environment (the background is represented by the intense plasma self-emission) strongly affects the signal-to-background ratio. Once determined the total photopeak efficiency (0.1–0.2%), the sensitivity of the PANDORA experiment was checked in a "virtual experimental run," by exploring the measurability of isotope decay rates for the first three physical cases of PANDORA: ^{176}Lu, ^{134}Cs and ^{94}Nb. The preliminary results demonstrated the feasibility of the measurement in terms of the signal-to-background ratio and significance that it is possible to reach. The results indicated that experimental run durations could take from several days to 3 months, depending on the isotope under investigation, thus shedding new light on the role of weak interactions in stellar nucleosynthesis.

KEYWORDS

Geant4 simulations, magnetoplasma, gamma-ray detectors, beta decay, nucleosynthesis, plasma trap, plasma diagnostics

1 Introduction

The main aim of the PANDORA (Plasmas for Astrophysics, Nuclear Decay Observation and Radiation for Archaeometry) project [1, 2] is the in-plasma measurement of β-decay lifetime of selected radioisotopes which, due to the plasma environment, is expected to undergo a significant variation relative to the value measured in neutral atoms [3–5]. The driving mechanism which can lead to such a change in the β-decay lifetime is represented by the opening of a new decay channel, the bound state β-decay [6]. Such a decay becomes effective due to the high degree of ionization of the atoms in the plasma which allows the electron emitted in the β-decay to be captured into a bound electron state of the daughter nucleus. The astrophysical relevance and implications of bound state β-decay, in particular for the s-process, have been widely discussed by several authors. Its observation in plasma whose conditions can mimic the hot stellar environment is expected to have a major impact on the study of nuclear-astrophysics processes [7–9] and cosmology. In particular, the experimental results could support the possibility of using specific long-lived isotopes as cosmological tools (chronometers), since the current uncertainties in their lifetime do not allow to be confident in estimating the age of a given astrophysical object by just looking at the relative abundances of certain isotopes (i.e., measuring the "father–son" abundances ratio).

To reach this goal, we will make use of a compact and flexible plasma trap equipped with a multi-diagnostic setup [10, 11] to monitor the density and temperature of the plasma and the charge state distribution (CSD) of the ions. The plasma working conditions will be characterized by electron density values $n_e \sim 10^{11}$–10^{13} cm^{-3} and a range of temperatures $k_B T_e \sim 0.1$–30 keV. In this environment, ions remain cold with $k_B T_{ion} \leq 20$ eV.

The decay of the radioactive ions will be measured through the detection of the γ-rays emitted by the β-decay daughter nuclei. This task will be accomplished by an array of several HPGe detectors placed around the trap, in specific positions where holes were made in the cryostat structure to directly look into the plasma through thin aluminum windows. The design of the detection array proposed for the project is the result of Geant4 simulations [12] performed to evaluate the main features of the γ-ray detection setup and its efficiency in the decay tagging.

In the following study, we will discuss the numerical simulations focused on the design of the γ-ray detector array and the technical solutions (in terms of type, number, position of the γ-ray detectors, collimation and shielding system) foreseen to achieve the goals of PANDORA. Furthermore, a statistical significance study will be presented, including simulations supporting the feasibility of the measurement of the decay rate in plasma, for the first three physical cases selected for the phase-1 of PANDORA. The preliminary results demonstrated the feasibility of the measurement in terms of 3σ significance that it is possible to reach, determining the expected duration of experimental runs (which varies from a several days to 3 months, depending on the isotope under investigation) thus shedding new light on the role of weak interactions in stellar nucleosynthesis.

2 The plasma trap design

In order to investigate the variations in β-decay lifetime due to a high degree of ionization of the ions in a plasma environment, the PANDORA project will make use of a dedicated trap [13] where the plasma is confined by a three-dimensional magnetic well. The trap will be realized by means of a fully superconducting magnetic system, similar to the one used in ECR (electron cyclotron resonance) ion sources, consisting of three coils for axial confinement and a nested hexapole for radial confinement which will be tuned in order to create the so-called minimum-B magnetic-field configuration, mandatory to match magnetohydrodynamical (MHD) equilibrium and the stability of the plasma. The magnetic system will be surrounded by an ARMCO® iron yoke, placed at a radial distance of about 20 cm from the coils' outer radius, having a thickness of about 2.5 cm used to confine the magnetic field. The cryostat includes a central warm bore which allows the insertion of the plasma chamber made of aluminum.

The magnetic system will be able to operate at any value in the range of about 1.7–3 T allowing for a proper tuning of the plasma parameters and ensuring plasma stability. It will surround a cylindrical plasma chamber of outer radius of about 15 cm and length of about 70 cm. The size has been optimized to increase the confinement time, one of the parameters governing the production of high charge states (the other is the plasma density), to increase the microwave to plasma coupling efficiency and to have enough space for non-invasive diagnostic tools and the array of γ-ray detectors. Since the plasma density scales with the square of the frequency ω_{RF}^2 [14], to increase the plasma density, the trap has been designed to operate at high frequencies, using the technique of double frequency heating which improves plasma stability and source performances [15, 16]. In particular, the PANDORA trap will operate at 18 + 21 GHz frequencies in MHD-stable configuration. The plasma will be fed by three microwave generators with about 6 kW of total RF power (scalable up to 10 kW) allowing it to reach a power density (considering only the

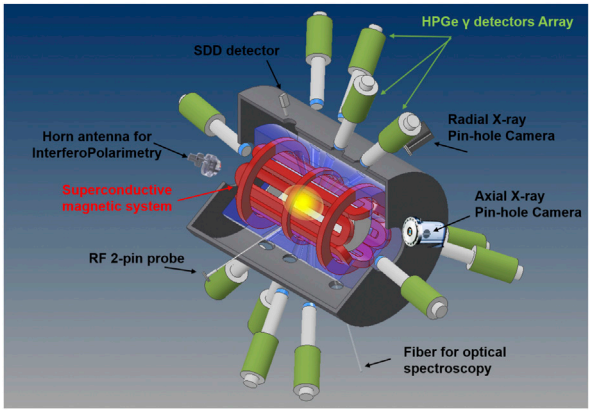

FIGURE 1
Rendering of the PANDORA setup, including the superconducting magnetic system (in red) inside its cryostat and iron yoke; the array of HPGe detectors; the main diagnostics (optical, X-ray and interfero-polarimetry); the mass spectrometer and the RF system.

plasmoid volume) in the range between 1.38 and 2.5 kW/L. This selected total microwave power that could be delivered to the PANDORA plasma chamber depends on a compromise between the performances that can be reached (mainly in terms of the charge state distribution) and the engineering challenge for its cooling [13].

The trap design included a set of radial lines of sight, in order to access the plasma to detect the γ-rays emitted in the decay of daughter nuclei populated in the β-decay process and for a proper positioning of specific diagnostic tools whose use is fundamental to measure the plasma parameters. These lines of sight are placed radially between the warm bore radius and the external iron yoke through the cryostat and the inner cold mass so that the different materials used to build the magnetic system and the yoke would shield both the γ-rays and plasma radiation. For this reason, the apertures in the cryostat have been placed in the interspaces of each coil of the hexapole. Such a choice has the advantage of using the hexapole itself as a collimator and shield for the photon flux emitted from the plasma chamber walls, therefore, improving the signal-to-background ratio.

The results of simulations performed using Geant4 suggested that the best compromise, considering the mechanical problems in the creation of the lines of sight, the possible modification of the magnetic field shape and the necessary γ-ray detection efficiency, can be obtained by creating three conical apertures in each hexapole element allowing for the placement of 12 HPGe detectors and six plasma diagnostic tools. All their axes point to the center of the plasma chamber so that opposite apertures are collinear. The position of the apertures used for the γ-ray detectors has been chosen in order to avoid the so-called magnetic branches (i.e., the region of the magnetic trap where the B-field lines are more intense) for which the background due to intense bremsstrahlung X-ray emission (due to axial and radial losses impinging on the plasma chamber walls) is expected to be more intense.

The HPGe detectors will be placed around the trap, at a radial distance of a few centimeters from the yoke using a dedicated mechanics. At such a distance the stray field, according to the technical specifications, will be of the order of 100 G, and therefore, no effects due to the magnetic field are expected on the charge collection efficiency which could lead to a worsening of the detector resolution. Two further HPGe detectors (and eight further plasma diagnostic tools) will be placed axially looking into the plasma through aluminum windows present in the walls of the plasma chamber.

A sketch of the PANDORA setup, including the superconducting magnetic system (in red) inside its cryostat (in blue) and iron yoke (in gray) is shown in Figure 1. The figure also includes the HPGe detector array and some of the non-invasive diagnostic tools comprising the advanced multi-diagnostic system (i.e., optical, X-ray, interfero-polarimetry, RF probe and pin-hole camera) that will surround the plasma trap.

3 The experimental approach

The experimental method is based on the possibility of maintaining a dynamical equilibrium between the quantity of atoms injected into the trap and the losses due to the intrinsically imperfect magnetic confinement, in order to keep stable density and temperature (thus, the concentration of decaying nuclei in the trap) for a long period of time, extending up to months. The experimental procedure includes the following five steps:

1. A *buffer plasma* is created from He, O, or Ar up to a density of 10^{13} cm^{-3}.
2. The isotope is flushed directly (if gaseous) or vaporized by proper ovens [13] (if metallic) and then fluxed into the chamber to be transformed into a plasma state. Relative abundances of buffer versus isotope densities reach a ratio up to 100:1 (if the isotope is in metal state) or 3:1 (in the case of gaseous elements).
3. The plasma is maintained in MHD equilibrium by equalizing the input fluxes of particles to the losses.
4. While the isotopes decay, the plasma-confined daughter nuclei emit γ-rays of hundreds of keV, which are detected by a HPGe detector array surrounding the magnetic trap.
5. Radioactivity measured in plasma can be directly correlated to plasma density and temperature, monitored by an innovative non-invasive multi-diagnostics setup.

The number of decays per unit time $\frac{dN}{dt}$ can be written as:

$$\frac{dN}{dt} = \lambda\left(n, f\left(\epsilon\right)\right) n_i V_p. \tag{1}$$

where λ is the isotope activity, $f(\epsilon)$ is the electron energy distribution function, n is the electron density, n_i is the plasma ion density of the isotope, and V_p is the plasma volume.

Since the ECR plasma confined in the magnetic minimum-B configuration will be kept in dynamical equilibrium [14, 17], the term $\lambda(n, f(\epsilon))\ n_i V_p$ is constant over time and Equation (1) can be easily integrated. Therefore, the total amount of decays detectable via γ-ray tagging can be determined according to the following formula:

$$\int_0^{t_{meas}} \frac{dN\left(t\right)}{dt} dt = \int_0^{t_{meas}} \lambda\left(n, f\left(\epsilon\right)\right) n_i V_p dt, \tag{2}$$

$$N\left(t_{meas}\right) = \lambda\left(n, f\left(\epsilon\right)\right) n_i V_p t_{meas} \tag{3}$$

where t_{meas} is the overall measurement time during which the γ-rays emitted in the decay of the excited states of the decay products are measured by the HPGe detector array.

Equation (3) implies that the number of expected decays scales linearly with respect to the measurement time t_{meas}. Since the plasma parameters can be kept constant over time, the proportionality is due to the nuclear decay constant only, which is, in turn, a function of the plasma density and energy distribution: $\lambda(n, f(\epsilon))$. The core issue is, therefore, to univocally determine n and $f(\epsilon)$, inherently fixing the CSD, to be correlated with the γ counting rate. In fact, any physical condition (combination of density and temperature) in non-LTE (non-local thermal equilibrium) determines a certain CSD (charge state distribution) of the ions in plasma, similarly to what happens in the stars' interiors (where, however, the plasma is in LTE equilibrium).

In particular, Equation (3) implies that the plasma density and volume must be known and monitored online all along the measurement to deconvolve λ (it is worth noting that $n \equiv n(x, y, z)$). Their spatial dependence can be determined from spectrally resolved X-ray imaging [18, 19] and through other non-invasive diagnostic tools, such as microwave diagnostics [20, 21]. More generally, it is possible to monitor and measure online all plasma parameters and thermodynamical properties by means of the multi-diagnostics system made of a tens of non-invasive diagnostic tools [10] in order to verify that the parameters are constant over the time within the typical sensitivity range of measurement [1].

Moreover, the monitoring of the isotope evaporation can be performed by means of numerous diagnostic systems [22], that is, the QCM (quartz crystal microbalance) which is able to measure the mass of isotope that has been deposited on the surface of a quartz crystal exposed to the vapors in the vacuum chamber, thermocouples that are used to measure the temperature at various points on the oven and keep it at the required temperature, and thermal camera which is an infrared-sensitive camera that allows an image of the temperature of the various parts of the oven. On the other hand, the monitoring of losses can be performed by means of advanced analysis methods and non-invasive multi-diagnostics tools, which allow unprecedented investigations of magnetoplasma properties [10]. The high resolution spatially resolved soft X-ray spectroscopy by means a X-ray pin-hole camera setup represents a very powerful method to perform plasma structure evaluation and valuable studies on the dynamics of losses [23]. It is, in fact, possible to perform energy filtering analysis and online monitoring of the losses versus the plasma emission, by distinguishing online fluorescence lines (produced by the electrons escaping the trap and impinging on the metal surfaces) of each material of the plasma chamber from the ones coming from the plasma (due to the fluorescence of confined ions).

The performances of the setup were evaluated through a set of realistic simulations performed using Geant4. This approach allowed us to estimate the array detection efficiency and the feasibility of the experiments on the three physics cases identified for the first PANDORA experimental campaign, which are reported as follows:

- ^{176}**Lu**: $T_{\frac{1}{2}} = 3.78 \cdot 10^{10}$ years, E_γ = 202.88 & 306.78 keV;
- ^{94}**Nb**: $T_{\frac{1}{2}} = 2.03 \cdot 10^{4}$ years, E_γ = 702.65 keV;
- ^{134}**Cs**: $T_{\frac{1}{2}} = 2.06$ years, E_γ = 795.86 keV.

From a list of tens of radioisotopes of strong astrophysical interest, the choice of the three physical cases for the first series of PANDORA measurements was based on: 1) the scientific relevance, 2) the expected effects on the lifetime due to the ion CSD or ion temperature, 3) the type of element (gas, metal, rare isotope, commercial or not), and 4) selecting the isotopes whose daughter nuclei emit γ-rays, the identification of the decay products being based on the detection of γ-rays.

Only isotopes whose daughter nuclei emit γ-rays at energies higher than 200 keV have been selected; lower energy γ-rays would, in fact, be overwhelmed by the high-intensity background self-emitted by the plasma, which represents the main source of the background for the measurements, strongly affecting the signal-to-background ratio.

An example of the background spectrum, due to plasma self-emission at n = 10^{13} cm^{-3} having a V_p = 1500 cm^3, is shown in Figure 2. It was evaluated starting from measurements on existing traps and rescaling them to higher densities and volumes according to an emissivity model [24].

The spectrum shows the high emission rate of radiation emitted from the whole plasma volume. Due to this high intensity, each HPGe detector will undergo a rate of few tens of kHz and dedicated electronics are needed to work in such a harsh environment.

4 Geant4 simulations

Numerical simulations focused on the design of the γ-ray detector array were performed in Geant4 to study the best

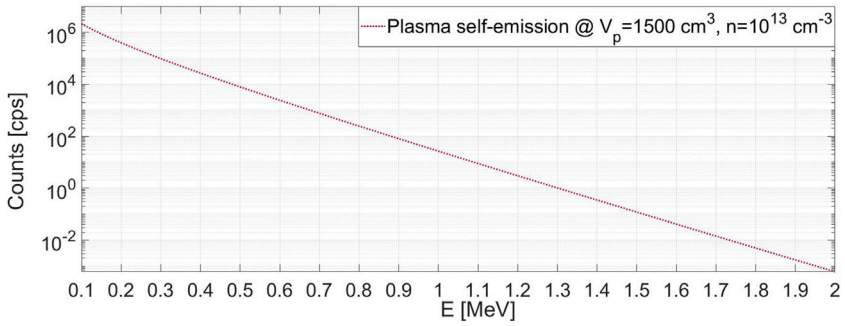

FIGURE 2
Example of the rate of plasma self-emission in the whole volume as a function of the energy of the radiation (the width of the bin in the *x* axis corresponds to 10 *eV*).

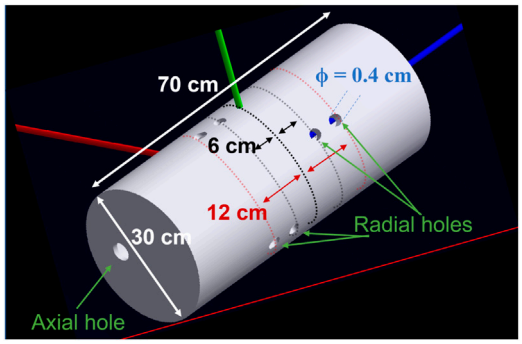

FIGURE 3
Sketch of the stainless steel plasma chamber including the 12 radial and two axial holes to be used for the detection of the γ-rays; quotations of hole displacement along the lateral chamber walls are shown.

configuration achievable in terms of the total number, type of detectors, and their optimal distribution around the trap, including collimation systems and shielding.

In the following Sections 4.1 and 4.2, the setup design in Geant4 and the total efficiency estimation of the whole system are, respectively, shown. In addition, the sensitivity of the PANDORA experiment was also specifically checked by exploring the measurability of isotopes lifetimes in a virtual experiment for the physical cases mentioned earlier. Preliminary results demonstrating the feasibility of the experiment are shown in Section 5.

4.1 Design of the PANDORA setup

The trap geometrical design was implemented in Geant4 using the PANDORA magnetic design described in [13], with the same materials and dimensions of each component. The final design consists of:

- A *stainless steel chamber* with an external radius of 150 mm, a length of 700 mm, and a thickness of 10 mm. The chamber has 14 holes with a diameter of 40 mm, aligned with the cryostat line of sight for the detection of γ-rays. A total of 12 azimuthal holes placed along four rings, symmetrically placed at 6 and 12 cm with respect to the center of the chamber were simulated (Figure 3). Three holes at 120° were made for each ring, building a symmetrical geometric configuration with respect to the center of the chamber. Two axial holes (injection and extraction) with a diameter of 40 mm have been added to the entrance and exit endplate of the chamber. Each hole has an aluminum window with a thickness of 3 mm and a diameter of 40 mm.
- An overall *magnetic system*, shown in Figure 4A, is made of three NbTi superconducting coils (in yellow) and a NbTi superconducting hexapole (in red). The inner and outer radii of the coils (for the injection, the middle, the extraction coil) and of the hexapole superconductor are summarized in table 1.
- *A single cryostat*, containing the three coils and the hexapole magnet, was simulated as a cylindrical aluminum structure (shown as pink color in Figure 4B) surrounding the entire magnetic system and distant 30 mm from both ends of the hexapole (along the axis). Holes were created in the cryostat structure—along the interspaces of the conductor hexapole—in order to use it as a multi-collimator and to suppress as much as possible the photon flux coming from the walls and not directly from the plasma core, improving the signal-to-background ratio. A total of 14 holes were created in the cryostat structure: two tilted axial conical holes and 12 radial ones having a lower diameter of 40 mm, properly aligned with 14 holes

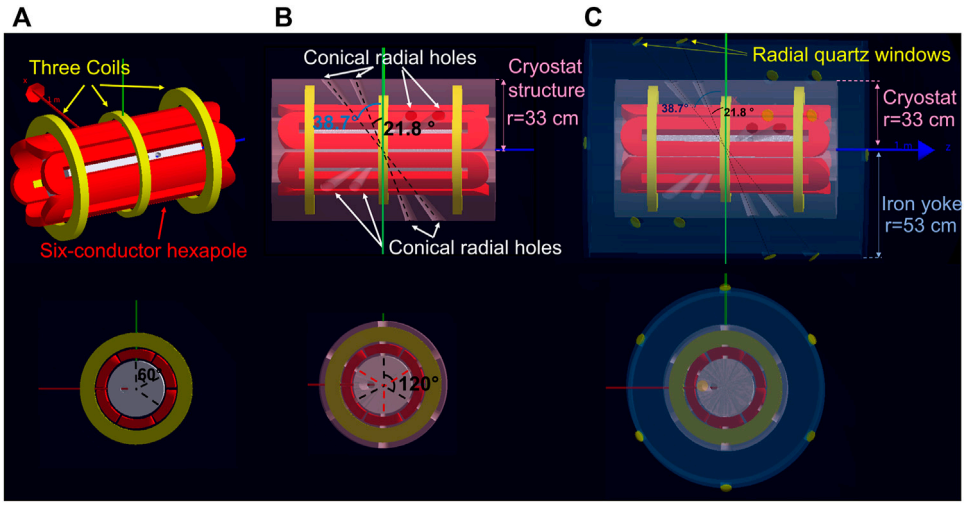

FIGURE 4
(A) Plasma chamber surrounded by superconducting coils (yellow) and hexapole (red); **(B)** magnetic system surrounded by the cryostat structure (pink) in which tapered holes used as lines of sight for gamma-ray detection are shown; **(C)** ARMCO® iron yoke (blue) surrounding the magnetic plasma trap.

TABLE 1 Geometry of the PANDORA trap showing for each component: the inner radius (R_I), the outer radius (R_O), and the length or width (L/W).

	R_I (mm)	R_O (mm)	W/L (mm)
Plasma chamber	140	150	700
Injection coil	225	300	44
Middle coil	225	253	46
Extraction coil	225	300	44
Hexapole conductor	165	212	~ 900
Cryostat	150.5	330	~ 950
Iron yoke	500	525	~ 1050

created in the plasma chamber. Conical holes point to the center of the plasma chamber and pairs opposite to the center are collinear.

- The magnetic trap is surrounded by an *ARMCO® iron yoke*, distant 150 mm from the ends of the hexapole (along the axis), 200 mm distant from the outer radius of the injection and extraction axial coils, having a thickness of 25 mm. The iron yoke is shown as blue color in Figure 4C. The iron yoke exhibits the same number of holes (88 mm in diameter) along the cone of view of the 14 collimators. At the end of each collimator was placed a quartz window with a thickness of 3 mm and a diameter of 88 mm (yellow);
- An *array of 14 γ-ray detectors* (two placed axially and 12 radially). Each detector was placed collinearly at each collimator (Figure 5A). The HPGe detectors [25] have a length of 82 mm and a radius of 38 mm and are surrounded by a 1 mm thick layer of Al (Figure 5B). The Al cylinder is shown in transparent pink, while the active part of the detector is colored cyan inside of it.

The position and orientation of the collimators and γ-ray detectors have been chosen so as to avoid, within the field of view, the magnetic branch regions where the background due to intense bremsstrahlung X-ray emission (caused by axial and radial losses impinging on the plasma chamber walls) is expected to be more intense. Figure 6 shows 3D views of the detector array surrounding the trap: each pair of HPGe has been placed outside the regions where the magnetic field lines are more intense and intercept the plasma chamber walls.

4.2 Evaluation of the array efficiency

The first aim of the simulations was to estimate the total detection efficiency needed to evaluate the feasibility of the experiment using γ-rays and to choose the type of detector giving the best performances in terms of efficiency and energy resolution. Two different types of detectors were compared in the simulations: the hyper-pure germanium (HPGe) and the lanthanum bromide ($LaBr_3$). Initial simulations were performed considering the emission from an isotropic point–like source; once the best detector type was determined, a complete characterization was performed in terms of the position of the detectors and of the collimation system (including the size and shape of the holes) assuming the

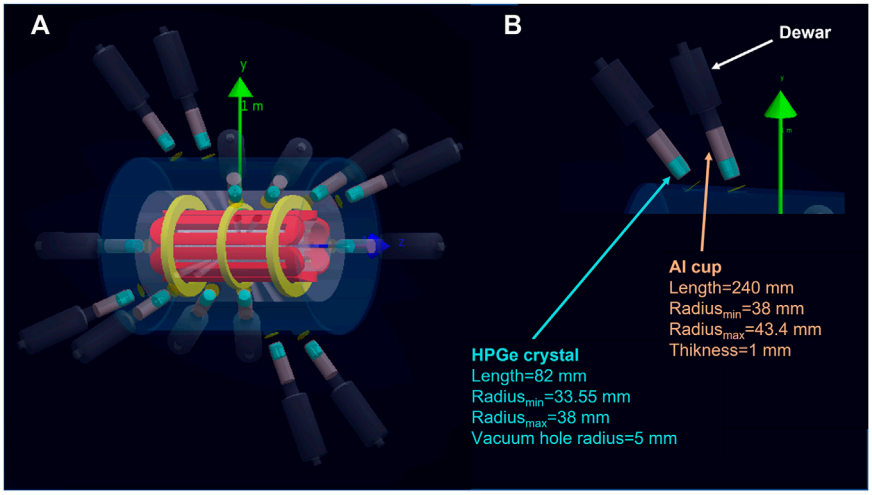

FIGURE 5
(A) Final design of the PANDORA trap with the magnetic system (coils, hexapole, cryostat, and iron yoke) and the array of detectors placed collinearly at each collimator as implemented in Geant4. **(B)** Details of the HPGe array show the dimensions of the detectors (crystal + Al cup) used in the simulations.

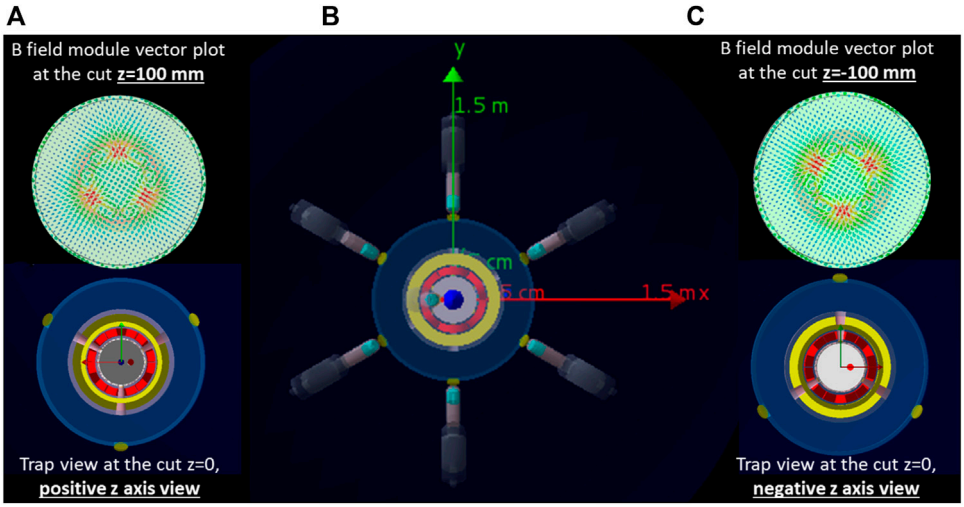

FIGURE 6
Sketch of the detector positions **(B)** compared to B field lines distribution. Two cut views are shown in **(A)** for z = 100 mm and in **(C)** for z = −100 mm. Each pair of HPGe (shown in the lower panels A and C) has been placed outside the regions where the magnetic field lines are more intense (shown on upper panels A and C).

emission from an isotropic ellipsoidal source whose size corresponds to the plasma volume in the PANDORA trap.

4.2.1 Array efficiency: HPGe vs $LaBr_3$ detectors for a point-like source

As a first step, simulations were performed considering the emission from an isotropic point–like source placed in the center of the plasma chamber [26]. The detection efficiency of the array to γ-rays of different energies was simulated by changing the energy of the source in the range from 100 keV to 2 MeV. The results, which take into account geometrical and photopeak efficiency, are shown in Figure 7A for an array of 14 HPGe detectors (blue symbols) and for an array of 14 $LaBr_3$ (red symbols), using the same detector sizes. Since for the purposes

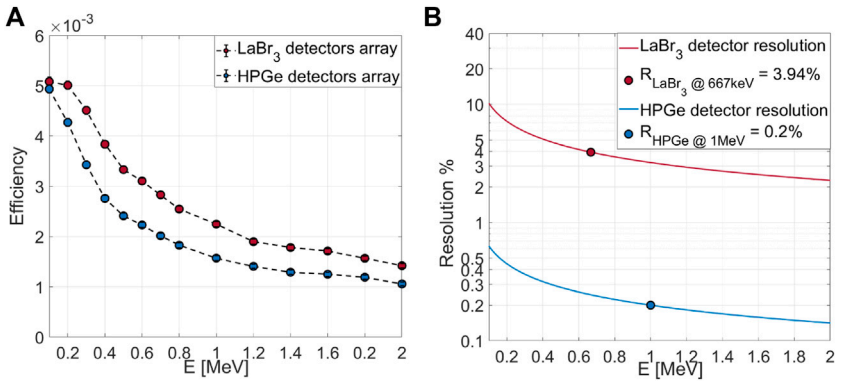

FIGURE 7
(A) Efficiency versus γ-ray incident energy for the HPGe detectors (blue symbols) and $LaBr_3$ (red symbols) detectors. **(B)** Energy resolution versus γ-ray incident energy for HPGe (blue symbols) and $LaBr_3$ (red symbols).

of the PANDORA project, the main goal is to detect only the characteristic γ-rays emitted by daughter nuclei following the β-decay process which populates the lowest excited states of the daughter nuclei, the expected experimental multiplicity is one and no coincidence analysis is needed. Thus, the plot was obtained with multiplicity one, one energy after the other. The efficiency for the two types of the detector is very similar and of the order of few per mille.

However, the main difference between the two types of detectors is the energy resolution. The typical resolution as a function of the energy of the incident γ-ray [27] is shown in Figure 7B for the HPGe (blue symbols) [28] and $LaBr_3$ (red symbols) [29] detectors, respectively. They differ more than one order of the magnitude, and this strongly affects the signal-to-background ratio.

Starting from the typical background spectrum due to plasma self-emission shown in Figure 2, it has been possible, once the total efficiency of the system has been determined, to evaluate the background rate that would be measured by the PANDORA setup. Such a rate was compared to the rate of the γ-rays emitted from the daughter nuclei after the β-decay and detected in the array. A comparison of the performances between the HPGe detector array and the $LaBr_3$ detector array was performed to evaluate the time needed to achieve a 3σ significance. We considered, as an example, a signal of 0.25 cps in plasma (counts per second) in the multi detector array at a given energy (which is a value of rate corresponding to a variation of the mean lifetime of ^{176}Lu of about six orders of magnitude, as expected by the theoretical models according to the thermodynamic properties of the plasma that will be generated in PANDORA, section 5). The adopted procedure was to integrate the background spectrum in the energy window corresponding to the intrinsic detector resolution. The error over this background was taken as the square-root of counts in the energy resolution window, while the counts due to the real decays occurring in the plasma were summed up linearly with time. The procedure was repeated for different run durations spanning a time window up to 10^7 s.

Figure 8A shows the trend of the signal counts (in black) and of the three times the background level (in blue for HPGe, in red for $LaBr_3$), in order to see where and when the cross-over point between the two curves occurs. The intersection of the two lines indicates the point where the signal exceeds the 3σ background level and the corresponding abscissa indicates the measurement time needed to have a 3σ significance. The comparison shows that after about several days it is possible to obtain a 3σ significance using the HPGe detector array (as shown in Figure 8A), while using a $LaBr_3$ detector array the time needed is much longer, the measurement is very challenging or, eventually, not-feasible, depending on the physics case investigated.

A similar plot (Figure 8B) was performed to evaluate the measurement time needed to have only a 1σ significance. In this case, the $LaBr_3$ detector array could allow to reach this significance in about 2 months, drastically higher than what is required using the HPGe detector array.

Due to the strong difference observed in the performances of the arrays, we have decided to use the high performance HPGe detector array in PANDORA. Therefore, in the following sections, we will discuss the performances of an array based on HPGe detector.

4.2.2 Characterizations of collimator-hole position using an ellipsoidal source

As a following step, in order to realistically reproduce the experimental conditions, simulations were performed considering an isotropic ellipsoidal source placed around the center of the plasma chamber, having semi-axis lengths of 79 mm, 79 mm and 56 mm, respectively, for the x, y, and z axis (corresponding to the plasma volume and shape provided by

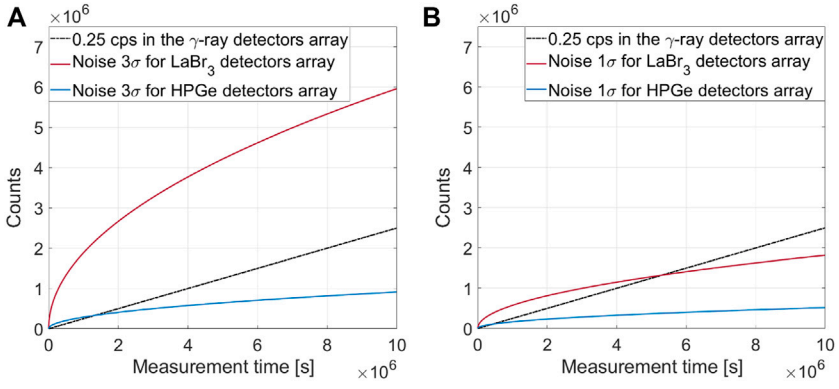

FIGURE 8
Trend of the counts of the expected signal (in black), considering a rate of 0.25 *cps* (counts per second) in the multi detector array, and of the 3σ background level **(A)** for $LaBr_3$ and HPGe detectors (in red and blue, respectively). **(B)** Similar plot as in **(A)** for a rate of the 1σ background levels.

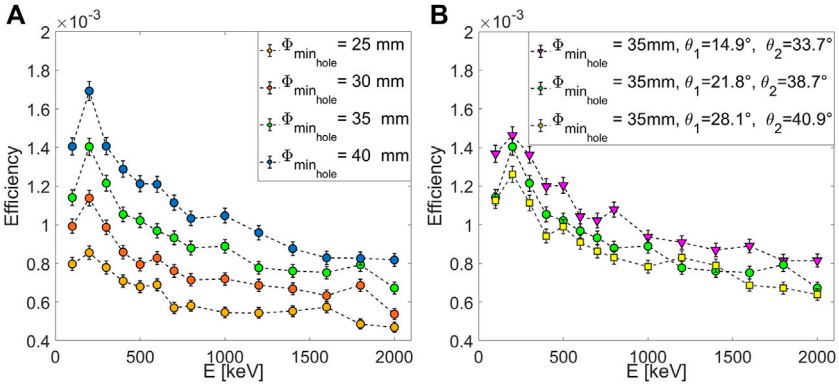

FIGURE 9
(A) Efficiency plots as a function of the incident γ-ray energy for HPGe detectors. An ellipsoidal source was used. The colors of the symbols correspond to simulations performed using different hole sizes for collimators. **(B)** Same as A but in this case the effect of different angles of inclination of the conical holes was investigated.

the magnetic field profiles in the PANDORA plasma trap). Similarly to what was previously performed for the point-like source, the γ-ray energy range explored extends from 100 keV to 2 MeV. For the evaluation of the background due to plasma self-emission, we considered a density of $n = 10^{13}$ cm^{-3}, and a volume of 1,500 cm^3. The trend of the array efficiency as a function of the incident γ-ray energy is shown in Figure 9A (in blue) assuming 14 HPGe detectors. The comparison between the results shown in Figure 7A indicates that the efficiency in the case of the ellipsoidal source is a factor of 2.5 lower than that of a point-like source for the lowest energies, while the difference reduces to about a factor of 1.5 for higher energies.

Further simulations were performed to investigate the effect due to the position and size of the collimator holes. The values shown in Section 4.1 are, in fact, the outcome of this study. In particular, the effects due to the reduction of conical holes and to the different choices of inclination angle (with respect to the y vertical axis) and position were investigated. The purpose of this characterization was also to define a tolerance range for each parameter, taking into account the technical limitations that can arise in the design study of the magnetic trap (e.g., mechanical constraints imposing a certain angle for the conically shaped holes). The simulated efficiency plots associated with four different diameters $\phi_{min_{hole}}$ are shown in Figure 9A. At 300 keV (i.e., close to the energy of the emitted γ-ray for the physic case of ^{176}Lu), the efficiency changes by a factor of two from the largest to the smallest diameter.

The effect related to three different choices of the inclination angle of the collimators is instead shown in Figure 9B. It shows that the overall average change in efficiency at the three

representative couple of angles chosen is less than 20%, somehow relaxing any requirement from this point of view.

The results of the simulations suggested that the best compromise between detection efficiency and mechanical constraints for the HPGe array is to build a collimation system with holes having a diameter of 40 mm and placed at a relative inclination corresponding to a first angle of $\theta_1 = 21.8^{\circ}$ (it corresponds to a distance of 60 mm from the *y*-axis, along the plasma chamber external surface) and a second angle of $\theta_2 = 38.7^{\circ}$ (corresponding to a distance of 120 mm from the *y*-axis, along the plasma chamber external surface), as shown in Figure 4C. This choice guarantees greater flexibility and tolerance for the realization of the plasma trap.

Moreover, numerical simulations finalized to investigate the distribution of the various electrons' population, with special attention to the warm component on which depends the obtained ions' CSD, allowed to benchmark the choice of the specific orientation of the 14 HPGe detectors. The recent results [30] demonstrated that the cones of view perfectly intercept the warm electrons spatial distribution. Thus, they will point exactly where most of the ionizations will take place, increasing the detection sensitivity to variations of the in-plasma charge state distribution.

5 Simulations of virtual experimental runs

Once the overall diagnostics tools, as well as the HPGe detector array, have been defined, the setup was tested in a simulated experiment to assess the feasibility and sensitivity of the method to be adopted for the different isotopes of interest. Different theoretical predictions about lifetime dependence on the temperature [31] were used to evaluate the feasibility of the measurements—estimating the run duration to get statistically meaningful results in terms of significance. It was also possible to demonstrate that future PANDORA measurements will have the adequate sensitivity to discriminate between different sets of theoretical predictions of the expected variation of the mean lifetime (i.e. [32]) and to eventually better fit the data of nucleosynthesis which disagrees with the current decay rate predictions (i.e., in [33] one needs to assume that the temperature dependence of the decay rate for ^{134}Cs is less steep than that suggested by [31] by around a factor eight to level the production of ^{134}Ba and ^{136}Ba according to the model).

In order to estimate the measurement time needed to reach the 3σ significance taking into account different lifetimes, that is, different rates in the detector array, we made dedicated plots showing the total counts and the expected significance (starting from the decay rate (or the lifetime) of the radionuclide) as a function of the measurement time for the first three physics cases (section 3) selected for the PANDORA phase-1.

Figure 10 shows the simulation result for the physical case of ^{176}Lu. The first (from the left) green vertical axis reports a decreasing lifetime expressed in years, starting from the lifetime of the neutral isotope ($5.45{\cdot}10^{10}$ years) to the values of lifetimes predicted by the theory and that are reachable in our plasma trap. The expected collapse of the lifetime as theoretically evaluated is about six order of magnitude for the case of ^{176}Lu (at a plasma temperature of about 10 keV) [31].

Considering these lifetimes, the effective activity in the plasma (expressed in cps)—assuming a plasma of 1,500 cm^3 in volume with a relative concentration of 1% of Lu with respect to the buffer density (10^{13} ions/cm^3)—can be estimated and is shown on the blue vertical axis. Finally, including the efficiency of the HPGe detector array estimated by the aforementioned Geant4 simulations, we evaluated the counting rate of the detector array shown in the third, black vertical axis. The *x*-axis indicates the measurement time. Pseudo-colors give the total number of counts at the peak of interest (i.e., the number of γ-rays emitted by Hf at E_γ = 306.78 keV). As performed in the data analysis shown in Figure 8, also in this case, the error on the background was estimated as the square-root of counts in the same energy window used to integrate the γ-peak of interest (306.78 keV), while the counts due to the real decays occurring in the plasma grow up linearly with time. The condition that the signal overcomes the 3σ background level defines the measurement time needed to have a 3σ significance. Black dashed lines shown in the plot in Figure 10 represent iso-significance contours at each given combination of expected activity and measurement time. In particular, several significances in the range 1σ-7σ are labeled in the plot and the black region is such that the significance is worse than 1σ.

The feasibility of the measurement, depending on the relevance of lifetime decrease, is deemed to last from a day (in the case of six orders of magnitude collapse) up to 3 months (as shown in Figure 10). Assuming, for example, a variation of the lifetime of six orders of magnitude (corresponding to a rate of γ-rays in the multi-detectors array of 0.4 cps), about 15 h are necessary to obtain the 3σ significance, while about 1 h is enough to reach the 1σ significance. For a smaller variation of the lifetime (e.g., of five orders of magnitude, rate ~ 0.05), it should take up to 3 months to reach the 3σ significance. Moreover, in the present calculations, only one-peak of γ-rays for each radionuclide has been considered, while in the reality we can take profit of a further γ-ray with an energy of 202.88 keV emitted in the decay process, which will improve the significance within shorter acquisition times.

Similar plots for ^{134}Cs and ^{94}Nb were also performed. Due to their shorter lifetime, the needed quantities of these two nuclides are much smaller than the one for the ^{176}Lu. For example, a density of 10^6 cm^{-3} of ^{134}Cs ions should be sufficient to get 3σ significance already after 7–11 h, at the expected in-plasma lifetime. The significance plot for ^{134}Cs is shown in Figure 11.

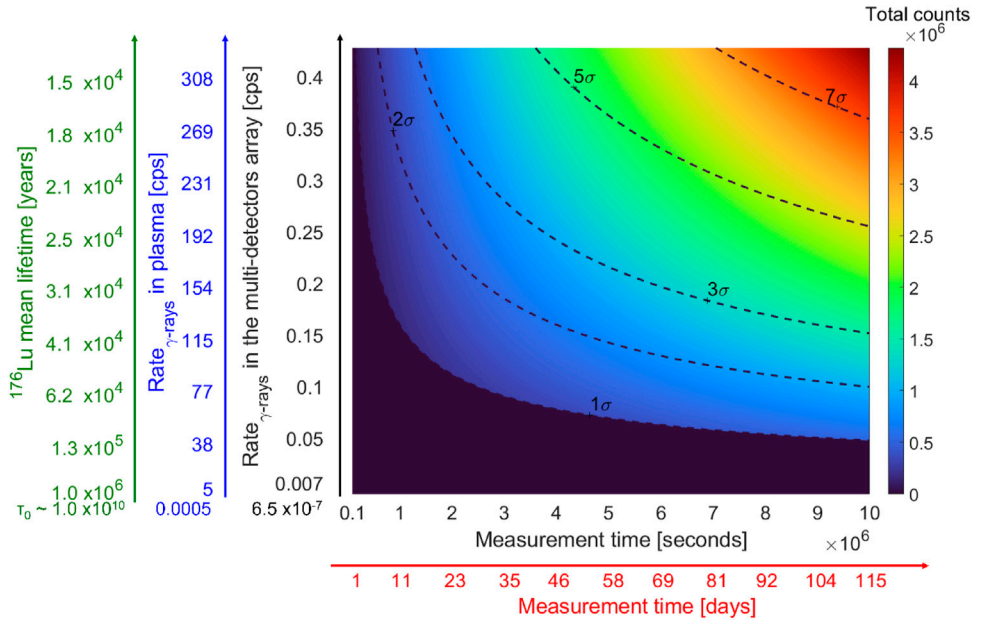

FIGURE 10
Total counts of gamma-rays emitted (pseudo-colors scale) and iso-significance contours (dashed lines) for different ^{176}Lu isotope lifetimes (green vertical axis) as a function of the measurement lifetime. Blue and black vertical scales show the predicted decay rate in plasma and the counting rate measured in the array associated to the different isotope lifetime.

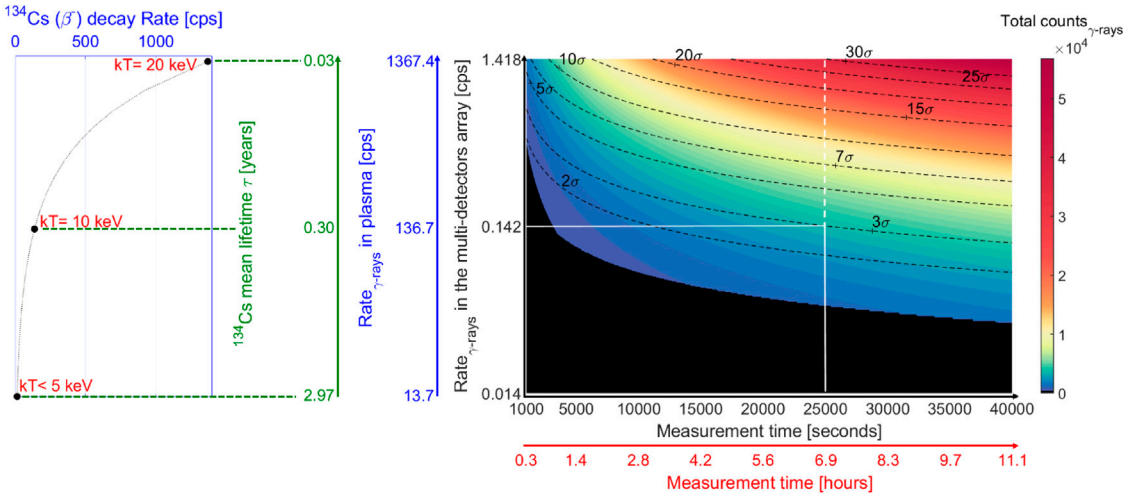

FIGURE 11
Total counts of gamma-rays emitted (pseudo-colors scale) and iso-significance contours (dashed lines) for different ^{134}Cs isotope lifetimes (green vertical axis) as a function of the measurement lifetime. Blue and black vertical scales show the predicted decay rate in plasma and the counting rate measured in the array associated to the different isotope lifetime.

The green vertical axis reports on the lifetime expressed in years, starting from the mean lifetime of the neutral isotope (2.97 years) to the values of lifetimes predicted by the theory; the expected collapse of the lifetime as theoretically evaluated in [31] is about two orders of magnitude at around 20 keV, about one order of magnitude at around 10 keV while no variations are expected for values lower than 5 keV. Considering the trend of lifetime as a function of temperature as depicted in Figure 11, the

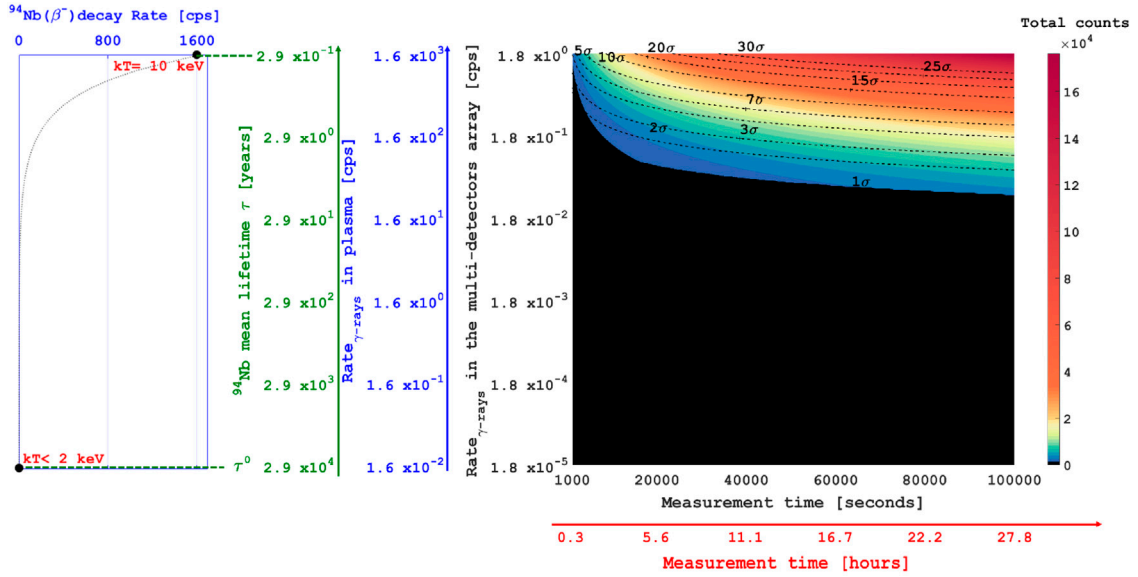

FIGURE 12
Total counts of gamma-rays emitted (pseudo-colors scale) and iso-significance contours (dashed lines) for different ^{94}Nb isotope lifetimes (green vertical axis) as a function of the measurement lifetime. Blue and black vertical scales show the predicted decay rate in plasma and the counting rate measured in the array associated to the different isotope lifetime.

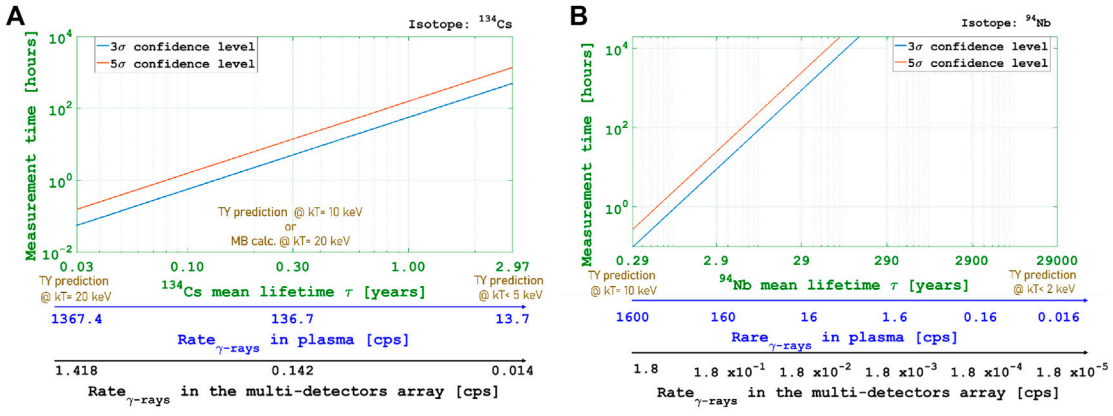

FIGURE 13
"*Iso-significance*" level at 3σ and 5σ reached after a given measurement time, reported on the *y*-axis, versus the decay rate (or the lifetime) of the ^{134}Cs radionuclide **(A)** and of the ^{94}Nb **(B)**.

effective activity in the plasma (expressed in cps)—assuming an ellipsoidal plasma of 1,500 cm^3 in the volume with a relative concentration of 0.00001% of ^{134}Cs with respect to the buffer density (10^{13} ions/cm^3)—is shown in the blue vertical axis and, taking into account the efficiency estimated by Geant4 simulation, we obtained the counting rate expected in the γ detector array (black vertical axis).

Assuming, for example, a variation of the lifetime of an order of magnitude (counting rate of HPGe array of 0.14 cps), about 5 h are necessary to obtain the 3σ significance, while about 2 h are enough to reach the 2σ significance.

A similar plot for the ^{94}Nb was performed (Figure 12). In this case, the expected collapse of the lifetime as theoretically evaluated in [31] is about five orders of magnitude (at around 10 keV). We assumed an ellipsoidal plasma of 1,500 cm^3 in the volume with a concentration of 0.0001%. Also, in this case; several significance contours in the range 2σ–30σ are shown. Assuming a variation of the lifetime of four orders of magnitude

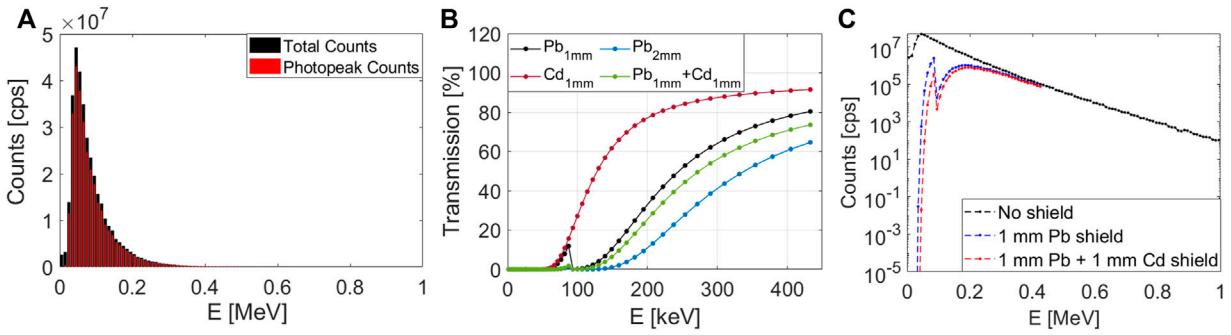

FIGURE 14
(A) Counting rate in HPGe detector array as a function of gamma-ray energy. Red area corresponds to photopeak events while the black one is associated to the total number of events hitting the array. **(B)** Transmission trend versus the γ-ray energy for different shield thicknesses and/or materials. **(C)** Shield effects on the background spectrum (log scale). The black dashed line corresponds to the rate in an unshielded array while blue and red ones show the suppression effect due to lead or lead and cadmium shields, respectively.

(corresponding to a rate of γ-rays in the multi-detectors array of 0.18 cps) about 20 h is necessary to obtain the 3σ significance.

Finally, in the plots shown in Figure 13, the *iso-significance* curves at 3σ and 5σ were reported (in the log–log scale) for the ^{134}Cs (Figure 13A) and ^{94}Nb (Figure 13B) cases, respectively. The results suggested that for the ^{94}Nb case, it will be possible to obtain the 3σ significance in a reasonable measurement time (within 3 months) only if the mean lifetime was at least three orders of magnitude shorter than the mean lifetime of the neutral isotope.

Regardless of the experimental result, it will put important constraints on theoretical model predictions. The possibility to discriminate among different models will depend on the uncertainties which will affect the lifetime measurement. The in-plasma λ can be, in fact, estimated by Equation (3) with an uncertainty of around 28% (considering error propagation). We have considered the following relative uncertainties for the parameters that will be measured: $\frac{dN}{N} \sim 0.3\%$ (3σ significance measurement), $\frac{dV}{V} \sim 15\%$ (the error in estimating the radius is around 5% [23]), and $\frac{dn_i}{n_i} \sim 25\%$ (the plasma density can be measured by the interfero-polarimentric tool [20] or by optical [34, 35] and X-ray [24, 36]) spectroscopy and also by means of a novel numerical tool that has been developed for analyzing spatially anisotropic electron populations in ECR plasmas [37]. It is worth noticing that new techniques and advanced algorithm of analysis which we are developing could allow to further reducing the aforementioned uncertainties, improving the performances of the measurement.

6 Perspectives: The background suppression investigation

Investigations about the background suppression have been performed in order to increase the signal-to-background ratio, to reduce the very high rate due to the intense plasma self-emission, and to improve the working conditions of the HPGe detectors. For this purpose, we started to perform simulations in Geant4 considering the background contribution emitted from the plasma, in order to estimate the thickness of different kinds of absorbers to be used to shield detectors and the amount of Compton scattering due to absorber layers.

Preliminary simulations have been performed, assuming the emission from an isotropic point–like source placed in the center of the plasma chamber, with the an energy distribution as the typical background spectrum due to a plasma self-emission at n = 10^{13} cm^{-3} and with a volume of 1,500 cm^3 (Figure 2).

Figure 14A shows the comparison of the spectra including only events depositing the entire energy in the detector (indicated as photopeak counts) and the spectrum of all detected events. The difference in the yield is of the order of 10% and supports the previous estimate of the background contribution to the detected γ-ray spectrum.

In order to reduce the intense rate in the detectors due to plasma emission up to 250 keV, but at the same time reach a good transmission at 306 keV, a specific shield will be used. Some preliminary considerations have been performed, comparing the transmission trends (*NIST* database [38]) of different thicknesses of lead with an additional shield of Cd or Cu, in order to fully suppress the contribution of plasma self-emission to the background up to 100 keV (also the radiation due to the lead K-edge). In Figure 14B, the transmission trends of different materials are shown as a function of the γ-ray energy. In our specific case, due to the background spectral shape, a shield made of 1 mm of Pb or 1 mm of Pb + 1 mm of Cd could be effective to significantly reduce the background. A preliminary evaluation of the two different shields on the background spectrum is shown in Figure 14C. The background below 200 keV decreases significantly when the shield is included. In perspective, simulations will be

performed aimed at characterizing the system in order to have the best compromise between the increase in the signal-to-background ratio and the overall reduction of the background.

7 Advanced front-end electronics and acquisition system for operation at high background rate

The γ-ray hyper-pure Ge (HPGe) detector system of PANDORA has been developed to work under the particular conditions mentioned earlier as described in detail in [25, 39].

All the HPGe electronics chains are based on a custom R&D carried out in the framework of AGATA [40] and GALILEO [25] projects, to run HPGe detectors at high counting rates with the best γ-energy resolution.

Particular attention has been paid to the design of new pre-amplifiers which were modified and tested up to a rate of 60 kHz using different γ-ray sources, for simulating the typical low-energy background. The results already shown in [25, 39], indicate that HPGe detectors resolution did not show significative worsening at higher background rates, with a maximum γ-energy resolution value measured of about 3 keV.

To assure a high level of reliability and maintainability for running without interruptions over long-lasting measurements, the front and back-end electronics for PANDORA is now based on custom-made electronics, developed and adapted with the use of commercially high performance readout modules.

Finally, the HPGe detectors support infrastructure, including LV power supply, HV and the automatic HPGe cooling system has been designed to guarantee the best running conditions for the HPGe detectors and to maintain stable their performances (in terms of γ-energy resolution), during the long runs foreseen in PANDORA experiments. Of course, this system integrates the slow-control software to manage and monitor detector operation parameters, such as HV and temperature over time.

Furthermore, we want to explicitly mention that the numbers quoted in the study were currently obtained assuming negligible dead time, and further investigations are ongoing to evaluate its contribution mainly on the measurement time.

8 Conclusion

In this work, the numerical simulations performed in Geant4 focused on the design of the array of γ-ray detectors for the PANDORA project were presented. The best configuration in terms of the total number, type of detectors, and their optimal displacement around the trap, including collimation systems and shielding was investigated, modeling the response of the array and estimating the total efficiency for each configuration. The final detection system consists of an array of 14 HPGe detectors whose total photopeak efficiency is between 0.1 and 0.2%. The sensitivity of the PANDORA experiment was specifically checked in simulated experimental runs by exploring the feasibility of measuring the decay rates in terms of 3σ significance for the three physical cases of PANDORA. The run duration needed to get statistically meaningful results was determined. Expected measurement time, needed for at least 3σ significance, range from few hours (for ^{134}Cs) to 70–80 days (for ^{176}Lu, which is the most challenging case in PANDORA).

Data availability statement

The original contributions presented in the study are included in the article/Supplementary Material; further inquiries can be directed to the corresponding author.

Author Contributions

Conceptualization: EN, DS, SA, and DM. Numerical simulations: EN and SA. Formal analysis: EN, DS, SA, and DM. Funding acquisition: DS and DM. Methodology: EN, DS, SA, AGA, GM, AP, GT, and DM. Project administration: DS and DM. Software, EN, DS, SA, and DM. Supervision: DS and DM. Visualization: EN, DS, SA, LC, AGA, AGO, GM, MM, BM, DN, AP, GT, and DM. Writing–original draft: EN. Writing–sections of the manuscript: EN, DS, AGO, DN, and DM. Writing–review and editing: EN, DS, SA, LC, AGA, AGO, GM, MM, BM, DN, AP, GT, and DM. All authors have read and agreed to the published version of the manuscript.

Acknowledgments

The authors gratefully acknowledge the support of INFN by the Grants PANDORA_Gr3 (3rd Nat. Comm.).

Conflict of interest

The authors declare that the research was conducted in the absence of any commercial or financial relationships that could be construed as a potential conflict of interest.

Publisher's note

References

1. Mascali D, Santonocito D, Amaducci S, Andò L, Antonuccio V, Biri S, et al. A novel approach to β-decay: PANDORA, a new experimental setup for future in-plasma measurements. *Universe* (2022) 8:80. doi:10.3390/universe8020080

2. Mascali D, Musumarra A, Leone F, Romano FP, Galatà A, Gammino S, et al. PANDORA, a new facility for interdisciplinary in-plasma physics. *Eur Phys J A* (2017) 53:145. doi:10.1140/epja/i2017-12335-1

3. Litvinov Y, Bosch F. Beta decay of highly charged ions. *Rep Prog Phys* (2011) 74: 016301. doi:10.1088/0034-4885/74/1/016301

4. Bosch F, Faestermann T, Friese J, Heine F, Kienle P, Wefers E, et al. Observation of bound-state β^-decay of fully ionized ^{187}Re: ^{187}Re-^{187}Os cosmochronometry. *Phys Rev Lett* (1996) 77:5190–3. doi:10.1103/PhysRevLett.77.5190

5. Jung M, Bosch F, Beckert K, Eickhoff H, Folger H, Franzke B, et al. First observation of bound state β^- decay. *Phys Rev Lett* (1992) 69:2164–7. doi:10.1103/PhysRevLett.69.2164

6. Bahcall JN. Theory of bound-state beta decay. *Phys Rev* (1961) 124:495–9. doi:10.1103/PhysRev.124.495

7. Klay N, Käppeler F, Beer H, Schatz G. Nuclear structure of ^{176}Lu and its astrophysical consequences ii. ^{176}Lu, a thermometer for stellar helium burning. *Phys Rev C* (1991) 44:2839–49. doi:10.1103/PhysRevC.44.2839

8. Cristallo S, Piersanti L, Straniero O, Gallino R, Dominguez I, Abia C, et al. Evolution, nucleosynthesis, and yields of low-mass asymptotic giant branch stars at different metallicities. ii. the FRUITY database. *Astrophys J Suppl Ser* (2011) 197:17. doi:10.1088/0067-0049/197/2/17

9. Busso M, Gallino R, Wasserburg GJ. Nucleosynthesis in asymptotic giant branch stars: Relevance for galactic enrichment and solar system formation. *Annu Rev Astron Astrophys* (1999) 37:239–309. doi:10.1146/annurev.astro.37.1.239

10. Naselli E, Mascali D, Biri S, Caliri C, Castro G, Celona L, et al. Multidiagnostics setups for magnetoplasmas devoted to astrophysics and nuclear astrophysics research in compact traps. *J Instrum* (2019) 14:10008. doi:10.1088/1748-0221/14/10/C10008

11. Mazzaglia M, Biri S, Emma G, Finocchiaro G, Galatà A, Mauro G, et al. A system for plasma parameters evaluation in compact magnetic traps aiming at in plasma β-decay investigation. *Frontiers* (2022). submitted in this special issue.

12. Agostinelli S, Allison J, Amako KA, Apostolakis J, Araujo H, Arce P, et al. GEANT4—a simulation toolkit. *Nuclear Instruments and Methods in Physics Research Section A: Accelerators Spectrometers Detectors and Associated Equipment* (2003) 506:250–303. doi:10.1016/S0168-9002(03)01368-8

13. Mauro G, Celona L, Torrisi G, Pidatella A, Naselli E, Russo F, et al. An innovative superconducting magnetic trap for probing β-decay in plasmas. *Frontiers* (2022). submitted in this special issue.

14. Geller R. *Electron Cyclotron resonance ion sources and ECR plasmas*. Bristol, UK: J W Arrowsmith Ltd (1996).

15. Skalyga V, Izotov I, Kalvas T, Koivisto H, Komppula J, Kronholm R, et al. Suppression of cyclotron instability in electron cyclotron resonance ion sources by two-frequency heating. *Physics of Plasmas* (2015) 22:083509. doi:10.1063/1.4928428

16. Naselli E, Mascali D, Mazzaglia M, Biri S, Rácz R, Pálinkás J, et al. Impact of two-close-frequency heating on ECR ion source plasma radio emission and stability. *Plasma Sourc Sci Technol* (2019) 28:085021. doi:10.1088/1361-6595/ab32f9

17. Ioffe M, Sobolev R. Confinement of a plasma in a trap formed by a combined magnetic field. *J Nucl Energy Part C Plasma Phys* (1965) 7:501–13. doi:10.1088/0368-3281/7/5/306

18. Naselli E, Ràcz R, Biri S, Mazzaglia M, Celona L, Gammino S, et al. Innovative analytical method for x-ray imaging and space-resolved spectroscopy of ECR plasmas. *Condens Matter* (2022) 7:5. doi:10.3390/condmat7010005

19. Biri S, Ràcz R, Perduk Z, Pàlinkàs J, Naselli E, Mazzaglia M, et al. Innovative experimental setup for X-ray imaging to study energetic magnetized plasmas. *J Instrum* (2021) 16:P03003. doi:10.1088/1748-0221/16/03/P03003

20. Mascali D, Naselli E, Torrisi G. Microwave techniques for electron cyclotron resonance plasma diagnostics. *Review ofScientific Instruments* (2022) 93:033302. doi:10.1063/5.0075496

21. Torrisi G, Naselli E, Mascali D, Donato LD, Sorbello G. mm-wave interferometer-polarimeter and profilometry design study for retrieving plasma density in the PANDORA experiment. *Frontiers* (2022). submitted in this special issue.

22. Rizzolo A, Barbisan M, Bizzotto L, Capobianco R, Muri MD, Fadone M, et al. Characterization of the SPIDER Cs oven prototype in the CAesium Test Stand for the ITER HNB negative ion sources. *Fusion Engineering and Design* (2019) 146: 676–9. doi:10.1016/j.fusengdes.2019.01.053

23. Naselli E, Ràcz R, Biri S, Mazzaglia M, Galatà A, Celona L, et al. Quantitative analysis of an ECR Ar plasma structure by x-ray spectroscopy at high spatial resolution. *J Instrum* (2022) 17:C01009. doi:10.1088/1748-0221/17/01/C01009

24. Gumberidze A, Trassinelli M, Adrouche N, Szabo CI, Indelicato P, Haranger F, et al. Electronic temperatures, densities, and plasma X-ray emission of a 14.5 GHz electron-cyclotron resonance ion source. *Rev Scientific Instr* (2010) 81:033303. doi:10.1063/1.3316805

25. Goasduff A, Mengoni D, Recchia F, Valiente-Dobon JJ, Menegazzo R, Benzoni G, et al. The GALILEO γ-ray array at the legnaro national laboratories. *Nuclear Instruments and Methods in Physics Research Section A: Accelerators Spectrometers Detectors and Associated Equipment* (2021) 1015:165753. doi:10.1016/j.nima.2021.165753

26. Naselli E, Mascali D, Caliri C, Castro G, Celona L, Galatà A, et al. Nuclear β-decays in plasmas: How to correlate plasma density and temperature to the activity. *EPJ Web Conf* (2020) 227:02006. doi:10.1051/epjconf/202022702006

27. Knoll G. *Radiation detection and measurement*. New York: John Wiley & Sons (2010).

28. Goasduff A, Mengoni D, Recchia F, Valiente-Dobón J, Menegazzo R, GBenzoni, et al. The GALILEO γ-ray array at the legnaro national laboratories. *Nuclear Inst. and Methods inPhysics Research A* (2021) 1015.

29. van Loef E, Dorenbosa P, van Eijka C, Kramer K, Gudel H. Scintillation properties of $LaBr_3:Ce^{3+}$ crystals: Fast, efficient and high-energy-resolution scintillators. *Nuclear Instruments and Methods in Physics Research Section A: Accelerators Spectrometers Detectors and Associated Equipment* (2002) 486: 254–8. doi:10.1016/s0168-9002(02)00712-x

30. Galata A, Mascali D, Mishra B, Naselli E, Pidatella A, Torrisi G. On the numerical determination of the density and energy spatial distributions relevant for in-plasma β-decay emission estimation. *Frontiers* (2022). submitted in this special issue.

31. Takahashi K, Yokoi K. Beta-decay rates of highly ionized heavy atoms in stellar interiors. *Data Nucl Data Tables* (1983) 36:375–409. doi:10.1016/0092-640X(87)90010-6

32. Taioli S, Vescovi D, Busso M, Palmerini S, Cristallo S, Mengoni A, et al. Theoretical estimate of the half-life for the radioactive ^{134}Cs and ^{135}Cs in astrophysical scenarios. *arXiv:2109.14230* (2021).

33. Palmerini S, Busso M, Vescovi D, Naselli E, Pidatella A, Mucciola R, et al. Presolar grain isotopic ratios as constraints to nuclear and stellar parameters of asymptotic giant branch star nucleosynthesis. *ApJ* (2021) 921:7. doi:10.3847/1538-4357/ac1786

34. Mazzaglia M, Celona L, Gammino S, Naselli E, Reitano R, Torrisi G, et al. Optical emission spectroscopy measurements of hydrogen and argon plasmas at high resolution. *IL NUOVO CIMENTO* (2021) 44:58. doi:10.1393/ncc/i2021-21058-9

35. Giarrusso M, Avila G, Zanna GD, Landi E, Leone F, Munari M, et al. High resolution spectropolarimetry: From astrophysics to ECR plasmas. *J Instrum* (2018) 13:C11020. doi:10.1088/1748-0221/13/11/C11020

36. Mascali D, Castro G, Biri S, Rácz R, Pálinkás J, Caliri C, et al. Electron cyclotron resonance ion source plasma characterization by X-ray spectroscopy and X-ray imaging. *Review of Scientific Instruments* (2016) 87:02A510. doi:10.1063/1.4939201

37. Mishra B, Pidatella A, Biri S, Galatà A, Naselli E, Rácz R, et al. A novel numerical tool to study electron energy distribution functions of spatially anisotropic and non-homogeneous ECR plasmas. *Phys Plasmas* (2021) 28: 102509. doi:10.1063/5.0061368

38. [Dataset] Technology of Standards NNI. *X-ray form factor, attenuation and scattering tables* (2020).

39. Goasduff A, Santonocito D, Menegazzo R, Capra S, Pullia A, Raniero W, et al. A high resolution γ-ray array for the PANDORA plasma trap. *Frontiers* (2022). submitted in this special issue.

40. Akkoyun S, Algora A, Alikhani B, Ameil F, de Angelis G, Arnold L, et al. Agata-advanced gamma tracking array. *Nuclear Instruments and Methods in Physics Research Section A: Accelerators, Spectrometers, Detectors and Associated Equipment* (2012) 668:26–58. doi:10.1016/j.nima.2011.11.081

frontiers | Frontiers in Astronomy and Space Sciences

TYPE Technology and Code
PUBLISHED 17 August 2022
DOI 10.3389/fspas.2022.936532

OPEN ACCESS

EDITED BY
David Mascali,
Laboratori Nazionali del Sud (INFN), Italy

REVIEWED BY
Mitchell L. R. Walker,
Georgia Institute of Technology,
United States
Jayr Amorim,
Instituto de Tecnologia da Aeronáutica,
Brazil

*CORRESPONDENCE
S. Tsikata,
sedina.tsikata@cnrs-orleans.fr
L. Maunoury,
laurent.maunoury@ganil.fr

SPECIALTY SECTION
This article was submitted to Nuclear Physics,
a section of the journal
Frontiers in Astronomy and Space Sciences

RECEIVED 05 May 2022
ACCEPTED 13 July 2022
PUBLISHED 17 August 2022

CITATION
Tsikata S, Maunoury L and Ducret J-E (2022), Incoherent Thomson scattering: future implementation and measurement capabilities on the PANDORA experiment.
Front. Astron. Space Sci. 9:936532.
doi: 10.3389/fspas.2022.936532

Incoherent Thomson scattering: future implementation and measurement capabilities on the PANDORA experiment

S. Tsikata[1]*, L. Maunoury[2]* and J-E. Ducret[2]

[1]Centre National de la Recherche Scientifique (CNRS), Institut de Combustion, Aérothermique, Réactivité et Environnement (ICARE), Orléans, France, [2]Grand Accélérateur National d'Ions Lourds (GANIL), Caen, France

The PANDORA (Plasmas for Astrophysics Nuclear Decays Observation and Radiation for Archaeometry) experiment aims to study the β-decay process inside a dense plasma mimicking stellar conditions. An electron cyclotron resonance plasma trap will be built at INFN-LNS in Catania, Italy, for the generation of the desired conditions in the laboratory. This type of non-equilibrium dense plasma (reaching densities of up to 10^{13} cm^{-3}) is expected to generate electron energy distribution functions with electron energies ranging from tens of eV up to tens of keV. In this work, we describe aspects of a planned implementation of an incoherent Thomson scattering diagnostic for the study of electron properties in the plasma trap of PANDORA. The performance of this high-sensitivity diagnostic, known as THETIS, has been previously validated in measurements across a range of low-density magnetized plasma environments and it is expected to provide access to electron energy information in PANDORA in the range of temperatures from 1 to 10^3 eV. This article will establish the potential of such a diagnostic for future characterization of the electron properties in the PANDORA experiment.

KEYWORDS

incoherent Thomson scattering, electron density, laser diagnostics, electron temperature, electron cyclotron resonance (ECR), stellar plasmas, magnetic trap

1 Introduction

Understanding β-decay processes in stellar conditions remains a challenge. Information on such processes can provide important clues regarding nucleosynthesis relevant to stars and the Big Bang. It has long been known that the β-decay rates for heavy ionized nuclides in stellar conditions differ significantly from those of neutrals seen on Earth, due to the partial occupations of the atomic electron orbitals of the ions, which can modify the available final states of the decay products such as the emitted electrons, and that the nature of this decay is affected by considerations such as the plasma density and temperature (Bahcall, 1962). These decay rates are also expected to potentially be influenced by the ionization states of

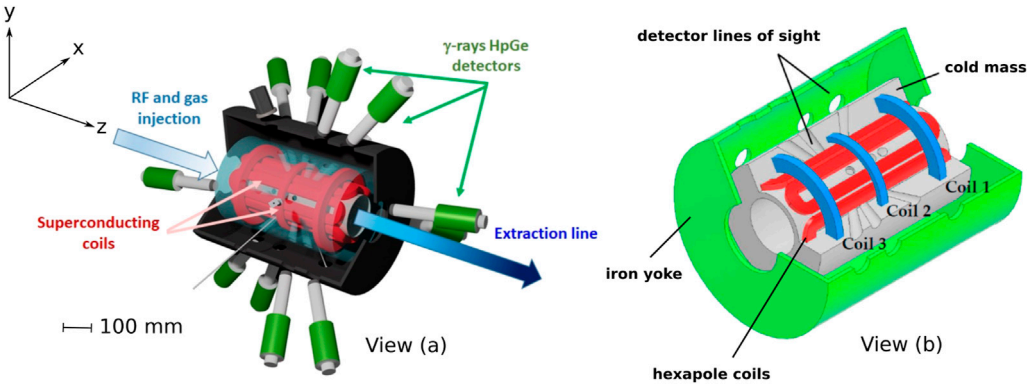

FIGURE 1
Schematics of the PANDORA chamber, in which an electron cyclotron resonance plasma will be created. View **(A)** shows a sectional view of the full experiment. View **(B)** shows details of the magnetic field configuration and its integration into the cold mass. Views **(A,B)** show the external iron yoke enclosing the plasma chamber, hexapoles (in red) and solenoids (in blue), and the cold mass in which the magnets are to be embedded. The lines of sight for γ-ray detectors and other diagnostics are also shown. Images have been adapted from (Mascali et al., 2022). A coordinate system has been defined in which z is coincident with the chamber axis and x and y are directions orthogonal to z.

nuclides; however, only limited experimental evidence for this is currently available, provided by experiments on storage rings, for example, in Ref. (Bosch et al., 1996).

To answer the myriad questions surrounding the role of the ionization states on nuclear decay processes in stellar conditions, an ambitious new experiment has been proposed, known as PANDORA (*Plasmas for Astrophysics Nuclear Decays Observation and Radiation for Archaeometry*) (Mascali et al., 2017; Mascali et al., 2020; Mascali et al., 2022). This project, initiated by the Italian National Institute of Nuclear Physics (INFN), aims to design and build a compact plasma trap enabling the study of stellar β-decay processes of isotopes. In addition to the development of a suitable trap reproducing the stellar-like electron densities and temperatures for the first time, this project will implement a range of diagnostic tools allowing plasma characterization and the monitoring of radionuclides. In this manuscript, we describe the proposed implementation of incoherent Thomson scattering (ITS) for the measurement of electron properties on PANDORA. Section 2 summarizes features of the PANDORA design. Thomson scattering principles and the main features of the diagnostic to be used in the future experiments are summarized in Section 3. Section 4 is devoted to the specificities of the PANDORA diagnostic implementation and the measurement ranges achievable. Conclusions are given in Section 5.

2 Features of the PANDORA chamber

The PANDORA project will produce an electron cyclotron resonance plasma using a radiofrequency source. Plasma containment will be ensured by a magnetic field configuration consisting of superconducting hexapoles and solenoids, generating radial and axial magnetic fields, respectively. This configuration produces a minimum of the magnetic field of magnitude 0.4 T at the center of the chamber, with a maximum magnetic field ranging between 1.7–3 T at both ends of the chamber. The plasma chamber has an inner radius of 140 mm and length of 700 mm. Simplified schematics of the chamber are depicted in Figure 1, adapted from (Mascali et al., 2022), showing 1) the external iron yoke enclosing the plasma chamber, 2) hexapoles (in red) and solenoids (in blue), and 3) the cold mass in which the magnets are to be embedded. The lines of sight for γ-ray detectors and other diagnostics are positioned around the chamber. Radiofrequency waves are introduced into one end of the chamber using waveguides. The working gas is injected from the same end to generate an initial buffer plasma, followed by the injection of a particular isotope. Full details of the planned setup, instruments and experiments envisaged are available in (Mascali et al., 2022).

The PANDORA experiment will generate a non-equilibrium, anisotropic plasma in which the electron densities n_e are expected to range from 10^{11} to 10^{13} cm^{-3} and electron temperatures T_e to range from 0.1 to 30 keV.

3 Incoherent Thomson scattering and the THETIS diagnostic

3.1 Thomson scattering principles

Thomson scattering describes the scattering of electromagnetic radiation by free charged particles (Froula

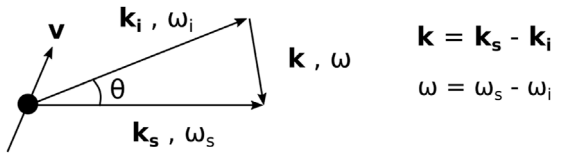

FIGURE 2
Definition of the observation wave vector **k**, as the vector sum of the incident ($\mathbf{k_i}$) and scattering ($\mathbf{k_s}$) wave vectors. Observation, scattering and incident frequencies are denoted by ω, ω_s and ω_i, respectively. The black dot depicts an arbitrary electron from which scattering occurs, moving at a velocity **v**.

et al., 2011). Information on the charged species dynamics and properties in plasmas is obtained via the analysis of the scattered field and differs according to two regimes. These regimes are identified according to a scattering parameter α, defined as

$$\alpha = 1/k\lambda_{De} \tag{1}$$

in which k is the observation wave number and λ_{De} the electron Debye length. The observation wave vector **k** is defined according to the vector sum of the incident and scattering wave vectors, $\mathbf{k_i}$ and $\mathbf{k_s}$ respectively, and a scattering angle θ, as illustrated in Figure 2, which depicts scattering from a charge moving at a velocity **v**. The observation, scattering and incident frequencies are denoted by ω, ω_s and ω_i, respectively. The observation wave vector modulus is written

$$|k| = \left(k_i^2 + k_s^2 - 2k_i k_s \cos\theta\right)^{1/2} \tag{2}$$

or more simply, $|k| \simeq 2|k_i| \sin(\theta/2)$, for non-relativistic charges where $|k_i| \simeq |k_s|$.

The angular frequency ω at a given measurement position reflects two Doppler shifts due to the particle motion: one due to particle motion towards the observation point ($\mathbf{k_s} \cdot \mathbf{v}$), and the other due to particle motion towards the incident wave ($\mathbf{k_i} \cdot \mathbf{v}$), i.e.,

$$\omega = (\mathbf{k_s} - \mathbf{k_i}) \cdot \mathbf{v} \tag{3}$$

As the scattered power per unit solid angle scales as the inverse of the square of the particle mass, the scattering from the free charges is dominated by the electrons, not the ions. For a small scattering parameter ($\alpha \ll 1$), the scattering is incoherent. The scattered field reflects thermal fluctuations of electrons, perceived at length scales shorter than the electron Debye length, and as such, the contributions of the individual electric fields are summed incoherently. The scattered spectrum in the incoherent regime can therefore be directly related to the electron properties in the plasma under investigation: the electron temperature or, more generally, the electron energy distribution function (EEDF), the electron density, and the macroscopic local electron drift velocity.

The electric field $\mathbf{E_s}$ scattered from one electron is expressed as (Hutchinson, 2002)

$$\mathbf{E}_s(\mathrm{x}, t) = \frac{r_e}{R}\, \mathbf{\Pi} \cdot \mathbf{E}_i \tag{4}$$

written in terms of the incident electric field $\mathbf{E_i}$, the electron radius r_e (2.82×10^{-15} m), and the far-field separation distance between the particle and the observation point R. $\mathbf{\Pi}$ is a tensor polarization operator. To express the scattered field in terms of the frequency spectrum $\mathbf{E_s}$ (ν_s), we calculate the Fourier transform of $\mathbf{E_s}$ ($\mathbf{x}$, t) and take the incident $\mathbf{E_i}$ to be a monochromatic wave (i.e., supplied by a coherent laser source). The scattered frequency ν_s is given by $\omega_s/2\pi$. We obtain an expression for the scattered field from the electron which is written

$$\mathbf{E}_s(\nu_s) = \frac{r_e e^{i\mathbf{k_s}\cdot\mathbf{x}}}{x} 2\pi\kappa\, \mathbf{\Pi} \cdot \mathbf{E_i}\, \delta(\mathbf{k} \cdot \mathbf{v} - \omega) \tag{5}$$

In this expression, the particle is moving at a velocity **v** and is located at a position **x** with respect to an origin. The term κ (Hutchinson, 2002) is given by $\frac{d(\mathbf{k}\cdot\mathbf{v}-\omega)}{d\omega_s}$. The power spectrum deduced from a consideration of this scattered field, summed over all the electrons for a solid angle $d\Omega_s$, will be found in the form

$$\frac{d^2P}{d\Omega_s d\nu_s} \propto f_k\left(\frac{\omega}{k}\right)\frac{1}{k} \tag{6}$$

The scattered power spectrum is directly proportional to the electron velocity distribution function f_k (EVDF) measured along **k**. In the case of a Maxwellian distribution, the distribution function f_k is written

$$f_k = n_e \sqrt{\frac{m_e}{2\pi T_e}}\, \exp\left[-\frac{m_e v_k^2}{2T_e}\right] \tag{7}$$

where m_e represents the electron mass and v_k the electron velocity in the direction of the observation wave vector.

The Gaussian spectrum width σ can then be used to directly deduce an electron temperature, using the expression

$$\sigma = 2\lambda_i \sin\left(\frac{\theta}{2}\right)\left(\frac{2kT_e}{m_e c^2}\right) \tag{8}$$

The electron density is proportional to the integral of the measured spectrum over the signal frequency, i.e., the greater the number of scatterers, the larger the amplitude of the scattered field. The absolute determination of this density is made using an appropriate calibration of spectra, typically from a Raman or Rayleigh spectrum. This calibration requires the measurement of the scattered signal amplitude with the same diagnostic configuration as for the intended Thomson scattering measurement (identical laser beam trajectory and dimensions, and identical configuration of the optics and acquisition system), with the chamber filled to a known gas pressure (density) in the absence of a plasma.

The ratio between the Raman or Rayleigh scattered power P_R and Thomson scattered power P_T can then be written

$$\frac{P_T}{P_R} = \frac{n_e \frac{d\sigma_T}{d\Omega}}{n_g \frac{d\sigma_R}{d\Omega}} \tag{9}$$

where $d\sigma_T/d\Omega$ and $d\sigma_R/d\Omega$ are the differential Thomson scattering cross-section and differential Raman or Rayleigh scattering cross-section, according to the method used. The ratio of scattered powers is equivalent to the ratio of the areas under the recorded spectra. Consequently, n_e can be found.

A large scattering parameter ($\alpha \gg 1$) concerns the regime in which the observation length scale exceeds the electron Debye length. At such scales, the correlated behavior of particles can be perceived, and the resulting scattered spectra can reflect both electron and ion collective behavior. This collective behavior can provide information on features such as plasma waves. In this work, the implementation is restricted to the incoherent Thomson scattering regime. This implementation will involve the diagnostic known as THETIS (*THomson scattering Experiments for low-Temperature Ion Sources*). This diagnostic (Vincent et al., 2018) was conceived as a high-sensitivity new tool for investigations of electron properties in low-density plasmas (n_e as low as 10^{10} cm^{-3}). In the magnetized plasmas of devices such as Hall plasma thrusters, electron cyclotron resonance sources, and planar magnetrons used for thin film generation, there is a lack of suitable measurement capabilities for electron properties, which hinders device modeling and development. Overcoming this limitation was the motivation for the development of a new non-invasive, high-performance ITS diagnostic.

With regards to electron cyclotron resonance sources, a number of notable early applications of incoherent Thomson scattering to the investigations of these discharges were carried out in the 1990s (Sakoda et al., 1991; Bowden et al., 1993; Muraoka and Kono, 2011). The investigations on PANDORA will differ significantly from such prior studies. In addition to the different plasma parameters expected (PANDORA will feature higher densities and higher temperatures), the improved diagnostic capabilities now achievable provide new measurement opportunities.

The development of the THETIS diagnostic was initiated in 2015 in the framework of a new collaboration established by researchers at three French laboratories: S. Tsikata, ICARE, Orléans, CNRS; T. Minea, LPGP, Orsay, CNRS and O. Tuske, J. Fils, J. Schwindling, IRFU, Saclay, CEA. The compact diagnostic was successfully developed and applied to plasma source investigations at all three laboratories, confirming its value for electron property measurement in both pulsed and steady-state plasmas and the capacity for measurement in very low-density plasma environments (Tsikata et al., 2019; Vincent et al., 2020a; Vincent et al., 2020b).

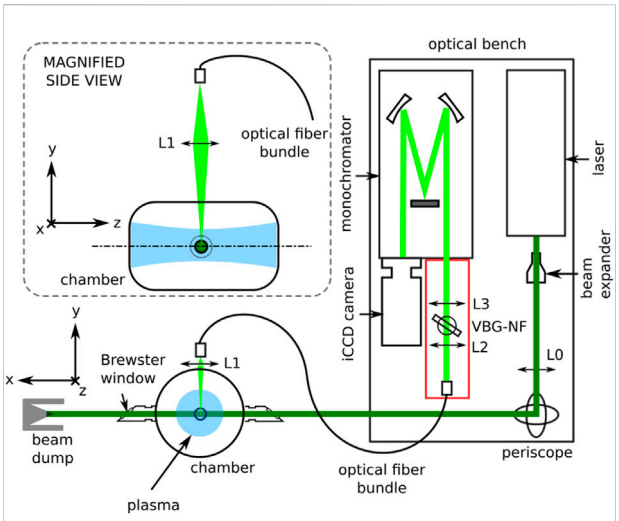

FIGURE 3
Main components of the THETIS optical bench, with an illustration of an example implementation on a vacuum vessel (views not to scale). This depiction shows the laser light (dark green) sent across a plasma (blue), with recovery and transmission of the scattered light (light green) for detection.

3.2 The THETIS diagnostic: key features

A number of key features of the THETIS diagnostic are summarized in this section, with more extended discussions available in other articles, such as in Ref. (Vincent et al., 2018). A schematic of the diagnostic (optical bench and example implementation) is shown in Figure 3. The compactness of the optical bench (dimensions 0.75 × 1.5 m) was a key objective of the original design to facilitate investigations of multiple plasma sources at different laboratories.

The main components of the diagnostic are: the radiation source, the optics for light guiding and focusing, the stray light filtering, the radiation dispersion and the light detection.

3.2.1 Radiation source

The incident radiation for scattering is provided by a pulsed, 532 nm-wavelength Nd:YAG laser with a nominal energy of 430 mJ per pulse and a 10 Hz repetition rate. The initial beam from this laser, 9 mm in diameter, is transmitted through a beam expander to increase the beam diameter by a factor of 3, in order to reduce the focused beam divergence in the plasma by the same factor.

3.2.2 Optics for light guiding and focusing

High-reflectivity mirrors (reflectance > 99%) are used for the direction of light towards the plasma. Fused silica lenses focus the collimated laser beam in the plasma (*L0*), collect photons from the plasma (*L1*), and collimate the collected radiation for filtering of stray light (*L2*), for final focusing onto the entry slit of a monochromator/spectrometer (*L3*) of 750 mm focal length. An optical fiber bundle

consisting of an array of 45 fused silica fibers of 300 μm diameter is used to collect scattered photons, with one end facing the lens $L1$ and the other coupled to the slit of the spectrometer.

3.2.3 Stray light filtering

The THETIS diagnostic uses the recently-commercialized volume Bragg grating (Glebov et al., 2012) as a method of filtering stray radiation at 532 nm. The use of this element, in combination with a single monochromator, as opposed to the standard and widely-used triple grating spectrometer assemblies, e.g., in (Muraoka and Kono, 2011; Carbone and Nijdam, 2014), allows for improved photon transmission and detection, and hence, greater diagnostic sensitivity than is normally achievable. This technique of stray light filtering was first applied to Raman scattering measurements by Klarenaar in 2015 (Klarenaar et al., 2015) and implemented by us for incoherent Thomson scattering measurements (Vincent et al., 2018). This method is now being adopted by several other research groups.

3.2.4 Radiation dispersion

The collected light is dispersed in wavelength using a spectrometer currently equipped with three gratings (2,400 lines/mm, 600 lines/mm and 300 lines/mm), all of which correspond to different degrees of spectral dispersion and hence, different ranges of accessible electron temperatures. This point will be revisited later in this paper.

3.2.5 Light detection

An intensified charge coupled device (iCCD) camera is used to record light transmitted from the monochromator. The CCD dimensions are 1,024 × 1,024 imaging pixels (13.3 × 13.3 mm). The CCD, when cooled to -25 °C, registers a dark current of 2 e-/p/sec. The intensifier is a Gen III filmless type with a quantum efficiency of 50% at 500 nm. The equivalent background illumination of the intensifier is 0.002 e-/p/sec. Conventional photomultiplier tubes (Polyakov, 2013) have also been widely used for detection in incoherent Thomson scattering systems but have lower quantum efficiencies in the visible spectrum (10–30%).

As illustrated in Figure 3, the laser beam (entering with horizontal polarization) is directed across the vacuum chamber depicted in this figure, along x. The laser beam passes across fused silica windows mounted at Brewster angles, allowing transmission of the polarized light. In past implementations, these windows have been mounted at the ends of long tubes connected to the vacuum vessel, ensuring that any reflections from the windows are located far from the plasma volume of interest. Apertures to limit stray light propagation (not shown) have also been implemented along the path of the laser beam. The side view inset image illustrates the light collection at the top of the vacuum chamber (at 90° with respect to the laser line), using lens $L1$ positioned above a fused silica window for focusing onto the end of the optical fiber bundle, which subsequently transmits photons to the optical bench for filtering, dispersion and detection.

TABLE 1 Diagnostics for electron temperature measurement on PANDORA.

Type	Measurement range
Silicon drift detector (SDD)	1–30 keV
HPGe gamma ray detector	30–2000 keV
Visible light camera	1–12 eV

4 Implementation of incoherent Thomson scattering on PANDORA

The implementation of the THETIS incoherent Thomson scattering diagnostic on PANDORA aims to provide access to local electron properties in a temperature and density range not readily accessible via other electron diagnostics to be implemented, while preserving a high spatial resolution and sensitivity. The electron populations generated in such a trap are expected to be comprised of three different electron groups, broadly classed as hot ($kT_e \sim 100$ keV), warm ($kT_e \sim 100$ eV - tens of keV) and cold ($kT_e \sim 1$–100 eV). Table 1, adapted from Ref. (Mascali et al., 2022), summarizes the electron temperature diagnostics to be implemented and their measurement ranges. As will be shown shortly, the features of the planned incoherent Thomson scattering implementation provide complementary information for the warm and cold electron temperature range in particular. In addition to these listed diagnostics, the electron density will be measured using line-integrated diagnostics tools: a W-band super-heterodyne polarimeter and microwave imaging.

4.1 Experimental configuration

Figure 4 illustrates a schematic of the proposed implementation of incoherent Thomson scattering on PANDORA. A number of its key features will be highlighted.

4.1.1 Configuration for light transmission

The incident laser will be transmitted along the axis of the chamber as shown in Figure 4 with horizontal polarization through fused silica windows. The entry window will be mounted such as to accommodate the presence of other components and connectors along the axis. Due to the presence of the exiting laser beam, it will be necessary to replace a combined mass spectrometer and Faraday cup intended for mounting at the end of the chamber with a simple fused silica window. Both input and exit windows will be mounted at Brewster angles. The available diameter for both windows will accommodate the laser beam, which will have a diameter of 27 mm on entering and will be focused using a 2000 mm-focal length lens to a waist in the plasma of 0.3 mm. This focused diameter

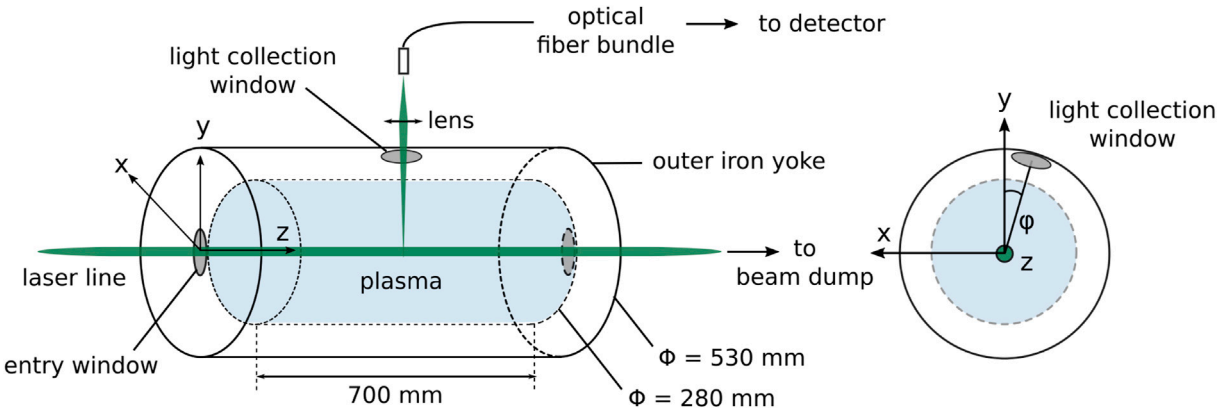

FIGURE 4
Planned laser beam access and scattered light recovery on PANDORA (not to scale), showing the longitudinal vessel view (at left) and section view (at right).

has been judged to be sufficient for the purposes of the experiments, but can be modified as required.

4.1.2 Configuration for light recovery

The iron yoke depicted in Figure 4 has been designed with ports of diameter 88 mm providing 14 lines of sight converging on the center of the plasma, for the mounting of the γ-ray HPGe detectors. At present, the most likely scenario is that one of these ports will be reserved for the ITS photon collection (Figure 1). In the current design, the port to be used for light collection has an angle of inclination from y which is 22°. Based on the iron yoke radius and the size of the ports, the maximum solid angle $\Delta\Omega$, for the collection lens positioned at the light collection window located on the iron yoke, is at maximum 9.5°. In reality, this angle will be slightly reduced according to the restrictions on the placement of the lens (for example, due to the presence of connectors and instruments positioned on the iron yoke).

Based on the chamber dimensions, imaging characteristics for the collection optics can be selected. An aspheric lens of diameter 100 mm and focal length of 400 mm positioned at the light collection window will give an image distance to the optical fiber of 691 mm, which would be a suitable configuration. The volumetric resolution can be varied according to the number of fibers from which photons are collected (a volumetric resolution of 1 mm^3, providing high spatial resolution and sufficient photon collection, has been achieved in past implementations).

4.1.3 Choice of optics material

The chamber windows, collection lens and optical fiber cores will be made of fused (amorphous) silica, due to the high transmission of visible radiation it offers. The nature of this experiment means that degradation of the transmission properties due to bombardment by γ-rays must be considered. Some evidence from past studies, such as in Ref. (Nagasawa et al., 1984; Colby et al., 2002), suggests that some modification of silica is to be expected, due to the creation of absorption bands in the visible spectrum, and is highly dependent on the radiation dose received. This feature will be examined in detail in the coming months, however, the spectral ranges of the measurement are not expected to be affected. It should be noted that the optical bench will not itself be located in close proximity to the plasma chamber.

4.1.4 Stray light mitigation

The Bragg volume grating used for filtering of stray light at 532 nm (created by reflections off surfaces) offers a maximum theoretical attenuation factor of 10^4, within a narrow suppression band of width 0.3 nm. The narrowness of this band preserves much of the Thomson spectrum and thus ensures that measurements are possible even for cases where the electron temperature is below 1 eV. In the PANDORA implementation, stray light is likely to be encountered from surfaces within the plasma chamber, and the windows (entry, exit and collection). The level of stray light is difficult to predict before the setup of the experiment, however, to ensure stray light mitigation, the option of using a second volume Bragg grating in series with the first will be provided. This can easily be integrated into the proposed implementation as needed.

4.2 Accessible measurement range and measurement protocol

4.2.1 Scattering parameter

On PANDORA, the scattering parameter α can be determined from the expected plasma parameters. The electron Debye length on PANDORA is determined as

$$\lambda_D = \sqrt{\frac{\epsilon_0 k_B T_e}{n_e q_e^2}} \tag{10}$$

where ϵ_0 is the permittivity of free space, k_B is the Boltzmann constant, and q_e the elementary charge. On PANDORA, based on the expected range of electron temperatures (T_e: 0.1–30 keV) and electron densities (n_e: 10^{11}–10^{13} cm^{-3}), an upper and lower bound for the Debye length can be calculated. This is found to be:

$$2 \times 10^{-5} \leq \lambda_D \leq 4 \times 10^{-3} \quad \text{(m)} \tag{11}$$

The observation wavenumber k is calculated from the laser wavenumber k_i (the inverse of the laser wavelength) and the observation angle θ, using the relation $k \approx 2k_i \sin(\theta/2)$ given earlier. The angle θ corresponds to 78° in the configuration used for PANDORA, according to the observation port likely to be available. The calculated observation wavenumber k is 2×10^6 m^{-1}.

The value $\alpha = 1/(k\lambda_D)$ is therefore in the range

$$1 \times 10^{-4} \leq \alpha \leq 3 \times 10^{-2} \tag{12}$$

i.e., $\alpha \ll 1$, hence for all conditions of the Thomson scattering implementation, observations will correspond to the incoherent regime.

4.2.2 Electron temperature range

The spectral dispersion will be achieved with a Princeton Instruments Acton Standard Series SP-2756 imaging spectrograph, with detection provided by a Princeton Instruments PI-MAX 4: 1024f iCCD camera. The use of different gratings during the recording of the scattered spectra results in different ranges of wavelength (or frequency) which can be perceived. Table 2 summarizes a list of gratings of the spectrometer (2400, 600 and 300 lines/mm currently used, 150 lines/mm an option to be provided for PANDORA investigations) and the corresponding resolutions and electron energies accessible by the combined spectrometer and camera system.

The equivalence between the electron velocity v and the wavelength shift $\Delta\lambda$ which can be perceived can be expressed as

$$v = \frac{c\Delta\lambda}{2\lambda_i \sin(\theta/2)} \tag{13}$$

And the corresponding wavelength coverage expressed as electron energy is determined as $\frac{1}{2}mv^2$, shown in eV in Table 2.

As Table 2 shows, decreasing the number of lines/mm of the grating used decreases the electron temperature resolution but increases the wavelength coverage. We may identify the spectrum width (Gaussian standard deviation) as $\Delta\lambda_e$, depicted in Figure 5. Figure 5 illustrates Thomson spectra (green profiles) acquired with the laser wavelength λ_i 1) centered in the spectral range, and 2) shifted. The vertical axis represents the number of photon counts recorded by the camera, an amplitude dependent on the wavelength, written as $I(\lambda)$, and $\Delta\lambda_T$ the full accessible wavelength range. The gray bar depicts the regions where spectral information is blocked due to the presence of the volume Bragg grating notch filter. As depicted in Figure 5, the recording of the Thomson spectra allows for the centering of the laser wavelength within the spectral range, or the shifting of the position of this central wavelength in order to access larger electron temperatures. Using option 2) would result, at maximum, in a doubling of the achievable λ coverage shown in Table 2.

4.2.3 Electron energy distribution function

The normalized electron energy distribution function $f(E)$ is obtained from the scattering spectrum using the expression (Vincent et al., 2018):

$$f(E) = -\frac{\frac{dI}{d\lambda}\,\mathrm{sgn}(\Delta\lambda)}{\Sigma\left(\frac{dI}{d\lambda}\delta E\right)} \tag{14}$$

where $\Delta\lambda$ is a given wavelength shift with respect to the central laser frequency, $\frac{dI}{d\lambda}$ the derivative of the scattered light intensity (counts) with respect to wavelength, *sgn* the mathematical sign function, and δE is the energy step corresponding to a single pixel.

The calculation of the electron energy distribution function requires a sufficiently large signal to noise ratio, as any artifacts or noise present in the spectrum result in distortions of the calculated EEDF due to the application of the derivative. A Savitzky-Golay (Savitzky and Golay, 1964) smoothing procedure can be applied to the acquired spectra to render the subsequent EEDF calculation less noisy. The wings of the spectra, where the signal to noise ratio is low, can be particularly challenging to resolve, whereas the central portion of the spectrum (representing the bulk electron energies) can be more readily be used in the calculation of the EEDF.

4.2.4 Measurement procedure

The implementation of future Thomson scattering measurements will be performed according to the following procedures: Table 3.

1) **Optical bench setup**: the diagnostic will be installed on PANDORA according to the provisional implementation described in this paper. The installation will accommodate the constraints of the final plasma vessel configuration (accessible ports, presence of other instruments, and so on).
2) **Measurement types**: For a given experimental condition, a number of spectrum types must be recorded in order to obtain the final Thomson scattered spectrum (Table 3). These spectra contain several contributions: 1) the Thomson scattered signal, 2) stray light (centered at the laser wavelength), 3) natural plasma emission, 4) noise inherent to the camera photodetector, and, depending on the configuration, 5) fluorescence from solid interfaces. The combination of these spectrum types allows for the calculation of the final Thomson spectrum. This is obtained using the following form if fluorescence is present:

TABLE 2 Accessible electron energies and detection resolution based on choice of spectrometer grating.

Grating (lines/mm)	λ coverage (nm)	Resolution (eV)	λ coverage (eV)
2400	5.08	0.009	4.67
600	28.4	0.298	146
300	58.0	1.24	608
150	117	5.02	2470

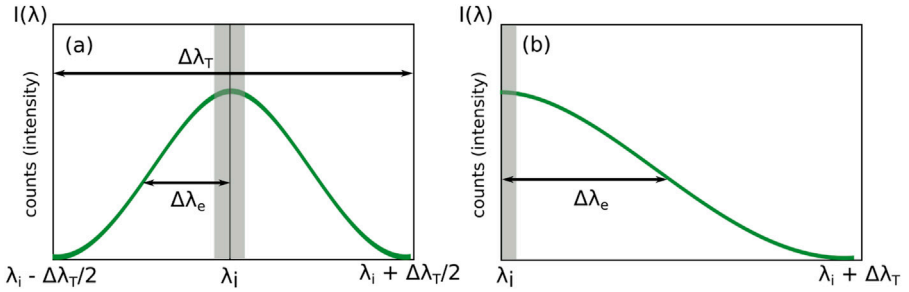

FIGURE 5
Illustration of Thomson spectra (green lines) acquired with **(A)** the laser wavelength λ_i centered in the spectral range or **(B)** shifted, to access a larger spectra range. The gray bar depicts the regions where spectral information is blocked due to the presence of the volume Bragg grating notch filter. The vertical axis represents the number of photon counts recorded by the camera, an amplitude dependent on the wavelength, written as $I(\lambda)$. The full spectral range accessible is $\Delta\lambda_T$ and the Gaussian standard deviation is shown as $\Delta\lambda_e$.

TABLE 3 Conditions used for signal acquisitions.

Spectrum type	Acquisition conditions
A (full signal)	plasma present, laser on
B (background)	plasma present, laser off
C (fluorescence)	plasma absent, laser on
D (camera noise)	plasma absent, laser off
Raman	fixed pressure N_2, laser on

$$\text{Thomson} = A - B - C + D \tag{15}$$

In the absence of fluorescence, the final Thomson spectrum is obtained from

$$\text{Thomson} = A - B \tag{16}$$

A Raman scattering spectrum is recorded for the purposes of calibration, with the chamber filled to a known pressure of a gas such as nitrogen, without the plasma present. It is worth mentioning that spectrum acquisitions have been carried out using this diagnostic in a photon accumulation mode, whereby the recorded scattered photons over multiple laser shots (6000) have been summed on the detector in order to constitute a single spectrum. Given the laser repetition rate of 10 Hz, this corresponds to individual spectrum records of 10-min duration. It will be necessary to measure spectra on a fully stabilized or reproducible pulsed plasma on PANDORA in order to accommodate this measurement duration.

3) **Measurement conditions**: an experimental protocol for the investigation of β-decay has been outlined in Ref. (Mascali et al., 2022), in which a buffer plasma is generated, then injected with different isotopes which are ionized to produce a dense plasma. The role of the incoherent Thomson scattering experiment will be to probe electron properties at the core of the plasma generated, under conditions which will include: 1) varying injected radiofrequency power, 2) varying magnetic field configurations, 3) varying isotope types, among others. As shown earlier in this section, the electron temperatures measurable will range from the 1 eV–10^3 eV range (Table 2), providing information which complements the range accessible to the other electron diagnostics (Table 1).

5 Conclusion

In this manuscript, a concise analysis of the potential application of a recently-developed incoherent Thomson scattering diagnostic known as THETIS has been made for the PANDORA experiment. This diagnostic is notable for its high sensitivity (giving access to information on plasma environments where densities are as low as

10^{10} cm^{-3}) and its application to PANDORA would provide an important addition to the array of electron diagnostics techniques needed for the characterization of the plasmas produced in PANDORA. It is expected that electron temperatures in the range of 1 eV–10^3 eV (cold and warm electrons) may be measured by this diagnostic in the future implementation. The non-invasive nature of the diagnostic and its ability to reflect direct information on electron properties will be particularly valuable.

Data availability statement

The original contributions presented in the study are included in the article. Further inquiries can be directed to the corresponding authors.

Author contributions

ST undertook the writing of the article and implementation proposal, with contributions on the PANDORA configuration provided by LM and J-ED.

Acknowledgments

ST thanks the LPGP (T. Minea), CEA Saclay and CNES for support of the THETIS diagnostic development.

Conflict of interest

The authors declare that the research was conducted in the absence of any commercial or financial relationships that could be construed as a potential conflict of interest.

Publisher's note

All claims expressed in this article are solely those of the authors and do not necessarily represent those of their affiliated organizations, or those of the publisher, the editors and the reviewers. Any product that may be evaluated in this article, or claim that may be made by its manufacturer, is not guaranteed or endorsed by the publisher.

References

Bahcall, J. N. (1962). Beta decay in stellar interiors. *Phys. Rev.* 126, 1143–1149. doi:10.1103/physrev.126.1143

Bosch, F., Faestermann, T., Friese, J., Heine, F., Kienle, P., Wefers, E., et al. (1996). Observation of bound-state β- decay of fully ionized ^{187} Re: ^{187} Re - ^{187} Os cosmochronometry. *Phys. Rev. Lett.* 77, 5190–5193. doi:10.1103/physrevlett.77.5190

Bowden, M. D., Okamoto, T., Kimura, F., Muta, H., Uchino, K., Muraoka, K., et al. (1993). Thomson scattering measurements of electron temperature and density in an electron cyclotron resonance plasma. *J. Appl. Phys.* 73, 2732–2738. doi:10.1063/1.353046

Carbone, E., and Nijdam, S. (2014). Thomson scattering on non-equilibrium low density plasmas: Principles, practice and challenges. *Plasma Phys. control. Fusion* 57, 014026. doi:10.1088/0741-3335/57/1/014026

Colby, E., Lum, G., Plettner, T., and Spencer, J. (2002). Gamma radiation studies on optical materials. *IEEE Trans. Nucl. Sci.* 49, 2857–2867. doi:10.1109/tns.2002.806019

Froula, D. H., Glenzer, S. H., Luhmann, N. C. J., and Sheffield, J. (2011). *Plasma scattering of electromagnetic radiation: Theory and measurement techniques*. Elsevier.

Glebov, A. L., Mokhun, O., Rapaport, A., Vergnole, S., Smirnov, V., and Glebov, L. B. (2012). Volume Bragg gratings as ultra-narrow and multiband optical filters. *Proc. SPIE* 8428, 84280C.

Hutchinson, I. H. (2002). *Principles of plasma diagnostics*. 2 edn. Cambridge University Press. doi:10.1017/CBO9780511613630

Klarenaar, B. L. M., Brehmer, F., Welzel, S., Van Der Meiden, H. J., van de Sanden, M. C. M., and Engeln, R. (2015). Note: Rotational Raman scattering on CO2 plasma using a volume Bragg grating as a notch filter. *Rev. Sci. Instrum.* 86, 046106. doi:10.1063/1.4918730

Mascali, D., Busso, M., Mengoni, A., Amaducci, S., Giuseppe, C., Celona, L., et al. (2020). The PANDORA project: An experimental setup for measuring in-plasma β-decays of astrophysical interest. *EPJ Web Conf.* 227, 01013. doi:10.1051/epjconf/202022701013

Mascali, D., Musumarra, A., Leone, F., Romano, F. P., Galata, A., Gammino, S., et al. (2017). PANDORA, a new facility for interdisciplinary in-plasma physics. *Eur. Phys. J. A* 53, 145. doi:10.1140/epja/i2017-12335-1

Mascali, D., Santonocito, D., Amaducci, S., Andò, L., Antonuccio, V., Biri, S., et al. (2022). A novel approach to β-decay: PANDORA, a new experimental setup for future in-plasma measurements. *Universe* 8, 80. doi:10.3390/universe8020080

Muraoka, K., and Kono, A. (2011). Laser Thomson scattering for low-temperature plasmas. *J. Phys. D. Appl. Phys.* 44, 043001. doi:10.1088/0022-3727/44/4/043001

Nagasawa, K., Tanabe, M., and Yahagi, K. (1984). Gamma-ray-induced absorption bands in pure-silica-core fibers. *Jpn. J. Appl. Phys.* 23, 1608–1613. doi:10.1143/jjap.23.1608

Polyakov, S. V. (2013). "Photomultiplier tubes," in *Experimental methods in the physical Sciences* (Elsevier), 69–82.

Sakoda, T., Momii, S., Uchino, K., Muraoka, K., Bowden, M., Maeda, M., et al. (1991). Thomson scattering diagnostics of an ECR processing plasma. *Jpn. J. Appl. Phys.* 30, L1425–L1427. doi:10.1143/jjap.30.l1425

Savitzky, A., and Golay, M. J. E. (1964). Smoothing and differentiation of data by simplified least squares procedures. *Anal. Chem.* 36, 1627–1639. doi:10.1021/ac60214a047

Tsikata, S., Vincent, B., Minea, T., Revel, A., and Ballage, C. (2019). Time-resolved electron properties of a HiPIMS argon discharge via incoherent Thomson scattering. *Plasma Sources Sci. Technol.* 28, 03LT02. doi:10.1088/1361-6595/ab0c67

Vincent, B., Tsikata, S., and Mazouffre, S. (2020). Incoherent Thomson scattering measurements of electron properties in a conventional and magnetically-shielded Hall thruster. *Plasma Sources Sci. Technol.* 29, 035015. doi:10.1088/1361-6595/ab6c42

Vincent, B., Tsikata, S., Mazouffre, S., Minea, T., and Fils, J. (2018). A compact new incoherent Thomson scattering diagnostic for low-temperature plasma studies. *Plasma Sources Sci. Technol.* 27, 055002. doi:10.1088/1361-6595/aabd13

Vincent, B., Tsikata, S., Potrivitu, G.-C., Garrigues, L., Sary, G., and Mazouffre, S. (2020). Electron properties of an emissive cathode: Analysis with incoherent Thomson scattering, fluid simulations and Langmuir probe measurements. *J. Phys. D. Appl. Phys.* 53, 415202. doi:10.1088/1361-6463/ab9974

frontiers | Frontiers in Astronomy and Space Sciences

TYPE Original Research
PUBLISHED 30 August 2022
DOI 10.3389/fspas.2022.949920

OPEN ACCESS

EDITED BY
Siming Liu,
Southwest Jiaotong University, China

REVIEWED BY
Jinlin Xie,
University of Science and Technology of China, China
Guanying Yu,
University of California, Davis, United States

*CORRESPONDENCE
G. Sorbello,
gino.sorbello@unict.it

SPECIALTY SECTION
This article was submitted to Nuclear Physics, a section of the journal Frontiers in Astronomy and Space Sciences

RECEIVED 21 May 2022
ACCEPTED 01 August 2022
PUBLISHED 30 August 2022

CITATION
Torrisi G, Naselli E, Mascali D, Di Donato L and Sorbello G (2022), Mm-wave polarimeter and profilometry design study for retrieving plasma density in the PANDORA experiment. *Front. Astron. Space Sci.* 9:949920. doi: 10.3389/fspas.2022.949920

Mm-wave polarimeter and profilometry design study for retrieving plasma density in the PANDORA experiment

G. Torrisi[1], E. Naselli[1], D. Mascali[1], L. Di Donato[1,2] and G. Sorbello[1,2]*

[1]Istituto Nazionale di Fisica Nucleare—Laboratori Nazionali del Sud, Catania, Italy, [2]Department of Electrical, Electronics, and Computer Engineering, University of Catania, Catania, Italy

In the recent past, the possibility to use a superconducting trap confining a hot and dense plasma as a tool to investigate radioactivity in astrophysical scenarios has been proposed. Making possible these kind of unprecedented measurements is the main aim of the PANDORA (Plasmas for Astrophysics Nuclear Decays Observation and Radiation for Archaeometry) project. In this context, it is planned to build a compact and flexible magnetic plasma trap where plasma reaches an electron density $n_e \sim 10^{11}$–10^{13} cm^{-3}, and an electron temperature, in units of kT, $kT_e \sim 0.1$–30 keV. The setup is conceived to be able to measure, for the first time, nuclear β-decay rates in stellar-like conditions in terms of ionization states. In this paper, the design study of a mm-wave polarimeter for the PANDORA plasma line-integrated electron density measurement is presented. The paper highlights the method of this type of measurements for the first time proposed for a magneto-plasma trap which represents an "intermediate" case between the ultra-compact plasma ion sources and the large-size thermonuclear fusion devices. Preliminary measurements at scaled microwave frequencies have carried out both on a "free-space" setup by using a wire-grid polarizer and a rotable Ka-band OMT + horn antennas system, and on a compact trap (called Flexible Plasma Trap) installed at INFN-LNS and used as PANDORA down-sized testbench are described. The polarimeter technique will support β-decay investigation by simultaneous measurements of the total plasma density, which is crucial to carefully evaluate the decay-constant and to extrapolate the laboratory observed data to the astrophysical scenarios. Moreover, this work proposes to adopt an electromagnetic inverse-scattering-based technique-based method to retrieve the electron density profile along the probing antennas line-of-sight. Numerical results of this so-called "inverse profilometry" are also shown.

KEYWORDS

plasma diagnostics, interferometry, orthomode transducers, polarimeters, mm-wave, profilometry

1 Introduction

Interferometers and Polarimeters are well-assessed tools, developed for plasma diagnostics in thermonuclear fusion machines (Zhang et al., 2012; Tudisco et al., 2013; Creely et al., 2020) to measure both line-averaged density and magnetic field, also in the so called "InterPol" combined setups. In compact electron cyclotron resonance (ECR) ion sources (ECRIS) this is a challenging task due to the extremely tenuous plasma (if compared to densities of thermonuclear fusion reactor plasmas) and to their compact size. Due to the typical density range of ECR plasmas (10^{11}–10^{12} cm^{-3}), in fact, the probing beam wavelength λ_p ~ cm is comparable to the plasma (L_P) and chamber (L_C) size: λ_p ~L_P ~ L_C. Moreover, in ECRIS the measurement is greatly complicated by the mechanical constraints, which limit considerably the ratio L/λ_p. The main problem consists in the multipaths given by probing signal reflections at the chamber walls (acting as reflecting surfaces). Starting from 2014, new tools and analysis techniques have been developed by INFN-LNS ion source group allowing the direct measurement of the absolute plasma density by using an interfero-polarimetric system. In particular:

- the interferometric measurement is based on a "frequency swept method", which moves from the one described in (Scime et al., 2001; Howard et al., 2018), and it has been specifically developed for the special ECRIS-like scenario (Torrisi et al., 2017; Mascali et al., 2022a).
- Also for the polarimetric technique in compact traps, such as ECRIS, a specific original approach has been proposed and implemented to discriminate the polarization plane rotation due to magnetoplasma Faraday rotation only, excluding the spurious effects induced by the cavity resonator thanks to a measurement protocol able to select whether or not polarization was following the Malus law. It was therefore possible to extrapolate the value of the electron density as a free-parameter of a best fit procedure, in good agreement with the value obtained by the interferometer technique. The complete analysis can be found in (Naselli et al., 2018).

While the above-mentioned measurements refer to compact plasma chamber testbench at INFN-LNS (Naselli et al., 2019) and on the ion source of ATOMKI laboratory, in Debrecen (Hungary) (Biri et al., 2018) having typical size of about 30 cm in length and 10 cm in diameter, the case at hand concerns a large plasma trap—referring to the PANDORA project (Mascali et al., 2022b) — which is 70 cm in length and 28 cm in diameter and it can be considered as a "bridge" case between compact traps and large size fusion plasma device also in terms of electron density n_e range (~ 10^{11}–10^{13} cm^{-3}). It should be mentioned that heterodyne interferometer for measuring the plasma electron density in the same range of the PANDORA case—for example in Helicon linear plasma devices - has been developed and characterized in the laboratory (Wiebold and Scharer, 2009; Li et al., 2021).

Anyway, from one hand, at least at the beginning of the PANDORA experimental test, the same method of the ECRIS (which are the only approaches which allowed up to now measuring the plasma density in very compact traps) will be applied as a cross-check and confirmation of the validity of the assumptions and numerical results. On the other hand, the new approach could allow to improve significantly the information, also reducing the measurement time; for the purposes of PANDORA it is in fact very important performing "live" measurement of the total plasma density. Beside supporting R&D in plasma based ion sources, the importance of diagnostics and multi-diagnostic setups is in fact growing for measuring the magneto-plasma properties in experiments devoted to astrophysics and nuclear astrophysics research in compact plasma traps, such as the PANDORA project (Mascali et al., 2022b) aiming to the study of β-decays of nuclear astrophysical interest for the first time in a ECR magnetoplasma (which represents an enviroment able to reproduce some stellar-like properties). This has motivated the development of techniques and devices probing these plasmas in a non-invasive way and operating in different energy ranges (Biri et al., 2018; Naselli et al., 2019; Mascali et al., 2022a). The PANDORA magnetic system, the overall injection system, including the microwave lines for plasma heating and the isotopes injection schemes with a focus on the developments of the oven for solid elements, has been presented in (Mauro et al., 2022).

The design study of a mm-wave polarimeter presented in this paper highlights the method of this type of measurements for the first time proposed for a magneto-plasma trap. In particular the proposed W-Band polarimeter - using intermediate frequency down-conversion (super-heterodyne) that uses a sub-harmonic mixer before the signal detection - finds strong similarities with experiments in the field of radio astronomy devoted to analyzing the Cosmic Microwave Background (CMB) polarization for the detection of the gravitational waves and other cosmological parameters (Cano et al., 2015; Pascual et al., 2021). In general, the main challenges are due to the limited accesses for the probing horn antennas which need to be tilted to illuminate plasma center, a large range of electron density (varying with the microwave power, magnetic field confinement) and eventual multipaths which have been mitigated by a proper sizing of the setup as shown in the following sections. The paper is organized as follows: In Section 2, the dimensioning and choice of the operating probing frequency/wavelength is described. In Section 3, the following two super-heterodyne schemes are presented and compared:

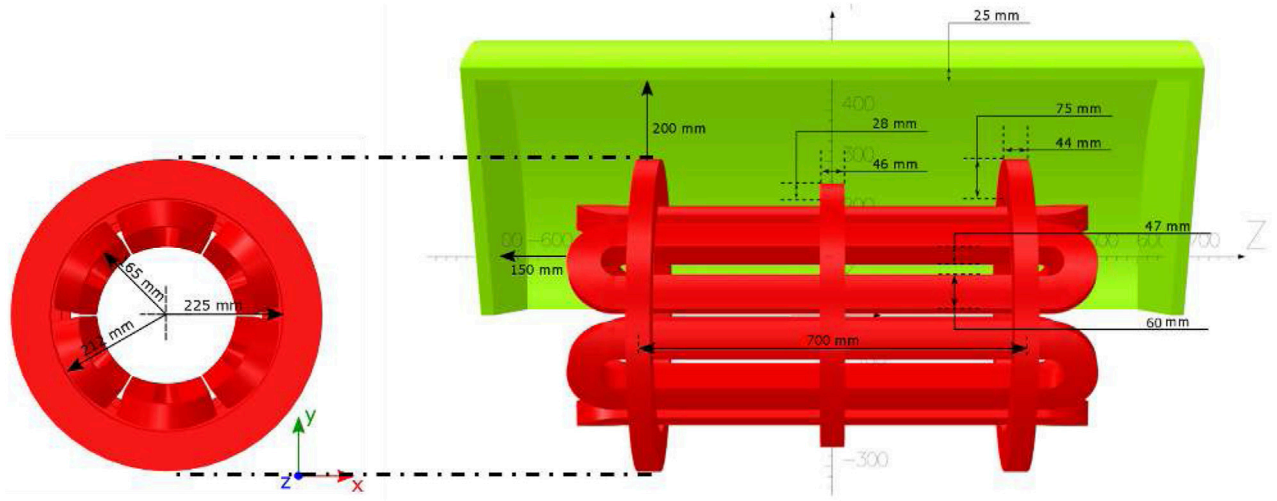

FIGURE 1
View of the magnetic system configuration with its fundamental simulated dimensions. Green element represents the iron yoke (1/3 symmetry).

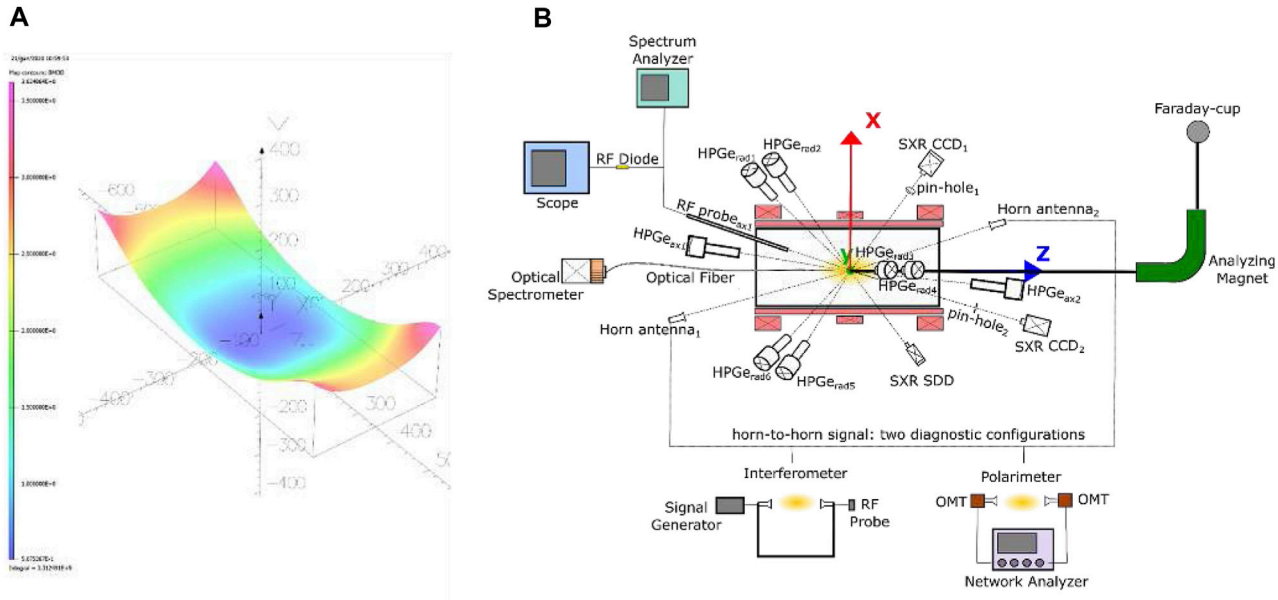

FIGURE 2
(A) 2D (histogram) plot of the magnetic field module $|B|$ inside the plasma chamber, on the xz plane. Values ranges from 1 (violet) to 3.5 (magenta) and are expressed in [T]. **(B)** Pictorial sketch of the integrated set of PANDORA diagnostics, highlighting the detectors for X-ray spectroscopy and imaging, optical emission spectroscopy and polarimetry.

1. *Detection of Lissajous figure*: direct RF signals detection which allow the real-time reconstruction of the State of Polarization (SOP) curve described by the electric field vector. This result can be obtained by using the Lissajous picture from a two channels scope in an x-y representation.
2. *Stokes Parameters detection* based on phase-switches processing.

In Section 4 polarimetric measurements performed in a free-space setup by using a rotating wire-grid polarizer and Ka-band

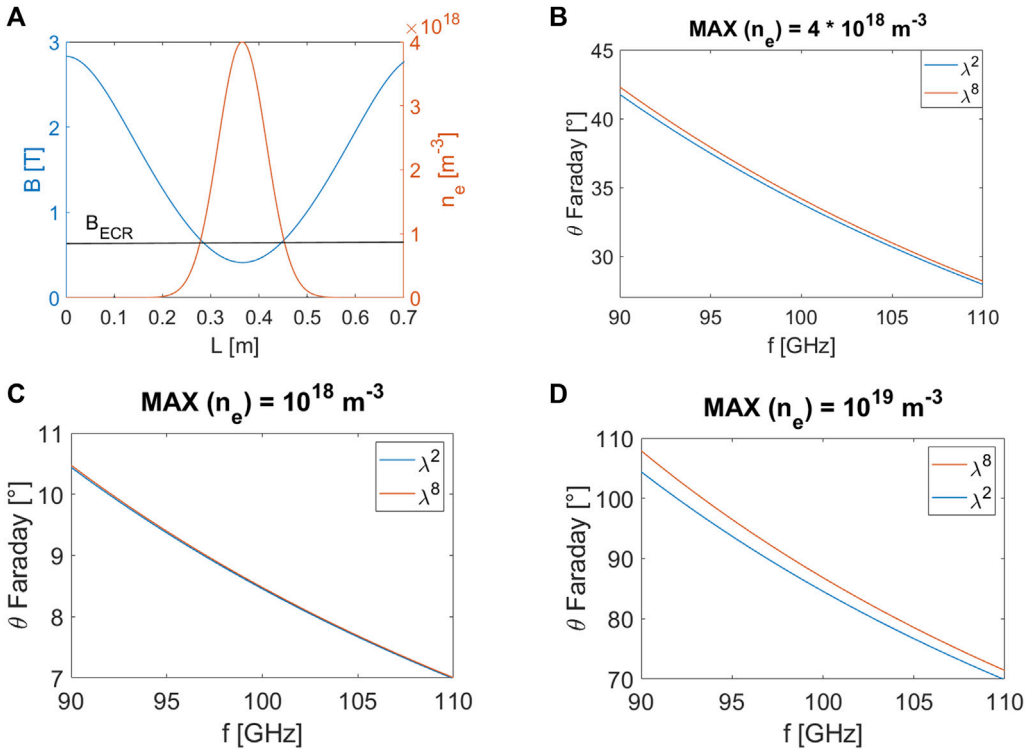

FIGURE 3
(A) Magnetic field (blue) and electron density (red) profiles on the longitudinal z-axis of the PANDORA plasma chamber, considered for the Faraday rotation angle estimation. **(B)** Faraday rotation angle $\theta_{Faraday}$ vs. probing frequency f considering a Gaussian density profile having a maximum value $n_0 = 4 \cdot 10^{18}\ m^{-3}$. **(C)** The same of (B) at a maximum value $n_0 = 10^{18}\ m^{-3}$. **(D)** The same of (B) at a maximum value $n_0 = 10^{19}\ m^{-3}$.

OMT + horn antennas system, and on a compact trap installed at INFN-LNS and used as PANDORA down-sized testbench, are described. In Section 5, the preliminary design of a profilometer is presented. Conclusion are drawn in Section 6.

2 An overview of the plasmas for astrophysics nuclear decays observation and radiation for archaeometry setup

In the frame of the PANDORA (Plasmas for Astrophysics Nuclear Decays Observation and Radiation for Archaeometry) project (Naselli et al., 2022), a new experimental approach aims at measure, for the first time, in-plasma β-decays lifetimes of isotopes of nuclear astrophysical interest as a function of thermodynamical conditions of the environment, namely a laboratory magnetized plasma able to mimic some stellar-like conditions. The experimental approach consists in a direct correlation of the plasma environment and nuclear activity, and this can be done by simultaneously identifying and discriminating - through an innovative multi-diagnostic system which will work synergically with a γ-rays detection system - the photons emitted by the plasma (from microwave to hard X-ray) and γ-rays emitted after the isotope β-decay. A high-performance electron-cyclotron-resonance plasma trap, with a fully superconducting magnetic system where the radionuclides can be maintained in a dynamical equilibrium for weeks, has been purposely designed. Setup and tools typically at the service of particle accelerators physics and applications have been thus redesigned on purpose, by means of innovative upgrade and improvements, for realizing new experimental system for fundamental and multidisciplinary studies of nuclear physics and astrophysical interest. The overall structure of PANDORA project can be structured on three main pillars:

1) Magnetic Trap: A set of superconducting coils able to confine the plasma. The design will allow access to the plasma core for the diagnostics system and γ-ray detectors (Mauro et al., 2022). The PANDORA magnetic confinement system will be fully superconductive and composed by three superconducting coils for axial confinement and by six superconducting hexapole coils for radial confinement, which are coaxial with respect to the axial coils (see

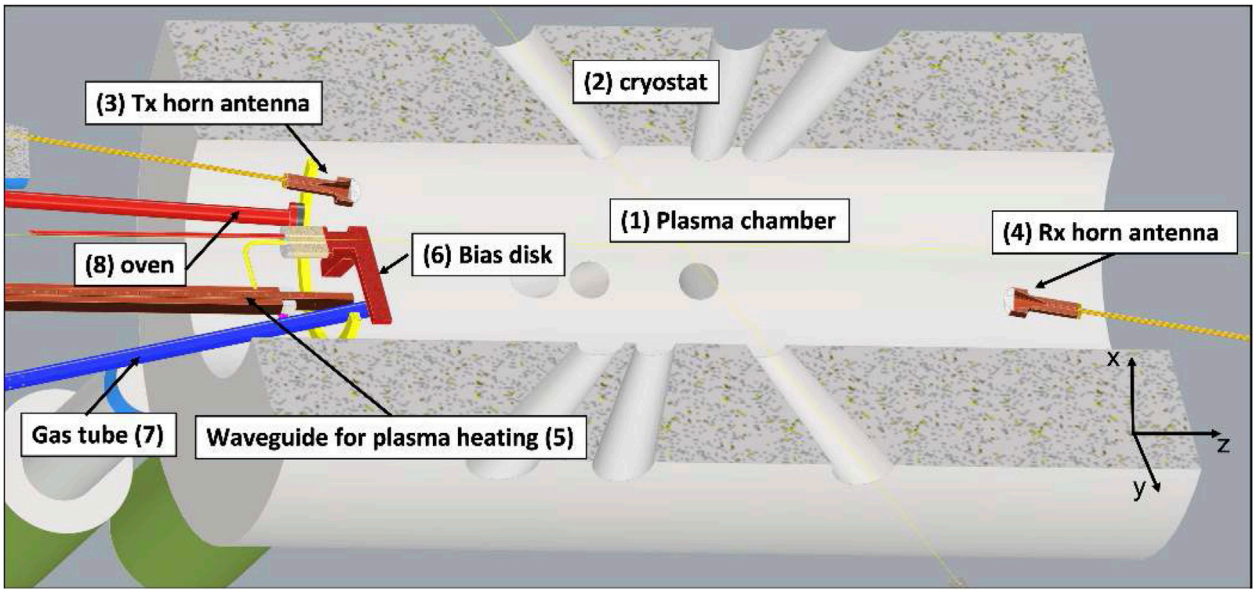

FIGURE 4
Cross-sectional view of the PANDORA plasma chamber (1) which will be installed inside the visible bore of the cryostat (2): the two horn antennas (3) and (4) are placed co-aligned and directed towards the plasmoid center. Plasma is heated through 5 kW microwave coming from rectangular waveguides, one is shown (5). Morever in the view it is shown: the bias disk (6) electrode negatively biased with respect to the source potential for ion beam current increase; the gas injection tube (7) for gaseous element production; the oven (8) for producing ions of metallic elements.

Figure 1). It is the largest magnetic trap ever designed in a B-minimum scheme, supporting a cylindrical plasma chamber of 700 mm length and 150 mm external radius (internal radius of 140 mm). The maximum fields of 2.7 T and 3 T along the chamber axis and 1.5 T along the chamber inner surface will allow stable plasma generation through an RF field at the frequencies of 18 and 21 GHz *via* ECR. Figure 2A shows the magnetic field intensity $|B|$ plot (values given in [T]) on a rectangular surface corresponding to the plasma chamber dimensions (280×700 mm^2) on the xy plane.

2) Array of 14 HPGe detectors for γ-ray spectroscopy: The array will be used to tag the in-plasma nuclear decays *via* the γ-rays emitted from the excited states of the daughter nuclei (Hartfuss and Geist, 2013).

3) Advanced plasma diagnostics system, made of tens of non-invasive diagnostics tools: For the non-intrusive inspection of the plasma environment proprieties and the measurement of plasma parameters to be correlated with the nuclear decays (Naselli et al., 2019).

In more detail, plasma will be characterized in terms of:

- Plasma density and temperature of the cold, warm and hot electron component by using, respectively, a Visible light (VL) camera, Silicon Drift Detector (SDD) and a High-purity Germanium (HPGe) detector;
- Plasma structure, volume, dynamics of losses and confinement by two (axial and radial) advanced X-ray pin-hole cameras for 2D space resolved spectroscopy;
- Line-integrated total electron density measurement by polarimetric system;
- Plasma emitted EM wave in GHz ranges, by means of a two-pins RF probe installed inside the plasma chamber connected to a Spectrum Analyzer (SA), in order to monitor and master plasma stability;
- Moreover, all diagnostics tools can operate simultaneously with the Faraday cup in order to measure the ion charge state distribution (CSD). It has been possible to correlate all the detected plasma parameters with the characteristics of the beam extracted on-line.

A sketch of the integrated set of PANDORA diagnostics and of the γ-ray HPGe array, is shown in fugure 2(B). Among the others diagnostic techniques, the polarimetric system is the only tool able to perform total line-integrated plasma density measurement, and both its dimensioning for the PANDORA scenario and preliminary benchmark measurements will be presented in this paper.

Since the design of the advanced PANDORA plasma trap is ongoing, the benchmark experimental measurements were carried out in a down-sized compact traps used as

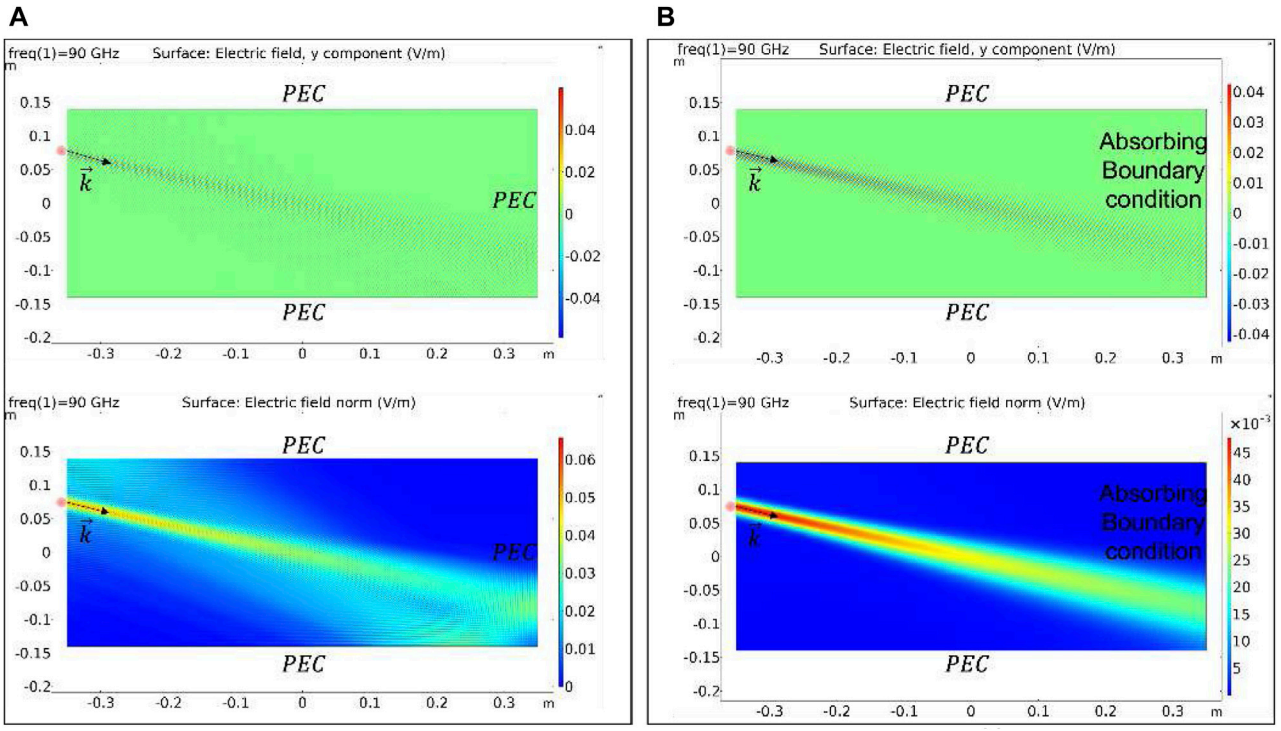

FIGURE 5
Simulated Electric field y component (top) and intensity (bottom) for the all "Perfect Electric Conductor" case **(A)** and in presence of the receiving horn antenna modeled as "Scattering" absorbing boundary **(B)**.

PANDORA test-bench, the compact Flexible Plasma Trap (FPT), installed at INFN LNS.

3 Design study of the polarimetric system

3.1 Polarimetric dimensioning for the plasmas for astrophysics nuclear decays observation and radiation for archaeometry plasma scenario

The proper choice of the probing frequency f (or wavelength λ_p) has important consequences from the accuracy and reliability of the diagnostic setup, therefore it must be selected carefully in order to balance several competing effects and aspects such as the maximum plasma density, profile shape, density gradient, plasma accessibility through vacuum ports. While for interferometry the phase shift decrease linearly with increasing the probing frequency, the Faraday effect decreased with the square of the probing frequency: the probing frequency should not be chosen too high in order to avoid marginalization of the quantities of interest. The probing wavelength λ_p used for plasma probing must fulfill first of all the condition that the corresponding critical density $n_c = 4\pi^2(c^2/\lambda^2)(\epsilon_0 m_e/e^2) = 1.115 \times 10^{15} m^2/\lambda^2$ m^{-3} is higher than the central electron density n_0 needed to avoid cutoff (Heald et al., 1965) which corresponds also to keep $\omega \gg \omega_p$ where ω is the probing (angular) frequency and ω_p is the plasma frequency. As a first preliminary estimation of the operating probing wavelength, since the expected peak density for PANDORA is about $n_0 = 4 \cdot 10^{12}$ cm^{-3}, and assuming $n_c = 2 \cdot 10^{13}$ cm^{-3}, a wavelength $\lambda_p < 16.7$ mm ($f > 90$ GHz) is demanded, which correspond to $\omega \sim 5\omega_p$. In principle further restrictions are imposed from ray refractions through the plasma since the ratio between plasma diameter D and wavelength (D/λ_p) must be large enough (Galata et al., 2022).

However, the PANDORA plasma chamber is a large cylinder (diameter $D_c = 280$ mm and length $L_c = 700$ mm) where it is possible to generate and confine a plasma with an estimated diameter of $D = 150$ mm with an electron density range from 10^{11}–10^{13} cm^{-3} (Gammino et al., 2017). Such a density range (the mean density values that can be achieved) combined with the large plasma size is less challenging with respect to the compact plasma case resulting in a (D/λ_p) ratio equal to ~ 9. Moreover, to obtain more precise and detailed information necessary for the design study, the density and magnetic profiles have been estimated. Figure 3A shows the magnetic field (in blue) and the electron density profile (in red) - considering a Gaussian

density profile having a maximum value $n_0 = 4 \cdot 10^{18}$ m^{-3}- along the longitudinal z-axis. This value refers to the maximum density giving a certain density profile (as shown in the Figure 3A) while the corresponding mean density is $2.5 \cdot 10^{18}$ m^{-3}. Density profiles and the Faraday rotation angles estimate are also shown for a case of a lower density (Figure 3C) and a case of higher density (Figure 3D). Lower density values lower are not expected in PANDORA, because it will be needed to operate at high density and temperature domain as much as possible in order to improve the effect of the physical processes (beta-decay lifetime variation in-plasma) that PANDORA aims at measuring.

The Faraday rotation angle $\theta_{Faraday}$ has been evaluated for two different approximations of the Faraday law: 1) the so-called "λ-square" law (blue curve in Figure 3B):

$$\theta_{Faraday} = \frac{q_e^3 \lambda_p^2 B_0 n_e}{8\pi^2 c^3 m_e^2 \epsilon_0} \tag{1}$$

That is valid in case $\omega \gg \omega_p$and $\omega \gg \omega_g$, and 2) the 4th order truncated Faraday law (red curve in Figure 3B) (Naselli et al., 2018)):

$$\theta_{Faraday} = \frac{q_e^3}{2c^3 m_e^2 \epsilon_0} \int_0^L \left(\frac{n_e B_0}{\omega^2} + \frac{q_e^2}{m_e \epsilon_0} \frac{n_e^2 B_0}{2\omega^4} + \frac{q_e^4}{m_e^2 \epsilon_0^2} \frac{n_e^3 B_0}{4\omega^6} + \frac{q_e^6}{m_e^3 \epsilon_0^3} \frac{n_e^4 B_0}{6\omega^8} \right) dx \tag{2}$$

vs. the probing frequency f. Figures 3B–D shows that in the mm-wavelength range corresponding to a frequency range of 90–110 GHz, the Faraday angle is large enough to be detected and constrained to avoid ambiguity of $\pm n\pi$. Therefore, as an optimal compromise between sensitivity, bandwidth (and costs) required by the components which will form the InterPol setup, the operating frequency range has been fixed between 90 and 100 GHz.

3.2 Space availability issue

An envisaged mechanical scheme of the two antennas mounted respectively in the injection and extraction flange of the PANDORA plasma chamber is shown in Figure 4. The position/orientation of the two antennas has been chosen in order to direct the probing wave through the plasma center and avoid any mechanical interferences with the other components (pumping microwave injection line, oven, bias disk, other diagnostics access (Hartfuss and Geist, 2013)). The maximum allowed antenna aperture diameter is 30 mm which allow to obtain good performances ($|S_{11}|$, directivity) in the operating mm-wave frequency range of 90–100 GHz and at same time, to avoid mechanical interference with other components. Special dielectric lens will be used with the double function to focus and provide the vacuum tightness and separation between the UHV (Ultra High Vacuum) inside the plasma chamber and the atmospheric pressure outside.

3.3 Wave optics simulation of horn-to-horn transmission in plasmas for astrophysics nuclear decays observation and radiation for archaeometry plasma chamber

The mm-waves radiated by the polarimeter horn antenna in the PANDORA plasma chamber has been simulated by using the "Wave Optics"® module of the COMSOL Multiphysic®package. It exploits the "Beam Envelope" approximation - based on the assumption that the electric field can be factored into a slowly varying amplitude factor and a prescribed rapidly varying phase factor - for solving problem which extends over domains that are a large number of wavelengths long, without requiring the use of large amounts of memory. The PANDORA plasma chamber domain is in fact much larger than the polarimeter operating wavelengths ($L \sim 200\lambda_p$, $R \sim 80\lambda_p$ @90 GHz). In order to check the wave behaviour a 2D rectangular geometry ($L \times R$) has been employed in place of the 3D cylinder. The source antenna has been modeled as an incident Gaussian beam electric field of beam radius $w_0 = 20$ mm and distance to focal plane p_0 equal to 0 mm. Moreover, a direction of wave propagation k has been imposed by setting $\theta = 22°$ in the following conditions $k_x = k_0 \cos\theta$ and $k_y = k_0 \sin\theta$ in order to resemble the mechanical tilt angle on the antennas to be in reciprocal visibility and let the wave passing through the plasma center. Finally two cases have been simulated:

1) All "Perfect Electric Conductor" (PEC) boundary conditions (see Figure 5A)
2) In correspondence of the receiving horn antenna a "Scattering" boundary makes the boundary transparent for the incoming wave (see Figure 5B)

These two boundary conditions represent the worst case where the receiving antenna is modelled as a reflector since all the surfaces surrounding the antenna are PEC resulting in an increase of multireflection and the best scenario where the receiving antenna is approximately modeled as a prefect absorber with an Absorbing Bundary Condition (ABC). In both cases it can be seen that the chosen position for the two antennas allows a line-of-sight propagation; this direct path from the Tx to Rx antenna: 1) illuminates the plasma center; 2) minimizes interference/multipaths. The adding of a dielectric lens will allow decreasing the mechanical size of horns (considering the reduced space that we have on the injection flange) by keeping a reasonable high gain (up to ~ 20 dB). This lens shall have a permittivity value chosen as a compromise between beam shaping and the undesired internal reflections. However, also considering the vacuum-tightness role of the lens and the high temperature plasma, possible material will be alumina or quartz.

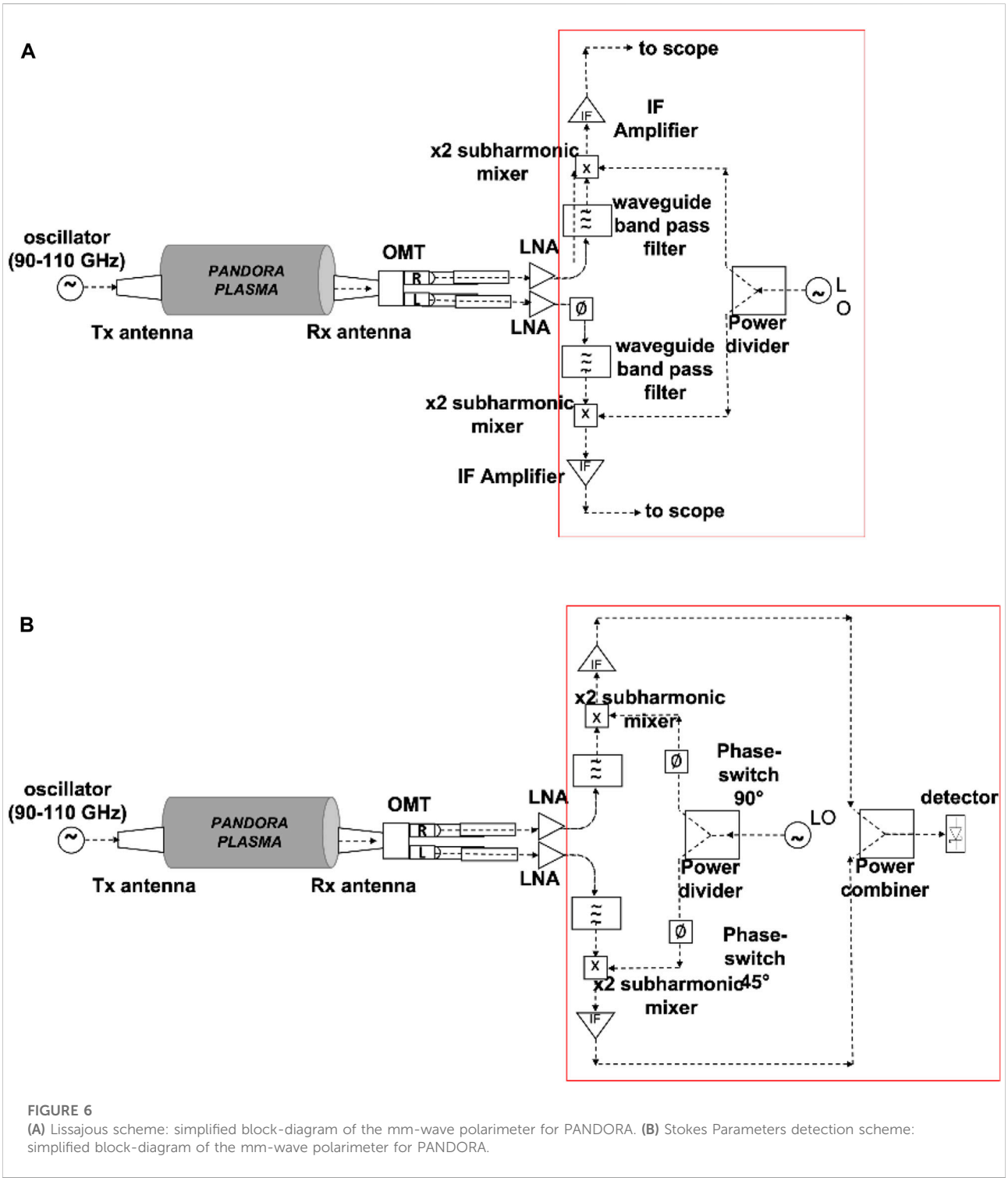

FIGURE 6
(A) Lissajous scheme: simplified block-diagram of the mm-wave polarimeter for PANDORA. **(B)** Stokes Parameters detection scheme: simplified block-diagram of the mm-wave polarimeter for PANDORA.

4 Polarimetry schemes

The polarimeter system employs a 90–100 GHz Gunn diode oscillator which generates ~20 dBm of microwave power. Gunn output power is coupled to the transmitting horn antenna. As stated in the Introduction, two super-heterodyne schemes are proposed. Both schemes consist of two W-band horn antennas, where the main characteristic should be a very low cross-polarization value (better than − 30 dB). The receiving one is connected to an orthomode transducer (OMT), two low-noise

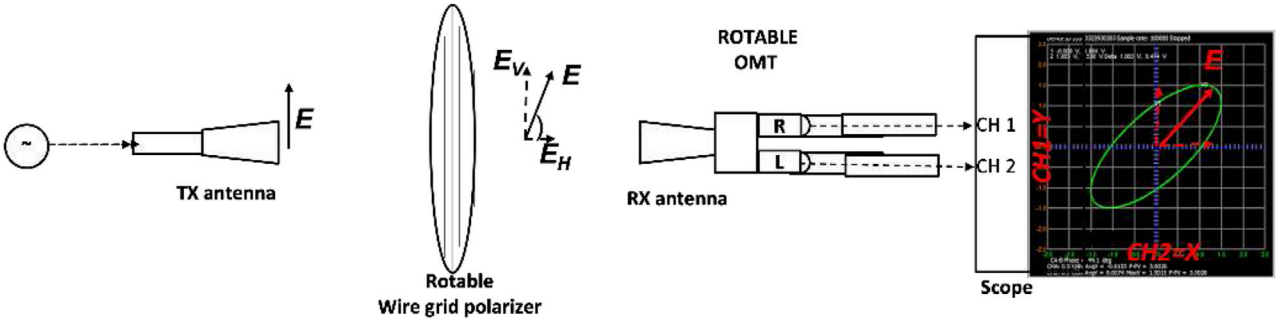

FIGURE 7
Scheme of the free-space setup for measuring the Lissajous's figures.

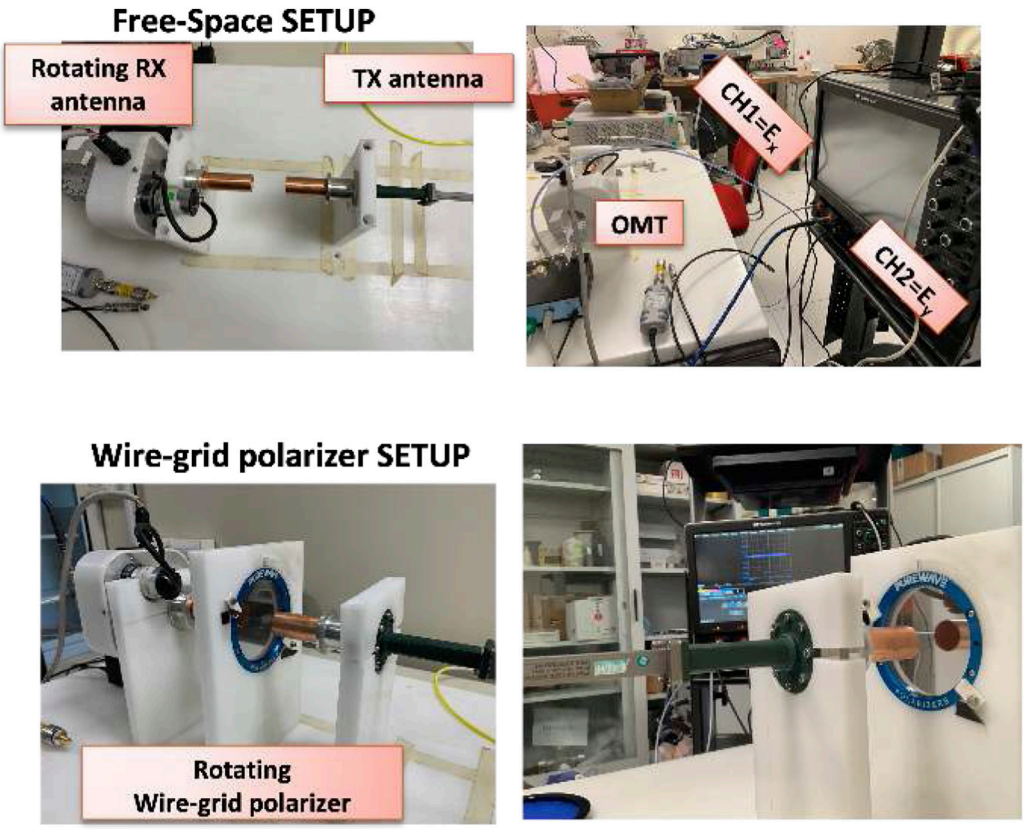

FIGURE 8
Photographs of the Free-space testbench showing the two Ka-band conical horn antennas, the OMT, the wire-grid polarizer and the 20 GHz 80 GS/s (40 Gs/s in this case since the detection is performed on the two channels, simultaneously) scope.

amplifiers (LNA) and two filter. The two output signals components of the wave received by the antenna are delivered to two subharmonic mixers which convert the mm-wave to intermediate frequency with conversion losses of around 15 dB and a wide IF bandwidth from 0.1 to 15 GHz. These signals are amplified and filtered. The bandpass waveguide filter in front of the mixer defines the system bandwidth, from 90 to 100 GHz, and rejects the image band. The use a sub-harmonic

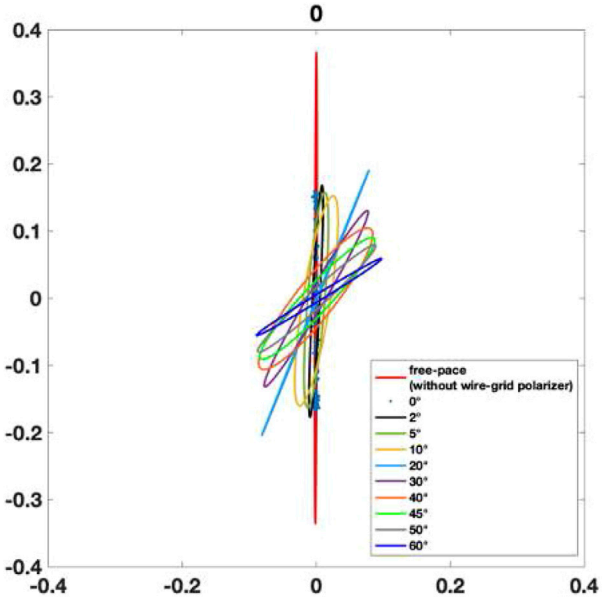

FIGURE 9
Experimental Lissajous figures produced from an elliptical fit of the Lissajous pattern X-Y scope detection at different angular position of the wire-grid polarizer.

TABLE 1 Imposed vs. measured angles of the wire grid polarizer orientation.

wire grid polarizer angle (Uncertainty= ± 2°)	Measured Angle (sensitivity= ± 0.1°)
0°	0°
2°	3°
5°	0 4.6°
10°	9.6°
20°	22.2°
30°	31.1°
40°	38.7°
45°	44°
50°	48.1°
60°	59°

mixer minimizes the W-band hardware thus making the hardware design easier and enables the usage of a 20 GHz 80 GS/s (40 Gs/s if operating with two channels simultaneously) scope to measure the Lissajous's figure. An adjustable phase shifter is inserted for initial calibration in absence of plasma.

The last part of the receiver block diagram depends on what scheme we are considering. The scheme based on the *Detection of Lissajous figure* (see Figure 6A) consists of direct RF signals detection through a scope. This allows the real-time reconstruction of the State of Polarization (SOP) curve described by the electric field vector. This result can be obtained by using the two channels scope in an x-y representation.

On the other hand, Figure 6B shows the scheme for the *Stokes Parameters detection* based on phase-switches processing. The OMT separates the left-hand and right-hand components of the incoming signal, providing the required signals for the Stokes parameters calculation. The IF signals, amplified using commercial amplifiers, are combined in order to allow the detection with a Schottky diode detector. In this case the polarimeter measures the Stokes parameters (I, Q and U) in order to characterize the polarization. Each element of the Stokes vector represents a measurable intensity which can be detected by a power meter without the need of expensive high-frequency high sample rate scope. These parameters are obtained after combining measurable output signals in the receiver based on electronic phase switching which provides different combinations. Since there are two different phase switches, the polarimeter will have four possible states. Therefore, the Stokes parameters required to measure the input signal polarization can be obtained following by covering all the states of the phase switches cycle. That is, the proposed scheme needs four times more time to collect the information.

5 Preliminary polarimetric test-bench measurements

5.1 Free-space test bench

n order to validate other possible methodologies of polarization angle measurements, we opted for making a series of measurements at scaled microwave frequencies have carried out on a free-space test-bench by using a rotating wire-grid polarizer and Ka-band OMT + horn antenna system (see the scheme in Figure 7). The measurement consists in the Lissajous figures detection - through the "X-Y" scope representation of the signals coming from the two orthogonal OMT ports - at different angle positions of the rotating wire grid polarizer (see the pictures of the experimental setup in Figure 8).

The objective of the measure is to find the angle between the *x*- axis and the major semiaxis which is imposed by the orientation of the wiregrid polarizer with respect to the linearly polarized (horizonal axis) electric field emitted by the Tx antenna.

This imposed wiregrid angle resembles the "Faraday" rotation angle induced by the plasma. The distance between the two horns has been fixed equal to 40 mm to ensure a good received signal level. The frequency has been fixed equal to 18 GHz, which the lowest operating frequency for the antennas, in order to improve the scope reconstruction at

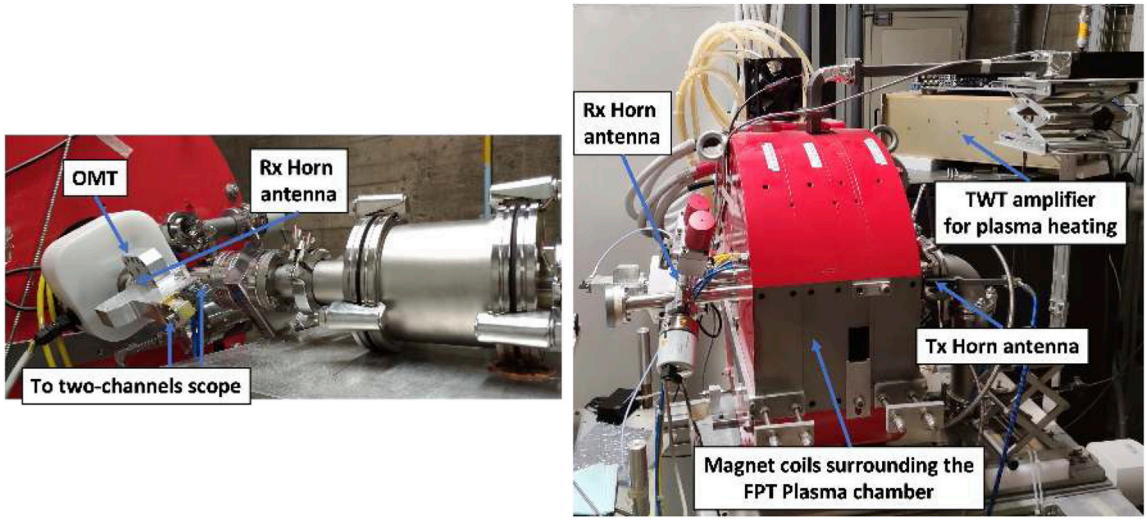

FIGURE 10
Pictures of the Flexible Plasma Trap (FPT) testbench showing the two Ka-band conical horn antennas and the two ports of the OMT connected to the 20 GHz 80 GS/s (40 Gs/s in this case since the detection is performed on the two channels, simultaneously) scope.

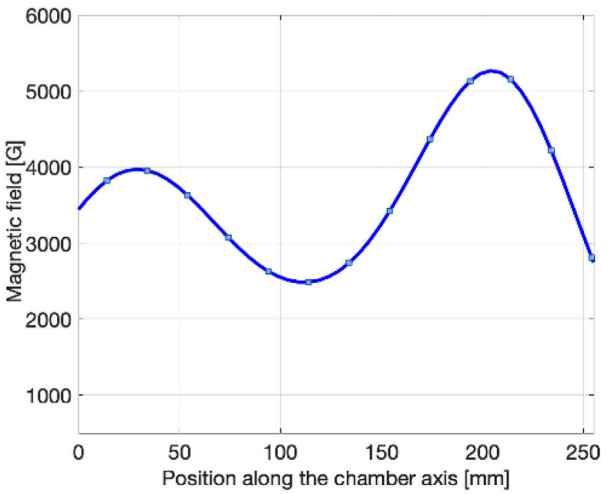

FIGURE 11
Simple-mirror confinement magnetic field profile of FTP.

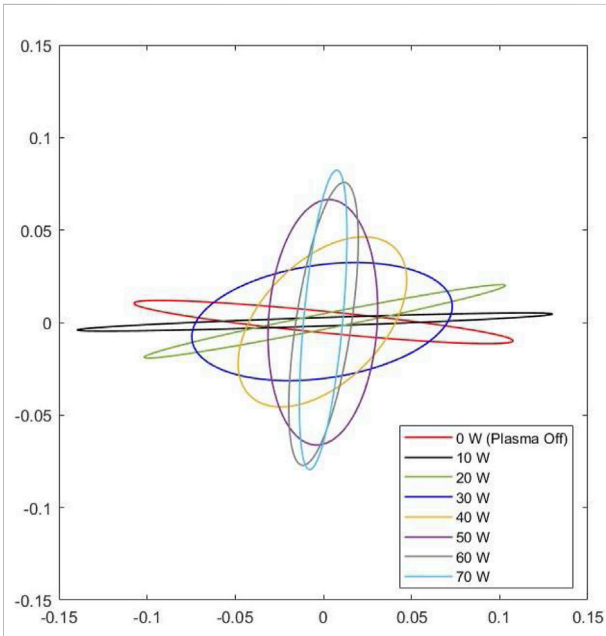

FIGURE 12
Experimental Lissajous figures produced from an elliptical fit of the Lissajous pattern X-Y scope detection at different heating powers.

40 GS/s (two channels). Even for this "low" operating frequency the scope was under sampling since the maximum oscilloscope sample rate is not sufficient for a accurate reconstruction of the 18 GHz signal. As a consequence - although the initial phase difference due to cables different length/delays was compensated by using the "deskew" function of the scope - this under sampling produces a reconstruction error; in particular, while the expected polarization pattern was a line segment, the detected shape of the Lissajous figures was an ellipse due to an artifact relative frequency/phase difference induced by the above-described under-sampling. However, despite these "hardware"-

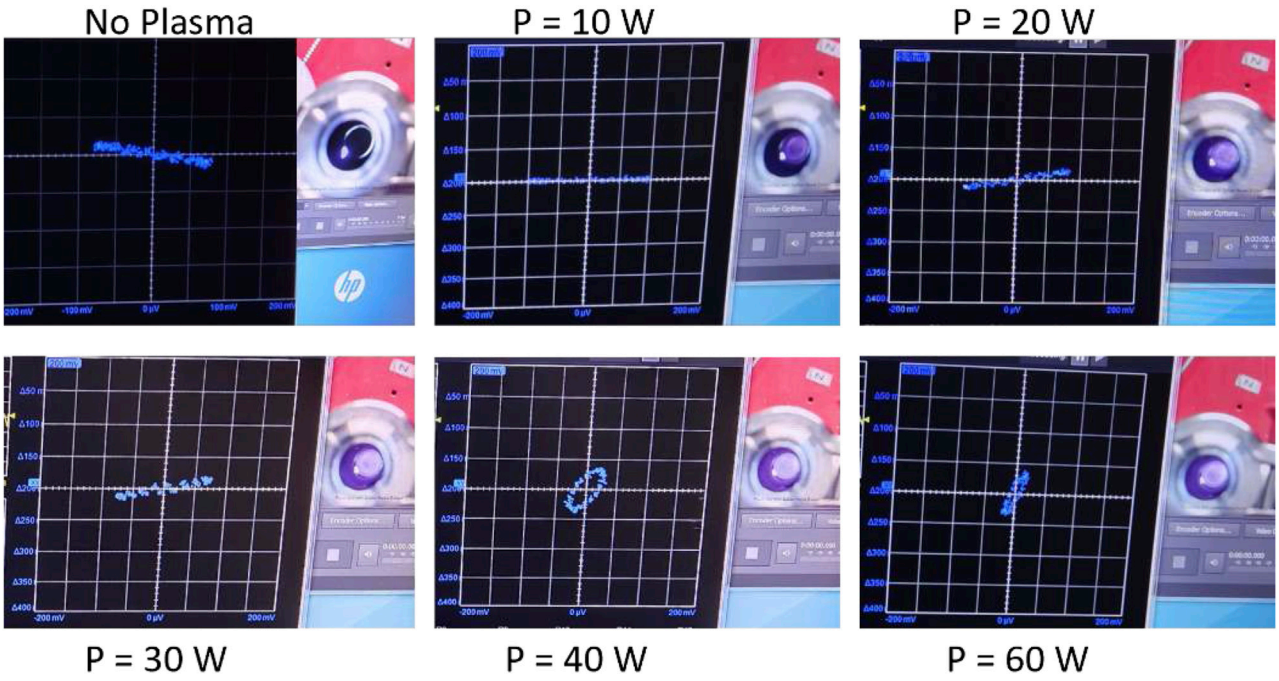

FIGURE 13
Visual inspection of the optical emission observed by a webcam thought a quartz window (on the right of each picture) in function of the pumping power. On the left of each picture is shown the screen of the scope and the corresponding Lissajous figure. The clockwise start with turn-off plasma.

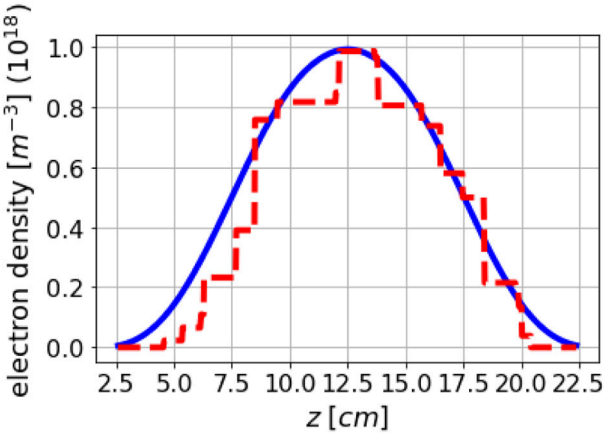

FIGURE 14
Typical numerical benchmark reconstruction of the electron density along the plasma chamber axis, the reconstruction is shown only in the core region of the chamber where the plasma density assumes largest values.

limitations, the obtained angles between the horizontal and major semi-axis are in very good agreement with the expected ones as it can be seen in Figure 9 and Table 1. The Lissajous's figures have been obtained at different position of the wire grid (the error of the polarizer angle setting is ± 2°, while the error of the estimated angle by Lissajous figure is ± 0.1°). The measured angles are perfectly compatible with the set ones within the error bars. This excellent agreement validates the *Detection of Lissajous figure*-based scheme; on the other hand it is needed a mixer to downshift the frequency at value inside the analog bandwidth and the sampling rate capability of the scope. In perspectives, the setup will be properly improved by adding two mixers (one for each output signal read by scope) for the future PANDORA measurements. In the case of "in-plasma" measurements, in which the density will be determined from the Faraday angle by means of a fit procedure, the uncertainty will increase and will be estimated by propagating the errors starting from the uncertainties obtained in the fit parameters. In the previous measurements performed on ECRIS (Naselli et al., 2018) we

obtained uncertainties of the order of 30%, but in PANDORA we expect to be able to reduce the corresponding uncertainties due to the larger size of the chamber and the consequent lower presence of spurious events than ECRIS case, that were, in fact, the main source of noise affecting the signal-over-background ratio.

5.2 Flexible plasma trap test bench

The option of making full and direct reconstruction of Lissajous patterns was attempted also considering a real plasma test-bench. Hence, further preliminary polarimetric measurements have been carried out by connecting the two horn antennas to the cylindrical vacuum chamber of the Flexible-Plasma-Trap (FPT) (Di Donato et al., 2019a), which is a compact plasma trap installed at INFN-LNS and used as down-sized test-bench of PANDORA.

In Figure 10, a photograph pf the plasma-testbench is shown. The plasma is heated thanks to a 500 W maximum RF TWT amplifier with a working frequency range 4–6 GHz. The simple-mirror confinement magnetic field profile along the longitudinal axis of the plasma chamber is shown in Figure 11.

Of course, also in this case, mixers are needed for an accurate reconstruction of the 18 GHz signal operating with a sampling rate of (40 GS/s). Anyway, preliminary and qualitative measurements were done in order to verify the sensitivity of the polarimetric system in detecting the plasma, i.e., using the tool only as "signature" of plasma ignition and not for quantitative estimations.

The measurements vs. the RF pumping power (from 0 to 70 W) have been performed and are shown in Figure 12. It can be seen that the polarization ellipse detected after the plasma ignition (at 10 W) is well distinguishable from that of the switched off plasma. Furthermore, it is possible to observe a variation in the angle between the semi-major axis and the horizontal by varying the RF power from 0 to 70 W.

Although the under-sampling and the phase difference due to cables different length do not allow a quantitative analysis, these results represent a fundamental demonstration of the instrument sensitivity to the plasma presence and to the power variation. This is an important "signature" of the capability of the polarimeter system and method to detect both the plasma ignition and the variation of the heating power (and the correlated electron density).

A rotation of almost 90° was observed and it seems to be in agreement to the gradually increasing of the optical emission vs. the pumping power observed by a simple visual inspection (pictures taken by the webcam shown in Figure 13).

Figure 13 shows that we are very sensitive to plasma ignition already at very low power 10W (see top left vs. top center), and in general to the power scan. Moreover, it shows the increase of the optical emission in a purely qualitative way (*via* a webcam), which is important preliminary feedback for this phase of the benchmark-test. Obviously, the multi-diagnostic system (described in Section 2) will allow to quantitatively characterize this emitted radiation (from visible, soft X, hard X, to gamma) to obtain the overall thermodynamical plasma properties by analyzing the experimental detected spectra. We do not report the spectra here because they are out of scope for the purpose of this paper. These preliminary tests represent a preliminary and necessary test before the next Faraday angle (and density) measurements that will be carried out thanks to a future setup upgrade (mixer for downshift the frequency and phase shifter to compensate the different lengths between the two channels).

6 Millimeter-waves inverse profilometry

All the techniques previously described allow the measurement of the average electron density along the line of sight. In this section we briefly describe an approach that allows the reconstruction of the density profile. In the perspective of the PANDORA setup, the microwave diagnostics tools are expected to be composed not only by polarimeters like the ones described above, but also including innovative techniques of plasma profile reconstruction along the line of sight. Analytical and numerical analyses have been performed up to now also to integrate the polarimetric and future profilometric in the PANDORA scenario Microwave/millimeter-waves inverse profiling requires the use of probing frequencies much higher than the cyclotron resonance and plasma frequency to consider plasma as transparent medium, avoiding anisotropy and strong scattering effects of waves propagating inside plasma. Such an assumption highly simplifies the formulation of the inverse scattering problem to be faced in performing inverse profilometry along the line-of-sight in plasma chamber. Under the above assumptions, plasma profiling can be afforded through the solution of a one-dimensional inverse scattering problem that requires the use of a large frequency bandwidth in order to gather a number of sufficient degrees of freedom of the scattered field data to be conveyed back by the retrieval process (Di Donato et al., 2019b). The numerical scattered field data has been simulated with a setup in 1D geometry resembling a beam propagation along the sight-line corresponding to the longitudinal axis of the plasma trap. In doing so, both the reflected and transmitted scattered field data have been gathered at two measurement points and the weak scattering Born approximation has been adopted to recover the plasma density profile as suggested in (Candès and Wakin, 2008). Finally, the recovery stage has been handled by means of a sparse reconstruction approach based on a "relaxed" version of the relaxed LASSO problem by the Compressive Sensing (CS) theory Candès and Wakin, 2008. Taking into

account expected peak values of 10^{12} [cm^{-3}] electron density at a ECR frequency of 18 GHz, 81 equispaced data samples in the frequency band 90–110 GHz is considered for the numerical benchmark resembling typical plasma profile shown in Figure 3B. The reconstruction results shown in Figure 14 is obtained exploiting prior support information on plasma region and slightly corrupting the scattered field data with white Gaussian noise. As it can be seen, the retrieved profile allows to roughly appraise the shape of plasma and its peak value, although a constant step-wise nature of the plasma profile is retrieved due to the assumption (not fully verified herein) about sparsity of the unknown.

The preliminary simulations are encouraging (as confirmed in Figure 14); however, the challenge of this approach will be, also, the actual implementation of the experimental setup at high frequency and the required sensitivity.

7 Conclusion

In this paper, the preliminary design study of a mm-wave polarimeter for the PANDORA experiment, allowing plasma line-integrated electron density measurements, has been described. The optimum frequency range, two possible mm-wave schemes and a possible technical implementation are proposed and evaluated. Preliminary benchmark measurements at scaled microwave frequencies have been reported: 1) the first one was carried out employing a"free-space" setup by using a wire-grid polarizer and a rotable Ka-band OMT + horn antennas system; 2) the second one was directly implemented on a compact plasma trap (called Flexible Plasma Trap) installed at INFN-LNS and used as PANDORA down-sized testbench; schemes for the proposed PANDORA scenario have been investigated. In perspective, further testbench measurements will be performed by using probing frequency in the range 90–110 GHz (as designed for the PANDORA measurements) by procuring the whole polarimetric system, i.e., the new microwave components such as mixer and phase shifter.

Data availability statement

The original contributions presented in the study are included in the article/supplementary material, further inquiries can be directed to the corresponding author.

Author contributions

GT, EN, and DM: mm-wave intefero-polarimeter design, study and simulation. PANDORA plasma chamber integration. Experimental measurements in free-space, Experimental measurements in plasma chamber. LD and GS: Experimental measurements in free-space, antenna simulations, profilometry simulations.

Acknowledgments

The authors wish to thank the 3rd Nat. Comm. of INFN, under the PANDORA Gr3, for the financial support. LD wish to thank project grant PLASMARE funded by University of Catania under research program Pia.ce.ri. 2020–2022.

Conflict of interest

The authors declare that the research was conducted in the absence of any commercial or financial relationships that could be construed as a potential conflict of interest.

Publisher's note

All claims expressed in this article are solely those of the authors and do not necessarily represent those of their affiliated organizations, or those of the publisher, the editors and the reviewers. Any product that may be evaluated in this article, or claim that may be made by its manufacturer, is not guaranteed or endorsed by the publisher.

References

Biri, S., Pálinkás, J., Perduk, Z., Rácz, R., Caliri, C., Castro, G., et al. (2018). Multi-diagnostic setup to investigate the two-close-frequency phenomena. *J. Instrum.* 13, C11016. doi:10.1088/1748-0221/13/11/c11016

Candès, E. J., and Wakin, M. B. (2008). An introduction to compressive sampling [A sensing/sampling paradigm that goes against the common knowledge in data acquisition]. *IEEE Signal Process. Mag.* 25 (2), 21–30. doi:10.1109/msp.2007.914731

Cano, J. L., Villa, E., Teran, V., Gonzalez, E., de la Fuente, L., Artal, E., et al. (2015). "A w-band polarimeter for radio astronomy applications: Design and simulation," in 2015 International Conference on Electromagnetics in Advanced Applications (ICEAA), Turin, Italy, 07-11 September 2015, 452–455. doi:10.1109/ICEAA.2015.7297152

Creely, A. J., Milanese, L. M., Tolman, E. A., Irby, J. H., Ballinger, S. B., Frank, S., et al. (2020). Design study of a combined interferometer and polarimeter for a high-field, compact tokamak. *Phys. Plasmas* 27, 042516. doi:10.1063/1.5142638

Di Donato, L., Mascali, D., Morabito, A. F., and Sorbello, G. (2019). A finite-difference approach for plasma microwave imaging profilometry. *J. Imaging* 5, 70. doi:10.3390/jimaging5080070

Di Donato, L., Morabito, A. F., Torrisi, G., Isernia, T., and Sorbello, G. (2019). Electromagnetic inverse profiling for plasma diagnostics *via* sparse recovery approaches. *IEEE Trans. Plasma Sci. IEEE Nucl. Plasma Sci. Soc.* 47, 1781–1787. doi:10.1109/tps.2019.2902469

Galata, A., Mascali, D., Mishra, B., Pidatella, A., and Torrisi, G. (2022). On the numerical determination of the density and energy spatial distributions relevant for in-plasma beta decay emission estimation. *Front. Astronomy Space Sci. Nucl. Phys. Sect.*

Gammino, S., Celona, L., Mascali, D., Castro, G., Torrisi, G., Neri, L., et al. (2017). The flexible plasma trap (FPT) for the production of overdense plasmas. *J. Instrum.* 12, P07027. doi:10.1088/1748-0221/12/07/p07027

Hartfuss, H. J., and Geist, T. (2013). *Fusion plasma diagnostics with mm-waves: An introduction*. Hoboken, New Jersey, US: Wiley VCH.

Heald, M. A., Wharton, C. B., and Furth, H. P. (1965). Plasma diagnostics with microwaves. *Phys. Today* 18, 72–74. doi:10.1063/1.3047729

Howard, A., Haberberger, D., Boni, R., Brown, R., and Froula, D. H. (2018). Implementation of a wollaston interferometry diagnostic on omega ep. *Rev. Sci. Instrum.* 89, 10B107. doi:10.1063/1.5036956

Li, X., Liu, Y., Xu, G., Zhou, T., and Zhu, Y. (2021). Design and characterization of a single-channel microwave interferometer for the helicon physics prototype experiment. *Fusion Eng. Des.* 172, 112914. doi:10.1016/j.fusengdes.2021.112914

Mascali, D., Naselli, E., and Torrisi, G. (2022). Microwave techniques for electron cyclotron resonance plasma diagnostics. *Rev. Sci. Instrum.* 93, 033302. doi:10.1063/5.0075496

Mascali, D., Santonocito, D., Amaducci, S., Andò, L., Antonuccio, V., Biri, S., et al. (2022). A novel approach to β-decay: Pandora, a new experimental setup for future in-plasma measurements. *Universe* 8, 80. doi:10.3390/universe8020080

Mauro, G. S., Celona, L., Torrisi, G., Pidatella, A., Naselli, E., Russo, F., et al. (2022). An innovative superconducting magnetic trap for probing β-decay in plasmas. *Front. Phys.* 10. doi:10.3389/fphy.2022.931953

Naselli, E., Mascali, D., Biri, S., Caliri, C., Castro, G., Celona, L., et al. (2019). Multidiagnostics setups for magnetoplasmas devoted to astrophysics and nuclear astrophysics research in compact traps. *J. Instrum.* 14, C10008. doi:10.1088/1748-0221/14/10/c10008

Naselli, E., Mascali, D., Torrisi, G., Castro, G., Celona, L., Gammino, S., et al. (2018). The first measurement of plasma density by means of an interferometric setup in a compact ECR-plasma trap. *J. Instrum.* 13, C12020. doi:10.1088/1748-0221/13/12/c12020

Naselli, E., Santonocito, D., Amaducci, S., Galatà, A., Goasduff, A., Sebastiano, G., et al. (2022). Design study of a hpge detectors array for β-decays investigation in laboratory ecr plasmas. *Frontiers* 10. doi:10.3389/fphy.2022.935728

Pascual, J. P., Aja, B., Villa, E., Terán, J. V., de la Fuente, L., and Artal, E. (2021). Performance assessment of w-band radiometers: Direct versus heterodyne detections. *Electronics* 10, 2317. doi:10.3390/electronics10182317

Scime, E. E., Boivin, R. F., Kline, J. L., and Balkey, M. M. (2001). Microwave interferometer for steady-state plasmas. *Rev. Sci. Instrum.* 72, 1672–1676. doi:10.1063/1.1347971

Torrisi, G., Naselli, E., Mascali, D., Castro, G., Celona, L., Sorbello, G., et al. (2017). A new interferometric/polarimetric setup for plasma density measurements in compact microwave-based ion sources. *J. Instrum.* 12, C10003. doi:10.1088/1748-0221/12/10/c10003

Tudisco, O., Lucca Fabris, A., Falcetta, C., Accatino, L., De Angelis, R., Manente, M., et al. (2013). A microwave interferometer for small and tenuous plasma density measurements. *Rev. Sci. Instrum.* 84, 033505. doi:10.1063/1.4797470

Wiebold, M., and Scharer, J. E. (2009). "Non invasive measurement on the pulsed and steady-state , high power madhex helicon plasma thruster," in The 31st International Electric Propulsion Conference (IEPC09), Ann Arbor, MI, USA, September 20–24, 2009.

Zhang, J., Peebles, W. A., Carter, T. A., Crocker, N. A., Doyle, E. J., Kubota, S., et al. (2012). Design of a millimeter-wave polarimeter for nstx-upgrade and initial test on diii-d. *Rev. Sci. Instrum.* 83, 10E321. doi:10.1063/1.4733735

frontiers | Frontiers in Physics

TYPE Original Research
PUBLISHED 31 August 2022
DOI 10.3389/fphy.2022.947194

OPEN ACCESS

EDITED BY
Paul Stevenson,
University of Surrey, United Kingdom

REVIEWED BY
Norbert Kaiser,
Technical University of Munich, Germany
Antonio Caciolli,
University of Padua, Italy

*CORRESPONDENCE
A. Galatà,
alessio.galata@lnl.infn.it

SPECIALTY SECTION
This article was submitted to Nuclear Physics,
a section of the journal
Frontiers in Physics

RECEIVED 18 May 2022
ACCEPTED 29 July 2022
PUBLISHED 31 August 2022

CITATION
Galatà A, Mascali D, Mishra B, Naselli E, Pidatella A and Torrisi G (2022), On the Numerical Determination of the Density and Energy Spatial Distributions relevant for in-Plasma β-Decay Emission Estimation.
Front. Phys. 10:947194.
doi: 10.3389/fphy.2022.947194

On the Numerical Determination of the Density and Energy Spatial Distributions relevant for in-Plasma β-Decay Emission Estimation

A. Galatà[1]*, D. Mascali[2], B. Mishra[2,3], E. Naselli[2], A. Pidatella[2] and G. Torrisi[2]

[1]Laboratori Nazionali di Legnaro, Istituto Nazionale di Fisica Nucleare, Legnaro, Italy, [2]Laboratori Nazionali del Sud, Istituto Nazionale di Fisica Nucleare, Catania, Italy, [3]University of Catania, Department of Physics and Astronomy, Catania, Italy

Aim of the PANDORA (Plasmas for Astrophysics, Nuclear Decays Observation and Radiation for Archeometry) project is the in-plasma measurements of decay rates of beta radionuclides as a function of the ionization stage. In this view, a precise calculation of plasma electrons density and energy is mandatory, being responsible for ions' creations and their spatial distribution following plasma neutrality. This paper describes the results of the INFN simulation tools applied for the first time to the PANDORA plasma, including electromagnetic calculations and electrons' dynamics within the so-called self-consistent loop. The distribution of the various electrons' population will be shown, with special attention to the warm component on which depends the obtained ions' charge state distribution. The strict relation of the results with the evaluation of the in-plasma nuclear decays will be also explained.

KEYWORDS

β-decay, plasma traps, numerical simulations, γ-spectroscopy, γ detectors

1 Introduction

Experiments carried out on storage rings demonstrated how the half-life of β-decaying radioactive species could vary considerably when they are in a highly ionized state, compared to the neutral one. In particular, measurements of the half-life of $^{187}Re^{75+}$ ions showed it to be nine orders of magnitude lower compared to the value of 42 Gyr measured for neutral ^{187}Re [1], decaying through bound-state β-decay. In addition, bare ^{163}Dy nuclei, being stable as neutral atoms, become radioactive with a half-life of 33 days [2]. The PANDORA (Plasmas for Astrophysics, Nuclear Decays Observation and Radiation for Archeometry) project Mascali et al. [3] proposes a complementary and challenging approach to measure nuclear β-decays, based on the production of a plasma resembling stellar-like conditions, in order to correlate the decay rate with the thermodynamical properties of the plasma-environment. The study will be

mainly focused on some radionuclides of relevance for Nuclear Astrophysics. To this scope, a compact magnetic trap, based on the Electron Cyclotron Resonance (ECR) principle Geller [4], will be built to confine plasmas of electron densities $n_e \sim 10^{11}$–10^{13} cm^{-3} or higher and temperatures $kT_e \sim$0.1–30 keV. By tuning the plasma parameters, it will be possible to establish ion charge state distributions that will mimic specific stellar environments: they will be inferred using an unprecedented set of diagnostics Naselli et al. [5], to which 14 High Purity Germanium (HPGe) detectors will be added to tag the γ-rays accompanying β-decays. In this way, decay rates will be evaluated as a function of the charge state distribution of in-plasma ions Naselli et al. [6]. The total detection efficiency has been estimated through numerical simulations carried out with GEANT4 Agostinelli et al. [7]; Naselli et al. [8], finding values between 0.1% and 0.2% depending on the energy of the γ-rays and supposing a relative efficiency of the detectors of 70%. The HPGe detectors will work in a rather harsh conditions due to the X-rays' and γ-rays' background of about 50 kHz (in each detector, in terms of detected counts per second), self-emitted by the plasma due to the electron bremsstrahlung: this means that each detector should point to an area of the plasma with the highest possible ion density, in order to maximize the counting rate of interest. ECR plasmas are typically far from being uniform, so the knowledge of their fine structure is mandatory: in this view, numerical simulations are a powerful predictive tool to fulfill this task. The two INFN Laboratories, LNL and LNS, have been dedicating their efforts to obtain a self-consistent descritpion of ECR plasmas, by joining precise electromagnetic calculations, carried out with COMSOL-Multiphysics©, with the electrons dynamics calculated with MatLab©. This paper presents the latest results applied to the plasma expected for PANDORA: after a description of the numerical approach adopted in section 2, the calculations portraying the fine structure of the plasma will be shown in section 3, as well as the distribution of electrons in different energy ranges, with a special focus on those relevant for the ionization process. The strict relation of the results with the evaluation of the in-plasma nuclear decays will be discussed in section 4, focusing the attention to the positioning and orientation of the HPGe detectors. Finally, some conclusions will be drawn.

2 The numerical approach

In ECR ion sources and traps a plasma is created by microwaves injected in a cylindrical vacuum chamber, called the plasma chamber, and confined by a particular magnetic structure called "B-minimum", obtained by superimposing the field generated by two or three coils (axial confinement) with the one generated by a sextupole (radial confinement): its characteristic is the production of a field that grows in any direction, going from the centre of the chamber towards its walls. For the specific case of PANDORA, a fully superconducting magnetic system was chosen, as described in Mauro et al. [9]: the two maxima of the axial field could be tuned between 1.7 and 3 T, the minimum value will be around 0.4 T, while the radial field at the plasma chamber wall will be 1.6 T. The condition for the ECR resonance to take place is that the microwave frequency ω is equal to the electron Larmor frequency $\omega_g = q_e B/2m_e$, where q_e and m_e are, respectively, the electron's charge and mass: considering the particular magnetic configuration, this condition is satisfied on specific points forming a closed ellipsoidal-like surface, called resonance surface. Figure 1 shows the resonance surface at 18 GHz (B_{ECR} = 0.64 T) for the typical magnetic configuration that will be used in PANDORA, together with the lateral walls of the plasma chamber: it encloses a volume of less than 3 L (the total value of the plasma chamber being around 44 L).

The frequency used and the geometry of the plasma chamber, working as a resonant cavity, allow the excitation of a given number of resonant modes: compared to the vacuum filled case, the presence of a magnetized plasma modifies the electromagnetic field distribution and the resonant frequencies, through its 3D dielectric tensor that depends (among other parameters) on the plasma density. In particular, the analytical formula implemented in the code is the following:

$$\begin{pmatrix} \epsilon_0\left(1-\frac{X(1+iZ)}{(1+iZ)^2-Y^2}\right) & i\epsilon_0\frac{XY}{(1+iZ)^2-Y^2} & 0 \\ -i\epsilon_0\frac{XY}{(1+iZ)^2-Y^2} & \epsilon_0\left(1-\frac{X(1+iZ)}{(1+iZ)^2-Y^2}\right) & 0 \\ 0 & 0 & \epsilon_0\left(1-\frac{X}{1+iZ}\right) \end{pmatrix} \quad (1)$$

wher $X = (\omega_p/\omega)^2$, $Y = (-\omega_g/\omega)$ and $Z = (\omega_{eff}/\omega)$, being ω_p the plasma frequency and ω_{eff} the collision frequency. From the considerations described above it is clear that simulating the ECR plasma necessitates of a self-consistent approach: in fact, on one hand the electromagnetic field set-up inside the plasma chamber determines, through a resonant interaction, the energetic content of electrons and then the plasma density. On the other hand, the plasma is an anisotropic and dispersive medium characterized by a 3D dielectric tensor, that must be taken into account for the calculation of the electromagnetic field in a kind of self-consistent loop Torrisi et al. [10]. The numerical approach, whose results are presented in this paper, models ECR plasmas by applying an iterative procedure to solve the collisional Vlasov-Boltzmann equation Mascali et al. [11]. By this approach, both an electromagnetic solver, such as COMSOL-Multiphysics© and a kinetic code (written in MatLab©) to solve particles' equation of motion are used in an iterative process, assuming a stationary plasma. The code developed by the two INFN Laboratories, LNL and LNS, has been extensively described elsewhere Galatà et al. [12,13]: it is able to describe both ions and electrons dynamics. In fact, it has been applied to the description of the capture of

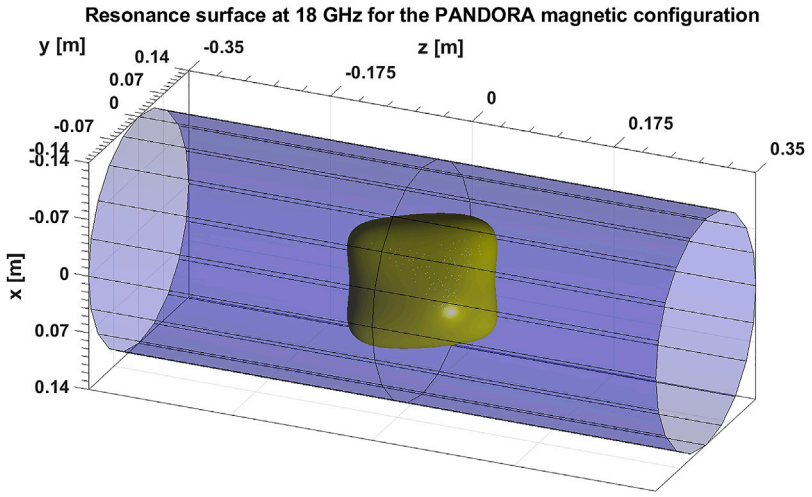

FIGURE 1
Resonance surface at 18 GHz (B_{ECR} = 0.64 T) for the typical magnetic configuration that will be used in PANDORA (in yellow) together with the lateral walls of the plasma chamber (in blue).

externally injected ions by the ECR plasma in the charge breeding process Galatà et al. [14,15], as well as electrons distribution in the ECR source installed at the ATOMKI Laboratory (Hungary), whose results have been used to calculate the characteristic X-rays emitted by an argon plasma Mishra et al. [16]. The domain of the simulation is the portion of the cylindrical plasma chamber between the two maxima of the axial magnetic field (length 700 mm, inner radius 140 mm for the case of PANDORA) and is discretized in cells of 1 mm^3, where COMSOL calculates the electromagnetic field and makes it available for the electrons dynamics as a 3D matrix. It is then loaded by the kinetic code that integrates the electrons equation of motion, including the confining magnetostatic field using the relativistic Boris method Birdsall and Langdon [17] and e-e collisions through the Langevin formalism Manheimer et al. [18]. This formalism is totally equivalent to the solution of the Fokker-Planck equation MacDonald et al. [19]: by supposing plasma particles' velocities being distributed according to a Maxwell-Boltzmann distribution, it is possible to obtain an analytic expression for the so-called coefficient of dynamical friction W_s and the coefficients of parallel and perpendicular diffusion, respectively $D_\parallel$ and $D_\perp$. At each time step of integration T_{step}, the velocity variation $\Delta\mathbf{v}_c$ of a particle as a consequence of Coulomb collisions can then be written as:

$$\Delta\mathbf{v}_c = -W_s\mathbf{v} + \mathbf{v}_{rand} \tag{2}$$

where $\mathbf{v}$ is the instantaneous particle's velocity, the first term on the right side represents the friction, while the second is a random vector taking into account for the build up of a spread in velocity. The components of this last vector are distributed according to the formula:

$$\phi(\mathbf{v}_{rand}) = \frac{1}{\left(2\pi T_{step}\right)^{3/2} D_\perp D_\parallel^{1/2}} \exp\left(-\frac{v_3^2}{2D_\parallel T_{step}} - \frac{v_1^2 + v_2^2}{2D_\perp T_{step}}\right) \tag{3}$$

where the index "3" is along the direction of the particle's velocity, while directions one and two are perpendicular to each other and to direction 3. These directions do not necessarily coincide with the spatial coordinates x, y and z, so are identified by the code every T_{step}. By using an ad-hoc routine, the code stores particles' positions and kinetic energies at each time step in 3D matrices reflecting the domain of the simulation, creating "occupation" and "energy accumulation" maps. The occupation maps are opportunely scaled in order to obtain real density maps, while by dividing the energy accumulation map with the occupation map the spatial distribution of the average energy $< sK >$ is obtained. By supposing it belongs to electrons with a Maxwell-Boltzmann (MB) distribution, it is possible to derive the most probable thermal speed c_s, necessary to calculate the various diffusion coefficients, as follow: 1) calculating first the gamma factor using the formula $\gamma = 1 + < K > /mc^2$; 2) then, from the γ factor calculating the average velocity of the MB distribution as $< v > = c \cdot \sqrt{1 - 1/\gamma^2}$; 3) finally, from the average velocity calculating the most probable thermal speed using the formula $c_s = < v > \cdot (\sqrt{\pi}/2)$. Moreover, the code checks also at each T_{step} if the simulated particles are still in the domain of the plasma chamber: if not, particles are removed from the calculation and their positions and

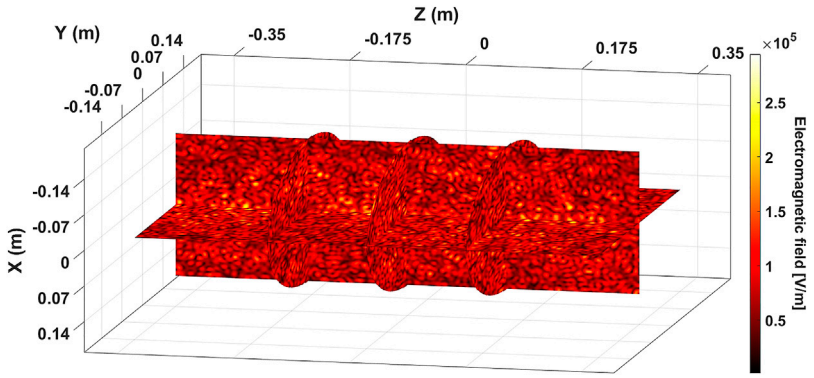

FIGURE 2
Electromagnetic fieldi n vacuum calculated at the end of the Step0.

velocities are stored in the so-called "losses matrix". The applied numerical approach is organized in steps as follows:

- Step0
  1 The electromagnetic field is calculated supposing a vacuum filled cavity, obtaining the field EM_0;
  2 The kinetic code integrates the equation of motion of N electrons uniformly distributed inside the plasma chamber without including the presence of a plasma and under the influence of the external confining magnetic field and EM_0. The output is a real density map $Dens_0$;
- Step1
  1. The map $Dens_0$ is used to derive the plasma 3D dieletric tensor and repeat the electromagnetic calculations including it. The output is a new field EM_1;
  2. The kinetic code integrates the equation of motion of electrons initially distributed as $Dens_0$, without including the presence of a plasma and under the influence of the external confining magnetic field and EM_1. The outputs are a real density map $Dens_{1A}$ and an average energy map $< K_1 >$ or, equivalently, the map of the most probable thermal speed c_{s1};
  3. The kinetic code integrates again the equation of motion, this time of electrons initially distributed as $Dens_{1A}$, including the presence of a plasma (distributed as $Dens_{1A}$ and whose most probable thermal speed is given by the map c_{s1}) through e-e collisions and using EM_1. The output is new real density map $Dens_{1B}$;
- . . .
- Step *i*th proceeds via the same methodology as presented in Step 1.

The iteration proceeds until the results show self-consistency, that is until the results from consecutive steps show negligible differences in the density and average energy matrices: this is verified, in particular, by plotting the respective maps, 1D density profiles along the coordinate axes and summing up the density matrices, in order to check if the total number of occupancies stays reasonably constant (within a few percent). As an example, Figure 2 shows the electromagnetic field in vacuum as calculated by COMSOL-Multiphysics© at the end of the Step0:The approach, called self-consistent loop, is schematically

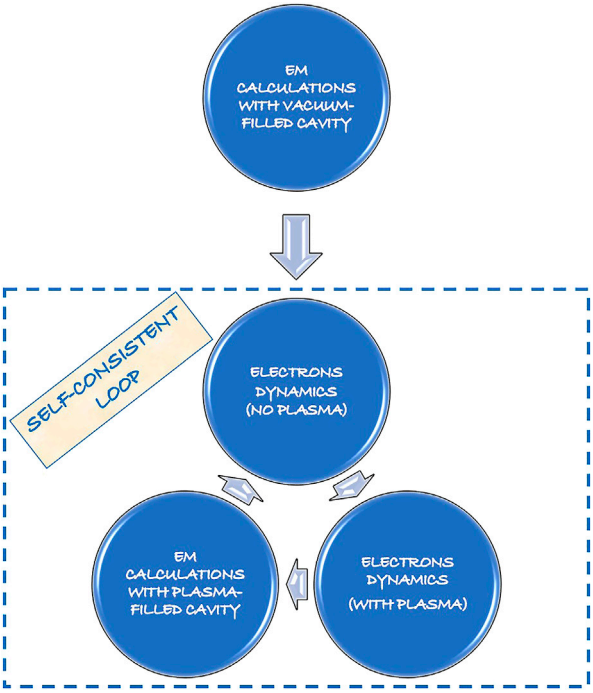

FIGURE 3
Schematic representation of the self-consistent loop.

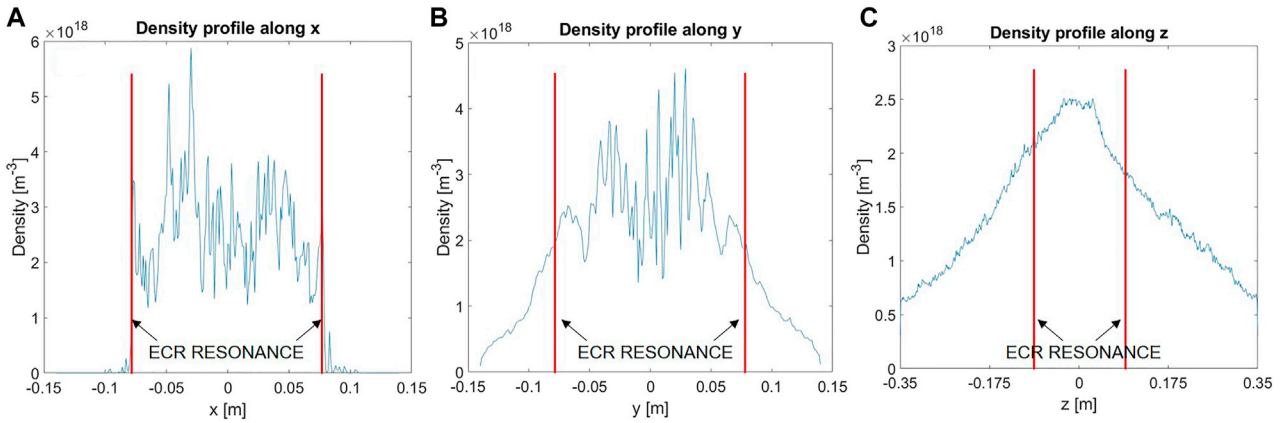

FIGURE 4
1D density profiles along the coordinate axes: **(A)** *x* direction; **(B)** *y* direction; **(C)** *z* direction. The positions correspoding to the ECR resonance are indicated with vertical red lines.

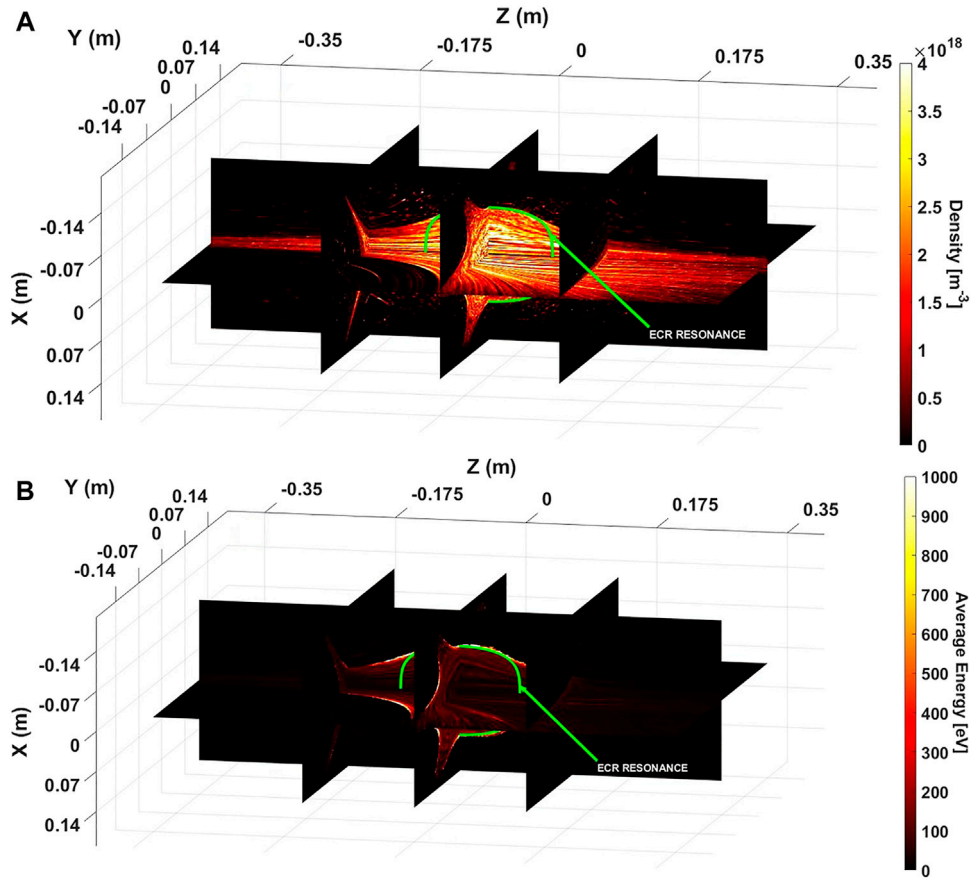

FIGURE 5
PANDORA's plasma characteristics; **(A)** 3D total density; **(B)** average energy. The contour of the ECR resonance is indicated in green.

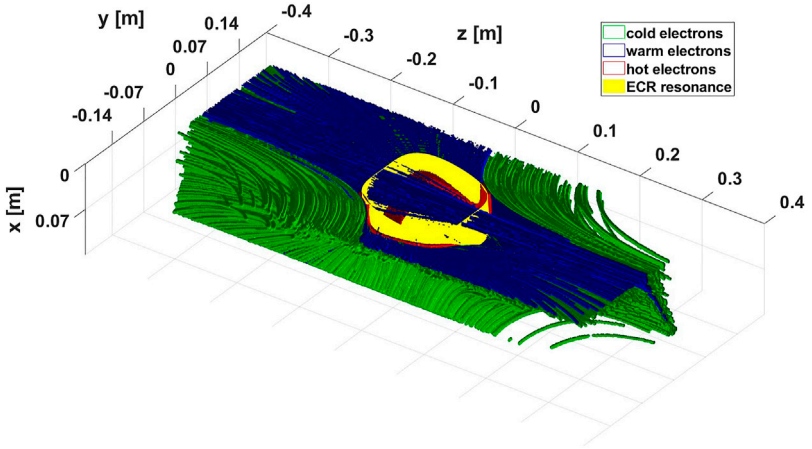

FIGURE 6
3D isosurfaces of the spatial distribution of the three electrons' populations: *cold* (green), *warm* (blue) and *hot* (red). The ECR resonance corresponds to the yellow surface.

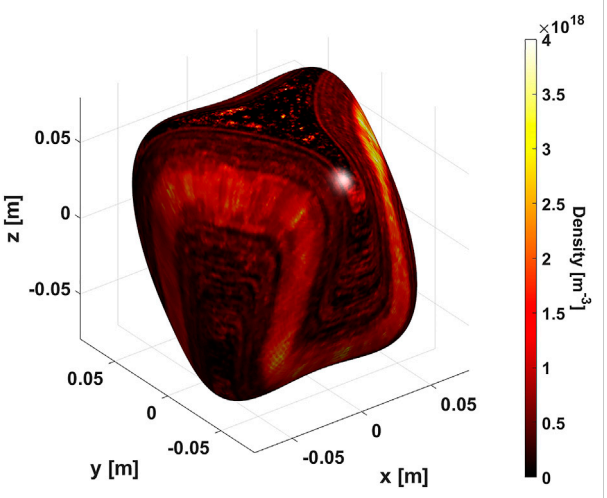

FIGURE 7
Density distribution of *warm* electrons on the resonance surface. The maximum of the color scale corresponds to the cut-off density at 18 GHz.

described in Figure 3: depending on the number of simulated particles, the integration step and time (of course besides the particular computer used) the calculations of a single step could last from one to several days.

In the previous version of the code Galatà et al. [13], the instantaneous position of a particle at each time step (x_{part}, y_{part}, z_{part}) was projected to the closest point of the 3D matrix reflecting the simulation domain, thus obtaining three indices (i, j, k): those indices were used to select the specific value of the electromagnetic field to be used in the integration of the equation of motion, as well as to store the respective quantities in the occupation and energy accumulation maps. In the latest version of the code the electromagnetic field seen by each particle is the result of the superpositions of the values stored on the eight grid points surrounding its instantaneous position, using proper weights Birdsall and Langdon [17]. In the same way, occupation and energy accumulation maps are created distributing the relative quantities on the same grid points. A further improvement concerns the implementation of the relativistic Boris method, through a computationally more precise and faster formalism described in Zenitani and Umeda [20]. The results shown in the following section concerns the first application of the above-mentioned simulation scheme to a high volume, high frequency ECR plasma: even if the global convergence is not fully achieved yet, they already give relevant indications on the plasma density and energy distribution in such a new configuration and can still be considered satisfactory.

3 Simulations results

As mentioned in the previous section, the simulation domain is the cylindrical plasma chamber of the PANDORA trap, with a length of 700 mm, a radius of 140 mm and discretized in cells of 1 mm^3. Electromagnetic simulations were carried out at a frequency $\nu = 18$ GHz and a power $P_\nu = 5$ kW. The various steps of the self-consistent loop followed the evolution of 10^5 electrons, whose initial velocities were distributed according to a Maxwell-Boltzmann distribution with a temperature of 5 eV:

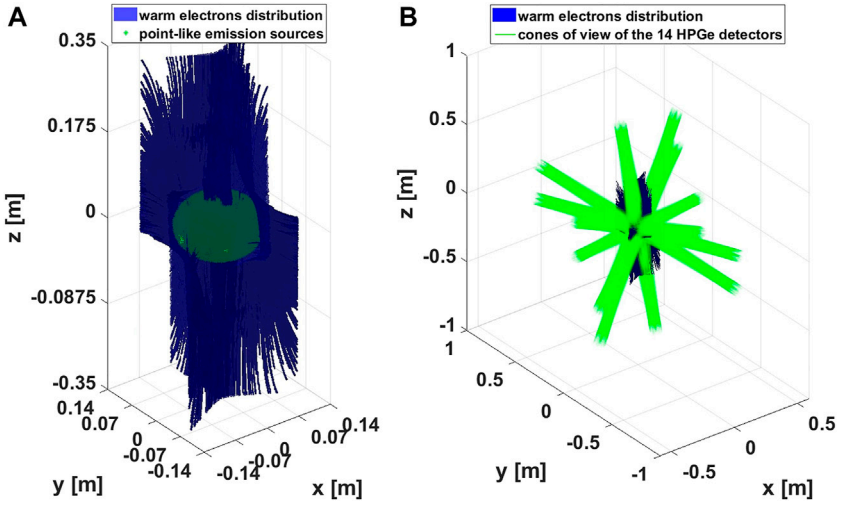

FIGURE 8
(A): distributon of warm electrons (blu) superimposed to the simulated point-like sources of γ emissions (green). **(B)**: cones of view of the 14 HPGe detectors (green) crossing the warm electrons distribution (blue).

considering all the characteristic times involved and in particular to describe properly the electrons' cyclotron motion, the integration step was chosen as $T_{step} = 10^{-12}$ s. To allow filling correctly the high energy part of the electrons' distribution as a consequence of the ECR resonance, the integration time was fixed to $T_{span} = 100$ μs: this translated in a total of 10^8 iterations. Following the scheme described in section 2, the self-consistent loop was iterated up to the Step3. ECR plasma electrons are usually grouped in three populations: *cold* electrons, characterized by a low kinetic energy, that constitute the bulk of the plasma; *warm* electrons, responsible for the ionization process; *hot* electrons, characterized by a very high kinetic energy, not involved in the ionization process, but that contribute considerably to the plasma self emission, especially in the hard X-rays region. By using the special routines implemented in the code, it was possible to create density and average energy maps for all the three electrons populations: we considered as *cold* those electrons with a kinetic energy $K \leq 100$ eV; *warm* those with $100 < K \leq 5000$ eV; finally, *hot* those with $K > 5000$ eV. In particular, the *warm* population is relevant for the scope of PANDORA, because its density and average energy will determine the charge state distribution set-up inside the plasma and will be used as a knob to experimentally verify its influence on the β-decay rate of several radionuclides (as expected by theoretical models).

Figure 4 shows the 1D total density profiles on both transversal planes (in the middle of the plasma chamber) and along the plasma chamber axis: it is worth noticing how the density reaches very high values, close to the cut-off density at the simulated frequency ($n_{cut-off} \sim 4 \cdot 10^{18}$ m^{-3}) and in some cases exceeding it. The asimmetry observed between the two transversal plane is a direct consequence of the asimmetry of the confining magnetic field, but especially along the x direction the formation of the so-called plasmoid/halo structure Ivanov and Wiesemann [21] is clearly visible.

Relevant information come from the distribution of the 3D total density and average energy: Figure 5 shows slice plots of both quantities. The colorbar of the density plot has been limited to the value corresponding to the cut-off density, in order to underline the fact that the PANDORA trap will create a very dense plasma, radially confined inside the resonance surface (whose contour is indicated in green) and with a density exceeding $n_{cut-off}$ in several locations. For what concerns the average energy, it reaches (and exceeds) 1 keV in the zones corresponding to the ECR resonance: if one considers that most of plasma electrons belong to the *cold* population, with a low kinetic energy, having such a high average energy is a clear indication of the creation of a huge amount of energetic electrons heated by the external microwave field.

It is interesting now to verify the distribution of electrons belonging to the three different populations: Figure 6 shows the isosurfaces corresponding to their spatial distributions, plotted in cut view for positive values of the x axis. It can be clearly seen how the three populations are nested one inside the other, going from the *cold* to the *hot* one: in particular, this last population is entirely distributed on (or in proximity of) the resonance surface (indicated in yellow), as a consequence of the extremely efficient energy transfer from the external

microwave field to plasma electrons. The high energy reached makes the cross section for elastic scattering of those electrons very low, thus implying a very small diffusion away from the resonance zone.

It is important now to analyse a bit more in details the results concerning the *warm* population, being relevant for the scope of PANDORA. The first significant result comes from the relative abundance of this population with respect to the total number of electrons. In fact, by summing up the total occupation map and the one of *warm* electrons it has been observed that they constitute about the 20% of the total. This results is absolutely unprecedented, even for very high performances ECR sources (where the fraction of *warm* electrons is usually lower) and is most likely due to the optimum coupling of the external microwave field with the plasma chamber in the first place Mauro et al. [9], then with the plasma itself. Having such a high percentage of *warm* electrons will translate in very high charge states produced in the plasma, thus increasing the probability to detect significant variations of the half-lives of the radioactive species of interest. The optimum coupling of microwave can be deduced also by looking at Figure 7, showing the density distribution of *warm* electrons on the resonance surface, near which energetic electrons spend most of the time due to the confining effect of the ECR resonance Geller [4]. As for the case of Figure 5, the maximum of the color scale has been limited to the value corresponding to $n_{cut-off}$: it can be seen how the density is extremely high on this surface, reaching and exceeding $n_{cut-off}$ in some locations.

4 HPGe detectors position benchmark

With the aim of fulfilling the goal of the PANODRA project, the choice of the γ-detectors, their number and implementation on the magnetic trap is a key point. As described in section 1, 14 HPGe detectors will surround the plasma trap in order to detect as efficiently as possible the γ-rays accompanying the β-decay of the radionuclides of interest. The detectors will see the plasma through apertures made on the cryostat, that has been specially designed to void distorting the confining magnetic field Mauro et al. [9]. Given the dimension of the apertures, the particular orientation of the cones of view of the detectors will determine the amount of γs produced that will be effectively detected, depending on the particular portion of the plasma intercepted. In order to maximize the detection of the γs of interest, this portion should be part of the distribution of *warm* eletrons, where most of the ionisatons to high charge states take place. The evaluation of the detection efficiency, described in Naselli et al. [8], has been carried out by supposing γs being emitted isotropically from point-like sources filling an ellipsoidal volume having semi-axes of 79 mm, 79 and 56 mm (along, respectively, x, y and z) and resembling the resonance surface, thus obtaining the cones of view intercepted by the detectors. It is interesting now to superimpose those cones to the distribution of warm electrons obtained by the previously described numerical simulations: the results are shown in Figure 8. From part (A) it can be observed how the sources are completely internalised in the cloud of *warm* electrons, thus validating the model used to deduce the detection efficiency. Much more important is the information coming from part (B) of Figure 8: it can be clearly seen how the cones of view of the detectors intercept perfectly the *warm* electrons distribution, thus maximizing not only the probability to detect the γs accompanying the β-decay but also the possibility to observe variations of the half-life by tuning the charge state distribution as a consequence of a variation of the electrons energy.

5 Conclusions

In conclusion, the latest version of the developed self-consistent approach demonstrated its ability to describe correctly the anisotropic magnetoplasmas produced inside an ECR trap, even in the case of a high volume, high frequency model. The plasma produced within PANDORA will be characterized by an unprecedented fraction of *warm* electrons, thus increasing dramatically the ionization efficiency. This aspect, together with the possibility to vary dynamically the plasma parameters and the implementation of a set af multi-diagnostics, will allow to correlate any possible variation of the half-lives of β-decaying radioactive species to the plasma ionization state. The results of the numerical simulations allowed also to benchmark the choice of the specific orientation of the 14 HPGe detectors, demonstrating how the cones of view perfectly intercept the *warm* electrons spatial distribution: this means that they will point exactly where most of the ionizations will take place, thus increasing the detection sensitivity to variations of the in-plasma charge state distribution.

t, and intellectual contribution to the work and approved it for publication.

Data availability statement

The raw data supporting the conclusions of this article will be made available by the authors, without undue reservation.

Author contributions

AG developed the original code and implemented new features DM provided the background physics in relation with

PANDORA EN followed the part of the work connected with the gamma rays detection BM and AP carried out the necessary data analysis in the different electrons' energy ranges explored GT is in charge of the electromagnetic simulations.

Acknowledgments

The authors greatfully acknowledge the support of INFN by the Grant PANDORA_Gr3 (3^{rd} Nat. Comm.) and the precious help of the colleagues L. Bellan and M. Comunian from INFN-LNL in carrying out the numerical simulations.

Conflict of interest

The authors declare that the research was conducted in the absence of any commercial or financial relationships that could be construed as a potential conflict of interest.

Publisher's note

References

1. Bosch F, Faestermann T, Friese J, Heine F, Kienle P, Wefers E, et al. Observation of bound-state β^- decay of fully ionized ^{187}Re: ^{187}Re–^{187}Os cosmochronometry. *Phys Rev Lett* (1996) 77:5190–3. doi:10.1103/PhysRevLett.77.5190

2. Jung M, Bosch F, Beckert K, Eickhoff H, Folger H, Franzke B, et al. First observation of bound-state β^- decay. *Phys Rev Lett* (1992) 69:2164–7. doi:10.1103/PhysRevLett.69.2164

3. Mascali D, Busso M, Mengoni A, Amaducci S, Castro G, Celona L, et al. The PANDORA project: An experimental setup for measuring in-plasma β-decays of astrophysical interest. *EPJ Web Conf* (2020) 227:01013. doi:10.1051/epjconf/202022701013

4. Geller R. *Electron cyclotron resonance ion sources and ECR plasmas*. Taylor & Francis (1996).

5. Naselli E, Rácz R, Biri S, Mazzaglia M, Galatà A, Celona L, et al. Quantitative analysis of an ECR ar plasma structure by x-ray spectroscopy at high spatial resolution. *J Instrum* (2022) 17(2022):C01009. doi:10.1088/1748-0221/17/01/c01009

6. Naselli E, Mascali D, Caliri C, Castro G, Celona L, Galatà A, et al. Nuclear β-decays in plasmas: How to correlate plasma density and temperature to the activity. *EPJ Web Conf* (2020) 227:02006. doi:10.1051/epjconf/202022702006

7. Agostinelli S, Allison J, Amako K, Apostolakis J, Araujo H, Arce P, et al. Geant4—A simulation toolkit. *Nucl Instr Methods Phys Res Section A: Acc Spectrometers, Detectors Associated Equipment* (2003) 506:250–303. doi:10.1016/S0168-9002(03)01368-8

8. Naselli E, Santonocito D, Amaducci S, Galatà A, Gaosduff A, Mauro GS, et al. *Frontiers in physics - research topics: Nuclear physics and Astrophysics in plasma traps (forthcoming)* (2022).Design study of a hpge detectors array for β-decays investigation in laboratory ecr plasmas

9. Mauro GS, Celona L, Torrisi G, Pidatella A, Naselli E, Russo F, et al. *Frontiers in physics - research topics: Nuclear physics and Astrophysics in plasma traps (forthcoming)* (2022).An innnovative superconducting magnetic trap for probing β-decay in plasmas

10. Torrisi G, Mascali D, Sorbello G, Neri L, Celona L, Castro G, et al. Full-wave fem simulations of electromagnetic waves in strongly magnetized non-homogeneous plasma. *J Electromagn Waves Appl* (2014) 28:1085–99. doi:10.1080/09205071.2014.905245

11. Mascali D, Torrisi G, Neri L, Sorbello G, Castro G, Celona L, et al. 3d-full wave and kinetics numerical modelling of electron cyclotron resonance ion sources plasma: Steps towards self-consistency. *Eur Phys J D* (2015) 69:27. doi:10.1140/epjd/e2014-50168-5

12. Galatà A, Mascali D, Neri L, Celona L. A new numerical description of the interaction of an ion beam with a magnetized plasma in an ECR-based charge breeding device. *Plasma Sourc Sci Technol* (2016) 25:045007. doi:10.1088/0963-0252/25/4/045007

13. Galatà A, Mascali D, Gallo CS, Torrisi G. Self-consistent modeling of beam-plasma interaction in the charge breeding optimization process. *Rev Scientific Instr* (2020) 91:013506. doi:10.1063/1.5130704

14. Galatà A, Mascali D, Neri L, Torrisi G, Celona L. A three-dimensional numerical modelling of the phoenix-spes charge breeder based on the Langevin formalism. *Rev Scientific Instr* (2016) 87:02B507. doi:10.1063/1.4935010

15. Galatà A, Mascali D, Torrisi G, Neri L, Celona L, Angot J. Influence of the injected beam parameters on the capture efficiency of an electron cyclotron resonance based charge breeder. *Phys Rev Accel Beams* (2017) 20:063401. doi:10.1103/PhysRevAccelBeams.20.063401

16. Mishra B, Pidatella A, Biri S, Galatà A, Naselli E, Rácz R, et al. A novel numerical tool to study electron energy distribution functions of spatially anisotropic and non-homogeneous ecr plasmas. *Phys Plasmas* (2021) 28:102509. doi:10.1063/5.0061368

17. Birdsall C, Langdon A. Plasma Physics via computer simulation. *Series in plasma physics and fluid dynamics*. Taylor & Francis (2004).

18. Manheimer WM, Lampe M, Joyce G. Langevin representation of coulomb collisions in pic simulations. *J Comput Phys* (1997) 138:563–84. doi:10.1006/jcph.1997.5834

19. MacDonald WM, Rosenbluth MN, Chuck W. Relaxation of a system of particles with coulomb interactions. *Phys Rev* (1957) 107:350–3. doi:10.1103/PhysRev.107.350

20. Zenitani S, Umeda T. On the boris solver in particle-in-cell simulation. *Phys Plasmas* (2018) 25:112110. doi:10.1063/1.5051077

21. Ivanov A, Wiesemann K. Ion confinement in electron cyclotron resonance ion sources (ecris): Importance of nonlinear plasma-wave interaction. *IEEE Trans Plasma Sci IEEE Nucl Plasma Sci Soc* (2005) 33:1743–62. doi:10.1109/TPS.2005.860078

frontiers | Frontiers in Physics

TYPE Original Research
PUBLISHED 03 October 2022
DOI 10.3389/fphy.2022.932448

OPEN ACCESS

EDITED BY
Paul Stevenson,
University of Surrey, United Kingdom

REVIEWED BY
Theocharis S. Kosmas,
University of Ioannina, Greece
Shixiang Peng,
Peking University, China

*CORRESPONDENCE
Bharat Mishra,
mishra@lns.infn.it

SPECIALTY SECTION
This article was submitted to Nuclear Physics,
a section of the journal
Frontiers in Physics

RECEIVED 29 April 2022
ACCEPTED 05 September 2022
PUBLISHED 03 October 2022

CITATION
Mishra B, Galatà A, Pidatella A, Biri S, Mauro GS, Naselli E, Rácz R, Torrisi G and Mascali D (2022), Modeling space-resolved ion dynamics in ECR plasmas for predicting in-plasma β-decay rates. *Front. Phys.* 10:932448.
doi: 10.3389/fphy.2022.932448

Modeling space-resolved ion dynamics in ECR plasmas for predicting in-plasma β-decay rates

Bharat Mishra[1,2]*, Alessio Galatà [3], Angelo Pidatella [1], Sándor Biri [4], Giorgio Sebastiano Mauro [1], Eugenia Naselli [1], Richárd Rácz [4], Giuseppe Torrisi [1] and David Mascali [1]

[1]Laboratori Nazionali del Sud, Istituto Nazionale di Fisica Nucleare, Catania, Italy, [2]Dipartimento di Fisica e Astronomia "Ettore Majorana", Università degli Studi di Catania, Catania, Italy, [3]Laboratori Nazionali di Legnaro, Istituto Nazionale di Fisica Nucleare, Legnaro, Italy, [4]Institute for Nuclear Research (ATOMKI), Debrecen, Hungary

Lifetimes of radioactive nuclei are known to be affected by the level configurations of their respective atomic shells. Immersing such isotopes in environments composed of energetic charged particles such as stellar plasmas can result in β-decay rates orders of magnitude different from those measured terrestrially. Accurate knowledge of the relation between plasma parameters and nuclear decay rates are essential for reducing uncertainties in present nucleosynthesis models, and this is precisely the aim of the PANDORA experiment. Currently, experimental evidence is available for fully stripped ions in storage rings alone, but the full effect of a charge state distribution (CSD) as exists in plasmas is only modeled theoretically. PANDORA aims to be the first to verify these models by measuring the β-decay rates of select isotopes embedded in electron cyclotron resonance (ECR) plasmas. For this purpose, it is necessary to consider the spatial inhomogeneity and anisotropy of plasma ion properties as well as the non-local thermodynamic equilibrium (NLTE) nature of the system. We present here a 3D ion dynamics model combining a quasi-stationary particle-in-cell (PIC) code to track the motion of macroparticles in a pre-simulated electron cloud while simultaneously using a Monte Carlo (MC) routine to check for relevant reactions describing the ion population kinetics. The simulation scheme is robust, comprehensive, makes few assumptions about the state of the plasma, and can be extended to include more detailed physics. We describe the first results on the 3D variation of CSD of ions both confined and lost from the ECR trap, as obtained from the application of the method to light nuclei. The work culminates in some perspectives and outlooks on code optimization, with a potential to be a powerful tool not only in the application of ECR plasmas but for fundamental studies of the device itself.

KEYWORDS

ECR plasma, ion CSD, PIC code, β-decay rates, MC routines, magnetic confinement, double layer

1 Introduction

Electron cyclotron resonance ion sources (ECRIS) have long been used as reliable devices supplying ion beams to particle accelerators with charge states and currents tuned as per experimental requirements [1]. Their working principle involves sequential ionization of atoms through collision with electrons which are energized using resonance heating and trapped long enough through magnetic confinement. By varying the frequency of the microwave radiation used for heating, as well as associated power, magnetic field profile and gas pressure, the charge state distribution (CSD) of the ions and output current can be tuned [2].

Coincidentally, the existence of a CSD in the ECR plasma interior is a doorway to performing in-plasma measurement of nuclear β-decay rates to emulate astrophysical scenarios. Decay lifetimes can vary according to the configuration of the surrounding atomic shell [3, 4] and such a modification has already been experimentally observed in fully stripped ions circulating in storage rings [5]. The PANDORA (Plasmas for Astrophysics, Nuclear Decay Observations, and Radiation for Archaeometry) facility aims to take this a step further and analyze the CSD-dependent $t_{1/2}$ of radioisotopes [6] based on the theory of perturbed decay rates in stellar environments [7]. For each standard β^- decay—continuum decay (cd), bound-state decay (bd), electron capture (ec), and continuum capture (cc)—there exists an associated Q-value which governs the reaction spontaneity.

$$Q_0 = \begin{cases} m_0\left({}^{\mathrm{A}}_{\mathrm{Z}}\mathrm{X_N}\right)c^2 - m_0\left({}^{\mathrm{A}}_{\mathrm{Z+1/Z-1}}\mathrm{Y_{N-1/N+1}}\right)c^2 & (\mathrm{cd, bd, ec}) \\ m_0\left({}^{\mathrm{A}}_{\mathrm{Z}}\mathrm{X_N}\right)c^2 - m_0\left({}^{\mathrm{A}}_{\mathrm{Z+1/Z-1}}\mathrm{Y_{N-1/N+1}}\right)c^2 + K_{e^-_f} & (\mathrm{cc}) \end{cases}. \tag{1}$$

Here, $m_0(X)c^2$ and $m_0(Y)c^2$ represent, respectively, the rest mass energy of the parent and daughter system, while $K_{e^-_f}$ is the kinetic energy of free electron captured from the continuum. When the parent atom is ionized or excited, the decay energetics may be modified as

$$Q_{i,j} = Q_0 + \left(E^*_{X,K} - E^*_{Y,K'}\right) + \left(\epsilon^{i,j} - \epsilon^{i',j'}\right) + (\Delta_X - \Delta_Y), \tag{2}$$

where $E^*_{X,K}$, $E^*_{Y,K'}$ are the energies of the two nuclei in levels K and K', $\epsilon^{i,j}$; $\epsilon^{i',j'}$ are the atomic energies of the parent (daughter) system in the i (i') charge state and j (j') atomic/ionic level, and Δ_X, Δ_Y are the contributions of the ionization potential depression from the surrounding charges. In case of decays with small Q_0 (~keV), the contribution of atomic levels can be strong enough to open up new decay channels or suppress existing ones. For any transition $K \rightarrow K'$, the decay half-life $t_{1/2}$ can be related to nuclear properties through the expression.

$$f_{K\rightarrow K'(m)}t_{1/2} = \frac{(\ln 2)2\pi^3\hbar^7}{g^2m_e^5c^4|M^{L(m)}_{K\rightarrow K'}|^2}, \tag{3}$$

where $|M_{K\rightarrow K'}|$ is the nuclear matrix element (NME) describing the coupling between the initial and final nuclear states, $f_{K\rightarrow K'(m)}$ is the lepton phase volume, m is the type of decay (allowed, unique forbidden, or non-unique forbidden) related to the angular momentum of the transition $L(m)$, and g is the weak interaction coupling constant. The RHS of Eq. 3 is atom-independent, making $f_{K\rightarrow K'}$ the chief quantity of interest when investigating the change in $t_{1/2}$. In the presence of a CSD, and by extension a level population distribution (LPD), the lepton phase volume can be calculated as

$$f^*_{K\rightarrow K'(m)} = \begin{cases} \sum_{i,j} p_{i,j}\int_1^{W_{\max(i,j)}} (W^2-1)^{1/2}W\left(W_{max\,(i,j)} - W\right)^2 F_0S_{(m)}(i,j)f_d(i,j)\mathrm{d}W & (\mathrm{cd}) \\ \sum_{i,j} p_{i,j}\int_{W_{\min(i,j)}}^{\infty} (W^2-1)^{1/2}W\left(Q_{i,j}/m_ec^2\right)^2 F_0S_{(m)}(i,j)f_c(i,j)\mathrm{d}W & (\mathrm{cc}) \\ \sum_{i,j} p_{i,j}\sum_{x\,(i,j)} \sigma_x\frac{\pi}{2}[g_x \text{ or } f_x]^2\left(Q_{i,j}/m_ec^2\right)S_{(m)x\,(i,j)} & (\mathrm{bc, bd}) \end{cases}, \tag{4}$$

and the modified decay rate λ given as

$$\lambda = \frac{\ln 2}{f_{K\rightarrow K'(m)}t_{1/2}}\sum f^*_{K\rightarrow K'(m)}. \tag{5}$$

The summation in Eq. 5 accounts for the contribution of multiple decay channels to the overall rate. In Eq. 4, $p_{i,j}$ stands for the occupation probability of the charge state i and level j, $W_{\max\,/\,\min(i,j)}$ are functions of $Q_{i,j}$, F_0 is the Fermi function, $S_{(m)}(i,j)$ and $S_{(m)x(i,j)}$ are shape factors associated to the momentum transfer, $f_{c/d}(i,j)$ are related to the relativistic Fermi–Dirac distribution function describing the continuum electrons, $x(i,j)$ represents the electronic levels within the atomic configuration j, σ_x is the probability of electron occupation/vacancy in that level and g_x/f_x is the maximum of the orbital radial wavefunction evaluated at the nuclear surface. It is quite evident then that calculating in-plasma decay rates requires inputs on the LPD and CSD of the plasma ions, as well as on the electron energy distribution function. Acquiring such data is a complicated process because ECR plasmas are inherently anisotropic and non-homogeneous, host multi-component electron distributions, and obey non local thermodynamic equilibrium. This calls for robust simulation tools capable of extracting spatially resolved information on charged particle properties, and associated comprehensive diagnostic methods to experimentally benchmark their results.

Over the past years, several research groups have tackled the aforementioned problem from different angles—a separate section has been devoted to discussing their methodologies and subsequent results. The INFN-LNS and LNL groups have also contributed to ECRIS simulations by developing a self-consistent model coupling electron dynamics with an EM field solver to obtain 3D space-resolved maps of electron density and energy and reproduced some well-known ECRIS phenomena like the frequency tuning effect and heavy ion charge breeding [8, 9]. These steady-state electron maps can now be used as a base to arrive at the complementary, stationary ion maps containing CSD and LPD of the species of interest as a function of their position in the plasma. This article is intended to provide an outline of the 3D coupled ion

dynamics and population kinetics algorithm developed to achieve the aforementioned aim.

The contents of the article are divided into eight subsequent sections as follows: in Section 2, an in-depth review of ECRIS simulation tools is presented, followed by Section 3 wherein a brief description of the self-consistent MATLAB©-COMSOL Multiphysics© simulation scheme used to obtain 3D maps of electron density and energy is provided. This is extended to cover the ion dynamics algorithm in Section 4. The important modules of the algorithm, namely, the particle pusher code, Monte Carlo (MC) sampling scheme, density scaling methodology, and electrostatic field evaluation are covered in detail in Sections 5–7 respectively. The complete code flow is detailed in Section 8 while the results of the simulation for a specific plasma configuration and select operating conditions are shown in Section 9 and compared with experimental data for benchmarking. Finally, important takeaways from the procedure are presented in Section 10, as well as perspectives for future work.

2 ECR simulation models: A review

Research into ECRIS simulation has been underway since the early 1990s, with most groups focusing on the dominant electrons. Heinen and coworkers developed codes to track the motion of electrons under the effect of the ECR magnetostatic field with and without collisions and included resonance heating from single-mode microwaves. They obtained insights into the 3D profiles of electron density and energy and used the results to explain well-known phenomena such as the afterglow effect, and established a connection between localization of electron energies and production of highly charged ions [10, 11]. A similar approach was also followed by Maunoury *et al* who used the TrapCAD code to investigate the properties of lost and confined electrons and indirectly inferred ion properties [12]. This code was developed by Vámosi and Biri in the 1990s, with the objective to calculate and visualize the magnetostatic field of the ECR trap and follow the paths of charged particles [13]. Analysis of electron population through relativistic particle-in-cell (PIC) simulations was also conducted by Dougar-Jabon, Umnov and Diaz [14] who found specific zones of periodic bounce oscillations and banana trajectories as well as multiple electron populations.

The first algorithms aimed at coupling electrons and ions were developed by Edgell and group, and implemented in progressively advanced versions of the GEM code. They used the Fokker–Planck equation with ECR heating to obtain the electron distribution in phase space and gave it as input to detailed density and power balance fluid equations that described the collisional ions. The codes were initially 0D [15] but later upgraded to model 1D axial transport as well [16] and successfully predicted the extracted ion CSD. The 1D nature of the code was, however, quite limiting, and applicable to only the plasma core from which ion loss is modeled.

Cluggish, Kim, and Zhao later used the 1D GEM code to open investigations into the effect of pressure and microwave power on plasma parameters such as total electron density, energy, and current. They deduced some scaling laws which were in general agreement with experiments performed on different ion sources [17]. They realized the importance of studying the feedback of the plasma on the wave propagation and absorption and developed a quantitative 1D model and qualitative 3D model to describe the RF-plasma coupling based on the hot electron approximation [18]. The idea and implementation were robust in 1D but lacked completeness in 3D owing to the absence of a full dielectric tensor. Additionally, both works were centered on the electrons and ion properties were inferred on a macroscopic scale.

The most rigorous and complete treatment of ECR plasmas in terms of electrons, ions, and microwaves has been performed by Mironov and coworkers starting from 2009. In contrast to the methodologies utilized by other groups, they began by focusing directly on the ion dynamics using a particle-in-cell Monte Carlo collision (PIC-MCC) model, taking electron energy distribution function as isotropic and uniform [19]. They simulated the motion of macroparticles under a min-B field assuming collisions, implemented atomic processes such as ionization and recombination in real time, and took into account the constant influx of neutrals to replenish extracted charges just like in a real ECRIS. As a consequence, they obtained a great degree of match between predicted and measured steady-state CSD and were able to analyze various aspects of ECRIS operation such as neutral density gradient and isotope anomaly effect. In later works, they extended their analysis to include multi-component, localized electron energy distribution functions and investigated the ion confinement processes in the plasma [20] and then applied their algorithms to investigate the behavior of the device with different working materials [21]. The local neutrality assumption was dropped by coupling an electron simulation code NAM-ECRIS(e) with its ion counterpart NAM-ECRIS(i), effectively modeling electron and ion evolution simultaneously in the plasma [22]. The final upgrade came in the form of RF-electron coupling in NAM-ECRIS(e) using the cold electron approximation on the ECR surface [23].

The simulation scheme reported in this work is complementary to the approach of Mironov and group in that it also aims to investigate ECR plasmas as a whole by appropriately extending the electron simulation module to the ions. While their method captures temporal evolution of the system in real time, we instead focus on developing suitable models to represent steady-state conditions. It can be argued that the latter is merely a special case of the former, but it gives us the advantage to model RF-electron coupling with a high degree of precision while still capturing the essence of ion dynamics. The

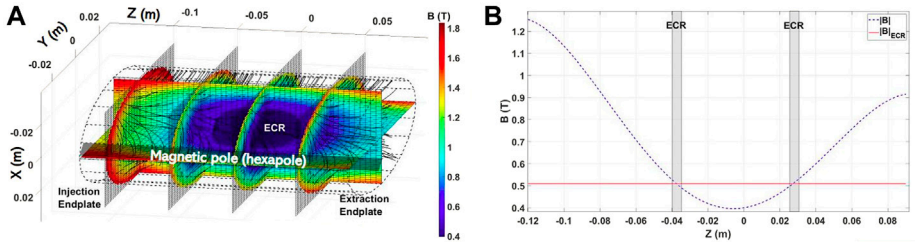

FIGURE 1
(A) 3D profile of magnitude of the magnetostatic field superposed with streamlines showing field flow and ECR surface, **(B)** 1D on-axis field profile with demarcated ECR zones. The min-B structure of the field can be clearly appreciated.

details of this methodology are presented in the following sections.

3 Self-consistent electron simulations under cold electron approximation

The importance of electrons in ECRIS has been well-established through the numerous works reported in Section 2. Mascali *et al* also realized the necessity to treat the plasma chamber as a resonant cavity to improve understanding of both electron and ion dynamics. They developed a hybrid model simulating electrons using a PIC code and ions using MC collisions, taking into account resonance heating from the standing-wave profile of microwaves in the resonant cavity. They reproduced the experimental beam shape and predicted the formation of the plasmoid-halo structure [24]. Some enhancements to the electron PIC module were later made by Neri *et al* who implemented Spitzer collisions and studied the effect of RF heating on electron confinement [25].

The simplest of ECRIS devices are operated with a peculiar magnetostatic field profile called the min-B structure as shown in Figure 1 which enables electron confinement along the axis. The electrons naturally gyrate about the magnetic field lines at their cyclotron frequency $\omega_c = e|\mathbf{B}|/m_e$ where e is the electric charge, $|\mathbf{B}|$ is the field magnitude, and m_e is the mass of the electron. Depending on the position, the field may be such that ω_c matches the frequency of the circularly polarized microwave launched into the plasma, leading to resonance heating. On account of magnetic and diffusion transport, the distribution of electrons in the plasma quickly becomes non-homogeneous and anisotropic, directly affecting the dielectric tensor of the medium and therefore the EM field profile. As mentioned in Section 2, the feedback of the plasma to the wave propagation was already calculated in [18] but using the hot electrons which made it necessary to replace the dielectric tensor with a constant. Torrisi *et al* revisited the subject to perform FEM calculations to deduce the field profile in magnetized plasmas using the cold electron approximation instead [26] leading to a more complete yet still precise formulation of RF-electron coupling since cold electrons constitute a majority of the plasma.

Based on their algorithm and results, Mascali *et al* developed an electron kinetics model to solve the collisional Vlasov–Maxwell and Fokker–Planck equation using a large number of representative macroparticles [9]. The idea was to tackle the wave–plasma coupling in a self-consistent manner by iteratively calculating the EM field distribution using COMSOL Multiphysics © based on the cold tensor approximation in the plasma, and then pushing the electrons using a particle mover code written in MATLAB © according to the Lorentz force including the newly generated EM field. By constantly accumulating macroparticle traces in cells of a 3D matrix, they obtained relevant occupation maps and used them to update the dielectric tensor, repeating all the steps till self-consistency between the electron maps and the EM field was achieved. In the end, one obtained 3D space-resolved maps of electron density and energy corresponding to the ECR plasma at steady-state, in the form of 3D MATLAB © matrices. Figure 2 shows the density and energy maps of electrons simulated in an Ar plasma operated at frequency 14.28 GHz and power 200 W. These maps will serve as the source of electron-driven reactions included in the ion dynamics model described in the following section. The simulation model is currently being upgraded and the details can be found in [27].

4 Coupled ion dynamics and population kinetics

The standard approach to model ion population kinetics is to start from the density balance equation.

$$\frac{dn_i}{dt} = \sum_{j \neq i} n_j G_{ji} - \sum_{i \neq j} n_i L_{ij} - \frac{n_i}{\tau_i}, \tag{6}$$

where $n_{i,j}$ are level populations of states i and j, G_{ji} and L_{ij} represent inter-level gain and loss rates, respectively, and τ_i is the characteristic confinement time. On extending Eq. 6 to include all levels and collision-radiative processes, a rate matrix $\mathbf{R}$ can be constructed and Eq. 6 can be reduced to $\frac{d\mathbf{n}}{dt} = \mathbf{R} \cdot \mathbf{n}$. Generally, Eq.

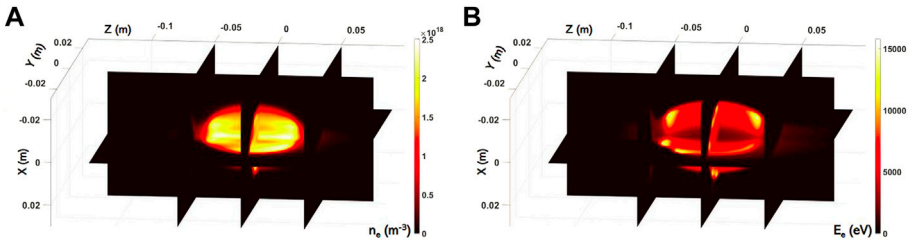

FIGURE 2
(A) 3D profile of simulated electron density (in m^{-3}) and, **(B)** electron energy (in eV).

6 is further simplified in ECR plasmas by considering only three important processes—electron collision ionization, charge exchange through collision with neutrals, and ion transport [15, 28]. The resultant balance equation is then

$$\frac{dn_i}{dt} = n_e n_{i-1}\langle\sigma_{ion,i-1\to i}v_e\rangle - n_e n_i\langle\sigma_{ion,i\to i+1}v_e\rangle + n_0 n_{i+1}\langle\sigma_{CEX,i+1\to i}v_i\rangle - n_0 n_i\langle\sigma_{CEX,i\to i-1}v_i\rangle - \frac{n_i}{\tau_i}, \quad (7)$$

where n_e is the electron density, $n_{i/i-1/i+1}$ represents the ion density in charge state $i/i-1/i+1$, σ_{ion} is electron collision ionization cross section, v_e is the electron speed, σ_{CEX} is charge exchange cross section, and v_i represents the ion collision speed. Although Eq. 7 is complicated enough in 0D, it is quite impossible to solve in 3D wherein the densities and energies of the interacting species vary spatially and particle transport takes place simultaneously with reactions.

We decided to adapt Eq. 7 to the established electron the PIC code mentioned in Sec. 3 to calculate steady-state ion maps [29]. The idea was to generate N macroparticles in the i^+ state obtained from the $(i-1)^+$ state (first term in Eq. 7) and track their evolution over a fixed time T_{span} discretized into a number of steps T_{step}. At each step, ionization to the $(i+1)^+$ state and exchange into the $(i-1)^+$ state would be evaluated according to their respective reaction probabilities (second and fourth terms in Eq. 7), resembling the rate matrix method. Charge exchange to the $(i+1)^+$ state (third term in Eq. 7) is ignored in this model. The remaining unperturbed macroparticles would be moved according to the equation of motion under the action of the Lorentz force $F_{L,i} = eq_i(\mathbf{E_{DL}} + \mathbf{v}_i \times \mathbf{B})$ and the Langevin formula, with q_i being the charge state of the macroparticle and $\mathbf{v}_i$ its velocity. The quantity $\mathbf{E_{DL}}$ represents the electrostatic field arising from the double layer in the plasma whose origin and importance are discussed in detail in Section 7. During the course of their motion, the macroparticle tracks would be mapped to a 3D occupation matrix n_i in much the same way as for electrons, until their eventual loss from the plasma (last term in Eq. 7). The ionized/exchanged particle positions would instead be added to corresponding ionization/exchange matrices, $n_{i\to i+1}$ and $n_{i\to i-1}$. At the end of the simulation, the occupation, ionization, and exchange maps would be passed to the next charge state as inputs, and all the steps repeated. The results of each preceding simulation would be embedded into the successive one. If the reaction rates are implemented correctly, the confined macroparticle tracks and relative weight of state calculated according to reaction-mediated transfer would ultimately lead to a CSD map consistent with the fixed electron distribution. A summary of the simulation scheme is shown in Figure 3.

The key elements of this algorithm are the ion transport model, MC population kinetics, density scaling, and double layer field calculation. The subsequent sections contain more comprehensive discussions on these topics. The simulation scheme was configured for the ATOMKI, Debrecen ECR plasma trap for the same operating conditions as the electron maps in Figure 2 (14.25 GHz frequency, 200 W power, and 10^{-6} mbar pressure) using Ar plasma and thus all discussions hereafter will take place assuming such a plasma.

5 Particle pusher algorithm: Ion transport

The motion of charged particles in a plasma is a notoriously difficult problem to tackle because unlike neutral atoms in a rarified gas which mostly travel in straight lines before stochastic collisions, plasma charges are subject to both long-range EM forces as well as short-range random collisions. The former, additionally, can arise from both internal as well as external fields, such as the magnetostatic field applied in ECR plasmas. The result of these forces is that ions and electrons in plasma gyrate along magnetic field lines while being simultaneously subject to continuous and infinitesimal perturbations in their trajectory on account of internal EM fields [30] while also getting randomly kicked due to head-on collisions with fellow constituents. The PIC simulations for electrons as described in Section 3 already addressed this complexity, allowing direct

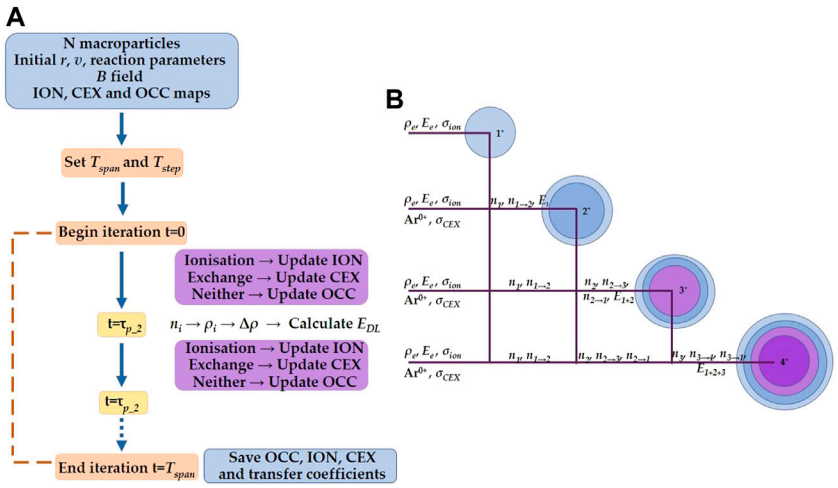

FIGURE 3
(A) Flowchart portraying the various inputs, outputs and steps in the simulation of a single charge state i^+. **ION**, **OCC,** and **CEX** refer to ionization, occupation, and charge exchange matrices, respectively. **(B)** Overall network of simulation schemes showing flow of data between successive charge states. Ar^{0+} represents neutral Ar atoms since the simulations were run for such plasmas.

adaptation to the ion dynamics scheme. In the presence of electric and magnetic fields, the equations of motion of a charged particle can be analytically written as

$$\frac{\mathrm{d}\mathbf{r}}{\mathrm{d}t} = \mathbf{v}, \tag{8}$$

$$m\frac{\mathrm{d}\mathbf{v}}{\mathrm{d}t} = q(\mathbf{E} + \mathbf{v} \times \mathbf{B}), \tag{9}$$

where $\mathbf{r}$ and $\mathbf{v}$ are the position and velocity of the particle, respectively, q is the charge, m is the mass, $\mathbf{E}$ and $\mathbf{B}$ are the electric and magnetic field, respectively, and the RHS of Eq. 9 is the Lorentz force. Numerical implementation of the same has been traditionally performed with the Boris method [31] which solves the particle motion in a leapfrog manner and breaks down the acceleration into a number of steps.

$$\frac{\mathbf{r}^{n+1} - \mathbf{r}^{n}}{T_{step}} = \mathbf{v}^{n+1/2}, \tag{10}$$

$$\mathbf{u}^{-} = \gamma\mathbf{v}^{n+1/2} + \frac{q}{2m}\mathbf{E}^{n+1}T_{step}, \tag{11}$$

$$\theta = \frac{qT_{step}}{m\gamma}|\mathbf{B}^{n+1}|, \tag{12}$$

$$\mathbf{t} = \tan\frac{\theta}{2}\mathbf{b}, \tag{13}$$

$$\mathbf{u}' = \mathbf{u}^{-} + \mathbf{u}^{-} \times \mathbf{t}, \tag{14}$$

$$\mathbf{u}^{+} = \mathbf{u}^{-} + \frac{1}{2 + |\mathbf{t}|^2}(\mathbf{u}' \times \mathbf{t}), \tag{15}$$

$$\mathbf{v}^{n+3/2} = \frac{1}{\gamma}\left(\mathbf{u}^{+} + \frac{q}{2m}\mathbf{E}^{n+1}T_{step}\right). \tag{16}$$

Here, $\gamma = [1 - (|\mathbf{v}|^2/c^2)]^{-1/2}$ denotes the known Lorentz factor, n is the index tracking the leapfrog procedure, $\mathbf{b} = \mathbf{B}^{n+1}/|\mathbf{B}^{n+1}|$ is the unit vector of the magnetostatic field, and T_{step} is the discrete time interval. To save on computational time, most groups apply Eq. 13 in the "small θ" limit such that the tangent is replaced by its argument. Although this is a good approximation, the gyrophase error tends to accumulate if the number of iterations is large, which is precisely the case here. As such, a modified form of the Boris solver was used for the ion transport which is analytically exact and relatively time-saving [32]. According to the formalism, Eqs 13–15 were replaced with a rotation matrix R_{rot} such that

$$\mathbf{u}^{+} = R_{rot}\mathbf{u}^{-}, \tag{17}$$

and R_{rot} is defined as

$$R_{rot} = \begin{pmatrix} \cos\theta + b_x^2(1-\cos\theta) & b_xb_y(1-\cos\theta) + b_z\sin\theta & b_zb_x(1-\cos\theta) - b_y\sin\theta \\ b_xb_y(1-\cos\theta) - b_z\sin\theta & \cos\theta + b_y^2(1-\cos\theta) & b_yb_z(1-\cos\theta) + b_x\sin\theta \\ b_xb_z(1-\cos\theta) + b_y\sin\theta & b_yb_z(1-\cos\theta) - b_x\sin\theta & \cos\theta + b_z^2(1-\cos\theta) \end{pmatrix}, \tag{18}$$

The evolution of phase space of a test particle in a plasma due to long- and short-range collisions is usually modeled by the Fokker–Planck equation and simplified using the formalism of McDonald and Rosenbluth [33]. Further reduction is made possible by assuming the species of interest as test particles moving through a field composed of other plasma constituents. The previously mentioned procedure yields two important quantities at the end—friction frequency ν_s and diffusion coefficients $D_{\parallel}$, $D_{\perp}$ which, respectively, correspond to the continuous drag force motion and the head-on collisions. The PIC electron simulations adapted the Fokker–Planck equation to macroparticle formalism by using ν_s, $D_{\parallel}$, and $D_{\perp}$, in the Langevin equation which is identical to the former to first order accuracy in

T_{step}. The theory has been rigorously discussed in [34]. Taking, at any point in time, a surrounding total plasma density n_s with particle mass m_s, atomic number Z' , and most probable thermal speed as c_s, the friction and diffusion coefficients are obtained as

$$D_{\parallel} = \langle \mathbf{v}_{\parallel}^2 \rangle = \frac{A_D}{|\mathbf{v}^{n+1/2}|} G\left(\frac{|\mathbf{v}^{n+1/2}|}{c_s}\right), \tag{19}$$

$$D_{\perp} = \langle \mathbf{v}_{\perp}^2 \rangle = \frac{A_D}{|\mathbf{v}^{n+1/2}|} \left\{ \Phi\left(\frac{|\mathbf{v}^{n+1/2}|}{c_s}\right) - G\left(\frac{|\mathbf{v}^{n+1/2}|}{c_s}\right) \right\}, \tag{20}$$

$$\nu_s = \left(1 + \frac{m}{m_s}\right) \frac{A_D}{c_s^3} \frac{G\left(\frac{|\mathbf{v}^{n+1/2}|}{c_s}\right)}{\frac{|\mathbf{v}^{n+1/2}|}{c_s}}, \tag{21}$$

where

$$A_D = \frac{(ZZ')^2 e^4 n_s \ln \Lambda}{2\pi \epsilon_0^2 m^2}, \tag{22}$$

$\Phi(x)$ is the error function and $G(x) = [\Phi(x) - \Phi'(x)]/2x^2$. Z represents the atomic number of the test particle while $\ln \lambda$ is the Coulomb logarithm. Using these coefficients, contributions to velocity of the test particles were calculated as

$$\mathbf{v}_{fric} = \nu_s \mathbf{v}^{n+1/2} T_{step}, \tag{23}$$

$$\mathbf{v}_{rand} = P_{\parallel} N\left(0, D_{\parallel}\right) + P_{\perp} N\left(0, D_{\perp}\right), \tag{24}$$

where $N(0, D_{\parallel})$, $N(0, D_{\perp})$ indicate random sampling from a normal distribution with mean 0 and standard deviation as given by the diffusion coefficients, while $P_{\parallel}$, $P_{\perp}$ are projection matrices mapping the parallel and perpendicular components to the basis vector of the velocity. The final expression to advance the velocity was then

$$\mathbf{v}^{n+3/2} = \frac{1}{\gamma}\left(\mathbf{u}^{+} + \frac{q}{2m}\mathbf{E}^{n+1} T_{step}\right) + \mathbf{v}_{fric} + \mathbf{v}_{rand}. \tag{25}$$

The motion of ions in the plasma was fully realized through Eqs. 10–12, 17, and 25.

6 Generalized Monte Carlo routine: Population kinetics

The density and temperatures of ECR plasmas are such that the various constituents of the system obey non local thermodynamic equilibrium, meaning ion LPD and CSD cannot be described analytically using the Boltzmann and Saha equations, respectively. Instead, one needs to apply the general collision–radiative model using the rate matrix formalism as described in Eq. 6, and take into account a multitude of reactions and levels to construct the differential equation. The model accuracy is directly correlated with the amount of physics considered because of the following reasons.

1) The reaction rates govern the percentage transfer of macroparticles within charge states and ionic levels thus defining the relative weights of each charge in the overall CSD
2) The ion transport and occupation map rely on the self-generated plasma density n_s (Section 5) and consequently, on the weights of the various charge states.

As such, while one may be limited by the availability of data on reaction cross sections or atomic levels, it is nevertheless a good idea to develop a generalized algorithm to model the population kinetics which can be later expanded to include as many levels and reactions as needed. This is particularly important not just for modeling the CSD and LPD in the plasma, but also for the β-decay model in [7].

In keeping with the simplified balance equation in Eq. 7, electron collision ionization and charge exchange after collision with neutral Ar atoms were the only reactions considered. The analytical formula for single ionization $i \rightarrow i + 1$ is given as

$$\sigma_{ion,i\rightarrow i+1} = \frac{10^{-17}}{I_i E_e}\left[\sum_{n=1}^{6} A_n \left(1 - \frac{I_i}{E_e}\right)^n + B \ln\left(\frac{E_e}{I_i}\right)\right], \tag{26}$$

where $\sigma_{ion,i\rightarrow i+1}$ is the ionization cross section in m^2, I_i and E_e are the ionization energies of the charge state indexed by i and electron collision energy (in eV), respectively, and A_n, B are the fitting coefficients which vary with i. The expression, as well as the values of the coefficients, is detailed in [35].

The charge exchange cross section for the transition $i \rightarrow i - 1$ was taken from the works of Müller and Salzborn [36] and given as

$$\sigma_{CEX,i\rightarrow i-1} = A i^{\alpha} (I_0)^{\beta}, \tag{27}$$

where σ_{CEX} is the exchange cross section in m^2; A, α, and β are fit coefficients; and I_0 is the ionization energy of the $0^+ \rightarrow 1^+$ transition of Ar which acts as the "target" in this reaction. The values of the fit coefficients are taken as $A = 1.43 \times 10^{-17}$, $\alpha = 1.17$, and $\beta = 2.76$.

In order to reconcile the rate matrix formalism with macroparticles in a PIC algorithm, the reaction rate was replaced with the reaction frequency ν calculated for the processes under consideration as

$$\nu_{ion} = n_e \sigma_{ion,i\rightarrow i+1} \nu_e, \tag{28}$$

$$\nu_{CEX} = n_0 \sigma_{CEX,i\rightarrow i-1} \nu_i, \tag{29}$$

where n_e and n_0 are the electron and neutral ion density, respectively, and ν_e and ν_i are the electron and ion collision velocity in CM frame of reference, respectively. Naturally, the higher the frequency, the more the probability of the reaction taking place in a given time interval. The interplay of collisional ionization and charge exchange in the context of ECR plasma ion population kinetics is shown in Figure 4. Exchange cross sections are independent of the ion energy below 25 keV/u (which is orders of magnitude higher than ECR ion energies) so the cross sections are reported in Figure 4A for each charge state

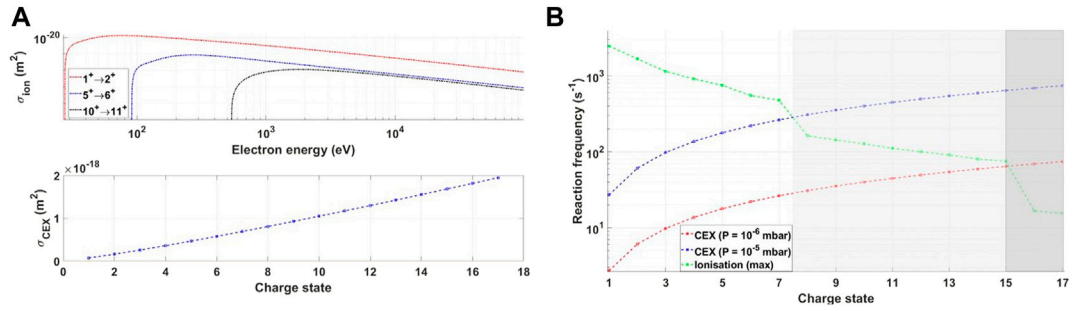

FIGURE 4
(A) Single ionization cross section as a function of electron collision energy for three different charge states of Ar ions (top) and charge exchange cross section for different charge states taking ion temperature k_BT = 0.5 eV (bottom) and **(B)** frequency of ionization under most optimum electron conditions and frequency of exchange for two different gas pressures as a function of charge state. The shaded area denotes the charge state after which CEX dominates over ionization, effectively lowering the plasma CSD.

following Eq. 27. The ionization cross sections are, instead, reported for a range of electron energies well into 100 keV, and it can be clearly seen that the values decrease with the increasing charge state and always remain below the exchange cross sections. On the other hand, converting σ into ν, it can be seen that high n_e and E_e initially drive up the reaction frequency for low-charge states (Figure 4B) but are soon overtaken by exchange reactions with the intersection charge state depending on the pressure of gas in the system. This is an important point because it implies that highly charged ions are shuffled into lower states, leading to an overall decrease in the mean charge of the plasma.

The main task at hand was to develop a MC routine that would allow expressing CEX, ionization or the lack of any reaction thereof as unique and mutually exclusive outcomes of a single "effective" collision marked by a summed reaction frequency $\nu_{tot} = \nu_{ion} + \nu_{CEX}$, so as to simplify and generalize the sampling procedure. The formalism was akin to modeling absorption by a material composed of two absorbers of coefficients, namely, μ_1 and μ_2. The transmission probability through such an element would be simply $T = e^{-(\mu_1+\mu_2)x}$ and the corresponding probability distribution function would then be $p_{abs} = (\mu_1 + \mu_2)e^{-(\mu_1+\mu_2)x}$. Hence in our case the probability distribution function is taken as

$$p_{tot}(t) = \nu_{tot} e^{-\nu_{tot} t}, \tag{30}$$

and thus in a given time interval T_{step}, the probabilities associated with no reaction and some reaction are

$$\bar{P}_{tot}\left(T_{step}\right) = \int_{T_{step}}^{\infty} \nu_{tot} e^{-\nu_{tot} t} dt = e^{-\nu_{tot} T_{step}}, \tag{31}$$

$$P_{tot}\left(T_{step}\right) = \int_{0}^{T_{step}} \nu_{tot} e^{-\nu_{tot} t} dt = 1 - e^{-\nu_{tot} T_{step}}. \tag{32}$$

Furthermore, the probabilities associated with ionization and CEX were derived from $P_{tot}(T_{step})$ as

$$\begin{aligned} P_{tot}\left(T_{step}\right) &= 1 - e^{-\nu_{tot} T_{step}} = \frac{\nu_{ion} + \nu_{CEX}}{\nu_{tot}} \left(1 - e^{-\nu_{tot} T_{step}}\right) \\ &= \frac{\nu_{ion}}{\nu_{tot}} \left(1 - e^{-\nu_{tot} T_{step}}\right) + \frac{\nu_{CEX}}{\nu_{tot}} \left(1 - e^{-\nu_{tot} T_{step}}\right). \\ &= P_{ion}\left(T_{step}\right) + P_{CEX}\left(T_{step}\right) \end{aligned} \tag{33}$$

This new formalism mapped the continuous probability distribution function to a discrete probability distribution with three outcomes which sum to 1 as expected. By sampling a *single* random number $r \in [0, 1]$, a decision was made between ionization, CEX, and nothing as

- Ionization if $0 <= r < P_{ion}$
- CEX if $P_{ion} <= r < (P_{ion} + P_{CEX})$
- Nothing if $(P_{ion} + P_{CEX}) <= r < 1$

The method is general in the sense that more the number of reactions considered, the more would be ν_{tot} and thus the smaller the probability of nothing happening. Meanwhile, the probability of individual reactions would vary depending on the weight $\frac{\nu_X}{\nu_{tot}}$. The method eliminated the need to implement sequential or conditional probabilities and allowed interpreting all possible outcomes, whether mutually exclusive or not originally, as "effectively" exclusive through integration into a single collision event.

The procedure is not without its demerits. As much as it simplifies the sampling, the reactions are not *truly* mutually exclusive. The source of each reaction is different physical systems and there is no rule that both reactions may not occur simultaneously or in rapid succession. The correct approach would be to devise a joint probability distribution function for a sequential application of the reaction probabilities which would require use of multiple sampling variables and/or more involved techniques such as Markov chains. The approximation proposed here can eliminate the problem of simultaneity as long as T_{step} is small enough such

that only one reaction may occur in that period. Even if the actual reactions are independent, this would enforce mutual exclusivity within the chosen interval. Coincidentally, this is precisely what one performs in a rate matrix algorithm—choose a time step Δt small enough that the populations of involved species changes slowly. This reduces the chances of cross-talk and hence errors in the final results. Numerically, this accounts for the discretization error when solving a differential equation. In our model, mutual exclusivity is naturally enforced because T_{step} is fixed to 10^{-10} s as a conservatively small percentage of the Larmor gyration time ($\sim 10^{-6}$ s) and characteristic reaction times in Figure 4 are 2–3 orders of magnitude higher.

7 Convergent density scaling and double layer field

As already mentioned in Sections 3, 4, the trajectories of macroparticles were used to update a 3D matrix that served as an occupation or accumulation map representative of the true physical density. For ions, devising a robust scaling procedure was of utmost importance because charge states were sequentially simulated and the relative weights of all preceding occupation maps were constantly changing. The objective was to allow the dynamic weights to converge to the real steady-state value and thus correctly reproduce the plasma CSD. For this, it was essential that the ion transport, and consequently the occupation maps, be modeled accurately.

Unlike in electron simulations, the ions moved in a self-generated field and thus the transport coefficients were only as precise as the total scaled density n_s. This interdependence between scaling and transport implied that a rapid and correct convergence of the weights of the various charge states could only occur if the occupation maps were scaled regularly enough. It was, thus, decided to extract the occupation maps at specific intervals before T_{span} was reached, denoted by the checkpoints τ_p in Section 4. This helped avoid over/underestimation of the contribution of the various charge states toward n_s while remaining relatively fast to execute. Initially, it was decided to set τ_p as 10% of the effective confinement time τ_d given as the inverse sum of characteristic diffusion and magnetic confinement times [37] but this greatly increased the number of extraction points. As such for the sake of this preliminary study, it was decided to set four checkpoints at τ_p as 1%, 10%, 70%, and 100% T_{span} for each charge simulation.

Density scaling also allowed adding the electrostatic field arising from the double layer potential into the ion transport model. At a steady state, ECR plasmas separate into an electron-rich ellipsoidal shell in the interior called the plasmoid and a rarified zone surrounding it called the halo. The boundary between them is the ECR surface containing fewer, but hotter, electrons than the plasmoid. Electrons diffusing out of the plasmoid are reflected back inside while ions continue entering the halo—this creates a space–charge separation. A layer of positive ions forms just outside the electron layer and the potential generated from the double layer balances the flow of charges to maintain global neutrality. The existence of the double layer and subsequent potential dip has been a matter of debate, with some experiments even pointing to its absence [38]. Even the first results from Mironov *et al* inferred the same [19] but later models confirmed their existence [22]. The double layer has been theoretically modeled by Mascali *et al* [37, 39] and even experimentally verified by Takahashi, Kaneko, and Hatakeyama [40]. Thus, a dedicated electrostatic model was developed in COMSOL Multiphysics © to calculate ϕ_{DL} and $\mathbf{E_{DL}}$ (as mentioned in Section 4) from the charge imbalance $\rho_\Delta = \rho_{tot} - \rho_e$ using the Poisson equation, where ρ_{tot} is the total positive charge density evaluated using the scaled ion occupation maps. The effect of the electrostatic field $\mathbf{E_{DL}}$ is shown in Figure 5 where the ratio of ion and electron accumulation within a region of interest (ROI) defined deep in the plasmoid is plotted for regular intervals. The ROI was chosen as the space between two ellipsoidal surfaces in the plasma interior. If the electrostatic field worked as expected, the ratio of scaled ion density and electron density N_i/n_e would converge to a constant value so that the charge flows would be equalized. Although this has not been fully achieved yet, the higher values in the presence of the field in Figure 5B point to the confining action.

The scaling procedure was based on global charge neutrality which posited that the total number of positive and negative charges in the plasma would be the same, even if there existed localized charge pockets. The simple and straightforward expression to convert any general occupation map n_i into the corresponding number density map N_i is

$$\oint_V n_e \mathrm{d}V = K_i q_i \oint_V n_i \mathrm{d}V, \tag{34}$$

$$N_i = K_i n_i, \tag{35}$$

where q_i is the charge state of the ion, K_i is the scaling factor, and the integrals represent volume integration. However at any checkpoint τ_p, there would be the additional presence of the ionization map $n_{i\to i+1}$ and pre-simulated occupation maps $n_1, \ldots, n_{i-1}$. Eqs 34, 35 were thus modified to account for $n_{i\to i+1}$ and n_{i-1} through coefficients representing the degree of ionization and exchange, respectively, and for other preceding occupation maps through weights emulating successive ionization from one charge state to the next. These are collectively referred to as transfer coefficients hereafter. As an example, at checkpoint τ_p for 1^+ ions, density scaling was implemented as

$$\oint_V n_e \mathrm{d}V = K_1 \left[(1 - k_{1\to 2}) \oint_V n_1 \mathrm{d}V + 2k_{1\to 2} \oint_V n_{1\to 2} \mathrm{d}V \right], \tag{36}$$

$$N_1 = K_1 (1 - k_{1\to 2}) n_1, \tag{37}$$

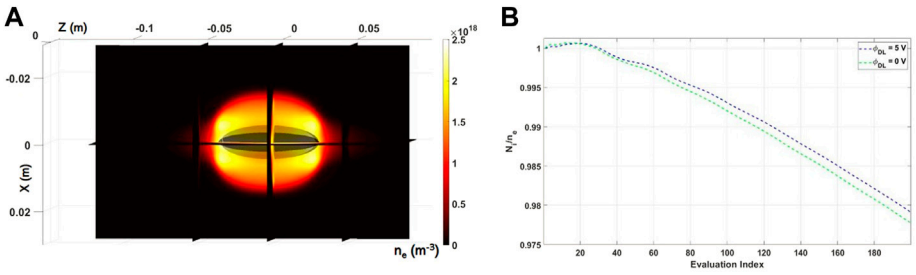

FIGURE 5
(A) Space between two centered and skewed ellipsoids in the plasmoid where ratio N_i/n_e was calculated as and **(B)** N_i/n_e in said space as evaluated at regular intervals with and without double layer $\mathbf{E}_{DL}$ field.

where $k_{1\to2} = \frac{\oint_V n_{1\to2}\mathrm{d}V}{N}$ and N is the initial number of macroparticles. The term in parenthesis indicates that the contribution of 1^+ to the overall positive charge in the plasma was reduced by $k_{1\to2}$ because this amount of macroparticles was ionized to the next charge state. As another example, at τ_p for the 3^+ simulations, density scaling resembled.

$$\begin{aligned}\oint_V n_e\mathrm{d}V = K_3\Big[&(1-k_{1\to2}+2k_{1\to2}k_{2\to1}+k_{1\to2}k_{2\to3}k_{3\to2})\oint_V n_1\mathrm{d}V+\\ &2k_{1\to2}(1-k_{2\to3}-k_{2\to1}+k_{2\to3}k_{3\to2})\oint_V n_2\mathrm{d}V+\\ &3k_{1\to2}k_{2\to3}(1-k_{3\to4}-k_{3\to2})\oint_V n_3\mathrm{d}V+\\ &4k_{1\to2}k_{2\to3}k_{3\to4}\oint_V n_{3\to4}\mathrm{d}V\Big]\end{aligned}, \tag{38}$$

$$N_1 = K_3(1-k_{1\to2}+2k_{1\to2}k_{2\to1}+k_{1\to2}k_{2\to3}k_{3\to2})n_1, \tag{39}$$

$$N_2 = K_3k_{1\to2}(1-k_{2\to3}-k_{2\to1}+k_{2\to3}k_{3\to2})n_2, \tag{40}$$

$$N_3 = K_3k_{1\to2}k_{2\to3}(1-k_{3\to4}-k_{3\to2})n_3, \tag{41}$$

where $k_{1\to2} = \frac{\oint_V n_{1\to2}\mathrm{d}V}{N}$, $k_{2\to3} = \frac{\oint_V n_{2\to3}\mathrm{d}V}{N}$, $k_{2\to1} = \frac{\oint_V n_{2\to1}\mathrm{d}V}{N}$, $k_{3\to4} = \frac{\oint_V n_{3\to4}\mathrm{d}V}{N}$, $k_{3\to2} = \frac{\oint_V n_{3\to2}\mathrm{d}V}{N}$ and N still represents the number of macroparticles. By regularly extracting simulated occupation and ionization maps and dynamically updating the transfer coefficients in the charge neutrality expressions Eqs. 36, 38, convergence toward true CSD was ensured. Additionally, keeping track of the transfer coefficients allowed simulating the same number of macropartices for each charge state while accurately gauging their contribution to the total positive charge, avoiding errors from low statistical counts in the process. The charge density was calculated from the number density as $\rho_i = eq_iN_i$ whereas the total plasma density for friction and diffusion coefficients was $n_s = \sum_i N_i$. Once ρ_i was obtained, it was used to calculate the imbalance $\rho_\Delta = \rho_{tot} - \rho_e = \sum_i \rho_i$ and passed to the electrostatic solver to evaluate 3D maps of double layer potential ϕ_{DL}. The raw ϕ_{DL} maps were peak normalized and scaled with a reasonable potential of 5 V [39] and the field components were re-evaluated using the gradient of the scalar field to obtain $\mathbf{E}_{DL}$. These were passed back to MATLAB © to perform the ion transport until the next extraction checkpoint.

8 Description of code flow

Based on the discussion in the preceding sections, the detailed algorithm is presented below for the first two charge states and can be extrapolated similarly for the remaining.

8.1 $1^+ \to 2^+$

- Initialization
  - Generate $N = 10^6$ macroparticles distributed throughout the plasma simulation domain. The initial positions would follow a pre-generated ionization map $n_{0\to1}$ while the velocities would be generated according a Maxwell distribution of temperature k_BT_i.
  - Use the electron density map ρ_e and energy density map E_e to calculate the ionization frequency for each plasma cell according to the expression $\nu_{ion} = \rho_e\sigma_{ion,1\to2}v_e$. Calculate plasma-averaged collision time $\langle\tau_{ion}\rangle$ and set the total simulation time $T_{span} = 10\langle\tau_{ion}\rangle$ during which full ionization of the particles would be achieved.
  - Define the magnetostatic field **B** configuration. Initialize occupation n_1 and ionization $n_{1\to2}$ maps to 0 with same dimensions as the plasma simulation domain ($59 \times 59 \times 211$, 1 mm^{-3} cell volume). Also, initialize the lost particle map to 0. Set iteration step time $T_{step} = 10^{-10}$ s to increase precision. The value can be optimized later for more efficient computation.
  - Set an estimate for the checkpoint τ_p at which the double layer field **E** should be evaluated. The importance of τ_p and evaluation method is discussed in Section 7.
- Evaluation

  - Check for occurrence of ionization at each cell according to ν_{ion}. If the macroparticle is ionized, map to ionization matrix $n_{1\to2}$. More details are given in Sec. 6.
  - Apply the equation of motion to the remaining 1^+ particles and update the position and velocity vectors. Check if the new position exceeds the plasma dimensions–if yes, update the lost particle matrix otherwise map the positions to the occupation map. The exact transport equations can be found in Section 5.
- Check extraction
  - If checkpoint τ_p is reached, scale the occupation map n_1 obtained so far to appropriate density ρ_1 and use the charge imbalance map $\rho_\Delta = \rho_{tot} - \rho_e = \rho_1 - \rho_e$ as input to COMSOL Multiphysics © to calculate the double layer potential ϕ_{DL} and the corresponding field $\mathbf{E_{DL}}$. Also, calculate the total plasma density N_s and mean charge $\langle Z\rangle$. More details on the methodology are presented in Section 7.
  - Give $\mathbf{E_{DL}}$ as input back to MATLAB © and re-trace the motion of the 1^+ macroparticles in presence of all fields. Update the occupation map n_1. Repeat from evaluation.
- Check termination
  - If all particles are lost or T_{span} is reached, save n_1 and $n_{1\to2}$ and final electrostatic field map $\mathbf{E_{DL}}$.

8.2 $2^+ \to 3^+$

- Initialization
  - Generate $N = 10^6$ macroparticles distributed in position according to $n_{1\to2}$. Velocities remain Maxwellian with temperature $k_B T_i$.
  - Use $n_{1\to2}$ and n_1 to calculate the total plasma density n_s and mean charge $\langle Z\rangle$. At this point, the contribution of 1^+ would be maximum. The methodology for calculation of N_s is given in Section 7.
  - Use ρ_e and E_e to calculate the ionization frequency for each plasma cell $\nu_{ion} = \rho_e \sigma_{ion,2\to3} v_e$. Calculate cell-averaged collision time $\langle\tau_{ion}\rangle$ and set the total simulation time $T_{span} = 10\langle\tau_{ion}\rangle$. Also, calculate the frequency of a single electron exchange with neutrals in each plasma cell, using the expression $\nu_{CEX} = \rho_0 \sigma_{CEX,2\to1} v_i$. Save the total reaction frequency map as $\nu_{tot} = \nu_{ion} + \nu_{CEX}$.
  - Define the magnetostatic field $\mathbf{B}$ configuration. Initialize occupation n_2, ionization $n_{2\to3}$, and charge exchange (CEX) $n_{2\to1}$ maps to 0. Initialize lost particle map to 0. Set iteration step time $T_{step} = 10^{-10}$ s.
  - Set a reasonable estimate for checkpoint τ_p at which density scaling and $\mathbf{E_{DL}}$ evaluation should be performed. More details are presented in Section 7.
- Evaluation
  - Check for occurrence of reaction at each cell according to ν_{tot}. If the macroparticle is ionized, map to ionization matrix $n_{1\to2}$ and if it is exchanged, map to CEX matrix $n_{2\to1}$. More details are presented in Section 6.
  - Apply the equation of motion to the remaining 2^+ particles and update the position and velocity vectors. Check if the new position exceeds the plasma dimensions–if yes, update the lost particle matrix otherwise map the positions to the occupation map. The exact transport equations can be found in Section 5.
- Check extraction
  - If checkpoint τ_p is reached, scale the occupation maps n_1 and n_2 to appropriate density maps ρ_1 and ρ_2, respectively, and pass the charge imbalance map $\rho_\Delta = \rho_{tot} - \rho_e = \rho_1 + \rho_2 - \rho_e$ as input to COMSOL Multiphysics© to calculate ϕ_{DL} and $\mathbf{E_{DL}}$. Also, calculate updated n_s and $\langle Z\rangle$—the contribution of 2^+ would gradually increase. More details on the methodology are presented in Section 7.
  - Give $\mathbf{E_{DL}}$ as input back to MATLAB © and re-trace the motion of the 2^+ macroparticles in presence of all fields. Update the occupation map n_2. Repeat from evaluation.
- Check termination
  - If all particles are lost or T_{span} is reached, save n_2, $n_{2\to3}$, $n_{2\to1}$, and final electrostatic field map $\mathbf{E_{DL}}$.

9 Results and discussion

The results obtained from the application of the algorithm to the ATOMKI plasma trap configuration are presented in this section. A total of $N = 10^6$ macroparticles were simulated for each charge state, using the magnetostatic field profile of Figure 1 and reaction cross sections from Eqs 26, 27. To be consistent with the electron maps, the simulation domain was taken as the 3D matrix of size $59 \times 59 \times 211$ mm^3, divided into cells of size 1 mm^3 each. All ionization, occupation, and exchange maps were set to the same dimensions.

Figure 6 shows the distribution probability of the initial positions of the macroparticles along the X, Y, and Z axes for three different charge states. Since the initial positions were generated according to the ionization maps of the preceding charge state as mentioned in Section 4, and the plots are representative of the local energy content in the plasma. The initial positions of high charge states are peaked on the axis because this is where the more energetic electrons with sufficient ionizing power are located. The energy distribution along the axis is more uniform, as can be evinced from the near identical distributions in Figure 6C.

A comparison of the initial and final positions of the macroparticles along the Cartesian axes is shown in Figure 7 for two charge states, namely, 2^+ and 5^+. The initial distributions

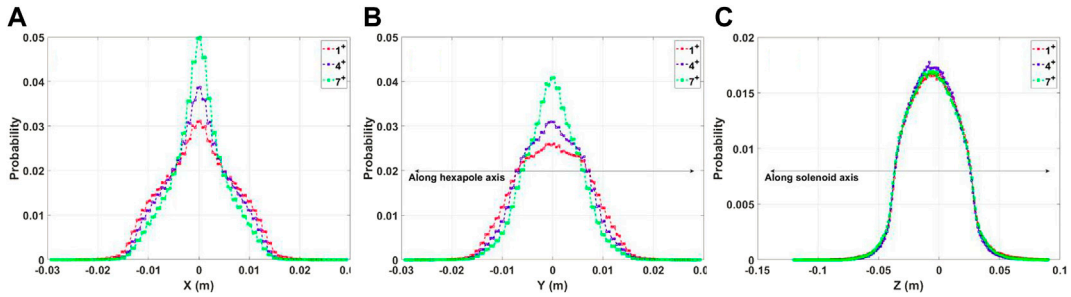

FIGURE 6
Normalized distribution of initial **(A)** X, **(B)** Y, and **(C)** Z coordinates of macroparticles for charge states 1^+, 4^+ and 7^+.

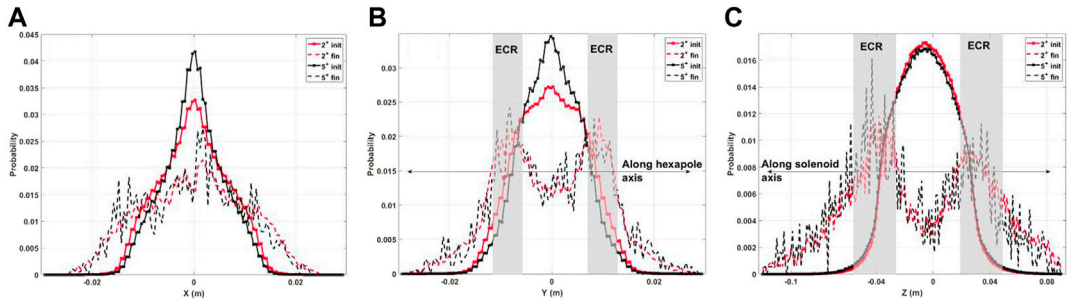

FIGURE 7
Normalized distribution of initial and final **(A)** X, **(B)** Y, and **(C)** Z coordinates of macroparticles for charge states 2^+ and 5^+.

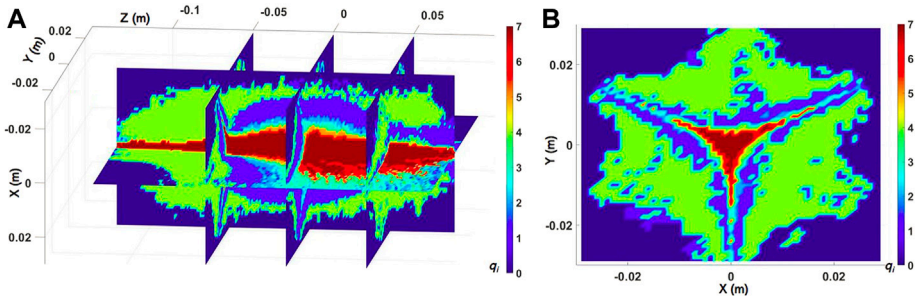

FIGURE 8
Region of peak occupancy of various charge states at the end of simulations until 7^+ in a **(A)** sliced view and **(B)** X–Y projection view. The localization of high charge states near the axis is clearly visible.

follow the same trend as in Figure 6 but the final positions are starkly different, particularly for the *Y* and *Z* axes. On their journey through the plasma, the macroparticles tend to exit the plasmoid along the magnetic field lines and those that are not lost remain aggregated near the ECR surface, marked by the sharp peaks in Figures 7B,C. The peaks are obscured in Figure 7A because the X-axis does not pass through any magnetic poles and the position histograms are projections from neighboring hexapole axes.

Moving on to the ion density profiles, a 3D map of regions with highest occupancy of various charge states is shown in Figure 8. Highly charged ions such as 6^+ and 7^+ tend to be

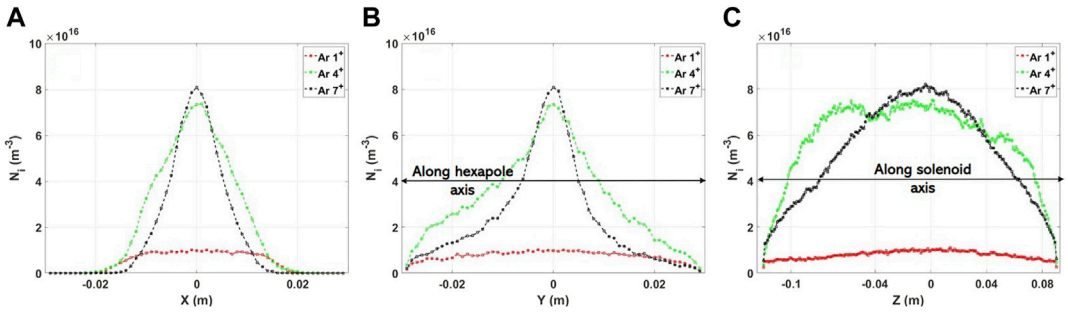

FIGURE 9
Density profiles of 1^+, 4^+, and 7^+ along the **(A)** X-axis at $Y = 0$, $Z = 0$, **(B)** Y-axis at $X = 0$, $Z = 0$, and **(C)** Z-axis at $X = 0$, $Y = 0$.

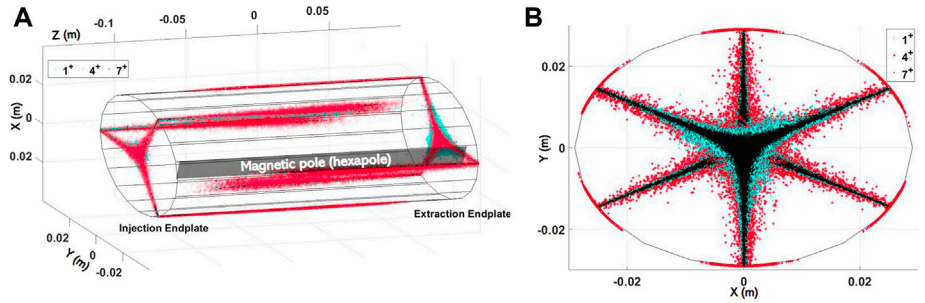

FIGURE 10
Scatter plots of macroparticles lost from the simulation domain in an **(A)** isometric view and **(B)** X–Y projection view for charge states 1^+, 4^+, and 7^+. The downward pointed tri-star corresponds to the extraction side at $Z = 0.09$ m and matches the profile in Figure 8B.

localized near the axis rather than in the halo or on the ECR surface, whereas 1^+–4^+ are the opposite. The same is shown in Figure 9 where the 1D profile of the density of 1^+, 4^+, and 7^+ along the coordinate axes is shown. Although these plots cannot be directly compared with results from other ECRIS simulations since the plasma configurations differ, the general trend of Figures 6, 7, 9 can be inferred from [20, 22] where the authors show tracks of Ar 1^+ and 8^+ in the plasma—the former (low charge) get regularly ionized in the near-axis region and leave traces around the plasma core leading to a spaced-out distribution while the latter (high charge) remain localized axially.

These peak occupancy maps can be correlated with the spatial distribution maps of the lost particles in Figure 10 where more diffused ions such as 4^+ appear to be spread out while other charges leave finer tracks. Also, as with Figure 8B, Figure 10B shows that higher charge states remain stagnated near the axis are lost from a smaller region. A similar behavior has been reported in [22].

In order to benchmark the simulations, the charge state dependent current extracted from the plasma during an experimental run at ATOMKI [41] was compared with that from the simulated density map. Figure 11A shows the experimental beam current as a function of the charge to mass ratio of the ions— Ar^{1+} correspond to $m/q = 40$, Ar^{2+} to $m/q = 20$, and so on. The current under each peak I_i until Ar^{7+} was added to obtain the total current for every charge. To calculate the simulated current distribution, the mean density inside the region of potential dip $\langle N_i \rangle$ (Figure 12) was considered and converted to current using the following expression.

$$I_i = \kappa \frac{(2L)S}{2} \frac{\langle N_i \rangle q_i e}{\tau_i}, \tag{42}$$

where κ is the transmission factor, L is the semi-plasma length, S is the area of the extraction hole, and τ_i is the confinement time. Given the high plasma density and existence of the potential dip, τ_i was calculated as

$$\frac{1}{\tau_i} = \frac{1}{\tau_{ES,i}} + \frac{1}{\tau_{d,i}}, \tag{43}$$

$$\tau_{ES,i} = R \frac{\sqrt{\pi} L}{v_i} \exp\left(\frac{q_i e \langle \phi_{DL} \rangle}{k_B T_i}\right), \tag{44}$$

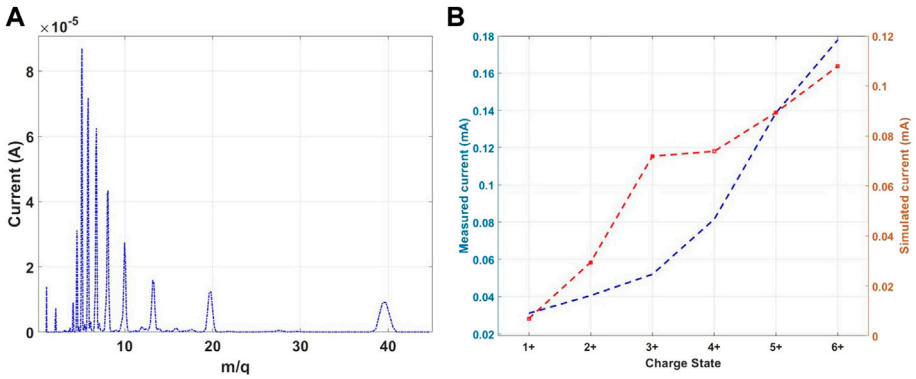

FIGURE 11
(A) Experimental spectrum of ion current as a function of the mass–charge ratio and **(B)** comparison of experimental vs. simulated extracted current data until 6^+. The blue (red) dotted line and axis correspond to the experimental (simulated) data. Simulations for higher charge states are still underway and will feed into 7^+ state, hence it is not shown.

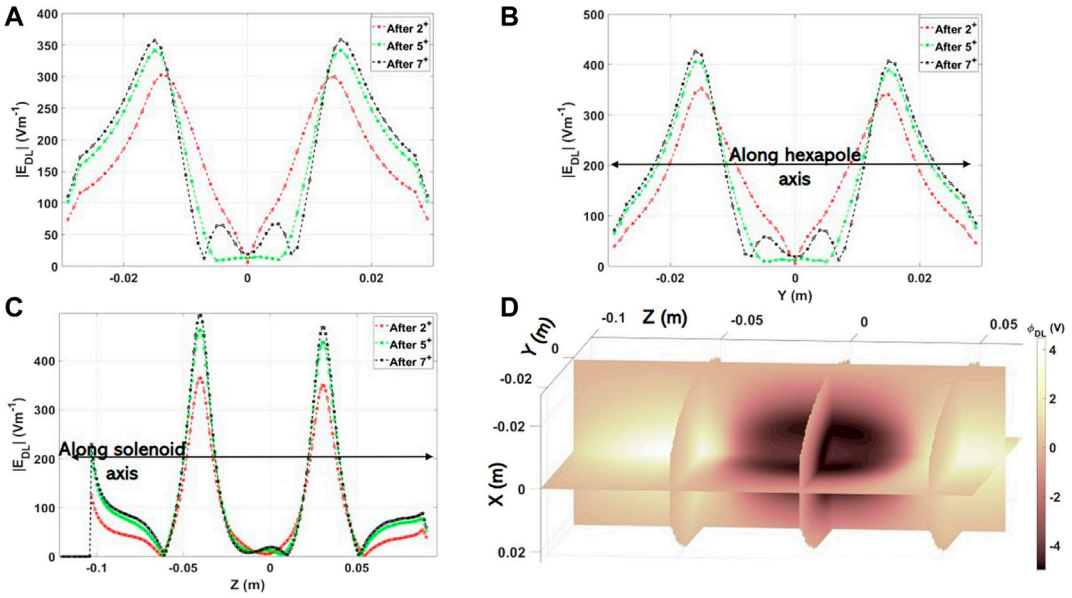

FIGURE 12
Norm of $\mathbf{E}_{DL}$ calculated at the end of simulation runs for 2^+, 5^+, and 7^+ along the **(A)** X-axis at $Y = 0$, $Z = 0$, **(B)** Y-axis at $X = 0$, $Z = 0$, and **(C)** Z-axis at $X = 0$, $Y = 0$, and **(D)** 3D map of ϕ_{DL} showing the potential dip confining the ions.

$$\tau_{d,i} = 7.1 \times 10^{-20} L q_i \ln \Lambda \sqrt{A}\, \frac{n_e Z_{eff}}{k_B T_i^{3/2} E}, \tag{45}$$

where $\tau_{ES,i}$ is the electrostatic confinement time arising from the double layer, $\tau_{d,i}$ is the ambipolar diffusion time connected to the space–charge field along the magnetostatic field lines [38], $R = B_{\max}/B_{\min}$ is the mirror ratio, $\langle \phi_{DL} \rangle$ is the average potential inside the dip, kT_i is the ion temperature, $\ln \Lambda$ is the Coulomb logarithm, $Z_{eff} = \sum N_i q_i^2 / n_e$ is the effective charge density of the plasma, and E is the ambipolar diffusion field. Taking $\langle \phi_{DL} \rangle$ slightly smaller than what is directly calculated from the potential map, $E \sim kT_i$, $L = 0.105$ m according to the chamber design and aperture diameter 18 mm, the current extracted from the plasma was calculated. Figure 11B shows the comparison between the experimental and simulated data. It can be seen that the general relation between the current and charge state is well reproduced,

as is the absolute magnitude. This match is not obtained without considering the electrostatic confinement model, and while this does not solve the debate about the existence of the double layer by itself, it at least confirms the equivalence between the particle transport strategy and the resultant current. There is, however, an inversion in trends for 2^+ and 3^+ which may be partly due to the ion recycling effect [42] but more probably due to an oversimplified implementation of Eq. 6. The match is expected to improve when the simulation of all other charge states is completed, and when a more rigorous charge exchange model is implemented to account for interactions between *all* ions and not just neutrals.

As a final remark, the profile of $|\mathbf{E}_{DL}|$ calculated by COMSOL Multiphysics © at the end of 2^+, 5^+, and 7^+ simulations is shown in Figure 12, as is the potential map obtained at the end of 7^+ run. The formation of the potential dip is noticeable and in keeping with the results of [22]. The convergence of the field profiles at the ECR layer after successive evaluations is clear, while the introduction of smaller peaks in the near-axis region is indicative of the localization of highly charged ions. A full comprehensive analysis of the electrostatic field behavior is still underway and will be a topic of discussion in future work.

10 Conclusion and future perspectives

A novel simulation scheme for modeling ion dynamics together with population kinetics in a space-resolved manner has been reported. The novelty does not arise from any breakthrough made in ECRIS simulations—as discussed in Section 2 numerous toolkits already exist to study the system—but from the adaptability of the technique which allows direct application to PANDORA. The algorithm has been developed in such a way as to exploit a pre-existing RF-electron coupling module and extend it to emulate the steady-state distribution of ions without starting from the scratch. The method simultaneously solves the CR-model to generate 3D space-resolved maps of level population and CSD consistent with steady-state electron maps. The scheme is general, makes few assumptions about the state of the plasma and can be extended to include reactions that populate ionic levels to generate the LPD needed in Eq. 4.

The algorithm presented earlier is still quite basic and needs improvement on several counts. For one, as already mentioned in Section 6, the effective mutual exclusivity approach only works as long as T_{step} is small enough to neglect simultaneous reactions. Even though this is true when considering only ionization and exchange, the approximation is expected to break down when increasing the number of reactions to include collisional excitation and spontaneous emission. The sampling procedure in such a case would inevitably require use of joint probability distributions invoking complex methods such as Markov chains. The development of such a model is underway. The implementation is also deficient in that the neutrals were considered uniformly distributed in the plasma chamber according to a fixed pressure, but this is not necessarily true because under stationary conditions the plasma core is almost devoid of neutral atoms due to ionization. The algorithm can, however, be very easily corrected for this effect, and the next version of the code will be free of this assumption.

Beyond this, as reported in Sec. 9, the precise self-consistent evaluation of $|\mathbf{E}_{\mathbf{DL}}|$ is still ongoing because while the spatial profile seems to converge after sequential runs, the magnitude of the raw ϕ_{DL} maps as extracted from the electrostatic solver remain too high and need to be scaled for implementing in the particle pusher code. The procedure is similar to what Mironov and group have reported in [22] but their overall approach is more physically intuitive because the double layer formation in their model is a natural artifact of equalization of electron and ion diffusion flux. In future work, we aim to implement a similar calculation to directly evaluate correct field potentials. With these modifications in place, the algorithm may turn out to be a useful tool for not only fundamental research in the working of ECR plasmas but for applied research as well, similar to those needed for PANDORA.

Data availability statement

The raw data supporting the conclusions of this article will be made available by the authors, without undue reservation.

Author contributions

Conceptualization: BM, AG, AP, GT, GM, and DM; Data curation: SB, RR, EN, and DM; Formal analysis: BM, AG, AP, and DM; Investigation: BM, AG, AP, SB, RR, GT, GM, EN, and DM; Methodology, BM, AG, AP, and DM; Resources, AG, SB, RR, and DM; Visualization: BM, AP, and RR; Writing—original draft: BM; Writing—review and editing: AG, AP, SB, RR, GT, GM, EN, and DM.

Funding

The authors gratefully acknowledge the support of 3^{rd} National Committee of INFN and funding from project PANDORA_Gr3.

Conflict of interest

The authors declare that the research was conducted in the absence of any commercial or financial relationships that could be construed as a potential conflict of interest.

Publisher's note

References

1. Geller R. *Electron cyclotron resonance ion source and ECR plasmas*. Bristol: IOP Publishing (1996).

2. Girard A, Hitz D, Melin G, Serebrennikov K. Electron cyclotron resonance plasmas and electron cyclotron resonance ion sources: Physics and technology (invited). *Rev Scientific Instr* (2004) 75:1381–8. doi:10.1063/1.1675926

3. Emery G. Perturbation of nuclear decay rates. *Annu Rev Nucl Sci* (1972) 22:165–202. doi:10.1146/annurev.ns.22.120172.001121

4. Bahcall J. Beta decay in stellar interiors. *Phys Rev* (1961) 136:1143–9. doi:10.1103/PhysRev.126.1143

5. Bosch F, Faestermann T, Friese J, Heine F, Kienle P, Wefers E, et al. Observation of bound-state β^- decay of fully ionized : - cosmochronometry. *Phys Rev Lett* (1996) 77:5190–3. doi:10.1103/PhysRevLett.77.5190 ^{187}Re ^{187}Re ^{187}Os

6. Mascali D, Santonocito D, Amaducci S, Ando L, Antonuccio V, Biri S, et al. A novel approach to β-decay: Pandora, a new experimental setup for future in-plasma measurements. *Universe* (2022) 8(2):80–16. doi:10.3390/universe8020080

7. Takahashi K, Yokoi K. Nuclear β-decays of highly ionised heavy atoms in stellar interiors. *Nucl Phys A* (1983) 404:578–98. doi:10.1016/0375-9474(83)90277-4

8. Galatà A, Mascali D, Gallo C, Torrisi G. Self-consistent modeling of beam-plasma interaction in the charge breeding optimization process. *Rev Scientific Instr* (2020) 91:013506–7. doi:10.1063/1.5130704

9. Mascali D, Torrisi G, Neri L, Sorbello G, Castro G, Celona L, et al. 3d-full wave and kinetics numerical modelling of electron cyclotron resonance ion sources plasma: Steps towards self-consistency. *Eur Phys J D* (2015) 69:27–7. doi:10.1140/epjd/e2014-50168-5

10. Heinen A, Ruther M, Ducrée J, Leuker J, Mrogenda J, Ortjohann H, et al. Successful modeling, design, and test of electron cyclotron resonance ion sources. *Rev Scientific Instr* (1998) 69:729–31. doi:10.1063/1.1148667

11. Heinen A, Ruther M, Ortjohann H, Vitt C, Rhode S, Andra H. Heating and trapping of electrons in ecris, from scratch to afterglow. *unpublished* (1999) 1–8.

12. Maunoury L, Pierret C, Biri S, Pacquet J. Studies of the ecr plasma using the trapcad code. *Plasma Sourc Sci Technol* (2009) 18:015019–7. doi:10.1088/0963-0252/18/1/015019

13. Vamosi J, Biri S. Trapcad - a program to model magnetic traps of charged particles. *Comput Phys Commun* (1996) 98:215–23. doi:10.1016/0010-4655(96)00053-7

14. Dougar-Jabon V, Umnov A, Diaz DS. Three-dimensional simulation of an ecr plasma in a minimum-b trap. *Rev Scientific Instr* (2002) 73:629–31. doi:10.1063/1.1429774

15. Edgell D, Kim J, Bogatu I, Pardo R, Vondrasek R. Model of charge-state distributions for electron cyclotron resonance ion source plasmas. *Phys Rev ST Accel Beams* (1999) 2:123502–6. doi:10.1103/PhysRevSTAB.2.123502

16. Edgell D, Kim J, Bogatu I, Pardo R, Vondrasek R. Electron cyclotron resonance ion source one-dimensional fluid modeling. *Rev Scientific Instr* (2002) 73:641–3. doi:10.1063/1.1427031

17. Cluggish B, Zhao L, Kim J. Simulation of parameter scaling in electron cyclotron resonance ion source plasmas using the gem code. *Rev Scientific Instr* (2010) 81:02A301–3. doi:10.1063/1.3259166

18. Cluggish B, Kim J. Modeling of wave propagation and absorption in electron cyclotron resonance ion source plasmas. *Nucl Instr Methods Phys Res Section A: Acc Spectrometers Detectors Associated Equipment* (2012) 664:84–97. doi:10.1016/j.nima.2011.10.015

19. Mironov V, Beijers J. Three-dimensional simulations of ion dynamics in the plasma of an electron cyclotron resonance ion source. *Phys Rev ST Accel Beams* (2009) 12:073501–10. doi:10.1103/PhysRevSTAB.12.073501

20. Mironov V, Bogomolov S, Bondarchenko A, Efremov A, Loginov V. Numerical model of electron cyclotron resonance ion source. *Phys Rev ST Accel Beams* (2015) 8:123401–23. doi:10.1103/PhysRevSTAB.18.123401

21. Mironov V, Bogomolov S, Bondarchenko A, Efremov A, Kuzmenkov K, Loginov V. Simulations of ECRIS performance for different working materials. *J Instrum* (2018) 13:C12002. doi:10.1088/1748-0221/13/12/C12002

22. Mironov V, Bogomolov S, Bondarchenko A, Efremov A, Loginov V, Pugachev D. Spatial distributions of plasma potential and density in electron cyclotron resonance ion source. *Plasma Sourc Sci Technol* (2020) 29:065010. doi:10.1088/1361-6595/ab62dc

23. Mironov V, Bogomolov S, Bondarchenko A, Efremov A, Loginov V, Pugachev D. Three dimensional modelling of processes in electron cyclotron resonance ion source. *J Instrum* (2020) 15:P10030–19. doi:10.1088/1748-0221/15/10/P10030

24. Mascali D, Neri L, Gammino S, Celona L, Ciavola G, Gambino N, et al. Plasma ion dynamics and beam formation in electron cyclotron resonance ion sources. *Rev Scientific Instr* (2010) 81:02A334–4. doi:10.1063/1.3292932

25. Neri L, Mascali D, Celona L, Gammino S, Ciavola G. A 3d Monte Carlo code for the modeling of plasma dynamics and beam formation mechanism in electron cyclotron resonance ion sources. *Rev Scientific Instr* (2012) 83:02A330–3. doi:10.1063/1.3670341

26. Torrisi G, Mascali D, Sorbello G, Neri L, Celona L, Castro G, et al. Full-wave fem simulations of electromagnetic waves in strongly magnetized non-homogeneous plasma. *J Electromagn Waves Appl* (2014) 28:1085–99. doi:10.1080/09205071.2014.905245

27. Galatà A, Mascali D, Mishra B, Pidatella A, Torrisi G. On the numerical determination of the density and energy spatial distributions relevant for in-plasma β-decay emission estimation. *Front Phys* (2022) 10:1–9. doi:10.3389/fphy.2022.947194

28. Angot J, Luntinen M, Kalvas T, Koivisto H, Kronholm R, Maunoury L, et al. Method for estimating charge breeder ecr ion source plasma parameters with short pulse 1+ injection of metal ions. *Plasma Sourc Sci Technol* (2021) 30:035018. doi:10.1088/1361-6595/abe611

29. Mishra B, Galatà A, Mengoni A, Naselli E, Pidatella A, Torrisi G, Mascali D Predicting β-Decay Rates of Radioisotopes Embedded in Anisotropic ECR Plasmas. *Nuovo Cimento C* (2022) 45 (5):1–4. doi:10.1393/ncc/i2022-22117-5

30. Chandrasekhar S. *Principles of stellar dynamics*. Chicago: The University of Chicago Press (1942).

31. Boris J. Relativistic plasma simulation—Optimization of a hybrid code. In: Proceedings of 4th Conference on Numerical Simulation of Plasmas. Washington, DC: Naval Research Laboratory (1970). p. 3–67.

32. Zenitani S, Umeda T. On the boris solver in particle-in-cell simulation. *Phys Plasmas* (2018) 25:112110–7. doi:10.1063/1.5051077

33. MacDonald W, Rosenbluth M, Chuck W. Relaxation of a system of particles with coulomb interactions. *Phys Rev* (1957) 107:350–3. doi:10.1103/PhysRev.107.350

34. Galatà A, Mascali D, Neri L, Celona L. A new numerical description of the interaction of an ion beam with a magnetized plasma in an ecr-based charge breeding device. *Plasma Sourc Sci Technol* (2016) 25:045007–17. doi:10.1088/0963-0252/25/4/045007

35. Povyshev V, Sadovoyl A, Shevelko V, Shirkov G, Vasina E, Vatulin V. Electron impact ionisation cross sections of H, He, N, O, Ar, Xe, Au, Pb atoms and their ions in the electron energy range from the threshold up to 200 keV. *IAEA INIS* (2001) 33:1–46.

36. Muller A, Salzborn E. Scaling of cross sections for multiple electron transfer to highly charged ions colliding with atoms and molecules. *Phys Lett A* (1977) 62A: 391–4. doi:10.1016/0375-9601(77)90672-7

37. Mascali D, Neri L, Celona L, Castro G, Torrisi G, Gammino S, et al. A double-layer based model of ion confinement in electron cyclotron resonance ion source. *Rev Sci Instrum* (2014) 85:02A511–4. doi:10.1063/1.4860652

38. Douysset G, Khodja H, Girard A, Briand JP. Highly charged ion densities and ion confinement properties in an electron-cyclotron-resonance ion source. *Phys Rev E* (2000) 61:3015–22. doi:10.1103/PhysRevE.61.3015

39. Mascali D, Gammino S, Celona L, Ciavola G. Towards a better comprehension of plasma formation and heating in high performances electron cyclotron resonance ion sources (invited). *Rev Scientific Instr* (2012) 83:02A336–6. doi:10.1063/1.3672107

40. Takahashi K, Kaneko T, Hatakeyama R. Double layer created by electron cyclotron resonance heating in an inhomogeneously magnetized plasma with high-speed ion flow. *Phys Plasmas* (2008) 15:072108. doi:10.1063/1.2951997

41. Biri S, Rácz R, Pálinkás J. Status and special features of the atomki ecr ion source. *Rev Scientific Instr* (2012) 83:02A341–3. doi:10.1063/1.3673006

42. Mironov V, Bogomolov S, Bondarchenko A, Efremov A, Loginov V. Simulations of charge-breeding processes in ecris. In: Lettry J, Mahner E, Marsh B, Pardo R, Scrivens R, editors. *Proceedings of 17th international conference on ion sources*. College Park, Maryland: AIP Publishing (2011). p. 1–3.

frontiers | Frontiers in Astronomy and Space Sciences

TYPE Original Research
PUBLISHED 04 October 2022
DOI 10.3389/fspas.2022.931744

OPEN ACCESS

EDITED BY
Isaac Vidana,
Ministry of Education, Universities and Research, Italy

REVIEWED BY
Carlos Frajuca,
Federal University of Rio Grande, Brazil
Ivano Lombardo,
Università di Catania, Italy

*CORRESPONDENCE
Angelo Pidatella,
pidatella@lns.infn.it

SPECIALTY SECTION
This article was submitted to Nuclear Physics,
a section of the journal
Frontiers in Astronomy and Space Sciences

RECEIVED 29 April 2022
ACCEPTED 03 August 2022
PUBLISHED 04 October 2022

CITATION
Pidatella A, Mascali D, Bezmalinovich M, Emma G, Mazzaglia M, Mishra B, Finocchiaro G, Galatà A, Marletta S, Mauro GS, Naselli E, Santonocito D, Torrisi G, Cristallo S, La Cognata M, Perego A, Spartà R, Tumino A and Vescovi D (2022), Experimental and numerical investigation of magneto-plasma optical properties toward measurements of opacity relevant for compact binary objects.
Front. Astron. Space Sci. 9:931744.
doi: 10.3389/fspas.2022.931744

Experimental and numerical investigation of magneto-plasma optical properties toward measurements of opacity relevant for compact binary objects

Angelo Pidatella[1]*, David Mascali[1], Matteo Bezmalinovich[2,3], Giulia Emma[1,4], Maria Mazzaglia[1], Bharat Mishra[1,4], Giorgio Finocchiaro[1,4], Alessio Galatà[5], Salvo Marletta[1], Giorgio Sebastiano Mauro[1], Eugenia Naselli[1], Domenico Santonocito[1], Giuseppe Torrisi[1], Sergio Cristallo[3,6], Marco La Cognata[1], Albino Perego[7,8], Roberta Spartà[1], Aurora Tumino[1,9] and Diego Vescovi[10]

[1]INFN, LNS, Catania, Italy, [2]Department of Science and Technology, University of Camerino, Camerino, Italy, [3]INFN, Sezione di Perugia, Perugia, Italy, [4]Department of Physics and Astronomy, University of Catania, Catania, Italy, [5]INFN, LNL, Legnaro, Italy, [6]INAF, Osservatorio Astronomico d'Abruzzo, Teramo, Italy, [7]Department of Physics, University of Trento, Trento, Italy, [8]TIFPA, INFN, Trento, Italy, [9]Department of Engineering and Architecture, University of Enna "Kore", Enna, Italy, [10]Institute for Applied Physics, Goethe University Frankfurt, Frankfurt am Main, Germany

Electromagnetic transients known as kilonovae (KN), are among the photonic messengers released in the post-merger phase of compact binary objects, for example, binary neutron stars, and they have been recently observed as the electromagnetic counterpart of related gravitational-wave (GW) events. Detection of the KN signal plays a fundamental role in the multi-messenger astronomy entering in a sophisticated GW-detecting network. The KN light curve also delivers precious information on the composition and dynamics of the neutron-rich post-merger plasma ejecta (relying on *r*-process nucleosynthesis yields). In this sense, studying KN becomes of great relevance for nuclear astrophysics. Because of the highly heterogeneous composition, plasma opacity has a great impact both on radiative transport and spectroscopic observation of KN. Theoretical models attempting in encoding the opacity of this system often fail, due to the complexity of blending plethora of both light- and heavy-*r* nuclei transition lines, requesting for more complete atomic database. Trapped magneto-plasmas conceived in PANDORA could answer to these requests, allowing experimental in-laboratory measurements of optical properties and opacities, at plasma electron densities and temperatures resembling early-stage plasma ejecta's conditions, contributing to shed light on *r*-process metallic species abundance at the blue-KN diffusion time. A numerical study has been recently performed, supporting the choice of first physics cases to be investigated and the design of

the experimental setup. In this article, we report on the feasibility of metallic plasmas on the basis of the results from the systematic numerical survey on optical spectra computed under non-local thermodynamic equilibrium (NLTE) for several light-*r* nuclei. Results show the great impact of the NLTE regime of laboratory magneto-plasmas on the gray opacity contribution contrasted with those under the astrophysical LTE assumption. A first experimental attempt of reproducing ejecta plasma conditions has been performed on the operative Flexible Plasma Trap (FPT) at the INFN-LNS and here presented, together with first plasma characterization of density and temperature, *via* non-invasive optical emission spectroscopy (OES). The measured plasma parameters have supported numerical simulations to explore optical properties of NLTE gaseous and metallic plasmas, in view of the near-future plasma opacity measurements through spectroscopic techniques. The novel work so far performed on these under-dense and low-temperature magneto-plasmas, opens the route for the first-time to future in-laboratory plasma opacity measurements of metallic plasma species relevant for KN light curve studies.

KEYWORDS

plasma physics, nuclear astrophysics, multi-messenger astronomy, plasma spectroscopy, kilonovae

1 Introduction

The interplaying network of observations, combining both gravitational-wave (GW) signals and their electromagnetic (EM) counterparts, is representative of the outstanding window on the cosmos offered by multi-messenger astronomy (Rosswog, 2015). In this context, the mergers of compact binary (CB) objects—such as the coalescence of two neutron stars—provide a unique physical opportunity to advance knowledge on the heavy elements nucleosynthesis (Korobkin et al., 2012; Kasen et al., 2017), and to study the post-merger ejecta dynamics (Perego et al., 2014; Wu et al., 2022). The CB merger powers EM transient signals, following the GW event, known as *kilonovae* (Metzger, 2019) (hereafter, KN), which are fed by a peculiar balance of thermalization and radioactive heating processes (Li and Paczyński, 1998). Depending on the non-trivial merging dynamics and on the ejecta neutron richness, large neutron fluxes could lead to the production of n-rich isotopes far from the beta-stability valley, enriching the CB merger ejecta both of heavy (mass number A $\gtrsim$140) and light (A $\lesssim$140) nuclei, synthesized *via* the rapid neutron capture nucleosynthesis process (*r*-process). The bolometric light curve broadband evolution of the bright optical transient AT2017gfo (Korobkin et al., 2012; Arcavi et al., 2017), detected after the GW170817 event (Abbott et al., 2017), has shown a fair agreement with the expected heating rate and opacity from freshly synthesized heavy elements (Metzger et al., 2010; Kasen et al., 2017), resulting from multi-component mass ejection and evolution. The *r*-process-powered KN transient emission has therefore a key role in the study of the complexity of *r*-process final abundance pattern, which relies on both thermodynamic conditions and radioactive decays. However, because of its heterogeneous composition, the CB merger ejecta *opacity* (κ) largely affects the KN emission, in turn influencing both the KN light-curve and the spectral energy distribution. Opacity reflects the plasma atomic level population distribution and the related radiative cross sections. It regulates the energy exchange between plasma and radiation through several absorption-scattering reactions driven by a plethora of atomic line transitions (Tanaka et al., 2020). Ejecta enriched in light *r*-process elements result in low opacity ($\kappa \lesssim 1\ \mathrm{cm^2\ g^{-1}}$), propagating optical light fading in days (*blue-KN*), whereas heavy *r*-process elements enlarges the opacity ($\kappa \gtrapprox 10\ \mathrm{cm^2\ g^{-1}}$), with redder light curves lasting even for weeks (*red-KN*) (Kasen et al., 2017). The color characterizing a specific phase of a KN event therefore acts as a diagnostics for the produced nuclei. However, state-of-the-art literature widely request for progresses on opacity modeling (Barnes and Kasen, 2013; Rosswog, 2015; Barnes et al., 2016; Metzger, 2019; Tanaka et al., 2020) to improve KN predictions. Indeed, limited experimental data on opacity of complex (*d*)- and (*f*)-shell elements (Bailey et al., 2009; Hoarty et al., 2010; Zhang et al., 2011; Bailey et al., 2015), as well as of their level structure and reaction rates, along with atomic constraints provided by oversimplified theoretical models, could lead to inconsistent results if compared with observations. Therefore, an experimental benchmark closing the gap between theory and observations would be highly desirable to draw quantitative conclusions on the nucleosynthetic yield from observations. At the INFN-LNS, a new plasma trap called PANDORA is under construction (Mascali et al., 2022a). The trap has been developed within the INFN funded PANDORA (Plasma for Astrophysics, Nuclear Decays Observation and Radiation for Archaeometry) project, with the aim to study weak-interaction rates in controlled and monitored electron cyclotron resonance (ECR) plasmas, reproducing stellar-like conditions, in terms of temperature and ion charge state distribution, and opening the route to interdisciplinary experiments relevant for the astrophysics

and nuclear astrophysics. In the framework of opacity measurements interesting for the KN light-curve study, trapped magneto-plasmas conceived in PANDORA offer an outstanding controlled environment, allowing first-of-its-kind in-laboratory measurements of optical properties and opacities, at plasma electron densities and temperatures resembling early-stage plasma ejecta's conditions, contributing to shed light on *r*-process metallic species abundance at the blue-KN diffusion time. A numerical study has been recently performed, supporting the choice of first physics cases to be investigated and the design of the experimental setup (Pidatella et al., 2021). In this article, we report on further considerations about the possibility of producing metallic light *r*-process plasmas eligible for the opacity measurements, using the PANDORA plasma trap (Section 2.1). On this track, we report on the first experimental attempt of reproducing ejecta plasma conditions carried out on the already operative Flexible Plasma Trap (FPT) at the INFN-LNS (Section 2.2.1), presenting first plasma characterization of density and temperature (Section 2.2.2), *via* non-invasive optical emission spectroscopy (OES). The measured plasma parameters have supported numerical simulations to explore optical properties of non-local thermodynamic equilibrium (NLTE) gaseous and metallic plasmas (Section 2.3), in view of the near-future plasma opacity measurements using spectroscopic techniques. Results of in-plasma spectroscopic measurements and of numerical investigations on plasma optical properties is presented and discussed in (Sections 3.1, 3.2), respectively. Finally, conclusion and possible outlook of the work is provided in (Section 4).

2 Methods

In the following, we report on the methodologies and experimental techniques employed in this work. Technological aspects are discussed in Section 2.1, based on the know-how gained at the INFN laboratories (LNS and LNL) on injection methods of metallic atoms into magnetically confined plasmas, and on the numerical feasibility study (Pidatella et al., 2021), providing further constraints on the physics cases suitable for opacity measurements. Moreover, a full description of the flexible plasma trap facility, the experiment design, and diagnostics techniques employed are provided in Section 2.2. Finally, details on the numerical calculations performed to study magneto-plasma optical properties are reported in Section 2.3.

2.1 On kilonovae ejecta constraints for in-laboratory electron cyclotron resonance plasma experiments: Metallic element injection

Fundamental elements for the interpretation of the KN light-curve are the *r*-process yields (determining the heating term) and opacities (leading the energy exchange between radiation and plasma). The AT2017gfo spectrum delivers absorption signatures suitable with blending of many atomic lines expected from actinides and lanthanides. For earlier-stages spectrum (~ 1.5 days), a prominent absorption feature compatible with *strontium* lines has been observed (Watson et al., 2019; Gillanders et al., 2022). Recently, the contribution to spectral features arising from *hydrogen* and *helium* was excluded (Perego et al., 2022), and other synthetic spectra calculations have reported about possible detection in future KN events of light elements such as *calcium* (Domoto et al., 2021), *platinum*, and *gold* (Gillanders et al., 2021). Despite the huge number of studies on KN light-curve predictions, still large uncertainties on the relative contributions from various isotopes remain, in part due to the lack of complete atomic transition data. In this view, we have recently performed a numerical study to draw feasibility conditions in the plasma trap for measuring opacity of some of these light elements, on the basis of inputs from KN ejecta models and *r*-process nucleosynthesis yields calculations (Pidatella et al., 2021). Inside a compact magnetic trap, such as PANDORA, dense and hot magneto-plasmas, composed of multi-charged ions in a bath of energetic electrons, are magnetically confined, and heated by microwave power, exploiting the ECR heating mechanism (Geller, 1996). ECR plasma typical electron densities go up to ~ 10^{13} cm^{-3} and energies in the range of eV- tens of keV (Mascali et al., 2022a). Within these plasma conditions, the KN stage reproducible in the trap belongs to 10^{-2} – 10^{0} days after the merger, corresponding to the *blue-KN* signal. The latter shows a peak of the light curve at optical frequencies, mostly determined by ejecta's light component with low opacity. The light *r*-process elements production is expected to be prominent at this stage, due to high *electron fraction* Y_e, this being indicative of the initial neutron richness. Since the blue-KN is largely shaped by light elements, the study was focused on plasma atomic species going from *selenium* ($Z = 34$) to *rhodium* ($Z = 45$). While theoretical predictions, based only on abundances and number of transition lines, promote elements as molybdenum, technetium, ruthenium, and rhodium as the most opaque species among those considered (Tanaka et al., 2020), we found that at typical NLTE regime and plasma parameters studied, the mean opacities of lighter elements as selenium, strontium, zirconium, and niobium are several orders of magnitude larger than those of the former elements (Pidatella et al., 2021). Injection of the aforementioned *metallic* elements in ECR plasmas requires specific vaporization techniques, both using *resistive ovens* (RO) to evaporate the metallic compound whose vapor pressure goes to 10^{-2} mbar at temperature $T \leq 2000$ K, or *sputtering* (Sp) techniques, usually used for refractory elements. The choice of methods also depends on the efficiency of injection (Mascali et al., 2022a; Mauro et al., 2022). On this basis, selenium and strontium are chosen as day-0 cases for the first measurements. In Table 1, we report on the results from injection efficiency calculations carried out on the aforementioned elements. It can be evinced that some elements

TABLE 1 Light *r*-process elements of interest for opacity measurements for the blue-KN stage. T_{vap} [K] is the evaporation temperature of the species. Species with larger injection efficiency and easier production are marked in green (▪), while those presenting some efficiency or availability limitations in yellow (▪).

	T_{vap} [K]	Compound	Method	Note
Se	500 (oven)	Se	RO/Sp	Low T_{vap} could be difficult to control.
Sr	796	Sr	RO	Handling rules typical of alkaline earth metals.
Zr	–	Zr	Sp	Yield: 1 atom/ion at 67.1 eV.
Nb	–	Nb	Sp	Yield: 0.9 atom/ion at 65.6 eV.
Mo	1073	MoO_3	RO	Used at LNL to produce Mo beams. Temperature stability requested.
Tc	–	Tc	Sp	Yield: 5.5 atom/ion at 17.1 eV. Radioisotope suppliers.
Ru	–	Ru	Sp	Yield: 1.8 atom/ion at 41.5 eV.
Rh	–	Rh	Sp	Yield: 2.1 atom/ion at 36.4 eV.

are more feasible than other, both in terms of availability, handling/control of the injection procedure, and efficiency.

2.2 First characterization of plasma parameters for *gaseous* electron cyclotron resonance plasmas

In this section, the main characteristics of the FPT are highlighted. The trap represents the outcome of the experience gained in the physics of plasma ion source at the INFN-LNS in the last decades (Gammino et al., 2017). It is characterized by a peculiar flexibility in terms of possible magnetic field configurations and microwaves heating frequency, exploiting the known ECR heating mechanism (Geller, 1996). Plasma parameters mostly depend on the particular tuning of the field profile, RF frequency and power, and gas buffer pressure, leading to many possible scenarios. Generated plasmas are suitable for studies of astrophysics, nuclear, and multidisciplinary physics, especially on the basis of their stellar-like temperature conditions. In this context, a particular effort has been spent at the INFN-LNS to develop a multi-diagnostics system to allow both a full characterization of the plasma parameters for all electron and ion species involved and interdisciplinary studies (Mazzaglia et al., 2018; Naselli et al., 2019a; Mazzaglia et al., 2019; Naselli et al., 2022a; Mascali et al., 2022b; Torrisi et al., 2022). The FPT is therefore a valuable experimental facility operative at the INFN-LNS to benchmark monitoring diagnostics and experimental techniques to be employed in PANDORA, of course on a larger scale, which is precious for the future envisaged in-laboratory plasma measurements relevant for the KN study. In the following, we report on the experimental setup adopted for the first non-invasive characterization of gaseous ECR plasma only *via* OES, generated, confined, and sustained *via* the FPT (Section 2.2.1). We also provide a general picture of the multi-diagnostic setup used in the experiment, particularly focusing on OES diagnostic, and the applied line-ratio method (Fantz, 2006; Fantz et al., 2006) for estimating electron plasma density and temperature for low-Z plasma buffer (Section 2.2.2), that is, *hydrogen* (H_2) and *argon* (Ar).

2.2.1 Experimental setup: Flexible plasma trap and diagnostic system

The FPT magnetic field is provided by means of three solenoids, which allow the tuning of the field profile. The plasma characterization in the FPT has been performed in both *simple mirror* and *quasi B-flat* configuration, adequately tuning the B_{min}/B_{ECR}, used as figure of merit for the plasma stability (Mazzaglia et al., 2018; Naselli et al., 2019b), and also modifying source parameters: microwave power (P_{RF}), heating frequency (f_{RF}), and gas neutral pressure (p_0). In the Figure 1A view of the FPT setup including all diagnostics used is shown. The FPT plasma has been generated *via* the radial microwave injection (perpendicular to the chamber longitudinal axis), leaving the parallel axis available for the diagnostics. The injection is carried at frequencies ranging between 4 and 7 GHz. The signal is generated by a *Rohde & Schwarz* generator, amplified by a traveling wave tube (TWT) and sent to the FPT by *WRD350* waveguides. A directional coupler allows to measure forward and reflected power, while an insulator safeguards the TWT by the power reflected backward. A differentially pumped system, using a small orifice (dosing valve), connects the plasma chamber vacuum with the vacuum reservoir developed for performing mass spectrometry. The two vacuum systems work at very different pressures (e.g., $p_{chamber} = 10^{-4\div-2}$ mbar, $p_{spectrometer} \leq 10^{-5}$ mbar) and requires the development of an independent vacuum piping system. A compact residual gas analyzer (RGA) was used for the vacuum diagnostics and for mass spectroscopy (*Pfeiffer Vacuum—QMG 250 PrismaPro*®). A view of the apparatus is shown in Figures 1C,D. The diagnostic line is quite complex, with

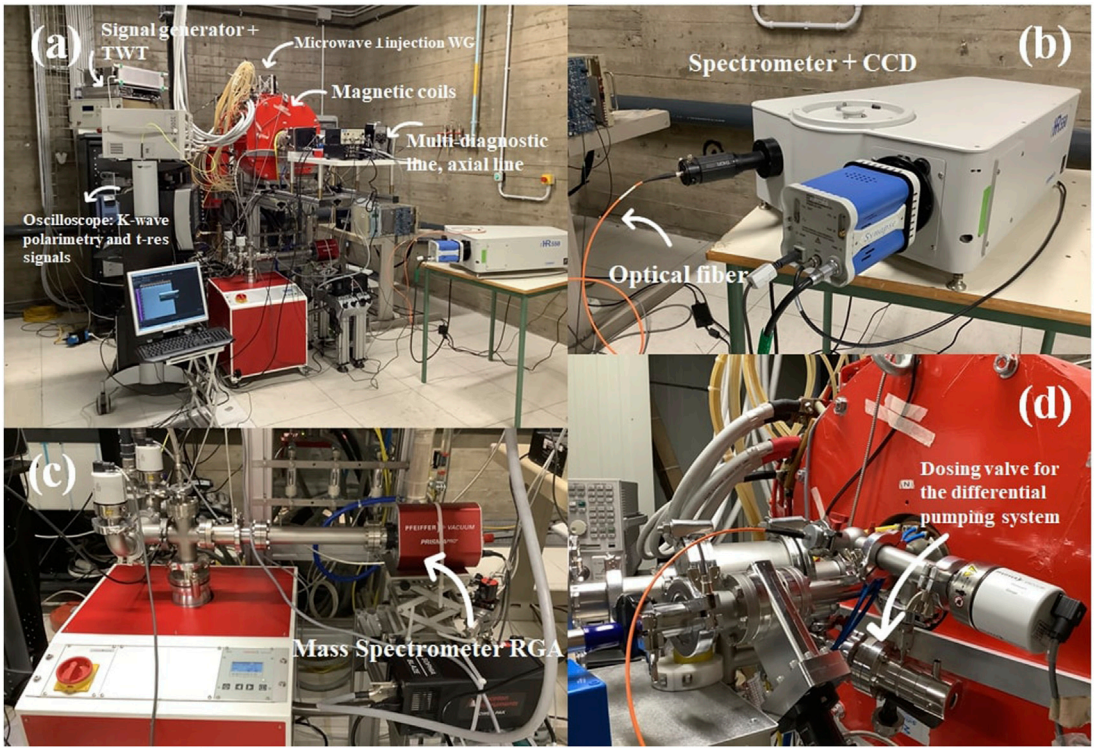

FIGURE 1
FPT experimental room and apparatus. **(A)** View of the FPT setup, including the chamber, magnetic coils, the RF instrumentation, and the axial diagnostic line. **(B)** *Horiba* spectrometer and the CCD detector, connected to the optical fiber. **(C)** RGA and the differential pumping system set to perform mass spectroscopy of gases in the chamber. **(D)** Part of the X-ray diagnostic line, with focus on the orifice to dose gas into the RGA.

the intent to perform non-invasive on-line cross-measurements in multi-diagnostics:

1) A pin-hole setup, coupled to a high-resolution CCD camera, able to perform space-resolved X-ray imaging of plasma emission (Rácz et al., 2016). The system is supported by an algorithm, which can analyze the single-photon counting (SPhC) images for energy-resolved investigation pixel-by-pixel to study the local plasma-emitted spectrum in a high-dynamic range (HDR) mode by distinguishing the fluorescence lines of the materials of the plasma chamber (Ti and Ta) from plasma, for example, (Ar) fluorescence lines (Naselli et al., 2022b);
2) OES has been developed to characterize the cold electron population ($k_B T_e \leq 30$ eV). It consists of an energy-calibrated spectrometer (*i-HR 550 Horiba*, diffraction grating 2,400 gr/mm, with nominal resolution of 35 pm at 486 nm, ranging from 300 to 750 nm), with relative calibration in intensity, coupled to a CCD detector (26 μm pixels)—a view of the detection system is shown in Figure 1B. OES allows not only to estimate the electron density and temperature of cold electrons in the plasma bulk (Mazzaglia et al., 2019) but also to advance knowledge on the relative percentage of the ion species within the plasma, by means of the *line-ratio method* (Fantz, 2006);
3) Microwave interfero-polarimetry to measure the line-of-sight integrated density of the whole plasma. Microwave polarimetry setup is able to investigate on the magnetoplasma-induced Faraday rotation in a compact plasma trap, monitoring plasma ignition, stability, and whole-density modulation led by changes in the source parameters (Mascali et al., 2022b);
4) RF probe placed axially and connected to an 80 Gsample/s oscilloscope, included to probe kinetic plasma instability and to make time-resolved measurements of the latter, based on the detection of emitted RF signals from the unstable plasma.

In this work, despite the synergistic effort spent to develop the aforementioned diagnostic system, we will only provide further insights on the OES diagnostic (b), and its related methods to investigate on optical properties of generated plasmas.

2.2.2 Plasma optical emission spectroscopy for hydrogen and argon plasmas

To interpret intensities measured by OES, a model describing the correlation between atomic level population densities of excited states with plasma parameters, for example, the

electron density (ρ_e) and, if the electron energy distribution function (EEDF) is Maxwellian, the electron temperature (T_e) must be used. Collisional-radiative (CR) models well suite typical NLTE plasma generated *via* the ECR mechanism (Fantz, 2006; Fantz et al., 2006). The models provide this description by balancing reactions that imply a change in the electron energy level of atoms or molecules in a plasma: the time-derivative of the population density n_p of an excited state p can be written as a function of the other state densities,

$$\frac{dn_p}{dt} = \sum_{q>p} n_q A_{qp} - \sum_{q<p} n_p A_{pq} + \rho_e \left(\sum_{q \neq p} n_q \chi_{q \to p} - \sum_{q \neq p} n_p \chi_{p \to q} \right), \tag{1}$$

with ρ_e being the electron density, A_{qp} is the Einstein coefficient for the transition from state q to p, $\chi_{q \to p}$ is the rate coefficient for electron collision excitation (if $E_q \leq E_p$) and de-excitation (if $E_q \geq E_p$). This quantity describes, given an initial and a final state, the number of considered electron collision processes per unit of time normalized by the densities of the colliding particles. In Eq. 1, by taking $p = 1, \ldots, N$, with N being the total number of excited levels of the considered emitting particle specie, a whole set of coupled differential equations, describing the temporal evolution of the population density of each excited state, is obtained. Such set is a simplified example of a CR model, which includes some of the most relevant processes for a low-pressure and low-temperature plasma. However, more processes can be included making models progressively closer to the reality. The resulting population densities n_p can be written in terms of population coefficients, $R_{0p} = n_p / (n_0 \cdot \rho_e(T_e))$, with n_0 being the ground state density, and n_p a function of ρ_e, as seen from Eq. 1. Since population coefficients are function of plasma parameters, they can be used to reproduce/match experimental measurements, and in particular to determine *averaged* electron density and temperature, inferred *via* emission-line ratios from plasma spectroscopy, along the line-of-sight. In this work, the Yacora CR model (Wünderlich et al., 2020) has been used, in which calculations assume only excitation from the respective ground state in both the atom and the molecule, mainly for diagnostics in low-pressure plasmas (namely for atomic hydrogen, molecular hydrogen, and helium). Line ratio, between two different emission wavelengths λ_j and λ_k, R_{λ_j/λ_k}, can be obtained by evaluating the ratio between effective emission rate coefficients,

$$R_{\lambda_j/\lambda_k} = \frac{\chi^{em}_{eff}(\lambda_j; \rho_e, T_e)}{\chi^{em}_{eff}(\lambda_k; \rho_e, T_e)} \propto \frac{I(\lambda_j)}{I(\lambda_k)}. \tag{2}$$

Thus, the line-ratio method only requires the analyzed spectra to have relatively calibrated their lines, making it more viable since no absolute intensity calibration is needed. However, the method is not fully exploitable for absolute information carried by single-line emission, leaving a possible full line interpretation only to absolutely calibrated spectra. With this limitation in mind, in the following we will present results on the basis of the line-ratio method, supported by a complete error analysis above the experimental results and the estimated plasma parameters. Several configurations of the plasma trap have been explored, and systematic data acquisition has been carried out. All spectra have been measured collecting the visible (VIS) light in the range 350–750 nm, *via* an optical fiber (NA = 0.22, core $\varnothing$ = 200 μm), connecting the spectrometer to a quartz window of a vacuum flange (see Figure 1D). Different acquisitions, ranging in 1–2 s, have been used dependent on the RF power employed to sustain the plasma. Figure 2 shows both magnetic field profiles used to confine the plasma and typical spectra collected in the VIS for both single-H_2 and H_2-Ar gas-mixture plasma. Further information on each experimental run are reported in Table 2.

2.3 Numerical investigation on electron cyclotron resonance plasma optical properties

Experimental activities would widely benefit of numerical studies of the plasma optical properties. The latter shows not only interesting properties as being an *active* medium but also ECR magneto-plasmas in trap are present with peculiar properties, such as high inhomogeneity and anisotropic energy distribution, due to the EM heating and the magnetic confinement. Therefore, in-laboratory ECR plasmas become an interesting physical *mean* to be described in terms of radiation–matter coupling, in order to support the envisaged experimental spectroscopic measurements. In the following, we present some numerical results concerning the impact of a *layered* plasma mean on the optical features of the plasma, in terms of varying electron density and temperature along one line-of-sight, including or not the presence of an external perturbing black-body radiation field (Section 2.3.1). By means of the same numerical approach, we provide some quantitative constraints on typical light-source properties, which can be compatible with the maximization of plasma opacity at given electron density and temperature, resulting from the OES experimental measurements (Section 2.3.2).

2.3.1 Impact of non-homogeneous plasma stratification on transmission spectroscopy

The problem of determining plasma parameters and structure from optically thin emission lines, whose emission coefficients and frequency-integrated intensities depend on both electron temperature and density, is widely discussed in the literature (Craig and Brown, 1976; Thompson et al., 1992), especially facing the fundamental limitations of observed spectral line-ratios as well-posed diagnostic method for inferring plasma parameters (Judge and Hubeny, 1995; Judge et al., 1997). The *inverse problem* is affected by large uncertainties in the case of non-isothermal and inhomogeneous emitting source, since the latter could be structured and layered along the line-of-sight of the detector, thus producing a *convoluted* spectral distribution

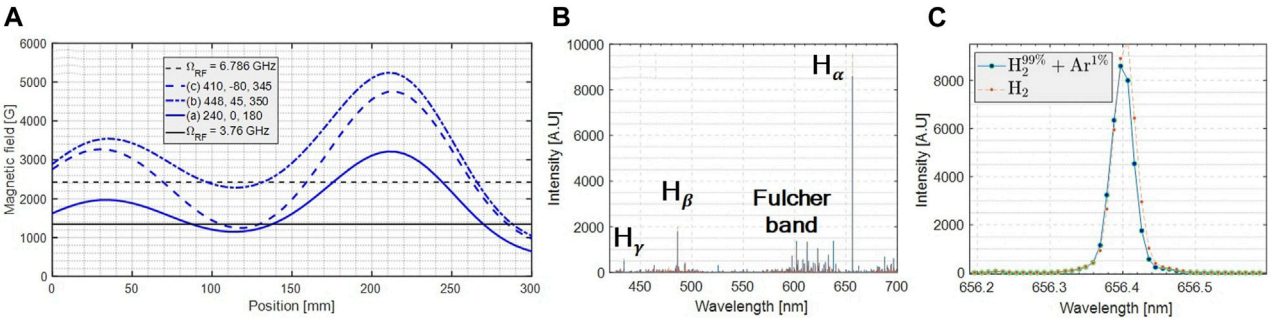

FIGURE 2
(A) Numerical calculation of the magnetic field profiles as function of solenoids currents, for the three configurations explored with OES, as reported in the legend. The microwave frequency ($B_{RF} = m_e 2\pi f_{RF}/e$), f_{RF} = 6.786(3.76) is drawn as solid (dashed) black line. **(B)** Spectra of emission-lines from H_2 plasma (orange) and $H_2^{99\%} + Ar^{1\%}$ gas-mixture plasma (blue). H-Balmer lines are indicated, along with the Fulcher-α band Q-branch lines ($d^3\Pi_u^- \rightarrow a^3\Sigma_g^+$). **(C)** Zoom-in of the H_α lines for both the single species and gas-mixture, for the high-frequency f_{RF} = 6.786, at 140 W, and p_0 = 10^{-2} mbar.

TABLE 2 OES experimental run details. Pure hydrogen (H_2) and hydrogen–argon mixture ($H_2^{99\%} + Ar^{1\%}$) cases are explicitly indicated. Configurations are labeled by n. (#) and B-field (a-c) - see also Figure 2A.

	B_{max}/B_{min}	f_{RF} [GHz]	p_0 [mbar]	P_{RF} [W]	t_{acq} [s]	N. of spectra
# 1, (a), H_2	2.7930	3.76	$9E-04$	100 ÷ 250	1	10
# 2, (a), H_2	2.7930	3.76	$1E-02$	100 ÷ 400	1	10
# 3, (a), $H_2^{99\%} + Ar^{1\%}$	2.7930	3.76	$1E-02$	100 ÷ 350	1	10
# 4, (b), H_2	2.2945	6.774	$1E-03$	40 ÷ 120	1	10
# 5, (c), H_2	3.8289	6.786	$1E-03$	40 ÷ 100	2	5
# 6, (c), H_2	3.8289	6.786	$1E-02$	40 ÷ 140	2	5
# 7, (c), $H_2^{99\%} + Ar^{1\%}$	3.8289	6.786	$1E-02$	40 ÷ 140	2	5

with an emission measure differential both in density and temperature. These layered-emission properties can be easily related to ECR plasmas. Therefore, studying this spectroscopic problem is of relevant interest for supporting experimental measurements. In this context, we performed numerical calculations of synthetic spectroscopic observables of emitting ECR plasmas, with a layered structure along one line-of-sight, at specific electron density and temperature. These latter are taken from previous self-consistent numerical simulations (Mishra et al., 2021) carried out to reproduce experimentally observed X-ray fluorescence emission of argon plasma, magnetically confined in a *minimum-B* profile, ignited, and sustained with microwave frequency and power, 12.84 GHz and 30 W, respectively. The numerical tool used is able to collect plasma electrons with similar parameters (density, EEDF) in regions of interest (ROIs) based on their *mean energy* content. *Clustering* of electrons in ROIs has been performed looking at electrons in the [0,2] keV energy range, along the longitudinal axis of the plasma chamber, crossing, the closed resonating magnetic isosurface at $B = B_{ECR} = 0.46$ T, as well as one of the employable spectroscopic line-of-sight designed for the plasma trap. Figure 3 shows the collection of nested mean energy isosurfaces inside the simulation domain, along with the ECR isosurface. A multi-slicing plot is superimposed on this, providing a cross-view of the space-dependent plasma's electron mean energy upon moving along the longitudinal axis. Seven main ROIs have been located here and are indicated as R in the figure. For each of these ROIs, one collective electron density and temperature (assuming a Maxwellian EEDF) is assigned. This simulation allows us to provide a hint of the structured plasma parameters along the experimental line. Electron density and temperature estimated supply the next numerical calculations by means of the ion population kinetics code known as FLYCHK (Chung et al., 2005). The code suite takes as inputs the plasma parameters to compute spectral observables of the plasma, such as opacity, emissivity, and intensity, according to the degree of plasma ionization and atomic level population distribution. Calculations have been performed in NLTE regime, which is typical of ECR sources, by solving the rate matrix equations arising from the CR model considered in the code suite, including

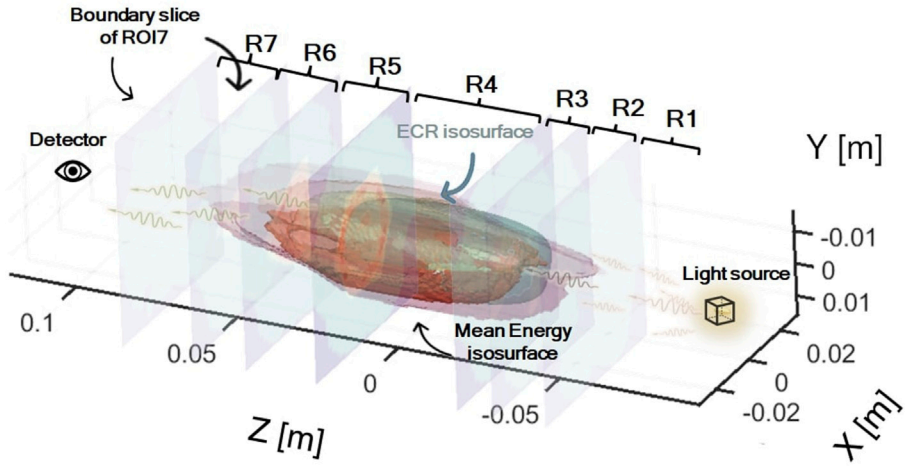

FIGURE 3
Representation of simulated plasma slicing along the longitudinal z-axis for studying the layered optical properties of Ar plasma. Nested isosurfaces refer to the volumetric collection of electron with the same mean energy content. Magnetic isosurface at the ECR (light-blue) is also shown. Along the z-axis regions of interest (R) have been selected and indicated in the figure, intersecting inhomogeneous plasma regions with different electron density ρ_e and energy $k_B T_e$, both numerically extracted in the [0,2] keV energy interval, and associated to each R. All the R is assumed as homogeneous plasma slab to be studied in FLYCHK, in the presence or not of a light source black-body radiation field.

both the collisional and radiative processes. The code is also capable to include the effects of external radiation field, on the basis of an input file containing the intensity of the source as a function of the radiation wavelength, which has been included and processed in our calculations. This latter has been performed to show the impact of a light source on the stratified optical properties of plasmas. Focusing on the numerical structure of opacity, this is computed in terms of the cross section for both *bound–bound* transitions (κ^{BB}), *bound–free* transitions (κ^{BF}), and *free–free* transitions (κ^{FF}). Radiation from BB transition peaks at a wavelength corresponding to the energy difference between two levels. BF transition is recombination radiation, whose wavelength corresponds to the sum of the kinetic energy of the recombining electron and the binding energy of the shell that the electron falls to. Bremsstrahlung radiation is emitted from FF transitions when free electrons lose their kinetic energy colliding with electrons or ions. While the FF process involves continuum states, whose opacity mostly depends on electron density and temperature, the BF and BB also depend on the ion stage population of excited levels in the atomic shell. For instance, the BB opacity is given as

$$\kappa_{\lambda}^{BB} = N_{\ell}\left(1 - \frac{N_u g_{\ell}}{N_{\ell} g_u}\right)\frac{\pi e^2}{\rho mc} f_{\ell u}\varphi_{\lambda} \quad [\mathrm{cm^2 g^{-1}}], \tag{3}$$

where the population density of the upper (lower) level is $u(\ell)$, $N_u(N_\ell)$, $g_u(g_\ell)$ are the degeneracy factors, ρ [g cm^{-3}] is the density of the specie, $f_{\ell u}$ is the oscillator strength, and φ is the line profile function. At low-temperature blue-KN ejecta conditions ($T \leqslant 10^4$ K), together with a low ionization level, typically κ^{BB} results to be prominent among the other terms. The numerical results from calculations of the plasma opacity including all three possible contributions, and performed for the argon plasma as structured from self-consistent simulations are presented and discussed in Section 3.2.

2.3.2 Light-source dimensioning for electron cyclotron resonance plasma spectroscopy based on optical emission spectroscopy measurements

Numerical calculations by using FLYCHK can also support the experimental design, and in particular the light-source dimensioning in terms of power and/or spectral irradiance to be used for transmission spectroscopy, and for measuring the line-integrated opacity of emitting plasma. We have performed calculations of synthetic spectral observables, focusing on the opacity term, to study the impact of external black-body radiation fields on the latter, for gaseous as well as for metallic species of interest for the KN studies. Contrarily to what has been carried out about the layered plasma emission, described earlier in Section 2.3.1, plasma parameters used in these calculations are not derived from 3D numerical simulations, but rather they are constrained by the estimates from OES observations during the experiment, as described in Section 2.2.2, which results are present in Section 3.1. In doing this, we have assumed plasma parameters for metallic plasmas similar to the gaseous experimentally explored so far, given that metallic species atom fractions with respect to the plasma buffer gas (e.g., Ar) is usually not exceeding 1 %. Moreover, and for

simplicity, no structured emission is considered in these calculations, but a rather homogeneous emitting plasma source. We aim at finding a good experimental trade-off among light-source intensity and the evidence of more opaque spectral region, whose absorption feature are better observable during the transmission measurements.

3 Results and discussion

In the following, we report on the experimental data collected *via* OES, and on the data analysis performed to estimate both electron density and temperature, along with their experimental uncertainties, as resulting from the line-ratio method applied to the hydrogen Balmer's lines (H_α, H_β, and H_γ). Moreover, numerical results concerning the plasma optical properties arose by the calculations with FLYCHK will be presented, focusing on the predicting power of simulations to support future experimental measurements, as well as to investigate on the plasma stratification problem, and thus on the light-emission convolution, along experimental line-of-sights.

3.1 Experimental data analysis

Several plasma trap configurations (hereafter, *cfgs*) have been investigated, but only seven of these have been chosen to make systematics in terms of RF power (P_{RF}), based on the plasma stability and reproducibility, as reported in Table 2. The latter, beyond the capability of the plasma trap to engage, ignite, and sustain, the plasma at a given frequency (f_{RF}) and magnetic confinement, has been probed *via* OES by looking at the stability of $H_{\alpha,\beta,\gamma}$ emission lines, and in particular on their ratios, that is, $H_{\alpha\beta}$ =H_α/H_β, and $H_{\beta\gamma}$ =H_β/H_γ, during many acquisitions at fixed P_{RF}. Example of such on-line analysis is shown in Figures 4A,B for one of the configurations. The ratios employed for monitoring are calculated from the analysis performed on each spectrum. A dedicated code written in MATLAB © has been developed to perform the spectral analysis, by means of least-square fit procedure of emission peak of interest, along with the error derivation from the fit procedure. Multiple-Gaussian fits are employed to improve the fit procedure, and the peak area is used as a central value of the ratios. In the end, the error analysis including both statistical error and uncertainty led by the fit procedure is computed *via* the error propagation formulas. The following analysis flow is considered:

- Fitting procedure on the peaks of the H-spectra. The general formula for the peak's area calculation fit by N Gaussian function ($f(\lambda) = a \cdot \exp(-(\lambda - b)^2/c^2)$), is given as

$$A_{\lambda_j} = \sum_{i=1}^{N} \frac{a_i \cdot c_i \cdot \sqrt{\pi}}{\Delta\lambda}, \tag{4}$$

where N is the number of Gaussian functions used, a_i, c_i, are the i-th coefficients from fit parameters, $\Delta\lambda$ is the spectral bin width. Areas of the peaks refer to the related line-intensities, and to the population rate coefficients, accordingly to Eq. 2.

- Calculation of the ratios, $H_{\alpha\beta} = A_{\lambda_\alpha}/A_{\lambda_\beta}$ and $H_{\beta\gamma} = A_{\lambda_\beta}/A_{\lambda_\gamma}$ for each spectrum and for all the configurations.
- Error propagation procedure to estimate uncertainties. For each spectrum, each calculated area below the peaks carries an error, given as

$$\delta A_{\lambda_j} = \sqrt{\sum_{i=1}^{N}\left[\left(\frac{\partial A_{\lambda_j}}{\partial a_i}\right)^2 \sigma_{a_i}^2 + \left(\frac{\partial A_{\lambda_j}}{\partial c_i}\right)^2 \sigma_{c_i}^2 + 2\sigma_{a_i c_i}\frac{\partial A_{\lambda_j}}{\partial a_i}\frac{\partial A_{\lambda_j}}{\partial c_i}\right]}, \tag{5}$$

with $\sigma_{a,c}$ the standard deviation on a, c fit coefficients, and σ_{ac} the *correlation coefficients* from the covariance matrix. The latter terms contribute to the total error only in case of correlations among the fit coefficients in the Eq. 4. The covariance analysis has shown generally non-zero correlation elements σ_{ac}, which however are negligible with respect the other terms, and hence they have been ruled out from later on estimates of errors. By means of Eqs 4, 5, error propagates also to the ratios as

$$\begin{aligned} \delta H_{\alpha\beta} &= H_{\alpha\beta}\sqrt{\left(\frac{\delta A_{\lambda_\alpha}}{A_{\lambda_\alpha}}\right)^2 + \left(\frac{\delta A_{\lambda_\beta}}{A_{\lambda_\beta}}\right)^2}, \\ \delta H_{\beta\gamma} &= H_{\beta\gamma}\sqrt{\left(\frac{\delta A_{\lambda_\beta}}{A_{\lambda_\beta}}\right)^2 + \left(\frac{\delta A_{\lambda_\gamma}}{A_{\lambda_\gamma}}\right)^2}. \end{aligned} \tag{6}$$

- Since we have a set of S independent measurements of the peaks area, each of them equally important, but with some of them carrying unequally large uncertainties, it is sounder computing the so-called *inverse variance weighting*, onto a *weighted mean* of ratios, which gives more weight to the measurements with less uncertainty (Taylor, 1996; Knoll, 2010). Thus, we proceed calculating the weighted mean ratio for each configuration, $\langle H_{\alpha\beta}\rangle$ and $\langle H_{\beta\gamma}\rangle$, according to

$$\langle H_{\alpha\beta,\beta\gamma}\rangle = \frac{\sum_{i=1}^{S} w_i^{\alpha\beta,\beta\gamma} H_{\alpha\beta,\beta\gamma}}{\sum_{i=1}^{S} w_i^{\alpha\beta,\beta\gamma}}, \tag{7}$$

with $w_i^{\alpha\beta,\beta\gamma} = 1/\delta H_{\alpha\beta,\beta\gamma}^2$ being the weights obtained through Eq. 6. The standard error associated to Eq. 7 can be then computed by applying the propagation formula to the latter (Knoll, 2010), which is given as

$$\begin{aligned} \sigma^2_{\langle H_{\alpha\beta,\beta\gamma}\rangle} &= \frac{\sum_{i=1}^{S} w_i^{\alpha\beta,\beta\gamma}\left(H_{\alpha\beta,\beta\gamma} - \langle H_{\alpha\beta,\beta\gamma}\rangle\right)^2}{\sum_{i=1}^{S} w_i^{\alpha\beta,\beta\gamma}} \frac{n_{eff}}{n_{eff}-1}, \\ \text{with} \quad n_{eff} &= \frac{\left(\sum_{i=1}^{S} w_i^{\alpha\beta,\beta\gamma}\right)^2}{\sum_{i=1}^{S}\left(w_i^{\alpha\beta,\beta\gamma}\right)^2}. \end{aligned} \tag{8}$$

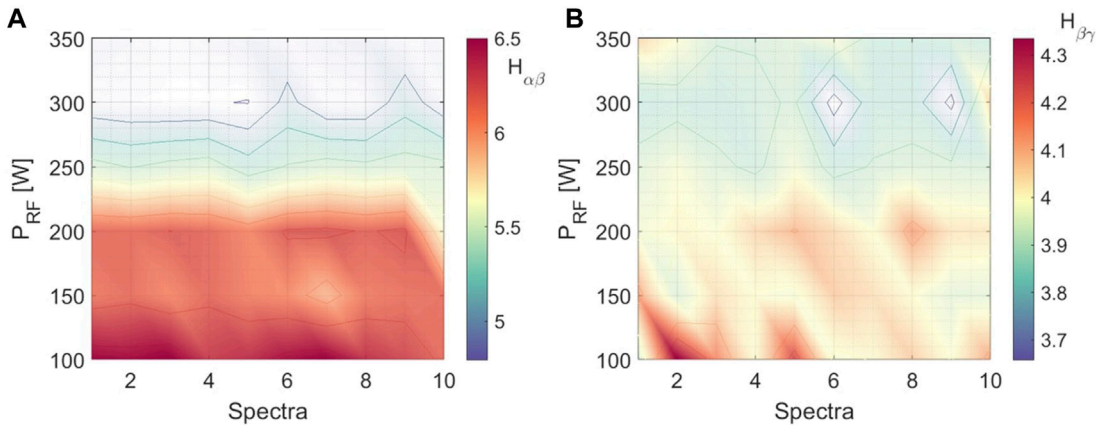

FIGURE 4
Monitoring of $H_{\alpha\beta}$ **(A)** and of $H_{\beta\gamma}$ **(B)** in the RF power (P_{RF} [W]) - spectra plane. Both refer to the experimental run 3, at f_{RF} = 3.76 GHz, p_0 = 1*E* – 03 mbar.

In Figures 5A,B the mean ratios given as from Eq. 7, and related uncertainties from the error analysis are shown as a function of RF power, for all the configurations examined. Considering the mean line-ratios and their experimental uncertainties, we therefore compared the latter to the theoretical ones, as resulting from numerical calculations using the Yacora CR model (Wünderlich et al., 2020). Theoretical ratios, $\mathcal{H}_{\alpha\beta}$ and $\mathcal{H}_{\beta\gamma}$, have been estimated for several electron densities ρ_e and energies (hereafter, *temperature* T_e, assuming a Maxwellian EEDF), and are shown in Figures 6A,B as surface plot in the (ρ_e, k_BT_e) plane. On top of theoretical data, we drew the observed isoline ratios, collecting all the possible points (ρ_e, T_e) matching with the observable (solid line). The same is made for the *upper* and *lower* values of ratios - as coming from adding uncertainties from Eq. 8 - generating other possible points, and providing a range of solutions for the *inverse* problem of inferring ρ_e and T_e from the spectroscopic observables $H_{\alpha\beta,\beta\gamma}(\rho_e, T_e)$. In particular, a solution can be found by solving the following non-linear system

$$\begin{cases} \mathcal{H}_{\alpha\beta}(\rho_e, k_BT_e) = \langle H_{\alpha\beta}\rangle + \sigma_{\langle H_{\alpha\beta}\rangle} \\ \mathcal{H}_{\beta\gamma}(\rho_e, k_BT_e) = \langle H_{\beta\gamma}\rangle + \sigma_{\langle H_{\beta\gamma}\rangle}, \end{cases} \tag{9}$$

which if exists, should be *unique*. In other words, this is equivalent to find a cross-point in the (ρ_e, T_e) plane between the experimental isolines $H_{\alpha\beta}$ and $H_{\beta\gamma}$. If it exists, then a solution to the system of Eq. 9 exists too, and this provides an estimate of the *averaged* electron density and temperature, along the spectroscopic line-of-sight. The error committed in the estimates should be calculated propagating the uncertainties of measured ratios in the equation system. However, this is not an easy task to be accomplished. Beyond the degree of complexity in solving this uncertainty analysis, due to the non-linearity nature of the problem, and to the lack of analytical functions describing both $\mathcal{H}_{\alpha\beta}$ and $\mathcal{H}_{\beta\gamma}$, determining the electron density and temperature uncertainties $\delta\rho_e$, δk_BT_e is both analytically and numerically difficult. To make progress on it, we faced the problem from a different perspective. In particular, as it is shown in Figure 7B, we found upper and lower limits for both ρ_e and T_e from graphical solutions, as led by crosses of observed ratio uncertainties on the theoretical surface, that is, $H_{\alpha\beta} \pm \sigma_{\langle H_{\alpha\beta}\rangle}$, and $H_{\beta\gamma} \pm \sigma_{\langle H_{\beta\gamma}\rangle}$, as also shown in Figures 6A,B. These results deserve to be further discussed. First, the range of electron density and temperature found still represent line-convoluted average quantities, still suffering from the mentioned emission measure differential in temperature and density of structured plasmas (see Section 2.3.1), depicting *global* rather than *local* plasma parameters. Second, the line-ratio method carries several uncertainties due to relative intensities of the spectral features, which cannot be alternatively treated in this work, and which require absolute calibration of the instruments to improve the physical interpretation of OES data. The quality of the modeling results, on which relies the accuracy of diagnostic outcome by the line-ratio method, also depends on the existence and quality of cross section and rate coefficient data for the CR processes. As it can be evinced by Figure 7A, derived plasma parameters from OES measurements are generally affected by small uncertainties, especially in the low-T_e region ($k_BT_e \leq 10$ eV), in contrast to those belonging to the high-T_e range, for which error bars are larger (up to 50% relative error, see Table 4). This can be partially addressed to the theoretical trend of ratio isolines on the (ρ_e, k_BT_e) plane, which for higher values of k_BT_e bend into a quasi-flat curve. Thus, assuming even a small $\delta\rho_e$, a larger δk_BT_e could be expected, and therefore a large range of possible crossed electron temperatures. Contrarily, in the low-T_e range, small uncertainties δk_BT_e could

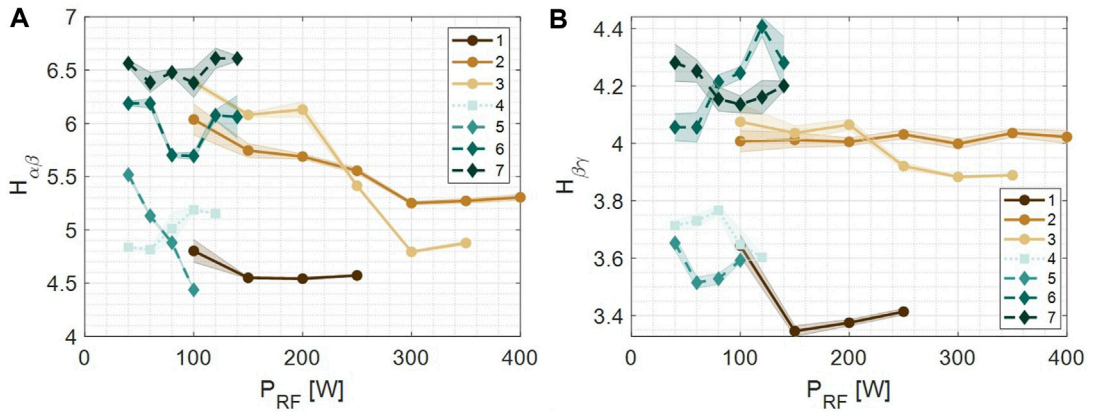

FIGURE 5
Averaged $\langle H_{\alpha\beta}\rangle$ **(A)** and $\langle H_{\beta\gamma}\rangle$ **(B)** vs. P_{RF} over all spectra for each RF power, including uncertainty from error propagation (shaded region). Different experimental run are labeled according to Table 2 and shown in the legend.

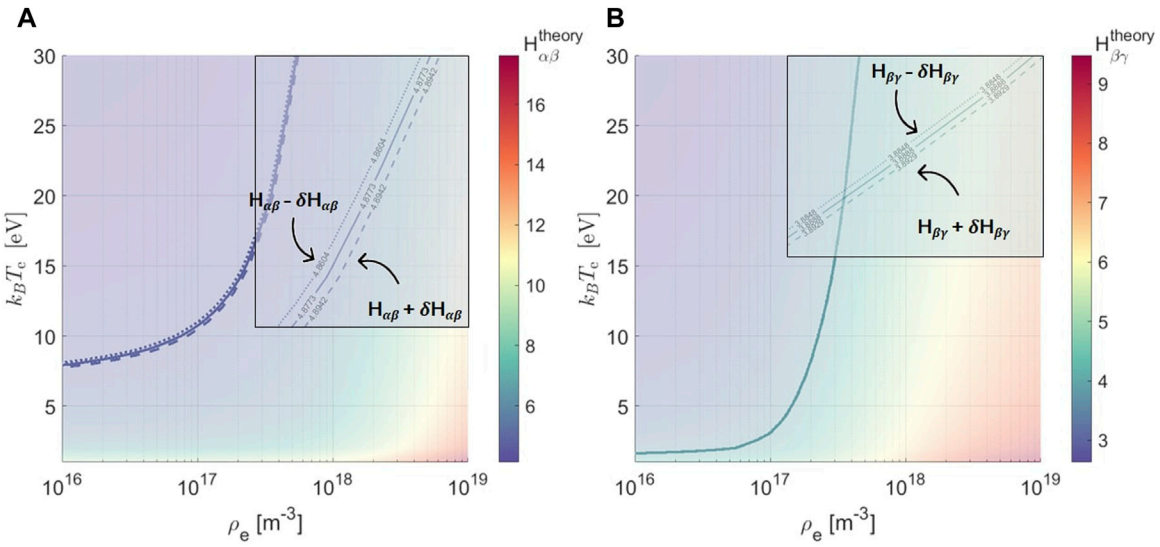

FIGURE 6
Surface-contour plot of experimental $\langle H_{\alpha\beta}\rangle$ *isoline* (solid line) on top of theoretical $\mathcal{H}_{\alpha\beta}$ *isosurface* **(A)**, and of experimental $\langle H_{\beta\gamma}\rangle$ *isoline* (solid line) on top of theoretical $\mathcal{H}_{\beta\gamma}$ *isosurface* **(B)**, from Yacora calculations, on the plane energy $k_B T_e$ [eV] vs. electron density ρ_e [m^{-3}]. Experimental uncertainties $\sigma_{\langle H_{\alpha\beta,\beta\gamma}\rangle}$ are shown as dashed (dotted) lines, better evinced in the insets. Both plots refer to the experimental run 3, at P_{RF} = 350 W.

lead to a larger $\delta\rho_e$, and thus to a large range of possible crossed densities. Moreover, looking at Figures 8A,B other important features on plasma parameters dependencies on RF power and neutral gas pressure can be evinced. Generally, the low-pressure configurations (1, 4, and 5) show the largest temperatures, whereas high-pressure ones largely decrease the electron temperature. This effect could be explained in terms of a larger number of collisions in the plasma chamber upon increasing the pressure, which thermalize electrons, hence providing a low-shifting of the EEDF peak. On the other side, upon increasing the RF power, there is an expected enhancement of T_e (see e.g., cfgs. 2,3) proportional to the electric field strength increasing with microwave power. Moreover, an increase of electron density, more likely driven by a combination of power- and pressure-dependent parameters such as *cyclotron electron number density*, neutral gas density supplied at the ECR zone, and gas flow rate within the ECR zone, is shown. These are very sensitive to the electromagnetic power released by

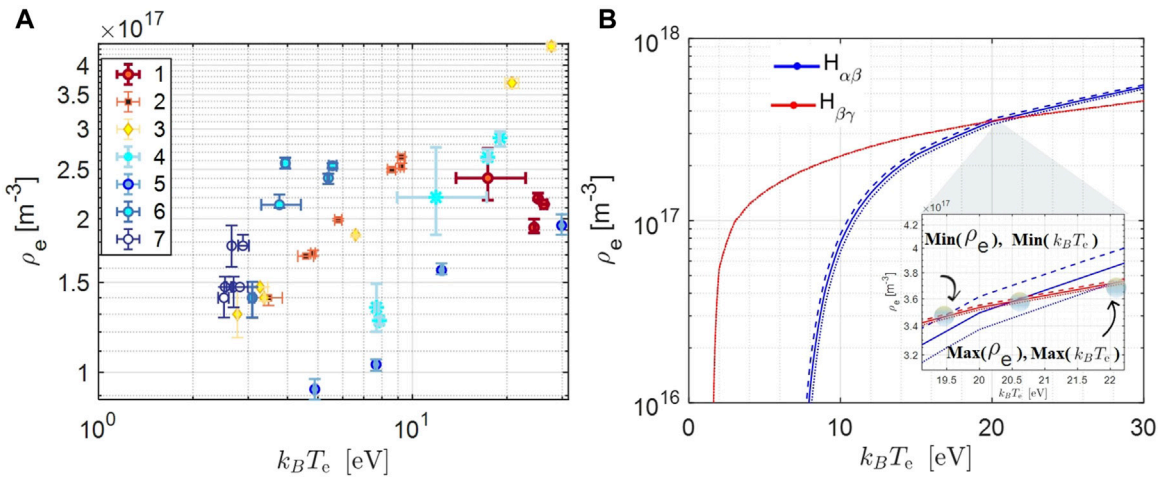

FIGURE 7
(A) Electron density ρ_e [m^{-3}] - energy $k_B T_e$ [eV] grid with uncertainties range ($\pm\delta\rho_e$, $\pm\delta k_B T_e$) on both (ρ_e, $k_B T_e$). Points belonging to the same experimental run are labeled according to the Table 2 and indicated in the legend. **(B)** Typical cross between experimental line ratios, $H_{\alpha\beta}$, $H_{\beta\gamma}$ on the (ρ_e, $k_B T_e$) plane, as arising from Figure 6. Same carried out for the increased (decreased) ratios by respective uncertainties, plot as dashed (dotted) lines. Blobs in the inset indicate the cross, and represent the estimates for the central value and uncertainty on electron density and electron energy. The data refer to the experimental run 3, at f_{RF} = 3.76 GHz, p_0 = 1*E* − 03 mbar, and P_{RF} = 350 W.

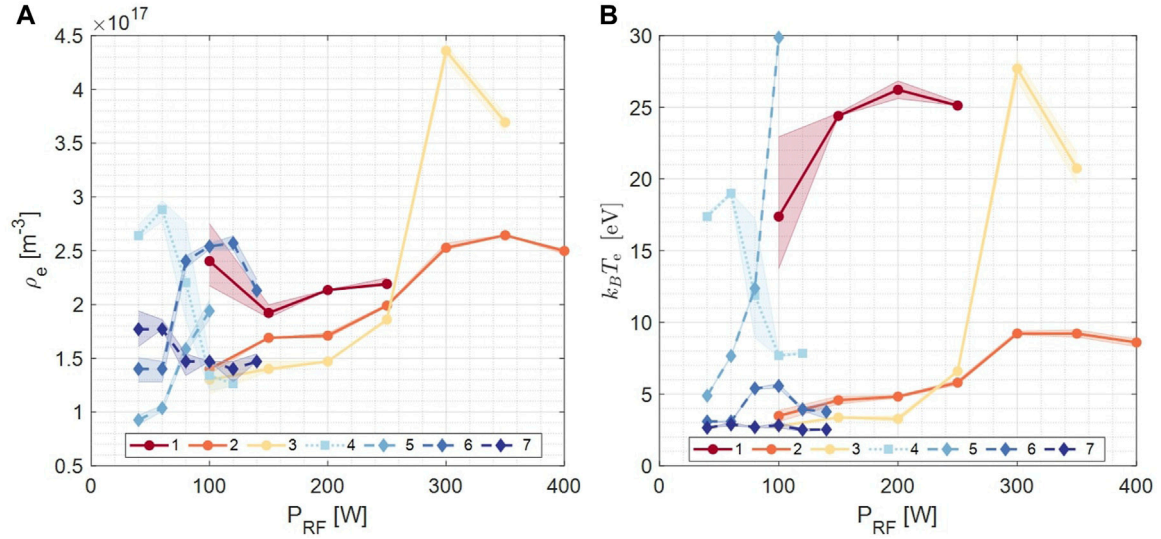

FIGURE 8
(A) Averaged density ρ_e [m^{-3}] vs. P_{RF} [W] over all spectra for each RF power, including uncertainty range from the graphical solution of the non-linear system, as shown in Figure 6 (shaded region). **(B)** Averaged electron energy $k_B T_e$ [eV] vs. P_{RF} over all spectra for each RF power, including uncertainty range from the graphical solution of the non-linear system, as shown in Figure 6 (shaded region). Different experimental run are labeled according to Table 2 and shown in the legend.

propagating microwaves in plasma and heating cyclotron electrons. Further observations can be provided by considering the RF frequency tuning and the different magnetic confinement adopted in each of the configurations. By increasing the microwave frequency from ~3.76 GHz (cfgs. 1–3) to ~6.78 GHz (cfgs. 4–7), we shifted up the density cut-off by almost a factor 4, going from $1.76 \cdot 10^{17}$ m^{-3} to $5.71 \cdot 10^{17}$ m^{-3}, respectively, which allowed to push up the electron density even

TABLE 3 Plasma parameters, *electron density* ρ_e [m^{-3}], and energy k_BT_e [eV], estimated from numerical simulations along the longitudinal z-axis of the plasma chamber, for argon plasma confined in minimum-B-field, sustained by 12.84 GHz frequency and microwave power of 30 W.

	ROI 1	ROI 2	ROI 3	ROI 4	ROI 5	ROI 6	ROI 7
ρ_e [10^{17} m^{-3}]	0.114	0.630	1.24	1.44	1.30	0.707	0.210
k_BT_e [eV]	38.10	100.10	140.40	112.50	138.30	103.40	46.80

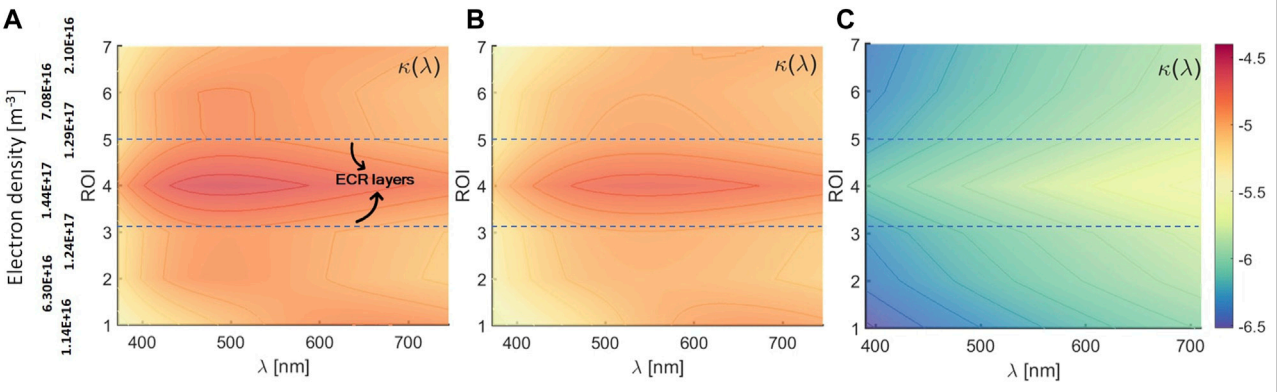

FIGURE 9
Numerical opacity $\kappa(\lambda)$ [cm^2g^{-1}] (log scale) of argon plasma in the VIS range, as resulting from NLTE CR calculations in FLYCHK, for **(A)** *unperturbed* self-emitting plasma, and plasma perturbed by an external black-body radiation field [erg m^{-2} s^{-1} Hz^{-1}] at 8000 K, with smaller **(B)** and larger **(C)** intensities. Opacity is shown in the wavelength λ [nm] - n. ROI (electron density ρ_e [m^{-3}]) plane. The ROI n. label increases upon moving from negative to positive z-axis position along the longitudinal z-axis of numerically simulated plasma , as described in Section 2.3.1 and shown in Figure 3. ECR layers are shown (blue-dashed lines).

if dealing with lower RF powers. Excluded few cases at large RF powers, where the electron density estimates slightly overcomes the cut-off (e.g., cfg. 3), the remaining cases do not overcome the cut-off values. In addition, a change in the axial magnetic field profile modifies the confinement, then influencing the electron heating efficiencies and plasma stability (Mazzaglia et al., 2018). Finally, in some of the configurations explored, we made use of a small amount of Ar gas (1%) as contaminant and tracer, adequately dosed by means of the RGA system described in Section 2.2.1, with the intent to make self-consistent cross-measurements of density from both H-lines and Ar-lines, assuming that theoretical hydrogen line-ratios are still comparable with the spectral outcome from this mixture. Beyond the Ar-lines analysis, which is missing in this article and still under analysis, one could preliminarily speculate on possible beneficial effects led by the Ar component in the H_2-gas buffer. In particular, concerning the decrease of electron temperature observed in the cfg. 7 with respect the cfg. 6, possibly due to non-resonant interactions between the species (Phelps, 1992) (e.g., charge exchanges, gas mixing effects (Antaya, 1989; Delaunay, 1992; Tarvainen et al., 2005)). Indeed, collisions of H with Ar are peculiar because of the very large cross sections for excitation of the H atoms at low energies (Phelps, 1992). Moreover, gas mixing beneficial impact has long been discussed in the ECR ion source community, explained through the energy exchange between the lighter and heavier species, with the heavier ones cooled down (*ion cooling* mechanism (Tarvainen et al., 2005)). This leads to a better confinement of the heavier species, while deteriorates that one of the lighter species. In our case, the mixing-driven deconfinement of H atoms might lead to a depletion of the reservoir of excited H atoms, which should turn into a decreasing intensity of emission line. This fact seems compatible with what observed, as it is shown in Figures 2B,C looking at the H_α line. However, further studies are necessary for sounder conclusions on the electron temperature decreasing mechanism, making use of absolutely calibrated spectra, which would certainly shed light on these properties. To conclude, among the several characterized plasmas, the most promising plasma parameters for the envisaged opacity measurements in the context of the blue-KN ejecta stage have been collected within the high-frequency and high-pressure cases (cfgs. 6 and 7), with electron temperature close to few eV and densities suitable to the astrophysical scenario.

TABLE 4 Plasma parameters (*electron density* ρ_e [m^{-3}], and energy k_BT_e [eV]), estimated from OES measurements for different experimental configurations, in terms of *B-field* (Injection, Mid, and Extraction coil polarized current) [(a): 240 A, 0 A, 180 A; (b): 448 A, 45 A, 350 A; (c): 410 A, − 80 A, 345 A], *RF frequency* (f_{RF} [GHz]), *gas pressure* p_0 [mbar], and *RF power* P_{RF} [W]. Gradient-color (red−white−blue) provides indications on the energy (temperature) gradient (■ hotter, ■ colder) for the many configurations explored. Gas-mixture cases are explicitly reported in the table.

	B	f_{RF}	p_0							
P_{RF}	**(a)**	3.76	$9E-04$	100	150	200	250			
ρ_e	$\mathbf{H_2}$			$2.40^{-2.17}_{+2.75}E17$	$1.92^{+2.00}_{-1.87}E17$	$2.13^{+2.13}_{-2.13}E17$	$2.19^{+2.24}_{-2.17}E17$			
k_BT_e				$17.38^{-13.76}_{+22.94}$	$24.40^{+24.60}_{+24.45}$	$26.22^{-25.61}_{+26.84}$	$25.12^{+25.26}_{+25.36}$			
P_{RF}	**(a)**	3.76	$1E-02$	100	150	200	250	300	350	400
ρ_e	$\mathbf{H_2}$			$1.40^{-1.35}_{-1.40}E17$	$1.69^{+1.69}_{-1.69}E17$	$1.71^{+1.74}_{-1.69}E17$	$1.99^{+2.00}_{-1.98}E17$	$2.53^{+2.57}_{-2.51}E17$	$2.64^{+2.65}_{-2.64}E17$	$2.50^{+2.51}_{-2.47}E17$
k_BT_e				$3.48^{-3.08}_{+3.85}$	$4.56^{-4.31}_{+4.85}$	$4.83^{-4.75}_{+4.90}$	$5.80^{-5.65}_{+5.96}$	$9.23^{-9.15}_{+9.40}$	$9.22^{-8.98}_{+9.47}$	$8.60^{-8.32}_{+8.84}$
P_{RF}	**(a)**	3.76	$1E-02$	100	150	200	250	300	350	
ρ_e	$\mathbf{H_2^{(99)}}$			$1.30^{+1.47}_{-1.17}E17$	$1.40^{+1.47}_{-1.38}E17$	$1.47^{+1.47}_{-1.47}E17$	$1.86^{+1.86}_{-1.84}E17$	$4.36^{-4.29}_{+4.41}E17$	$3.69^{-3.60}_{+3.77}E17$	
k_BT_e	$+\mathbf{Ar^{(1)}}$			$2.77^{-2.76}_{+2.78}$	$3.37^{-3.35}_{+3.40}$	$3.27^{-3.09}_{+3.46}$	$6.50^{-6.49}_{+6.66}$	$27.70^{-26.88}_{+28.76}$	$20.74^{-19.72}_{+21.79}$	
P_{RF}	**(b)**	6.774	$1E-03$	40	60	80	100	120		
ρ_e	$\mathbf{H_2}$			$2.64^{+2.74}_{-2.61}E17$	$2.88^{+2.96}_{-2.77}E17$	$2.20^{-1.86}_{+2.76}E17$	$1.34^{+1.49}_{-1.20}E17$	$1.26^{+1.28}_{-1.24}E17$		
k_BT_e				$17.37^{+17.63}_{+17.53}$	$19.00^{+19.02}_{-18.83}$	$11.88^{-8.94}_{+17.25}$	$7.69^{+7.81}_{-7.58}$	$7.85^{-7.83}_{+7.89}$		
P_{RF}	**(c)**	6.786	$1E-03$	40	60	80	100			
ρ_e	$\mathbf{H_2}$			$0.93^{+0.97}_{-0.88}E17$	$1.03^{+1.06}_{-0.97}E17$	$1.58^{+1.63}_{-1.01}E17$	$1.94^{+2.04}_{-1.56}E17$			
k_BT_e				$4.88^{-4.84}_{+4.92}$	$7.66^{-7.58}_{+7.71}$	$12.37^{-12.33}_{+12.54}$	$29.86^{+29.99}_{-29.75}$			
P_{RF}	**(c)**	6.786	$1E-02$	40	60	80	100	120	140	
ρ_e	$\mathbf{H_2}$			$1.40^{+1.50}_{+1.86}E17$	$1.40^{+1.47}_{-1.28}E17$	$2.40^{+2.45}_{-2.34}E17$	$2.54^{+2.57}_{-2.51}E17$	$2.57^{+2.63}_{-2.51}E17$	$2.13^{+2.23}_{+2.10}E17$	
k_BT_e				$3.09^{-3.09}_{-3.08}$	$3.09^{-3.01}_{+3.14}$	$5.40^{-5.35}_{+5.43}$	$5.56^{-5.41}_{+5.74}$	$3.93^{-3.84}_{+4.05}$	$3.77^{-3.30}_{+4.42}$	
P_{RF}	**(c)**	6.786	$1E-02$	40	60	80	100	120	140	
ρ_e	$\mathbf{H_2^{(99)}}$			$1.77^{+1.94}_{-1.61}E17$	$1.77^{+1.86}_{-1.77}E17$	$1.47^{+1.54}_{-1.34}E17$	$1.47^{+1.47}_{-1.47}E17$	$1.40^{+1.47}_{-1.28}E17$	$1.47^{+1.54}_{-1.47}E17$	
k_BT_e	$+\mathbf{Ar^{(1)}}$			$2.65^{-2.65}_{+2.66}$	$2.88^{-2.78}_{+3.01}$	$2.69^{-2.67}_{+2.70}$	$2.82^{-2.64}_{+2.99}$	$2.51^{-2.40}_{+2.60}$	$2.53^{-2.51}_{+2.56}$	

10.3389/fspas.2022.931744

3.2 Numerical results on optical properties

The numerical results on the plasma opacity performed by using FLYCHK for the argon plasma as structured from self-consistent simulations are presented and discussed here. Despite no numerical data are available yet on plasma conditions that could be suitable for opacity measurements, like those at high-pressure and low-power, which could provide under-dense and low-temperature plasmas in FPT, as shown in Section 3.1, the main goal for the moment is to demonstrate that we are able to unfold non-uniform plasma data collection. The latter in order to get reliable results from the observable that we need to measure: the opacity. Thus, according to the numerical tools we have described in Section 2.3.1, it is more straightforward to start from a higher energy content plasma than it is actually needed. In Table 3 we report on the density and temperature numerically estimated for each of the ROIs considered along the line-of-sight. As it can be evinced, there is a gradual increase of density upon moving toward the center of the chamber axis (ROI 4), where the plasmoid core is expected to be more dense, with respect to the external (halo) region. The same ROI presents a higher temperature compared to the external ROIs, however smaller if compared with neighboring ones, ROI 3 and 5, which correspond to the ECR layer and to the regions maximizing the electron heating, thus their energy. Because of the relative high electron temperature, the total amount of opacity in the VIS range turns out to be very low ($\kappa < 10^{-4}$ cm^{2}g^{-1}), as it is possible to observe in Figure 9. Indeed, electrons with hundreds of eV of energy will impact more on level population distribution and atomic line transitions belonging to higher energy states, in the soft-X-ray emission range, which is out of the EM range of interest for this work. The influence of higher-density ROIs in Figure 9 is also highlighted, where as expected the most opaque plasma arises from the inner plasmoid region in between of the ECR layers. Furthermore, we also explored the influence of an external black-body radiation field to the plasma opacity, which results are shown in Figures 9B,C, with a photon flux of ~ 10^{25} s^{-1}m^{-2}, and ~ 10^{32} s^{-1}m^{-2}, respectively. An important effect can be evinced with respect to the unperturbed plasma opacity shown in Figure 9A (i.e., without any external radiation field), especially in the case of the largest photon flux affecting the plasma source - see Figure 9C. Here, the opacity decreases by 1–2 orders of magnitudes ($\kappa < 10^{-5}$ cm^{2}g^{-1}). This phenomenon can be explained by a radiation-driven progressive de-population mechanism of lower energy levels for given atomic transition lines, thus reducing N_ℓ and tending to equilibrate the latter to the corresponding upper level density population, N_u, which accordingly to Eq. 3 pushes the system in the limit of zero opacity (i.e., transparent plasma) upon increasing the radiation field intensity. An analysis of the occupation number of energy levels, as resulting from FLYCHK calculations, has confirmed this hypothesis. We have extended calculations of synthetic opacity to further study the impact of external black-body radiations on the latter, for gaseous as well as for metallic species of interest for the KN studies. In doing this, we have considered measured electron density and temperature from OES, in particular studying, the case of plasma from cfg. 7 at P_{RF} = 120 W, neglecting for a moment the plasma stratification problem. Input plasma parameters are considered from estimates in Table 4. We started by studying the gaseous case (Ar), which results for the opacity contribution are shown in Figure 10. As it is possible to observe in Figure 10A, numerical opacity at this temperature is extremely larger ($\kappa \lesssim 1$ cm^{2}g^{-1}) if compared with results shown in Figure 9, effect apparently only due to the lower temperature. Indeed, at higher plasma temperature, the opacity largely decreases as expected from the energy shifting of absorption transition lines led by more energetic electrons, as shown in Figure 10B, also changing the expected dependency on the wavelength. An increasing radiation field intensity similar to that shown in Figure 9 impacts on the opacity terms, which quickly drops down of several orders of magnitude. Looking at metallic species, we performed the same calculations for the argon plasma, but considering metallic plasmas made of selenium, strontium, zirconium, and niobium, among the most favored elements for the experimental measurements. Results are shown in Figure 11, where both low-temperature (top row) and high-temperature (bottom row) cases are shown. All the self-emitting metallic plasmas (no external photon flux) are extremely opaque, with $\kappa \sim 10^3$ cm^{2}g^{-1}. Including a radiation field, slightly impacts these numbers, unless one goes for sources with a high photon flux (~ 10^{32} s^{-1}m^{-2}), which would decrease such values. As similar to results obtained for the argon plasma, by increasing the electron temperature, the opacity decreases several orders of magnitude. This is not the case of niobium opacity, which seems to be enhanced in the case of hotter plasma, likely due to an increasing complexity of electronic shells. To conclude, the numerical investigation has highlighted peculiar modification of plasma opacity led by a structured ECR plasma, providing numerical predictions of the latter, accordingly to the atomic database on argon transitions, which could support future experimental measurements in gaseous plasmas. Further investigations, extending the method by giving additional inputs to FLYCHK for more precise calculations, for example, the ECR charge state distribution expected for metallic/gaseous plasmas, which numerical study is under development (Mishra et al., 2020), will produce outputs more tight to real scenarios achievable with experiments. Thus, having access to layered optical properties of the plasma would help in deconvolving the stratified emission, otherwise only partially decoded by the inverse problem techniques, and still suffering from residual large uncertainties. Finally, numerical simulations of opacity under experimentally explored plasma conditions, and close to the blue-KN ejecta parameters, can certainly support the dimensioning of light source features for future transmission spectroscopic measurements, finding a good trade-off between the source and its transparency through the plasma.

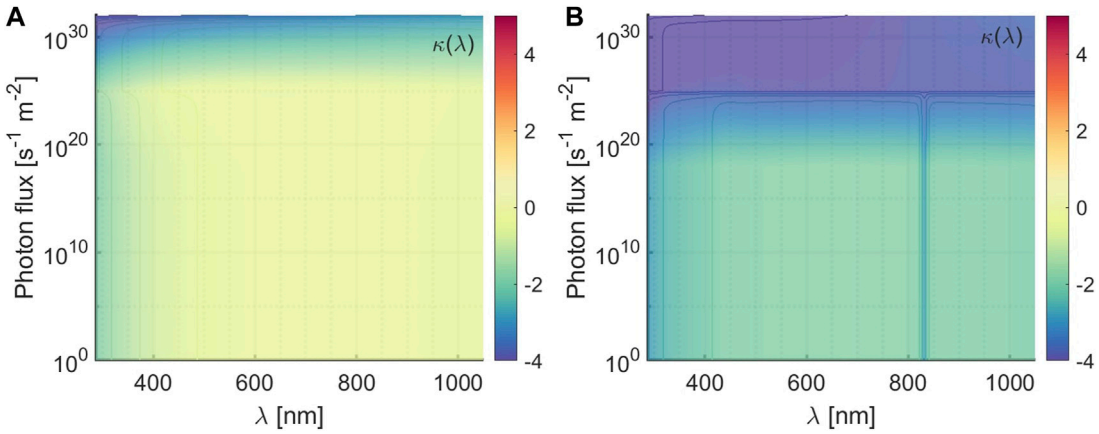

FIGURE 10
Numerical opacity $\kappa(\lambda)$ [cm^{2}g^{-1}] (log scale) of argon plasma in the VIS range, as resulting from NLTE CR calculations in FLYCHK, at electron density $\rho_e = 1.4 \cdot 10^{17}$ m^{-3}, and energy of **(A)** $k_BT_e = 2.43$ eV, and **(B)** $k_BT_e = 7.88$ eV. Opacity is shown in the wavelength λ [nm] - external radiation photon flux s^{-1}m^{-2} plane. Plasma parameters of **(A)** have been selected from OES data from cfg. 7, at $P_{RF} = 120$ W (see Table 4), while for **(B)** the density has been maintained equal and the energy increased.

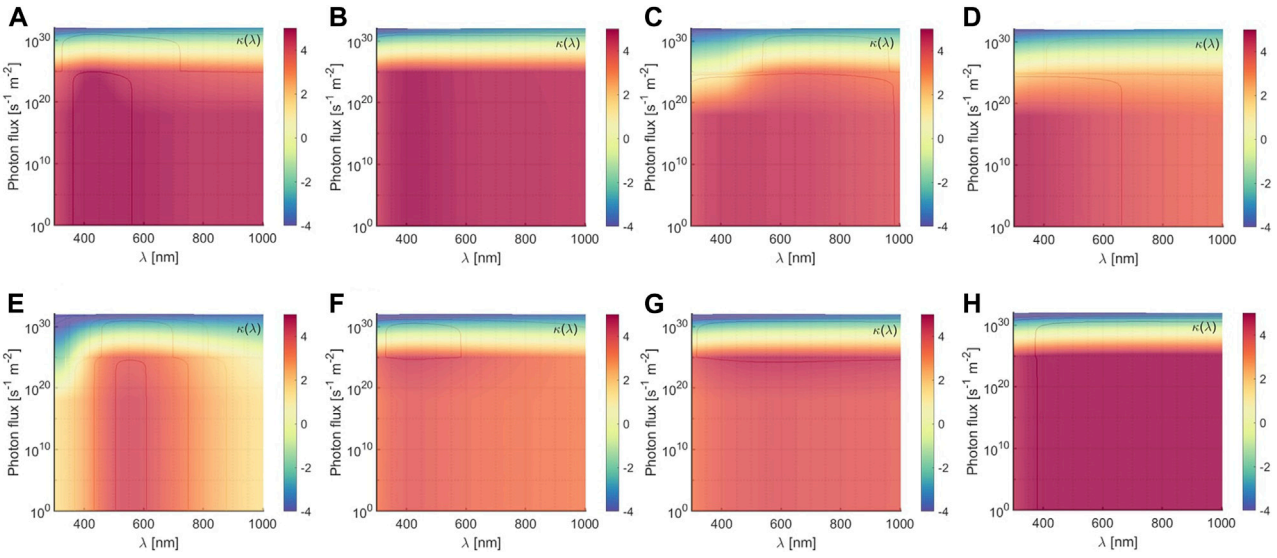

FIGURE 11
Numerical opacity $\kappa(\lambda)$ [cm^{2}g^{-1}] (log scale) of metallic plasmas in the VIS range, as resulting from NLTE CR calculations in FLYCHK, for **(A,E)** selenium (Se), **(B,F)** strontium (Sr), **(C,G)** zirconium (Zr), and **(D,H)** niobium (Nb), at electron density $\rho_e = 1.4 \cdot 10^{17}$ m^{-3}, and energy $k_BT_e = 2.43$ eV **(A–D)**, and $k_BT_e = 7.88$ eV **(E–H)**. Opacity is shown in the wavelength λ [nm] - external radiation photon flux s^{-1}m^{-2} plane.

4 Conclusion

In this work, we have reported on the first experimental attempt of reproducing kilonovae ejecta plasma conditions, carried out on the Flexible Plasma Trap at the INFN-LNS. The kilonovae signal plays a fundamental role in the multi-messenger astronomy, entering in a sophisticated GW-detecting network and delivers precious information on the composition and dynamics of the neutron-rich post-merger plasma ejecta. The ejecta opacity largely impacts on the kilonovae study, with consequent highly demanded experimental efforts to make progresses on the kilonovae opacity characterization. The novel work so far performed on *under-dense* and *low-temperature* magneto-plasmas opens the route for the first-of-

its-kind in-laboratory plasma opacity measurements of metallic plasma species relevant for kilonovae light curve studies, foreseen within the PANDORA project. Plasma parameter measurements have provided sounder bases for the reproducibility under early-stage kilonovae conditions and also benchmarked the efficiency of plasma diagnostics. Numerical efforts have been also spent to support future opacity measurements, by looking at the radiation–plasma matter interactions in the framework of highly inhomogeneous and anisotropic magnetically confined ECR plasmas. A synergistic use of spectroscopic measurements and numerical tools allowed to give some hints on typical light source to be employed in transmission spectroscopic measurements, designed for the future opacity measurements of light *r*-process element plasmas interesting for the kilonovae study. Experimental electron density and temperature obtained for high-pressure and high-frequency ECR plasmas are the most promising among the totality of experimental configurations explored, encouraging to extend experimental characterizations at larger pressures, in order to further decrease the average electron temperature, and hence to better reproduce conditions of the blue-kilonovae stage. The use of argon as contaminant looks promising for two reasons: first, an apparent beneficial effect as a thermal regulator in these plasmas, which requires further investigations; second, having theoretical line-ratios for argon line transitions will allow to make cross-check on the plasma parameters estimates arising from the hydrogen spectra analysis, thus providing more robust results. On the other side, numerical results have highlighted the influence on plasma opacity led by layered plasma parameters in the space, with important consequences for the convoluted line emission detected along the spectroscopic line-of-sight. Moreover, the study of the influence of external radiation acting on the plasma source optical observables has shown peculiar effects in terms of tuning the plasma opacity, accordingly to the level population of atoms involved, dependent on the electronic shell configurations and plasma temperature. Further numerical investigations are planned, extending CR calculations performed to three-dimensional properties of ECR plasmas, including spatial-dependent charge state distribution and ions residence time due to the magnetic confinement, not taken into account in the FLYCHK code suite. Next experimental steps are planned to perform opacity measurements of gaseous and metallic plasma sources based on the plasma trap configurations reported in this work.

Data availability statement

The original contributions presented in the study are included in the article/Supplementary Material; further inquiries can be directed to the corresponding author.

Author contributions

Conceptualization: AP, DM SC, ML, AP, and DV. Numerical simulations: AP, MB, GE, BM, and AG. Experimental data: AP, GE, MB, MM, BM, SM, DM GM, GF, EN, DS, and GT. Data analysis: AP, MB, GE, MM, DM, and BM. Funding acquisition: DM and DS. Writing—original draft: AP. Writing— review and editing: AP, DM, SC, DV, AG, AT, RS, GE, MB, BM, ML, and AP. All authors have read and agreed to the published version of the manuscript.

Acknowledgments

The authors wish to thank INFN for the support through the project PANDORA Gr3 funded by third Nat. Sci. Comm. and the whole PANDORA collaboration. DV acknowledges the financial support from the German-Israeli Foundation (GIF No. I-1500–303.7/2019).

Conflict of interest

The authors declare that the research was conducted in the absence of any commercial or financial relationships that could be construed as a potential conflict of interest.

Publisher's note

All claims expressed in this article are solely those of the authors and do not necessarily represent those of their affiliated organizations, or those of the publisher, the editors, and the reviewers. Any product that may be evaluated in this article, or claim that may be made by its manufacturer, is not guaranteed or endorsed by the publisher.

References

Abbott, B. P., Abbott, R., Abbott, T. D., Acernese, F., Ackley, K., Adams, C., et al. (2017). GW170817: Observation of gravitational waves from a binary neutron star inspiral. *Phys. Rev. Lett.* 119, 161101. doi:10.1103/PhysRevLett.119.161101

Antaya, T. A. (1989). A review of studies for the variable frequency superconducting ecr ion source project at msu. *J. Phys. Colloq.* 50, C1-707–C1-726. doi:10.1051/jphyscol:1989176

Arcavi, I., Hosseinzadeh, G., Howell, D. A., McCully, C., Poznanski, D., Kasen, D., et al. (2017). Optical emission from a kilonova following a gravitational-wave-detected neutron-star merger. *Nature* 551, 64–66. doi:10.1038/nature24291

Bailey, J. E., Nagayama, T., Loisel, G. P., Rochau, G. A., Blancard, C., Colgan, J., et al. (2015). A higher-than-predicted measurement of iron opacity at solar interior temperatures. *Nature* 517, 56–59. doi:10.1038/nature14048

Bailey, J. E., Rochau, G. A., Mancini, R. C., Iglesias, C. A., MacFarlane, J. J., Golovkin, I. E., et al. (2009). Experimental investigation of opacity models for stellar interior, inertial fusion, and high energy density plasmas. *Phys. Plasmas* 16, 058101. doi:10.1063/1.3089604

Barnes, J., and Kasen, D. (2013). Effect of a high opacity on the light curves of radioactively powered transients from compact object mergers. *Astrophys. J.* 775, 18. doi:10.1088/0004-637x/775/1/18

Barnes, J., Kasen, D., Wu, M. R., and Martínez-Pinedo, G. (2016). Radioactivity and thermalization in the ejecta of compact object mergers and their impact on kilonova light curves. *Astrophys. J.* 829, 110. doi:10.3847/0004-637x/829/2/110

Chung, H. K., Chen, M., Morgan, W., Ralchenko, Y., and Lee, R. (2005). Flychk: Generalized population kinetics and spectral model for rapid spectroscopic analysis for all elements. *High. Energy Density Phys.* 1, 3–12. doi:10.1016/j.hedp.2005.07.001

Craig, I. J. D., and Brown, J. C. (1976). Fundamental limitations of X-ray spectra as diagnostics of plasma temperature structure. *Astronomy Astrophysics* 49, 239–250.

Delaunay, M. (1992). Influence of ionization cross sections on the gas mixing effect for the production of ar9+ ions in a caprice ecr source. *Rev. Sci. Instrum.* 63, 2861–2863. doi:10.1063/1.1142778

Domoto, N., Tanaka, M., Wanajo, S., and Kawaguchi, K. (2021). Signatures of r-process elements in kilonova spectra. *Astrophys. J.* 913, 26. doi:10.3847/1538-4357/abf358

Fantz, U. (2006). Basics of plasma spectroscopy. *Plasma Sources Sci. Technol.* 15, S137–S147. –S147. doi:10.1088/0963-0252/15/4/s01

Fantz, U., Falter, H., Franzen, P., Wünderlich, D., Berger, M., Lorenz, A., et al. (2006). Spectroscopy—A powerful diagnostic tool in source development. *Nucl. Fusion* 46, S297–S306. doi:10.1088/0029-5515/46/6/s10

Gammino, S., Celona, L., Mascali, D., Castro, G., Torrisi, G., Neri, L., et al. (2017). The flexible plasma trap (FPT) for the production of overdense plasmas. *J. Instrum.* 12, P07027. doi:10.1088/1748-0221/12/07/p07027

Geller, R. (1996). *Electron cyclotron resonance ion sources and ECR plasmas*. United Kingdom: Institute of Physics.

Gillanders, J. H., McCann, M., Sim, S., Smartt, S., and Ballance, C. P. (2021). Constraints on the presence of platinum and gold in the spectra of the kilonova at2017gfo. *Mon. Notices R. Astronomical Soc.* 506, 3560–3577. doi:10.1093/mnras/stab1861

Gillanders, J. H., Smartt, S. J., Sim, S. A., Bauswein, A., and Goriely, S. (2022). Modelling the spectra of the kilonova at2017gfo – i: The photospheric epochs. doi:10.48550/ARXIV.2202.01786

Hoarty, D. J., James, S. F., Brown, C. R. D., Williams, B. M., Guymer, T., Hill, M., et al. (2010). High temperature, high density opacity measurements using short pulse lasers. *J. Phys. Conf. Ser.* 244, 012002. doi:10.1088/1742-6596/244/1/012002

Judge, P. G., Hubeny, V., and Brown, C. J. (1997). Fundamental limitations of emission-line spectra as diagnostics of plasma temperature and density structure. *Astrophys. J.* 475, 275–290. doi:10.1086/303511

Judge, P. G., and Hubeny, V. (1995). Solution to the bivariate integral inversion problem: The determination of emission measures differential in temperature and density. *Astrophysical J.* 448, 61–64. doi:10.1086/309594

Kasen, D., Metzger, B., Barnes, J., Quataert, E., and Ramirez-Ruiz, E. (2017). Origin of the heavy elements in binary neutron-star mergers from a gravitational-wave event. *Nature* 551, 80–84. doi:10.1038/nature24453

Knoll, G. F. (2010). *Radiation detection and measurement*. 4th ed. New York, NY: Wiley.

Korobkin, O., Rosswog, S., Arcones, A., and Winteler, C. (2012). On the astrophysical robustness of the neutron star merger r-process. *Mon. Notices R. Astronomical Soc.* 426, 1940–1949. doi:10.1111/j.1365-2966.2012.21859.x

Li, L. X., and Paczyński, B. (1998). Transient events from neutron star mergers. *Astrophys. J.* 507, L59–L62. doi:10.1086/311680

Mascali, D., Naselli, E., and Torrisi, G. (2022). Microwave techniques for electron cyclotron resonance plasma diagnostics. *Rev. Sci. Instrum.* 93, 033302. doi:10.1063/5.0075496

Mascali, D., Santonocito, D., Amaducci, S., Andò, L., Antonuccio, V., Biri, S., et al. (2022). A novel approach to β-decay: Pandora, a new experimental setup for future in-plasma measurements. *Universe* 8, 80. doi:10.3390/universe8020080

Mauro, G. S., Celona, L., Torrisi, G., Pidatella, A., Naselli, E., Russo, F., et al. (2022). An innovative superconducting magnetic trap for probing β-decay in plasmas. *Front. Phys.* 10. doi:10.3389/fphy.2022.931953

Mazzaglia, M., Castro, G., Mascali, D., Briefi, S., Fantz, U., Celona, L., et al. (2018). Study of the influence of magnetic field profile on plasma parameters in a simple mirror trap. *J. Instrum.* 13, C11014. doi:10.1088/1748-0221/13/11/c11014

Mazzaglia, M., Castro, G., Mascali, D., Celona, L., Neri, L., Torrisi, G., et al. (2019). Improvement of the characterization of the proton source for the European spallation source by means of optical emission spectroscopy. *Phys. Rev. Accel. Beams* 22, 053401. doi:10.1103/PhysRevAccelBeams.22.053401

Metzger, B. D. (2019). *KilonovaeLiving Rev. Relativ.* 23, 1. doi:10.1007/s41114-019-0024-0

Metzger, B. D., Martínez-Pinedo, G., Darbha, S., Quataert, E., Arcones, A., Kasen, D., et al. (2010). Electromagnetic counterparts of compact object mergers powered by the radioactive decay of r-process nuclei. *Mon. Not. R. Astron. Soc.* 406, 2650–2662. doi:10.1111/j.1365-2966.2010.16864.x

Mishra, B., Galata, A., Pidatella, A., Racz, R., Biri, S., Torrisi, G., et al. (2020) "Modelling space-resolved ion dynamics in ECR plasmas for predicting in-plasma β-decay rates," in *Frontiers in physics - research topics: Nuclear physics and astrophysics in plasma traps*. forthcoming (Lausanne, Switzerland: frontiers).

Mishra, B., Pidatella, A., Biri, S., Galatà, A., Naselli, E., Rácz, R., et al. (2021). A novel numerical tool to study electron energy distribution functions of spatially anisotropic and non-homogeneous ecr plasmas. *Phys. Plasmas* 28, 102509. doi:10.1063/5.0061368

Naselli, E., Mascali, D., Biri, S., Caliri, C., Castro, G., Celona, L., et al. (2019). Multidiagnostics setups for magnetoplasmas devoted to astrophysics and nuclear astrophysics research in compact traps. *J. Instrum.* 14, C10008. doi:10.1088/1748-0221/14/10/c10008

Naselli, E., Mascali, D., Mazzaglia, M., Biri, S., Rácz, R., Pálinkás, J., et al. (2019). Impact of two-close-frequency heating on ECR ion source plasma radio emission and stability. *Plasma Sources Sci. Technol.* 28, 085021. doi:10.1088/1361-6595/ab32f9

Naselli, E., Rácz, R., Biri, S., Mazzaglia, M., Celona, L., Gammino, S., et al. (2022). Innovative analytical method for x-ray imaging and space-resolved spectroscopy of ecr plasmas. *Condens. Matter* 7, 5. doi:10.3390/condmat7010005

Naselli, E., Rácz, R., Biri, S., Mazzaglia, M., Galatà, A., Celona, L., et al. (2022). Quantitative analysis of an ECR ar plasma structure by x-ray spectroscopy at high spatial resolution. *J. Instrum.* 17, C01009. doi:10.1088/1748-0221/17/01/c01009

Perego, A., Rosswog, S., Cabezón, R. M., Korobkin, O., Käppeli, R., Arcones, A., et al. (2014). Neutrino-driven winds from neutron star merger remnants. *Mon. Notices R. Astronomical Soc.* 443, 3134–3156. doi:10.1093/mnras/stu1352

Perego, A., Vescovi, D., Fiore, A., Chiesa, L., Vogl, C., Benetti, S., et al. (2022). Production of very light elements and strontium in the early ejecta of neutron star mergers. *Astrophys. J.* 925, 22. doi:10.3847/1538-4357/ac3751

Phelps, A. V. (1992). Collisions of h+, h2+, h3+, arh+, h-h, and h2 with ar and of ar+ and arh+ with h2 for energies from 0.1 ev to 10 kev. *J. Phys. Chem. Reference Data* 21, 883–897. doi:10.1063/1.555917

Pidatella, A., Cristallo, S., Galatà, A., La Cognata, M., Mazzaglia, M., Perego, A., et al. (2021). In-plasma study of opacity relevant for compact binary ejecta. *Il Nuovo Cimento C* 44, 4. doi:10.1393/NCC/I2021-21065-X

Rácz, R., Biri, S., Pálinkás, J., Mascali, D., Castro, G., Caliri, C., et al. (2016). X-ray pinhole camera setups used in the atomki ecr laboratory for plasma diagnostics. *Rev. Sci. Instrum.* 87, 02A741. doi:10.1063/1.4933085

Rosswog, S. (2015). The multi-messenger picture of compact binary mergers. *Int. J. Mod. Phys. D.* 24, 1530012. doi:10.1142/S0218271815300128

Tanaka, M., Kato, D., Gaigalas, G., and Kawaguchi, K. (2020). Systematic opacity calculations for kilonovae. *Mon. Not. R. Astron. Soc.* 496, 1369–1392. doi:10.1093/mnras/staa1576

Tarvainen, O., Suominen, P., Ropponen, T., Kalvas, T., Heikkinen, P., and Koivisto, H. (2005). Effect of the gas mixing technique on the plasma potential and emittance of the jyfl 14 ghz electron cyclotron resonance ion source. *Rev. Sci. Instrum.* 76, 093304. doi:10.1063/1.2038647

Taylor, J. R. (1996). *An introduction to error analysis: The study of uncertainties in physical measurements*. 2 sub edn. Sausalito, CA: University Science Books.

Thompson, A. M., Brown, J. C., Craig, I. J. D., and Fulber, C. (1992). Inference of non-thermal electron energy distributions from hard X-ray spectra. *Astronomy Astrophysics* 265, 278–288.

Torrisi, G., Naselli, E., Donato, L. D., Mauro, G., Mazzaglia, M., Mishra, B., et al. (2022). RF and microwave diagnostics for compact plasma traps and possible perspectives for fusion devices. *J. Instrum.* 17, C01050. doi:10.1088/1748-0221/17/01/c01050

Watson, D., Hansen, C. J., Selsing, J., Koch, A., Malesani, D. B., Andersen, A. C., et al. (2019). Identification of strontium in the merger of two neutron stars. *Nature* 574, 497–500. doi:10.1038/s41586-019-1676-3

Wu, Z., Ricigliano, G., Kashyap, R., Perego, A., and Radice, D. (2022). Radiation hydrodynamics modelling of kilonovae with SNEC. *Mon. Not. R. Astron. Soc.* 512, 328–347. doi:10.1093/mnras/stac399

Wünderlich, D., Giacomin, M., Ritz, R., and Fantz, U. (2020). Yacora on the web: Online collisional radiative models for plasmas containing h, h2 or he. *J. Quantitative Spectrosc. Radiat. Transf.* 240, 106695. doi:10.1016/j.jqsrt.2019.106695

Zhang, J., Xu, Y., Yang, J., Yang, G., Li, H., Yuan, Z., et al. (2011). Opacity measurement of a gold plasma at $T_e = 85$ eV. *Phys. Plasmas* 18, 113301. doi:10.1063/1.3660407

frontiers | Frontiers in Physics

TYPE Original Research
PUBLISHED 07 October 2022
DOI 10.3389/fphy.2022.936081

OPEN ACCESS

EDITED BY
Marialuisa Aliotta,
University of Edinburgh,
United Kingdom

REVIEWED BY
György Gyürky,
Institute of Nuclear Research (ATOMKI),
Hungary
Jack Henderson,
University of Surrey, United Kingdom

*CORRESPONDENCE
D. Santonocito,
domenico.santonocito@lns.infn.it

SPECIALTY SECTION
This article was submitted to
Nuclear Physics,
a section of the journal
Frontiers in Physics

RECEIVED 04 May 2022
ACCEPTED 06 September 2022
PUBLISHED 07 October 2022

CITATION
Goasduff A, Santonocito D,
Menegazzo R, Capra S, Pullia A,
Raniero W, Rosso D, Toniolo N, Zago L,
Naselli E and Napoli DR (2022), A high
resolution γ-ray array for the pandora
plasma trap.
Front. Phys. 10:936081.
doi: 10.3389/fphy.2022.936081

A high resolution γ-ray array for the pandora plasma trap

A. Goasduff[1], D. Santonocito[2]*, R. Menegazzo[3], S. Capra[4,5], A. Pullia[4,5], W. Raniero[1], D. Rosso[1], N. Toniolo[1], L. Zago[1,6], E. Naselli[2] and D. R. Napoli[1]

[1]Laboratori Nazionali di Legnaro, INFN, Legnaro, Italy, [2]Laboratori Nazionali del Sud, INFN, Catania, Italy, [3]Sezione di Padova, INFN, Padova, Italy, [4]Dipartimento di Fisica, Università degli Studi di Milano, Milano, Italy, [5]Sezione di Milano, INFN, Milano, Italy, [6]Dipartimento di Fisica e Astronomia, Università degli Studi di Padova, Padova, Italy

The measurement of β-decay rates in plasma, simulating stellar-like conditions, is of high interest for the investigation of radionuclides involved in nuclear astrophysics processes. In the new PANDORA plasma trap, to be built at the INFN—Laboratori Nazionali del Sud of Catania (Italy), the β-decay rates will be estimated by detecting the γ-rays emitted by the daughter nuclei trapped in the confined plasma. The present work describes the high efficiency High Purity Germanium (HPGe) detector array that will be placed around the magnetic trap for this purpose, as well as the front-end electronics and acquisition system suitable for the array operation in presence of a high counting rate background originating from Bremsstrahlung radiation.

KEYWORDS

γ-ray spectroscopy, HPGe detectors, front-end electronics, digital electronics, distributed DAQ, plasma trap

1 Introduction

The PANDORA (Plasma for Astrophysics Nuclear Decay Observation and Radiation for Archaeometry) experiment aims to develop a totally new approach to measure, for the first time, nuclear β-decay rates in a plasma simulating stellar-like conditions. To achieve this task a dedicated compact plasma trap will be built at the INFN—Laboratori Nazionali del Sud of Catania and will be used to run experiments in the forthcoming years.

The basic idea of the experiment is to gain some knowledge on weak interactions in s-process nucleosynthesis environments and is motivated by some theoretical predictions and experimental evidences showing that β-decay properties of radioactive nuclei can be strongly affected by the electron densities. In particular, highly ionized nuclides can display important variations in β-decay rates due to the opening of the bound state β-decay channel [1], an effect observed in few experiments performed using storage rings [2, 3]. The importance of this decay channel has to be clearly elucidated since it could have a major impact in astrophysical scenarios as *s*-process nucleosynthesis, where the competition between neutron capture and β-decay plays a major role in the synthesis of the elements. Only few experimental evidences showing variations in the β-decay rates as a function of the atomic fully-ionization state have been collected up to now (using

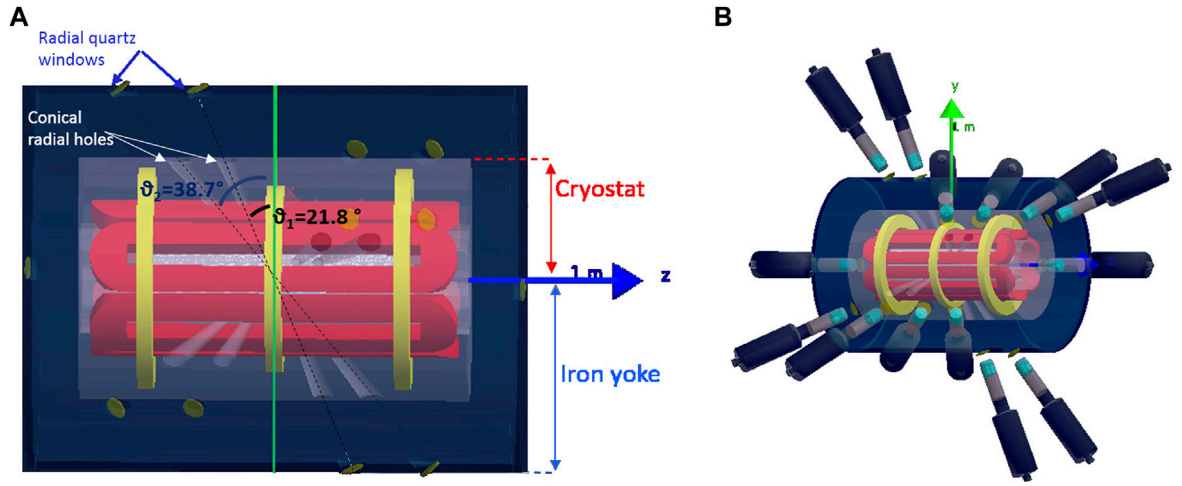

FIGURE 1
(A) Schematic drawing showing the three superconducting coils used for axial confinement (in yellow) and the hexapole used for radial confinement (in red). A single cryostat, depicted in light blue, contains all magnetic elements while the dark blue represents the region surrounded by the iron yoke. Radial quartz windows indicated in yellow are used in correspondence of the conical radial holes created in the chamber to allow for the measurement of the γ-rays emitted by the daughter nuclei following the β-decay. **(B)** Schematic drawing of the magnetic trap with HPGe detectors placed around it. HPGe detectors are placed around the trap in correspondence of conical apertures in the cryostat.

mainly storage rings); thus, the new experimental method proposed by PANDORA can shade new light on the role of weak interaction on the stellar nucleosynthesis.

This new approach, based on the study of decays rates in a laboratory magneto-plasma confined in a compact plasma trap, aims to carry out measurements in which the decaying ions display a charge state distribution resembling the one present in the hot stellar environment (or that can be properly scaled to it).

Plasma parameters will be inferred using dedicated non-invasive diagnostic tools [4] and the nuclear decay rates will be evaluated as a function of the charge state distribution of in-plasma ions [5].

In order to measure the β-decay rates with high efficiency, it is necessary to install around the magnetic trap an array of γ detectors, which will allow for the identification of β-decaying nuclei by measuring the energy of the γ-rays emitted by the daughter nuclei. High-resolution spectroscopy of ions within a trapping volume is challenging, with limited examples in the literature (e.g., [6]).

In the following, we will describe the high resolution detector array that will be placed around the trap with its dedicated electronics, acquisition system and infrastructure that will allow the γ-ray detector array operations during the relatively long measurement runs needed for each experimental campaign.

2 The gamma array

The γ-ray detector array of PANDORA plays an important role in the project. It will be used to measure the in-plasma decay rate of selected radionuclides, β emitters, through the detection of the γ-rays emitted by the daughter nuclei [7]. If the concentration of the radioisotope is kept in dynamical equilibrium in the plasma through a proper balance between plasma losses due to the finite confinement time of the ions and the amount injected in the trap, the measured decay rate dN/dt will depend on the product $\lambda \cdot n_i \cdot V$ where λ is the radioactive decay constant, n_i is the density of the radioactive ions in the plasma and V is the plasma volume. Since the plasma volume and the ion concentration can be measured [8-10] using non invasive diagnostic tools implemented in the magnetic trap [11], the measurement of the decay rate will allow for the in-plasma beta decay constant to be deduced. Such a value will depend on the plasma density and temperature which, in turn, determine a given charge state distribution of the ions in the plasma in non-Local Thermodynamical Equilibrium conditions. Therefore, varying the plasma conditions, one could try to map the evolution of the β-decay constant as a function of plasma main parameters [7]. To achieve this goal one needs to implement in the plasma trap the most effective, recently developed, multi-diagnostic tools with advanced analysis techniques and to use, simultaneously, a γ-detector array able to give statistically meaningful results in experimental runs whose duration can last up to a few months.

The γ array is made of 14 large volume HPGe detectors (with about 70% relative efficiency) which will be installed around the cylindrical magnetic trap [7, 12]. The HPGe detectors were chosen for the high resolution (0.2% *at* 1 MeV), since the harsh environment (the background noise is represented by the intense plasma self-emission) strongly affects the signal-

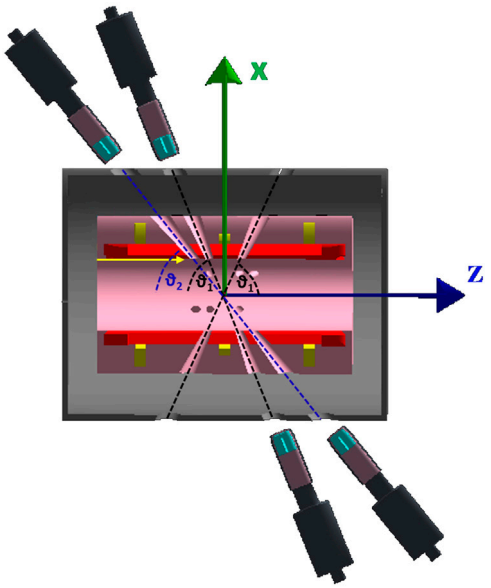

FIGURE 2
Cross-sectional drawing of the magnetic trap and the HPGe detectors. The lines of sight created in the cryostat and the yoke to have access to the plasma chamber and to be able to measure the in-plasma γ rays emitted after the β decay of the radioisotope are clearly visible.

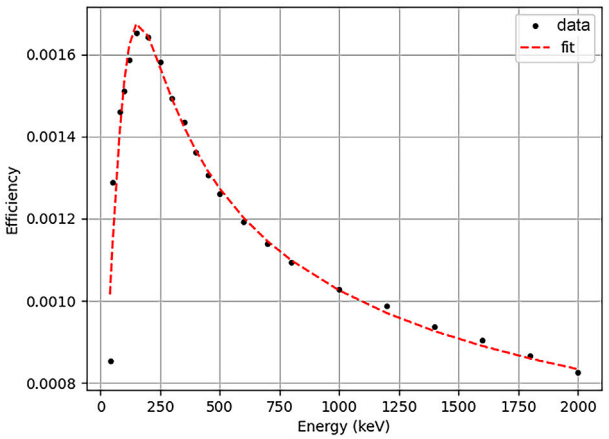

FIGURE 3
Total detection efficiency of the HPGe γ array as a function of the γ-ray energy. Dashed line shows the fit of the data with a Radware-like function.

to-noise ratio. The magnetic trap has a size of about 70 cm in length and about 33 cm in radius (including the cryostat), and will be used to confine the plasma using superconducting magnets able to generate a three-dimensional magnetic well. Twelve HPGe detectors will be placed radially in correspondence to dedicated apertures, conically shaped, created between the warm bore radius and the external iron yoke through the cryostat and the inner cold mass (see Figure 1A). Two further detectors will be added axially. They will "look" into the plasma through aluminum windows made in the walls of the plasma chamber (see Figure 1B).

No potential effects due to the presence of the magnetic field are expected on the charge collection efficiency (and therefore on the detector resolution) since the stray field will be of the order of 100 G.

2.1 The array geometry

The design of the γ array represents a compromise between the best detection efficiency achievable and the mechanical constraints imposed by the feasibility of creating a large number of apertures in the cryostat and the yoke without altering the magnetic field shape. Three conical apertures have been created in the interspace of each element of the hexapole in order to use it as a collimator and, at the same time, as a shield against the photon flux coming from the walls of the plasma chamber so to improve the signal-to-noise ratio. Such a choice allows for the placement, around the trap, of 12 HPGe detectors and six diagnostic tools (X-ray CCD pin-hole cameras, X-ray detectors, optical spectrometer, microwave polarimeter, RF probes and Thomson Scattering). As shown in Figure 2, two apertures are located at the same angle relative to the x axis while a third aperture is placed only on one side at a larger angles. This configuration rules out the regions of the magnetic trap where the B field lines are more intense and the electrons would be focalized by the magnetic field generating an intense background noise due to in plasma self-generated bremsstrahlung X-rays emission. All the aperture axis point to the center of the plasma chamber so that opposite apertures are collinear (see Figure 2). The same axis will be used to place the HPGe detector axis using a dedicated mechanical infrastructure.

GEANT4 simulations were performed to estimate the total detection efficiency of the setup and to evaluate the feasibility of the experiments. The total detection efficiency was evaluated assuming a cylindrical active part equal to one of GALILEO detectors (Gamma Array of Legnaro INFN Laboratories for nuclEar spectrOscopy [13]) which will be used during the first PANDORA experimental campaign thanks to a Collaboration Agreement, already signed, between the GAMMA and PANDORA collaborations. Gamma-rays of different energies were simulated changing the energy of the source in the range from 100 keV to 2 MeV. An isotropic ellipsoidal source placed in the center of the plasma chamber having the three semi-axes lengths equal to 79 mm, 79 mm and 56 mm (x, y, z) was used to simulate the γ-ray emission from the plasmoid, i.e., a plasma volume whose

TABLE 1 The three physic cases to be investigated during the first PANDORA experimental campaign. For each isotope the value of the half-life $T_{\frac{1}{2}}$ measured in neutral atoms and the energy/energies of the γ-rays emitted by the daughter nucleus after β-decay are shown.

Isotope	$T_{\frac{1}{2}}$ [yr]	E_γ [keV]
^{176}Lu	$3.78 \cdot 10^{10}$	202.88 & 306.78
^{134}Cs	2.06	795.86
^{94}Nb	$2.03 \cdot 10^{4}$	702.65

shape and size are defined by the employed confining magnetic field in the PANDORA plasma trap.

The results of the simulations are shown in Figure 3. The total photopeak detection efficiency reaches a maximum at E_γ =200 keV, then progressively decreases with increasing energy. Between 1400 keV and 2000 keV the efficiency is rather constant to a value of 8×10^{-4}. Such a value, while being apparently small compared to the typical values of the photopeak efficiency of the arrays used nowadays, is however sufficient, due to the high number of decaying ions present in the plasmoid, to measure the predicted variations in the decay rates. This critical aspect was verified, through simulations, for the first physic cases selected in PANDORA (see Table 1) for their relevance in s-process nucleosynthesis: ^{176}Lu, ^{134}Cs, ^{94}Nb [5]. All three nuclei are expected to undergo significant variations of their half-life in plasma environment.

At the working conditions of PANDORA (kT_e about 10 keV, where T_e is the electron temperature) the ^{176}Lu, a very long-lived nucleus in laboratory conditions with a $T_{1/2} = 3.78 \cdot 10^{10}$ yr, is expected to increase its decay rate up to about six order of magnitude while the neutral ^{94}Nb, characterized by a $T_{1/2} = 2.03 \cdot 10^4$ yr, is predicted to increase its decay rate in plasma (at kT_e around 10 keV) of five orders of magnitude relative to the value measured in neutral atoms. The ^{134}Cs has the shortest $T_{1/2}$ among the three isotopes to be investigated, its value being equal to 2.06 years. In this last case the predicted increase of the decay rate due to in plasma ionization is one order of magnitude. Simulations of real experimental runs, assuming a plasma volume of 1500 cm^3 and a concentration of the radioactive isotope ranging from 10^{11} ions/cm^3 for ^{176}Lu case to a much smaller value of about 10^6 ions/cm^3 for ^{134}Cs, show that to collect the statistics needed to achieve a 3σ-confidence level on the decay rate measurement, experimental runs should last from several days to about 3 months, depending on the isotope under investigation [5, 7]. Such a result clearly indicates that the sensitivity of the setup depends not only on the total detection efficiency of the HPGe array but also on the concentration of decaying ions confined in the trap (a value that can be tuned in each experiment considering also the possible limits imposed by radioprotection issues to the maximum total activity achievable) and on the expected variation of the half-life of the radioactive ion species.

Once the experimental approach will be well established, the PANDORA setup could allow a systematical investigation of several physic cases of β-decaying nuclei in plasma, related to nuclear-astrophysics processes and cosmology (BBN, s-processing nucleosynthesis, Cosmo-Chronometers, Early Solar System formation), with the restriction to those nuclei characterized by an emission of a γ-ray from the daughter nuclei populated in the β-decay process.

3 Front and back-end electronics

The standard readout chain of the HPGe from the GALILEO array [13] is based on custom-made electronics, from the pre-amplifier down to digitizers and pre-processing electronics. This electronic chain, developed in collaboration with the AGATA [14] collaboration, has been designed to accommodate a large number of channels, with a dedicated synchronization system. Due to the complexity of the system and the specificity of the PANDORA project whose experimental conditions in the magnetic trap lead to a high counting rate on HPGe array (up to 50 kHz on each detector) over a large period of time, the choice was made to simplify the readout electronics in order to improve its reliability and maintainability over long periods. For this reason it was decided to use commercially available modules for the readout.

3.1 Germanium detector pre-amplifiers

The PANDORA detector pre-amplifiers are based on the successful discrete-type model used to perform the readout of the GALILEO array. The circuit is divided into two parts: a cold one and a warm one. The cold part is constituted by the input JFET transistor, the feedback capacitor and feedback resistors. These are placed in close contact with the detector, inside the cryostat. The remaining part of the first pre-amplifier stage and the second stage are placed outside the cryostat and mounted on conventional FR4 boards. Given the non-conventional requirements in terms of linearity, noise and bandwidth, the operational amplifier that constitutes the warm part of the first stage is not a commercial one but instead is full-custom and made of discrete components.

The original device is powered with ±12 V and ±6 V, although these values have been changed to comply with the different requirements of PANDORA. In particular, the power rails have been modified as shown in Figure 4. A+24 V supply line has been added to extend the dynamic range of the integrator stage. This allows the pre-amplifier to handle a higher event rate that induces, due to the detector DC coupling, a natural random walk on the output node. This modification required the substitution of some bipolar transistors (MMBTH81) with similar models (MMBT3906) that are tolerant to higher voltages. This substitution was applied only on the integrator

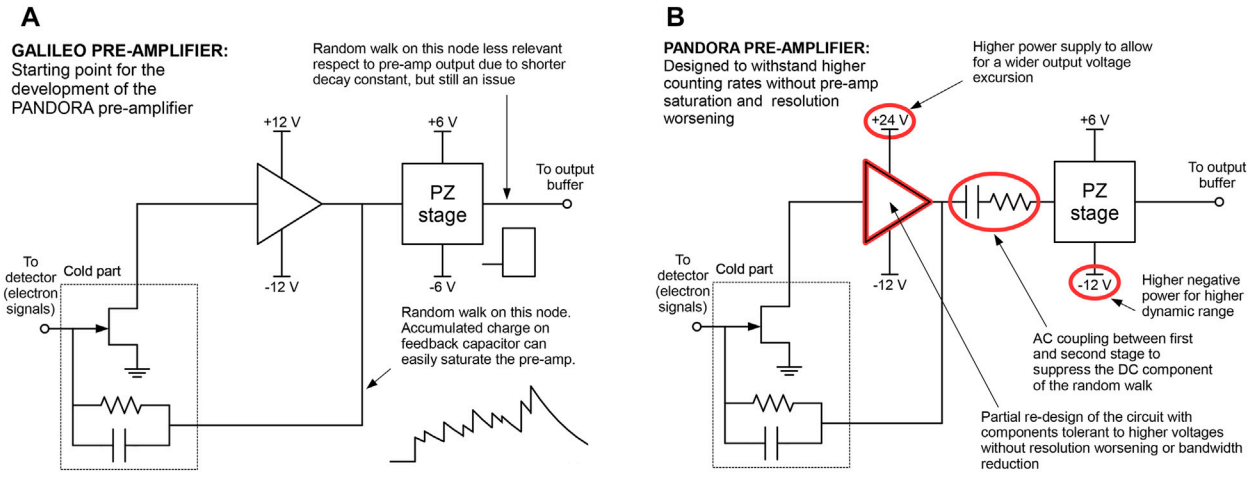

FIGURE 4
Simplified representation of the modifications of the PANDORA pre-amplifier [panel **(B)**] with respect to the GALILEO one [panel **(A)**].

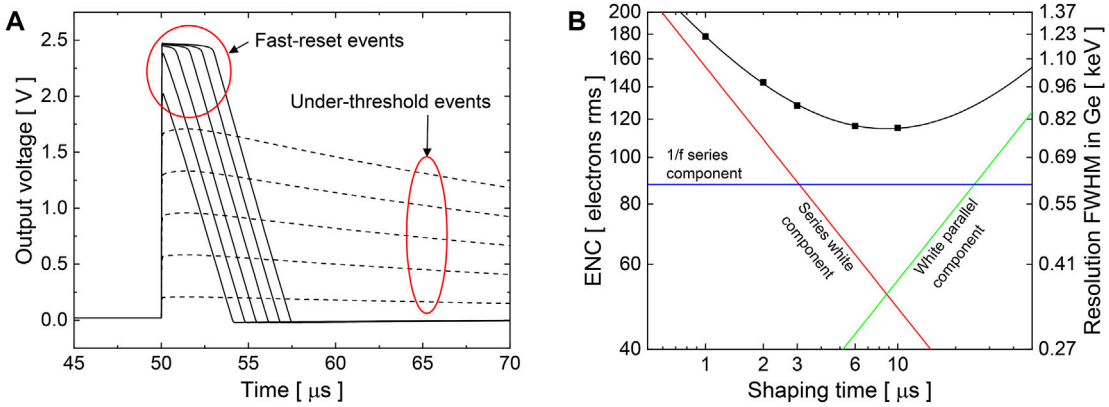

FIGURE 5
(A) Under-threshold events (dashed lines) compared to fast-reset events (solid lines). The signals with amplitude exceeding the ADC range are swiftly resetted thanks to a controlled current generator. **(B)** Pre-amplifier resolution in electrons r.m.s. and in keV_{Ge} FWHM. The calculated noise components are plotted against the experimental points. Equivalent noise charge data is reported in Table 2.

output stage and after careful considerations on the overall circuit bandwidth. The signal is then AC-coupled to the following Pole-Zero (PZ) stage, that reduces the signal decay constant down to 50 μs. At the same time the AC coupling suppresses the random walk and stabilizes the baseline.

Since the ADC dynamic range is narrower than the pre-amplifier one, high-energy signals can induce saturation in the digitizer. To avoid this, an innovative solution has been implemented. The PZ stage is based on a 4.7 nF capacitor and a resistive discharge network. When the signal crosses the chosen upper dynamic range limit, a current generator is activated that discharges the capacitor until the output voltage signal is brought back to 0 V in some microseconds. In this way the digitizer can correctly record the incoming signals without saturating and without waiting for the spontaneous decay of high-energy signals. Under-threshold events (dashed lines) with natural exponential decay are shown in Figure 5A) compared to fast-reset ones (solid lines). The latter have a triangular shape and fall back to the quiescent operating point in some microseconds.

More advanced techniques are under study to implement the fast-reset solution directly at the first pre-amplifier stage. Both hybrid discrete-integrated [15] and fully-integrated pre-amplifiers [16, 17] that include the fast-reset circuit referred directly at the input node are under development.

TABLE 2 Pre-amplifier resolution, measured with an analog quasi-gaussian shaping amplifier, expressed in electrons r.m.s. and keV FWHM in Germanium detector for different shaping times.

Shaping	ENC	FWHM in Ge
time [μs]	[el r.m.s.]	[keV]
1	178	1.22
2	143	0.98
3	128	0.88
6	116	0.80
10	115	0.79

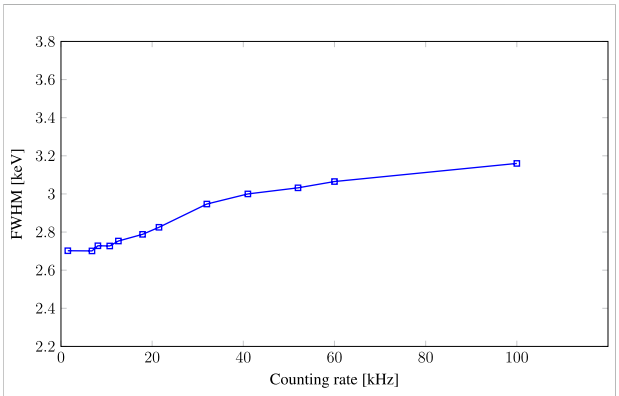

FIGURE 6
Measured FWHM of a GALILEO HPGe single crystal as a function of the counting rate using the V1725 CAEN digitizer. The HPGE detector was equipped with the new pre-amplifier. A 150 kBq ^{60}Co sources was placed at 10 cm from the detector, generating a fixed counting rate of 1.5 kHz. A stack of sources, composed of ^{241}Am, ^{133}Ba and ^{137}Cs, was placed on a movable vertical plate in order to simulate different low energy background counting rates. All the measurements were taken over 10 min runs.

An accurate selection of the input transistor, integrated in the cryostat, together with the minimization of the second-stage noise allows for a best resolution of 115 electrons rms, equivalent to 0.8 keV in Germanium. The trend of the detector resolution for different shaping times is plotted in Figure 5B) for the values reported in Table 2. The nominal signal leading-edge rise time (10%–90%) is 30 ns.

3.2 Readout electronics

First implementation of the readout electronics is based on the V1725S module from CAEN. Those 16-channels boards are equipped with Flash ADC with a 14-bit resolution and a 250 MHz sampling rate. Input signal of the CAEN digitizer are single-ended; since the pre-amplificator output of the GALILEO detectors are differential, dedicated conversion modules need to be developed. To test the readout, a Mesytec MDU-8 Differential-to-single-ended was used.

Since HPGe signals are long (rise time ~ 100–300 ns, decay ~ 45 μs), the amplitude of the signal, proportional to the incident energy of the photon, is extracted using a moving window deconvolution algorithm based on the Jordanov trapezoidal filter [18]. Standard parameters used at low rate (≤15 kHz) are based on an integration time around 6 μs. This long integration allows one to obtain energy resolution of 2–2.3 keV at 1332 keV using the coaxial detectors of GALILEO.

In the PANDORA configuration, our gamma detection system will work under harsh conditions due to the self-emitted background produced by electron Bremsstrahlung. Such a production mechanism will lead to a rather steep exponentially decreasing spectrum giving rise to a counting rate of about 50 kHz background in each detector. An evaluation of the behavior of the energy resolution of our detector/electronics system as a function of different low energy (50–300 keV energy range) counting rates is shown in Figure 6. For this test we have prepared a multi-source measurement system composed by a 150 kBq ^{60}Co source placed at 10 cm from the detector, generating a fixed counting rate of 1.5 kHz, and a stack of sources, composed of ^{241}Am, ^{133}Ba and ^{137}Cs placed on a movable vertical plate, in order to simulate different low energy background counting rates. In Figure 6, we reported the FWHM measured on the 1332 keV transition as a function of the total counting rate. All the measurements were taken over 10 min runs. It is worth pointing out that all the measurements were performed using the same configuration of the trapezoidal filter. Even so, at the rate expected for the PANDORA configuration, the resolution of the detector remains around 3 keV. For a better comparison, the obtained spectra at five different rates are reported in Figure 7, no large asymetry of the peak is observable. Due to the multi-source measurement and the activity of the Cs source, the pile-up of two 661-keV transition is visible at ~ 13320 ADC channel. It is worth pointing out that even at 100 kHz the peak from the ^{60}Co source (1332 keV) and resulting sum-peak of the ^{137}Cs source (1322-keV) are still well separated.

A second test was performed to check the stability of the system at large counting rate (50 kHz). Energy versus time matrix is shown in Figure 8 to illustrate the stability of the newly developed pre-amplifier and readout electronics. No significant deviation is observed over the 10 h run.

4 Data acquisition system

The proposed data acquisition system is based on the XDAQ framework. XDAQ has been developed and is maintained by CERN [19] and allows the end-users to focus on the development of specific applications tuned for their setup while taking advantage of all the tools present in the framework (peer-to-peer communication, application control and monitoring, etc.). All current developments are based on the XDAQ v15 and running under CentOS 7 with gcc 8.

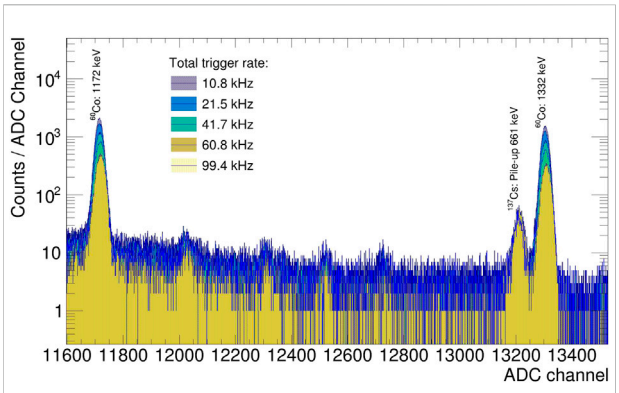

FIGURE 7
Stacked spectra obtained for five different total counting rates. The peak lying close to the 1332-keV line (13220 ADC channels) is due to the pile-up peak of the intense ^{137}Cs source.

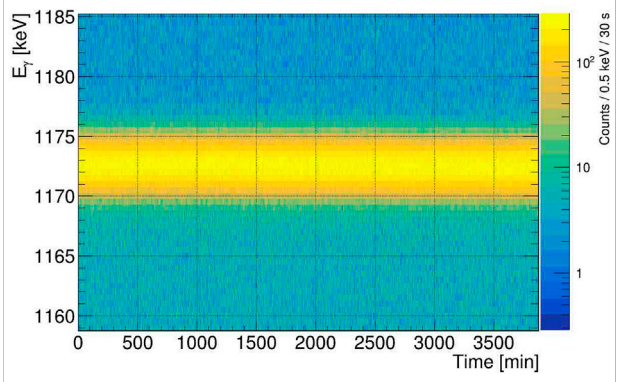

FIGURE 8
Energy vs. Time measured of 60 h using the multi-source with a total rate of 50 kHz. The energy axis has been zoomed on the 1172-keV transition coming from the ^{60}Co source.

4.1 Readout unit

The Readout Unit (RU) is the only application directly communicating with the back-end electronics. For simplicity, the RU is largely based on the CAENDigitizer library 1. The role of the RU can be described as follows: it takes the raw buffers from the electronic board and moves them to the XDAQ data stream to be sent to the next application of the distributed acquisition system.

4.2 Filter units

The high counting rate sustained by the electronics and the RU is mostly due to the background radiations originated by the electron bremsstrahlung in the plasma trap that will account for an average rate of 50 kHz per detectors. It is worth pointing out that state-of-the-art γ-ray arrays as AGATA and GRETA, although designed to withstand rates of 80–100 kHz, are generally not operating in trigger-less mode. In the case of AGATA, a trigger processor device allows to perform an hardware selection of the events based on fold conditions in AGATA and/or eventual coincidence with complementary detectors. While the detectors are able to trigger at more than 80 kHz, in the present configuration, the AGATA DAQ and in particular the pulse shape analysis (PSA) used to determine the γ-ray interaction position in the HPGe crystal can only be fully operated up to rates of about 4 kHz per crystal using the grid-search algorithm keeping the dead-time below 10%. In the case of PANDORA, reducing the data frame size to the minimum possible at 50 kHz per crystal, the resulting data bandwidth on disk would be around 1 TB per day. Since data taking will span over several weeks, a data reduction needs to be applied before writing data on disk.

For this reason, filter units have been implemented in the data chain. For example, the first filter unit is used to monitor the data stream and to extract information about the rates (trigger, pile-up, saturation, lost events) to be sent to the monitoring system. At this level, a first reduction of the data stream could be applied by using simple energy windows on the individual channels. The second filter unit, placed after a time sorter and event builder, could be used for a further reduction based on event fold. The system is modular and additional units could be added in function of the requirement of each experiment.

4.3 Data quality monitoring

Data quality monitoring can be performed in different ways:

- Implementing spectra directly in the DAQ applications;
- Adding a parallel output to the DAQ application, consisting in a TCP-server to spy the data.

The first solution offers the possibility to have a precise idea of the total statistics available in a certain amount of time. Thanks to recent developments, it is now possible to reset those spectra. However, since they are directly implemented within the DAQ applications, they are generally less flexible and cannot be modified easily (i.e., binning, range, conditions).

The second solution, is to spy the data flux to monitor the data quality. Depending on the experimental conditions, in particular the data bandwidth, only a fraction of the data can be monitored. Nevertheless, this solution offers the possibility to monitor the data at different level of the DAQ in a relatively easy way. Although it requires the development of small analysis codes, it is worth noting that the developed code could be used also for the offline analysis since both spy and data on disk have a common format.

4.4 Run control and system monitoring

XDAQ distributed acquisition is described in an XML-file containing all the applications and the relation between them. Each application corresponds to a process running on a specific computer. To simplify the organization and the control of the data acquisition, the choice was made to run all the applications within a terminal multiplexer using TMUX open-source solution. Management of the TMUX session is directly performed by the run control following the DAQ topology. Separated windows are automatically generated for each DAQ level and divided into panes in case more than one application per level is required.

A dedicated modular run control based on Python3 has been developed for the GALILEO array and further improved for the installation of the AGATA at the LNL. The present solution includes a constant monitoring and alert system of the run experimental conditions. Open-source time series solution, such as Graphite or InfluxDB, are used to keep track of the detector conditions (temperature, bias voltage and current), the electronic status (board temperature, triggering rate) and the DAQ system (load of the acquisition and disk server, data bandwidth). The system will be used for the HPGe data acquisition, its flexibility makes the inclusion of the information related to the plasma conditions relatively straightforward.

5 Detector support system

The detector support system (DSS) is a critical part of the project. It includes several hardware components (detector preamplifier and digitizer LV power supply, automatic HPGe cooling system, ...) as well as an integrated slow-control software to manage and supervise the detector operations (HPGe HV and temperature, preamplifier and digitizer LV, UPS status, ...). All these components are necessary to guarantee the normal operation of the 14 GALILEO detectors placed around the plasma trap.

The power consumption of the electronics (preamplifiers, HV system and HV shutdown board) is relatively small: about 20 W per channel, i.e. the total power requirements of a small array with 14 HPGe detectors is about 2 kW, including the internal dissipation of power supply modules and the LN2 cooling infrastructure.

5.1 Autofill system

Each HPGe detector cryostat is equipped with one Pt100 resistor, placed along the cold finger, close to the dewar, to monitor the detector behaviour and to guarantee a fast reaction of the cooling system if LN2 is missing. The measured resistance is also compared to a reference value to inhibit the HV bias if a temperature above the normal range of working conditions is detected.

A LN2 distribution system is needed to cool the HPGe detectors. The cryogenic system is based on a pressurized container, positioned in the proximity of the HPGe detectors and connected to distribution manifolds. Flexible hoses will connect the valve controlled ports in the manifold to individual detectors. Automatic/manual procedures are implemented to refill each detector Dewar with LN2 at regular intervals (usually every 12 h) or to keep the detector at the working temperature (forced fill). To define the volume of the LN2 container the total volume of the installation area and the minimum acceptable O_2 concentration for breathing will be considered. Oxygen level sensors will be installed in the area to monitor the saturation levels.

From the long-standing experience with GALILEO detectors, an array of 14 GALILEO detectors will have an estimated LN2 consumption of 100 L/day.

The control program of the filling system resides entirely on a cRio hardware without using external computing resources. In addition to monitor the status of the detectors and a restricted set of actions, accessible to the occasional user through a dedicated Graphical User Interface, an expert operator is able to access (read and modify) the parameters that control the behavior of the system.

The infrastructure (LN2 transport line, distribution manifolds, valves, sensors, . . .), the cRio hardware platform and the control program of the filling system use the same components already adopted in the system installed on the GALILEO spectrometer at LNL. The only modifications (internal/external pressurized container, metal pipes connecting the detectors, ...) are determined by the characteristics of the location where the new system will be installed.

5.2 LV and HV power supply

Due to the modification made on the pre-amplifiers to sustain the high-counting rate, new Low Voltage Power Supply will have to provide +24V, -12 V and ± 6 V. Considering the limited number of high voltage channels required for the setup, several technical solutions are still under evaluation. All of them are consistent with the possibility to implement a bias shutdown using an external signal, e.g. the signal generated from the autofill system combined with the shutdown signal from the detector.

5.3 High purity germanium detectors infrastructure

The experimental runs foreseen for PANDORA will have a duration which could extend up to a few months. Detector performances can deteriorate with time especially considering

the harsh conditions to which they will be exposed. Therefore, in order to be able to repair, test and run ordinary maintenance procedures on the HPGE detectors it was decided to build, at the LNS, a detector laboratory to cope with these needs. Due to the long-standing experience acquired by the researchers and technicians of the INFN—Laboratori Nazionali di Legnaro on the use and maintenance of HPGe detectors a period of training of the LNS personnel is foreseen as well as a remote support for the more complex repair works that will be coordinated with the GAMMA collaboration and the LNL DetLab [20]. This HPGe detectors facility would be the first laboratory of this type in Sicily and could become an excellent support for other activities which could make use of HPGe detectors in the LNS, the Universities or other institutions and companies in the Region.

6 Summary

The detection of the γ-rays emitted by daughter nuclei of highly ionized β-decaying isotopes trapped in the confined plasma, allows for the estimation of β-decay rates as a function of the plasma main parameters (density and temperature). From the point of view of the gamma detection, we have to deal with the trap geometrical constraints which limit the number and the solid angle covered by the γ-ray detectors and with the plasma self-emitted background radiation that produces a huge total counting rate.

The HPGe detector array for the PANDORA plasma trap has been designed with particular emphasis on maintaining the best resolution of the HPGe detectors during long periods of time since it affects the signal-to-noise ratio as well as the optimal data processing at the mentioned high counting rates. The HPGe pre-amplifiers, digitizers and pre-processing electronics chain developed at AGATA and GALILEO, have been adapted to PANDORA HPGe detectors by simplifying the readout and improving the reliability and maintainability over long periods. Tests of the energy resolution of the system as a function of the total counting rate indicate that the system is able to handle high counting rates (about 50 kHz) without any significant worsening of the detectors energy resolution which clearly remains the main parameter to be kept under control when dealing with high background counting rates. For this reason the project of the new array for PANDORA includes an efficient and safe detector support system which will assure stable conditions for the HPGe detectors for long time periods and a detector lab that could guarantee the maximum number of detectors working with the best achievable performances.

Data availability statement

The raw data supporting the conclusions of this article will be made available by the authors, without undue reservation.

Author contributions

DS and EN contributed to the design study of the array. EN did detailed simulation of the array geometry DS wrote the paragraphs 1 and 2 of the paper AG wrote paragraph three and four of paper and made tests on the electronics RM wrote the paragraph concerning the LN2 filling system (part of paragraph 5) SC and AP worked on design and realization of the modified pre-amp used in tests WR and DR wrote section 5.3 of the paper and worked on the HPGE detectors (test preparations) NT developed part of the DAQ LZ worked of the DAQ DN contributed to paper writing and coordinated the synergic activities between LNS and LNL. All authors contributed to manuscript revision, read, and approved the submitted version.

Conflict of interest

The authors declare that the research was conducted in the absence of any commercial or financial relationships that could be construed as a potential conflict of interest.

Publisher's note

All claims expressed in this article are solely those of the authors and do not necessarily represent those of their affiliated organizations, or those of the publisher, the editors and the reviewers. Any product that may be evaluated in this article, or claim that may be made by its manufacturer, is not guaranteed or endorsed by the publisher.

References

1. Bahcall J. Theory of bound-state beta decay. *Phys Rev* (1961) 124:495–9. doi:10.1103/PhysRev.124.495

2. Jung M, Bosch F, Beckert K, Eickhoff H, Folger H, Franzke B, et al. First observation of bound-state beta $^-$ decay. *Phys Rev Lett* (1992) 69:2164–7. doi:10.1103/PhysRevLett.69.2164

3. Bosch F, Faestermann T, Friese J, Heine F, Kienle P, Wefers E, et al. Observation of bound-state β^- decay of fully ionized ^{187}Re: ^{187}Re-^{187}Os cosmochronometry. *Phys Rev Lett* (1996) 77:5190–3. doi:10.1103/PhysRevLett.77.5190

4. Naselli E, Mascali D, Biri S, Caliri C, Castro G, Celona L, et al. Multidiagnostics setups for magnetoplasmas devoted to astrophysics and nuclear astrophysics

research in compact traps. *J Instrum* (2019) 14:10008. doi:10.1088/1748-0221/14/10/C10008

5. Mascali D, Naselli E, Torrisi G. Microwave techniques for electron cyclotron resonance plasma diagnostics. *Rev Scientific Instr* (2022) 93:033302. doi:10.1063/5.0075496

6. Leach KG, Grossheim A, Lennarz A, Brunner T, Crespo López-Urrutia JR, Gallant AT., et al. The TITAN in-trap decay spectroscopy facility at TRIUMF. *Nucl Instr Methods Phys Res Section A* (2015) 780:91–99. doi:10.1016/j.nima.2014.12.118

7. Naselli E, Ràcz R, Biri S, Mazzaglia M, Celona L, Gammino S, et al. Innovative analytical method for x-ray imaging and space-resolved spectroscopy of ECR plasmas. *Condens Matter* (2022) 7:5. doi:10.3390/condmat7010005

8. Mascali D, Santonocito D, Amaducci S, Andó L, Antonuccio V, Biri S, et al. A novel approach to β-decay: PANDORA, a new experimental setup for future in-plasma measurements. *Universe* (2022) 8:80. doi:10.3390/universe8020080

9. Naselli E, Santonocito D, Amaducci S, Galatá A, Goasduff A, Mauro G, et al. Design study of a HPGe detectors array for β-decays investigation in laboratory ECR plasmas. *Front Phys* (2022) 10:935728. doi:10.3389/fphy.2022.935728

10. Torrisi G, Naselli E, Mascali D, Donato LD, Sorbello G. mm-wave interferometer-polarimeter and profilometry design study for retrieving plasma density in the pandora experiment. *Front Astron Space Sci* (2022) 9:949920. doi:10.3389/fspas.2022.949920

11. Mazzaglia M, Biri S, Emma G, Finocchiaro G, Galatà A, Mauro G, et al. A system for plasma parameters evaluation in compact magnetic traps aiming at in plasma β-decay investigation. *Frontiers* (2022). submitted in this special issue.

12. Mauro G, Celona L, Torrisi G, Pidatella A, Naselli E, Russo F, et al. An innovative superconducting magnetic trap for probing β-decay in plasmas. *Front Phys* (2022) 10:931953. doi:10.3389/fphy.2022.931953

13. Goasduff A, Mengoni D, Recchia F, Valiente-Dobón J, Menegazzo R, Benzoni G, et al. The galileo γ-ray array at the legnaro national laboratories. *Nucl Instr Methods Phys Res Section A: Acc Spectrometers, Detectors Associated Equipment* (2021) 1015. 165753, doi:10.1016/j.nima.2021.165753

14. Akkoyun S, Algora A, Alikhani B, Ameil F, de Angelis G, Arnold L, et al. Agata—Advanced gamma tracking array. *Nucl Instr Methods Phys Res Section A: Acc Spectrometers, Detectors Associated Equipment* (2012) 668:26–58. doi:10.1016/j.nima.2011.11.081

15. Pullia A, Zocca F, Capra S. Note: A 102 dB dynamic-range charge-sampling readout for ionizing particle/radiation detectors based on an application-specific integrated circuit (asic). *Rev Scientific Instr* (2018) 89:026107. doi:10.1063/1.5012081

16. Capra S, Mengoni D, Duenas J, John P, Gadea A, Aliaga R, et al. Performance of the new integrated front-end electronics of the TRACE array commissioned with an early silicon detector prototype. *Nucl Instr Methods Phys Res Section A: Acc Spectrometers, Detectors Associated Equipment* (2019) 935:178–84. doi:10.1016/j.nima.2019.05.039

17. Capra S, Pullia A. Design and experimental validation of an integrated multichannel charge amplifier for solid-state detectors with innovative spectroscopic range booster. *IEEE Trans Nucl Sci* (2020) 67:1877–84. doi:10.1109/TNS.2020.3006892

18. Jordanov VT, Knoll GF, Huber AC, Pantazis JA. Digital techniques for real-time pulse shaping in radiation measurements. *Nucl Instr Methods Phys Res Section A: Acc Spectrometers, Detectors Associated Equipment* (1994) 353:261–4. doi:10.1016/0168-9002(94)91652-7

19. Gutleber J, Murray S, Orsini L. Towards a homogeneous architecture for high-energy physics data acquisition systems. *Comp Phys Commun* (2003) 153:155–63. doi:10.1016/S0010-4655(03)00161-9

20. Sajo-Bojus Se. a., Rosso D, Sajo Castelli A, Napoli D, Fioretto E, Menegazzo R, et al. Hpge detectors long time behaviour in high-resolution gamma spectrometry. *Nucl Instr Methods Phys Res Section A: Acc Spectrometers Detectors Associated Equipment* (2011) 648:132–8. doi:10.1016/j.nima.2011.03.031

frontiers | Frontiers in Astronomy and Space Sciences

TYPE Original Research
PUBLISHED 17 October 2022
DOI 10.3389/fspas.2022.956633

OPEN ACCESS

EDITED BY
Paul Stevenson,
University of Surrey, United Kingdom

REVIEWED BY
Claudia Lederer-Woods,
University of Edinburgh,
United Kingdom
Mounib El Eid,
American University of Beirut, Lebanon

*CORRESPONDENCE
Maurizio M. Busso,
maurizio.busso@unipg.it

SPECIALTY SECTION
This article was submitted to Nuclear Physics,
a section of the journal
Frontiers in Astronomy and Space Sciences

RECEIVED 30 May 2022
ACCEPTED 20 September 2022
PUBLISHED 17 October 2022

CITATION
Busso MM, Kratz K-L, Palmerini S, Akram W and Antonuccio-Delogu V (2022), Production of solar abundances for nuclei beyond Sr: The s- and r-process perspectives.
Front. Astron. Space Sci. 9:956633.
doi: 10.3389/fspas.2022.956633

Production of solar abundances for nuclei beyond Sr: The *s*- and *r*-process perspectives

Maurizio M. Busso[1,2]*, Karl-Ludwig Kratz[3,4], Sara Palmerini[1,2,5], Waheed Akram[6] and Vincenzo Antonuccio-Delogu[7]

[1]Department of Physics and Geology, University of Perugia, Perugia, Italy, [2]INFN, Section of Perugia, Perugia, Italy, [3]Department of Chemistry, Pharmacy and Geosciences, University of Mainz, Mainz, Germany, [4]Max-Planck-Institut für Chemie, Hahn-Meitner-Weg 1, Mainz, Germany, [5]INAF, Astronomical Observatory of Rome, Rome, Italy, [6]Department of Earth Sciences, University of Oxford, Oxford, United Kingdom, [7]INAF, Astrophysical Observatory of Catania, Catania, Italy

We present the status of nucleosynthesis beyond Sr, using up-to-date nuclear inputs for both the slow (*s*-process) and rapid (*r*-process) scenarios of neutron captures. It is now widely accepted that at least a crucial part of the *r*-process distribution is linked to neutron star merger (*NSM*) events. However, so far, we have found only a single direct observation of such a link, the kilonova GW170817. Its fast evolution could not provide strict constraints on the nucleosynthesis details, and in any case, there remain uncertainties in the local *r*-process abundance patterns, which are independent of the specific astrophysical site, being rooted in nuclear physics. We, therefore, estimate the contributions from the *r*-process to solar system (*S.S.*) abundances by adopting the largely site-independent *waiting-point* concept through a superposition of neutron density components normalized to the *r*-abundance peaks. Nuclear physics inputs for such calculations are understood only for the trans-Fe nuclei; hence, we restrict our computations to the Sr–Pr region. We then estimate the *s*-process contributions to that atomic mass range from recent models of asymptotic giant branch stars, for which uncertainties are known to be dominated by nuclear effects. The outcomes from the two independent approaches are then critically analyzed. Despite the remaining problems from both sides, they reveal a surprisingly good agreement, with limited local discrepancies. These few cases are then discussed. New measurements in ionized plasmas are suggested as a source of improvement, with emphasis on β-decays from unstable Cs isotopes. For heavier nuclei, difficulties grow as *r*-process progenitors lie far off experimental reach and poorly known branchings affect *s*-processing. This primarily concerns nuclei that are significantly long-lived in the laboratory and have uncertain decay rates in stars, e.g., ^{176}Lu and ^{187}Re. New measurements are urgently needed for them, too.

KEYWORDS

nuclear astrophysics, weak interactions, nucleosynthesis, s-processes, r-processes, stars

1 Introduction

Based on the first detailed geochemical abundance determinations of Suess and Urey (1956), the neutron shell structure investigations of Coryell (1956; 1961), and the discovery of radioactive Tc in the photospheres of evolved red giants (Merrill, 1952), the seminal works of Burbidge et al. (1957) (B^2FH) and Cameron (1957) laid down the fundamental astrophysical conditions for the production of heavy elements. This included, in particular, isotopes beyond Fe, which were found in those works to be synthesized by neutron-capture processes, either slow (the *slow* or *s*-process) or fast (the *rapid* or *r*-process). Here, the terms *slow* and *rapid* consider whether neutron captures proceed at rates slower or faster than those of typical β-decays occurring along the respective nucleosynthesis path.

The *slow* neutron captures (in particular, their *main* component, including isotopes across and beyond the neutron magic number $N = 50$ up to $N = 126$) were attributed to the final evolutionary stages of red giants (called *asymptotic giant branch* or AGB stars). This was possible owing to the demonstration by Ulrich (1973) that their repeated ignition of He burning in a thin, unstable shell offered a natural way to produce the exponentially decreasing distribution of neutron exposures, previously invoked by Seeger et al. (1965).

Afterward, several attempts were made in the 70s, adopting intermediate-mass stars (see Iben and Truran, 1978) (IMS) models ($4 \lesssim M/M_{\odot} \lesssim 8$) as s-process sites. There, the ^{22}Ne(α,n)^{25}Mg source can be easily activated. However, the excessive neutron densities ($n_n \geq 10^{11} cm^{-3}$) it generated at the local temperatures ($T \simeq 3.510^{8} cm^{-3}$) were shown to be incompatible with observations (Busso et al., 1988) so that lower-mass ($M/M_{\odot} \lesssim 3$) AGB stars were finally considered (Iben and Renzini, 1982; Gallino et al., 1988). This implied assuming that the alternative ^{13}C(α,n)^{16}O neutron source (requiring lower temperatures and producing lower n_n values, around $10^7\ cm^{-3}$) could be activated, as a consequence of some partial diffusion of protons from the envelope, sufficient to produce ^{13}C in the He-rich layers when the H-burning shell reignites.

This ^{13}C(α,n)^{16}O neutron source had been suggested to be at play many years before by Cameron (1957), but even now, the elusive mixing mechanisms necessary to its activation remain a subject of active research. Many attempts were dedicated along the past three decades to this goal, often on parametric grounds (Käppeler et al., 2011; Bisterzo et al., 2012), simulating various deep mixing events (Bisterzo et al., 2014, 2015; Cristallo et al., 2015; Battino et al., 2019). Partial accounts of these efforts can be found in Busso et al. (1999); Busso et al. (2007); Karakas and Lattanzio (2014); and Busso et al. (2021).

In particular, in the present study, we shall concentrate on results obtained in a recent series of models, where the formation of the mentioned neutron source was attributed to the buoyancy of magnetic flux tubes maintained by a dynamo process (Nucci and Busso, 2014).

For what concerns fast neutron captures, the same studies by Burbidge et al. (1957) and Cameron (1957) outlined a reasonable scenario for the first time. In these early studies, a steady-state formation of isotopes by neutron addition and hold-ups for nuclei with shells at $N = 50$, 82, or 126 neutrons was already postulated. This is presently better known as the *r*-process *waiting-point concept*. Since then, *r*-process research works have been quite diverse in terms of suggested stellar scenarios (for representative historical reviews, see Seeger et al., 1965; Hillebrandt, 1978; Kratz, 1988; Cowan et al., 1991; Kratz et al., 1993).

While for several decades the high-entropy (ν-driven) winds from core collapse supernovae type II (*ccSN-II*) were proposed as the favored r-process site (see Takahashi et al., 1994; Woosley et al., 1994; Freiburghaus et al., 1999a; Kratz et al., 2008; Farouqi et al., 2010; Kratz et al., 2014), attention was also given to complementary scenarios, in particular to the decompressed ejecta of neutron star mergers (*NSM*), which were discussed in important articles since the early epochs (Lattimer et al., 1977; Freiburghaus et al., 1999b; Rosswog et al., 1999).

However, still in the early 1990s, none of the suggested *r*-process scenarios could yield satisfactory results to fit the solar system (*S.S.*) *r*-process abundances. Hence, the Mainz –Basel –Los Alamos collaboration started to use improved site-independent calculations (Kratz et al., 1993). Although not (yet) pointed out explicitly in that work, these attempts also implied the possible existence of several *r*-process sites with different abundance patterns. Therefore, the S.S. abundances generated by fast neutron captures had to be explained by a superposition of *r*-process components, with varying neutron densities n_n (with $n_n \geq 10^{20}$ cm^{-3}), and occurring on time scales between 1 and 2 s.

First experimental information on anomalous local abundance yields of an unknown nucleosynthesis origin and corresponding attempts to determine their astrophysical conditions were from cosmochemical isotopic measurements in meteoritic *CAI*, together with presolar SiC – X grains and nanodiamonds (see Wasserburg et al., 1977; Niederer et al., 1980; Kratz et al., 2001; Pellin et al., 2006; Farouqi et al., 2009). In addition, *elemental* abundances were determined in metal-poor halo stars (for early articles, see Sneden et al., 1996, 2003; Hill et al., 2002; Honda et al., 2007; Mashonkina et al., 2007).

Initially, the suggested sites were based on a rather indirect way on nucleosynthesis modeling. Early research works suggested that light and intermediate trans-Fe elements could be synthesized due to a "weak *r*-process" component, while the heavier elements up to the $A = 195$ peak and the actinides could be synthesized in a "main r-process" variant. Recently, observations of gravitational waves from an *NSM* event (GW170817 see Abbott et al., 2017), together with the subsequent electromagnetic emission from a kilonova (see

Evans et al., 2017), showed the first direct evidence of the ongoing *r*-process nucleosynthesis (Rosswog et al., 2018). Based on the emission of the red wavelength lanthanide fraction, Ji et al. (2019) suggested however that this *NSM* event did not actually produce a typical S.S. *r* pattern: further observations of similar objects are needed to draw firmer conclusions.

In order to accumulate sufficient information on the various *r*-process contributions from heterogeneous sources, today, systematic and accurate observational constraints from many low-metallicity stars exist (see the *HERES* survey (Hamburg ESO R-process Enhanced Star) Mashonkina and Christlieb, 2014) and provide adequate databases for comparing model results.

In the present study, after recalling briefly the results of recent work on *n*-captures, the status of heavy-element production is studied by verifying the compatibility of the scenarios for *s*- and *r*-process nucleosynthesis, through a comparison of their respective predictions for the S.S. composition. With this goal in mind, the mentioned research on the classical *waiting-point* approach (Kratz et al., 2007) turned out to be of special relevance, as it can exclude uncertainties related to the modeling of specific sites.

Reasonably good nuclear inputs for this work are available only below $A \simeq 140$–142, so this is the mass range on which we focus. Predictions from fast neutron captures are then compared to those for *s*-processing in AGB stars of low mass (namely, for masses M = 1.3, 1.5, 2.0, and 3.0 $M_{\odot}$, computed at metallicities from [Fe/H] = 0.1 down to [Fe/H] = − 0.8), after weighting on the classical Salpeter's initial mass function (IMF) (Salpeter, 1955) and on the star formation rate (SFR) from Maiorca et al. (2012). Thus, we infer some new hints, including suggestions for future measurements.

A short outline of the adopted *s*-process models and of their predictions is presented in Section 2, while in Section 3, we discuss the assumptions for the *waiting-point* scenario of *r*-processing. The good agreement found between these complementary, independent views and the residual problems emerging are then outlined in Section 4, where improvements expected from future β-decay rate measurements are also underlined. Preliminary conclusions are drawn in Section 5.

2 A model for slow neutron captures and its results

In recent studies, revisions on the status of slow neutron captures, as occurring in evolved stars of low mass ($1.3 \lesssim M/M_{\odot} \lesssim 3$) during the *AGB* stages, were discussed. These works deal with the particular approach that considers the buoyancy of magnetic flux tubes in a stellar dynamo process as responsible for the deep mixing episodes mentioned in Section 1 (see Nordhaus et al., 2008; Denissenkov et al., 2009). This idea led to analytical models of the underlying physical mechanisms in terms of 3D solutions for the magneto-hydrodynamic (MHD) equations involved (Nucci and Busso, 2014), where the previously quoted recent upgrades were obtained with the help of full stellar models (Vescovi et al., 2020; Vescovi, 2021), subsequently integrated by post-process computations, derived with the aim of reproducing the relevant physical parameters without recomputing the energy generation (Busso et al., 2021). In those attempts, comparisons were presented between model predictions and some major available constraints to *s*-processing (from high-resolution spectroscopy of selected classes of evolved stars to the *S.S.* abundances as emerging from the chemical evolution of the Galaxy and to isotopic admixtures of heavy elements, as measured in presolar grains recovered in pristine meteorites). In that first analysis, the input data for cross-sections of stable isotopes were mainly obtained from the Kadonis 0.3 repository (Dillmann et al., 2006), partly integrated with more recent measurements. For radioactive nuclei, cross-sections were taken from Shibata et al. (2011) (*jend4.0*), while rates for $\beta^{\pm}$ decays and electron captures were from Takahashi and Yokoi (1987). The global accord obtained in that work between model predictions and S.S. abundances for *s*-only nuclei appeared to be fair, with a dispersion of model data roughly at the same level as measurement uncertainties (around $\sigma \simeq 15\%$). Also, general indications from other constraints suggested a reasonable agreement, although not much could be said on possible further improvements and on discrepancies for individual isotopes.

Recent research on nuclear cross-sections, on the other hand, pointed out that substantial work is still needed in that field, both through real new estimates and through reanalysis of existing datasets (e.g., by Monte Carlo techniques) (Reifarth et al., 2018). Partial results from this work have recently been used (Vescovi and Reifarth, 2021) to study the impact on nuclear upgrades in stellar models. So far, however, a global update of the Kadonis compilation is still waited for. For the aforementioned reasons, it is important that also from the point of view of stellar modeling, a search must be pursued for better constraints on nuclear parameters. Palmerini et al. (2021), in particular, adopted the compilation of cross-sections Kadonis 1.0 (Dillmann, 2014) and made a detailed comparison between stellar predictions from specific masses and metallicities and the record of isotopic anomalies measured in presolar SiC grains (Liu et al., 2015; Stephan et al., 2018), covering the atomic mass interval from Sr to Ba (again, $A \lesssim 140$). The analysis was, in particular, useful to verify the rather detailed agreement that could be reached and, at the same time, to indicate the need for revisions of some weak interactions, e.g., suggesting new measurements for the β-decay rates of Cs isotopes in ionized environments (see also Mascali et al., 2020; Li et al., 2021; Taioli et al., 2021).

As mentioned, the upgrades by Busso et al. (2021) and Palmerini et al. (2021) were based on the idea that, during the so-called *third dredge-up* or *TDU* episodes (see Lugaro et al., 2012; Karakas and Lattanzio, 2014), MHD mechanisms maintained by dynamo cycles

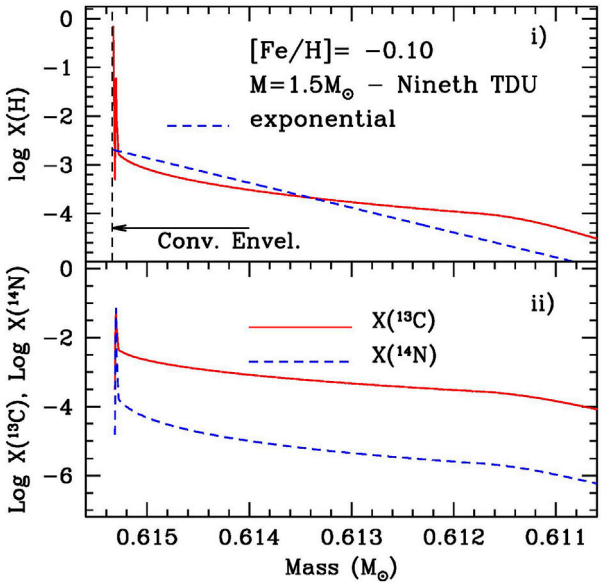

FIGURE 1
Pocket of protons (panel i) and the ensuing distributions of ^{13}C and ^{14}N (panel ii) in the layers below TDU, in one of the situations modeled by Palmerini et al. (2021). The abundances by mass (X) after the activation of extra-mixing mechanisms due to magnetic buoyancy are shown in the figure. We recall that, for an isotope – i, the abundance by number N_i and that by mass $X(i)$ are related by the formula $N_i = \frac{pX_i}{A_i m_H}$, where m_H is the atomic mass unit.

could induce the downward penetration of protons into the He-rich layers of an evolved star, as required to fuel *s*-processing. The ensuing models are characterized by the formation of distinctively large reservoirs of protons, up to 5–10 times those initially suggested in more standard articles on the subject (Kaeppeler et al., 1990). In contrast, the local concentration of pollutants, hydrogen primarily, remains very low (see Figure 1 panel i). It is so low, actually, that the subsequent re-ignition of the H-burning shell, allowing proton captures to occur on the abundant ^{12}C, can produce ^{13}C, but only minimal traces of ^{14}N (see Figure 1, panel ii). Under such conditions, the neutrons that are made available for heavy-element nucleosynthesis by the ^{13}C(α,n)^{16}O source are essentially unfiltered by intermediate-mass nuclei and remain quite abundant.

Three important differences emerge with respect to previous models.

- First of all, the possibility to synthesize fresh ^{19}F from the reactions starting at nitrogen itself is now strongly reduced, and the ensuing fluorine abundance predicted as a function of metallicity is now in close agreement with actual observations (Vescovi et al., 2021).
- A second remarkable implication is the very limited action of the so-called *neutron poisons*, i.e., the intermediate-mass nuclei with significant cross-sections (^{14}N being their

TABLE 1 Predictions of the fractional solar abundances from fast and slow *n*-captures (88 ≤ A ≤ 142).

Z	*A*	Element	*N*(S.S.)	S.S. *r* – %	S.S. *s* – %	AGB *s* – %
38	88	Sr	19.2	10.2	89.8	89.2
39	89	Y	4.35	23.8	76.2	78.6
40	90	Zr	5.621	34.5	65.5	66.9
—	91	—	1.226	36.1	63.9	72.8
—	92	—	1.873	35.4	64.6	72.2
—	94	—	1.899	17.1	82.9	92.1
—	96	—	0.306	95.7	4.4	8.40
41	93	Nb	0.780	33.8	66.2	58.7
42	95	Mo	0.412	53.9	46.1	42.7
—	97	—	0.249	51.0	49.0	45.4
—	98	—	0.630	57.7	42.3	75.7
—	100	—	0.253	97.2	2.8	(< 1)
44	99	Ru	0.230	69.6	30.4	24.9
—	101	—	0.228	81.2	18.8	15.6
—	102	—	0.570	37.9	62.1	42.8
—	104	—	0.336	100	(< 1)	4
45	103	Rh	0.338	83.0	17.0	13.1
46	105	Pd	0.3079	83.4	16.6	14.0
—	106	—	0.377	73.9	26.1	50.7
—	108	—	0.365	47.8	52.2	63.23
—	110	—	0.162	100	(< 1)	5
47	107	Ag	0.258	79.1	20.9	14.8
—	109	—	0.239	82.6	17.4	24.8
48	111	Cd	0.202	81.1	18.9	24.2
—	112	—	0.381	44.2	52.8	51.5
—	113	—	0.193	65.4	34.6	35.6
—	114	—	0.454	36.1	63.9	64.5
—	116	—	0.119	92.1	7.9	18.3
49	115	—	0.171	63.1	36.9	36.9
50	117	Sn	0.276	47.3	52.7	50.6
—	118	—	0.870	63.1	36.9	76.2
—	119	—	0.308	49.6	50.4	41.2
—	120	—	1.171	19.8	80.2	85.1
—	122	—	0.166	61.5	38.5	40
—	124	—	0.208	100	(< 1)	(< 1)
51	121	Sb	0.205	67.3	32.7	40.0
—	123	—	0.154	96.0	4.0	(< 1)
52	125	Te	0.337	72.5	27.5	22.9
—	126	—	0.894	48.3	51.7	46.6
—	128	—	1.494	100	(< 1)	(< 1)
—	130	—	1.594	100	(< 1)	(< 1)
53	127	I	1.59	97.7	2.3	5
54	129	Xe	1.507	97.1	2.9	4
—	131	—	1.198	93.3	6.7	8.1
—	132	—	1.449	64.3	35.7	42.3
—	134	—	0.535	89.4	10.6	(< 1)

(Continued on following page)

TABLE 1 (*Continued*) Predictions of the fractional solar abundances from fast and slow *n*-captures (88 ≤ A ≤ 142).

Z	*A*	Element	*N*(S.S.)	S.S. *r* – %	S.S. *s* – %	AGB *s* – %
—	136	—	0.435	100	(< 1)	(< 1)
55	133	Cs	0.368	82.2	17.8	16.7
56	135	Ba	0.300	78.5	21.5	72.2
—	137	—	0.515	41.2	58.8	60.4
—	138	—	3.264	15.8	84.2	91
57	139	La	0.459	21.3	78.7	79.8
58	140	Ce	1.030	13.1	86.9	80.4
—	142	—	0.129	74.9	25.1	14.3
59	141	Pr	0.175	45.4	54.6	66.2

progenitor) acting as filters and limiting the number of neutrons captured by iron and its progeny.

- Finally, a reduced ^{14}N concentration also implies a reduced formation of ^{22}Ne.

This last point follows from the activation of the chain:

$$^{14}\mathrm{N}(\alpha,\gamma)^{18}\mathrm{F}(\beta^{+}\nu)^{18}\mathrm{O}(\alpha,\gamma)^{22}\mathrm{Ne}. \quad (1)$$

Limiting its efficiency limits the neutron flux that can be released at a higher temperature and with a higher neutron density, when a *thermal pulse* finally develops, accompanied by the sudden enhancement of the He-burning rate (see Busso et al., 1999; Herwig, 2005, for details).

The aforementioned conditions can, in principle, be met by various mixing mechanisms, beyond the MHD one explored here. Some indications in this sense are contained in Appendix 1, where we present some general comments on the stellar models for neutron captures, which are maintained separate from the main text of this article, dedicated to nuclear issues.

We note that the scenario described here for the *s*-process is closer to the classical *phenomenological* approach (Kappeler et al., 1989) than most models discussed in recent years, especially in terms of its generally lower neutron densities, and hence of the operation of reaction branches. As compared to the mentioned models (see e.g., Cristallo et al., 2011), our production of the heavier stable isotopes of neutron-capture elements, like e.g., ^{86}Kr, ^{96}Zr, and ^{100}Pd (see Table 1), is now strongly reduced. This is relevant for our estimates of the Mo isotopes discussed later, where the neutron flow now proceeds mainly along the sides requiring low values of n_n (on average below 10^8 n/cm^3). In this respect, while the ^{22}Ne(α,n)^{25}Mg neutron source (yielding higher neutron densities than the ^{13}C(α,n)^{16}O one) remains important for fixing the operation of reaction branchings, its role is, however, reduced and so is that of IMS, where its activation would be very efficient. As far as one can judge now, super-AGB stars, of mass 8–10 M$_\odot$, currently considered the parents of *e*-capture supernovae (Leung et al., 186 2020), should be at the best

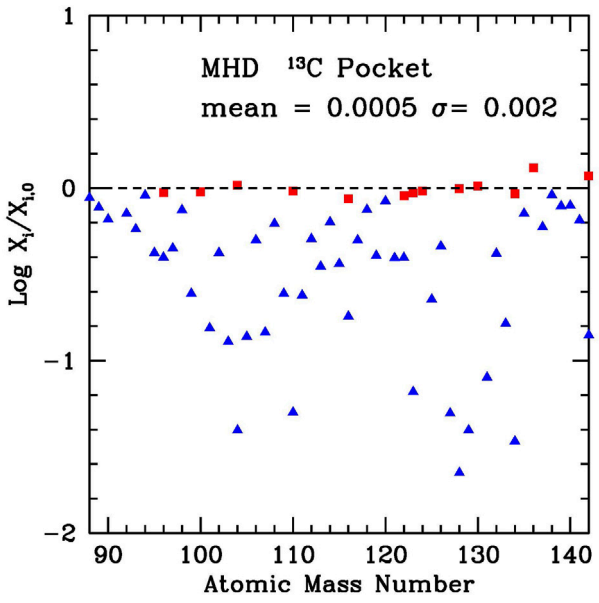

FIGURE 2
Distribution of *s*-process fractional abundances in the mass range 88 ≲ *A* ≲ 142 considered in the present work, as obtained with the weighting procedure described in Busso et al. (2021) and Palmerini et al. (2021) and (more synthetically) in Section 2. Red symbols refer to the so-called *s–only* nuclei, which are shielded by stable isotopes against contributions from the *r*-process.

marginal in establishing the galactic average of the *s*-nuclei, although they might be relevant in rare, individual cases.

In the computations discussed here, AGB models of the type described so far, extended to stellar masses for 1.3–3 M$_\odot$, with metallicities in the range −0.8 ≲ [Fe/H] ≲ 0.1, have been computed for the purposes described in Section 1, using the Kadonis 1.0 cross-section compilation. They were subsequently averaged on galactic time scales with the mentioned choices for the IMF and SFR. The results, expressed in terms of a distribution of abundances for the isotopes in the adopted atomic mass range, were divided by the solar initial concentrations from Lodders (2021) and normalized to unity so that they express average *s*-process contributions to the solar composition. This procedure, aimed at reproducing roughly the outcomes of a galactic chemical evolution model up to the solar formation era, is not exempt from serious drawbacks, which must be taken into account in estimating the global uncertainties. Indeed, while the choices for the IMF and SFR are rather standard, the method cannot account for the real complexity of the inter-relations among the many subsystems of the galaxy. In this respect, the accuracy achieved is roughly at the same level as the one for the *r*-process, described in Section 3; hence, it is adequate for the present purposes. However, in parallel to this, we have, in any case, undertaken a more sophisticated chemo-

dynamical simulation of the galaxy and of its enrichment in *s*- and *r*-isotopes (Antonuccio-Delogu et al., 2022), based on the GIZMO open-source code (see: http://www.tapir.caltech.edu/).

The resulting fractional S.S. abundances in the chosen mass range ($88 \lesssim A \lesssim 142$) are shown in Figure 2, adopting the solar composition from Lodders (2021). As discussed previously in various articles (see Trippella et al., 2016; Busso et al., 2021), the results are largely independent of the specific stellar models and type of mixing adopted, provided these consider some general crucial features. These essentially 1) maintain a moderate temperature in the thermal pulses (low mass Kaeppeler et al., 1990); 2) provide a dominant contribution from the $^{13}C(\alpha,n)^{16}O$ reaction (Käppeler et al., 2011); and 3) give rise to mixing mechanisms like those in Figure 1, providing extended ^{13}C distributions with little ^{14}N, to account for the effects on the neutron fluxes mentioned earlier (Liu et al., 2014, 2015; Trippella et al., 2016). By respecting these constraints, in general, one obtains predictions close to 100% for the so-called *s*-only isotopes, where remaining discrepancies can be attributed to nuclear effects. In this respect, given the complexities of stars, it is conceivable that further, non-magnetic, mechanisms suitable to give rise to the same effects might contribute to the picture (see Battino et al., 2016, 2019; Denissenkov and Tout, 2003).

The specific predictions obtained with our models are shown in Figure 2 (where the *s*-only nuclei are indicated in red). There, the reproduction of solar abundances is good, with an average dispersion around 11%. This check gives us a general confidence on the method, allowing us to compare our expectations for the other (non-*s* only) isotopes with the complementary estimates derived from *r*-processing. We then list our model *s*-process contributions to S.S. abundances in Table 1, column 7.

3 The waiting-point model for rapid neutron captures and its results

Since none of the presently discussed scenarios for rapid neutron-capture nucleosynthesis seems to produce a complete S.S. *r*-like pattern, ranging from the light trans-Fe region up to the actinides, for this study (i.e., for comparing the isotopic abundance fractions of the *s*-process and *r*-process in the S.S. composition), we decided to choose an updated version of the classical site-independent *waiting-point* concept (Coryell, 1956; Burbidge et al., 1957; Cameron, 1957; Kratz, 1988; Kratz et al., 1993). It assumes a chemical equilibrium between fast neutron captures (n, γ) and photo-disintegrations (γ, n) within isotopic chains, followed by a β-equilibrium during the freeze-out phase within isobaric chains. In our present approach, we combine the results from our early publications (see Kratz et al., 1993) with the later improvements from experimental data and microscopic models (see Pfeiffer et al., 1997; Kratz et al., 2000; Möller et al., 2003; Farouqi et al., 2010; Kratz et al., 2014, Kratz et al., 2019).

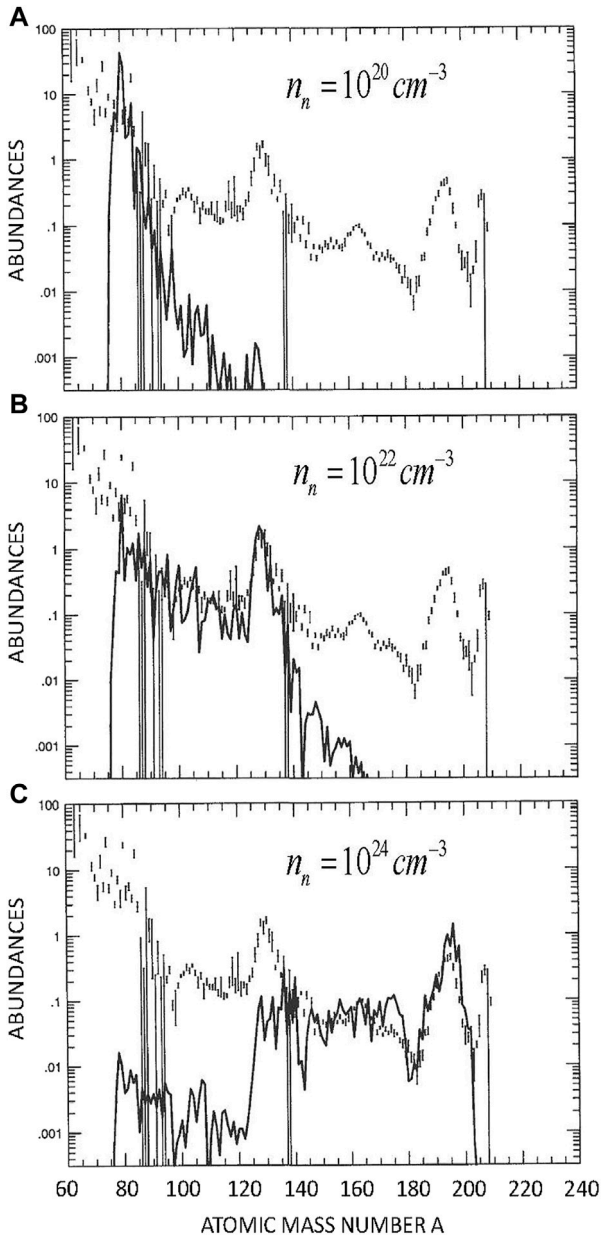

FIGURE 3
Results of time-dependent steady-flow *r*-process calculations with neutron densities $n_n = 10^{20}$ cm^{-3} **(A)**, $n_n = 10^{22}$ cm^{-3} **(B)**, and $n_n = 10^{24}$ cm^{-3} **(C)**, and corresponding process duration τ_r = 1.2, 1.7, and 2.1 s, respectively. The abundances by number are shown in the figure, in a scale in which $N(Si) = 10^6$. This is compared to the S.S. *r*-" residuals" in the same scale. In principle, adding up the abundances of those three *r*-process components will result in the complete S.S. *r*-process abundance blend (adapted from Kratz et al., 2000).

As an example of the *r*-process abundances we had obtained already two decades ago, in Figure 3, we show the results from three specific waiting-point calculations with different neutron densities and corresponding process duration (solid lines), in

comparison to the S.S. *r*- "residuals" from that time. In these calculations, the global deformed *Extended Thomas Fermi Model plus Strutinsky integral* and the *Bogolyubov-enhanced shell-quenching*, (*ETFSI-Q*) mass model (Pearson et al., 1996) have been used, together with the corresponding *Quasi-particle random-phase approximation* for *Gamow-Teller and first forbidden* transitions (*QRPA(GT + FF)*) (see Pfeiffer et al., 2002; Möller et al., 2003). We show here these exemplary results because, while documenting the importance of the N = 50, 82, and 126 bottlenecks of the *r*-matter flow, they are completely site-independent and, despite this, they already show the general *r*-abundance patterns of the different *r*-process scenarios, more or less as we know them today and as we have published later in Farouqi et al. (2010) and Kratz et al. (2014).

In the first panel of Figure 3, a low neutron density n_n = 10^{20} cm^{-3} and a process duration of τ_r = 1.2 s were chosen to obtain a "best fit" of the $A \simeq 80$ *r*-process peak from its known $N \simeq 50$ precursor isotopes between Z = 29 (Cu) and Z = 32 (Ge) (see Kratz et al., 1991). Beyond this peak, a steeply decreasing abundance pattern by about four orders of magnitude is observed for the mass region above, down to the minimum yields at $A \simeq$ 130. Currently, we know that this pattern "mimics" the isotopic distributions of Sr, Zr, Mo, and Ru observed in the presolar SiC grains of type *X*, measured by the Argonne–Chicago group (see Pellin et al., 2006; Farouqi et al., 2009; Kratz et al., 2019). The nucleosynthesis origin of this abundance pattern up to the rising wing of the second *r*-process peak at $A \simeq 130$ has been attributed to classical *ccSNe* (Kratz et al., 1993; Farouqi et al., 2009, 2022). The second panel of Figure 3 shows an abundance component obtained with a slightly higher neutron density of n_n = 10^{22} cm^{-3} and a process duration of τ_r = 1.7 s. It covers the S.S. *r*-region up to the full $A \simeq 130$ peak and continues with decreasing abundances in the light *R.E.E* region up to about Eu. This *r*-process component has been normalized to the *r*-only isotopes ^{128}Te and ^{130}Te, where again a number of experimental data for the progenitor isotopes from Z = 47 (Ag) up to Z = 51 (Sb) exist (see Kratz et al., 2000).

In addition to the $A \simeq 130$ *r*-abundance peak, a wide range of (β, γ) and delayed neutron spectroscopic data, as well as accordingly updated microscopic models, are available in the region near Z = 34 (Se) and Z = 40 (Zr), where the shape transition between the magic N = 50 shell *via* the spherical N = 56 subshell up to the onset of strong (rigid rotor) ground-state deformation plays a decisive role in the determination of various nuclear properties (see Kratz et al., 1983a,b; Lhersonneau et al., 1994; Möller et al., 2003). As an example, the improved understanding of the nuclear structure resulted in changes of theoretical β-decay properties for the $N \simeq 56$ isotopes by factors from 13 (e.g., for ^{89}Se) up to 53 (e.g., for ^{93}Sr). Fast neutron captures dominant in this regions above A $\simeq$ 90 (our second n_n component) are frequently denoted as the *weak r-process*. Today, we know that its abundance pattern "mimics" the elemental

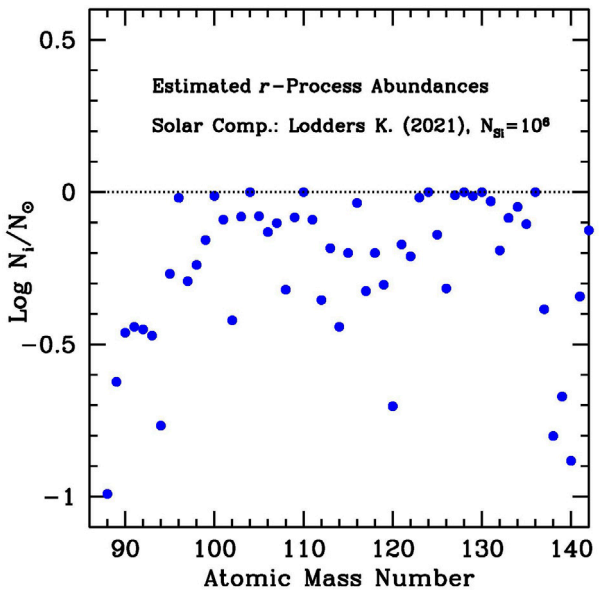

FIGURE 4
Distribution of *r*-process fractional abundances as estimated by our *waiting-point* approximation, according to the discussion in the text. Similar to what is shown in Figure 2 for the *s*-process, nuclei considered to be of essentially pure *r*-process origin (≥95%) are indicated with red symbols. It should be noted that, following a common habit, the second *r*-peak was normalized to ^{128}Te and ^{130}Te, assumed to be *r*-only. This has some support in the data of Table 1, column 7, where we show that, even in the estimates from AGB models, their *s*-fractions are predicted to be ≤1%.

distribution of metal-poor, *r-poor*, or *incomplete r* stars with [Eu/Fe] $\lesssim$ 0.2.

A typical example of such a type of star is the so-called "Honda star" (HD122563, see Honda et al., 2007), with its overabundances relative to the S.S. *r*-pattern of the light trans-Fe elements and its decreasing abundances in the rare earth element (*R.E.E.*) region between Z = 68 (Er) and Z = 70 (Yb). As one of the signatures to classify the different types of halo stars, astronomers use, for example, the abundance ratio of light-to-heavy mass regions, using Z = 38 (Sr) and Z = 63 (Eu) as representative elements. For the *r*-poor Honda star, the ratio (Sr/Eu) $\simeq$ 505, which is a factor 24, higher than the S.S. *r*-ratio of 21. The nucleosynthesis origin of these *r*-poor stars can very likely be attributed to *jet-like* or *magneto-rotational* SNe, with low strengths of magnetic fields and of rotation (see Nishimura et al., 2017; Farouqi et al., 2022).

The third panel in Figure 3 shows a typical abundance pattern for a *main r-process* component, with consequently higher neutron densities (here, n_n = 10^{24} cm^{-3}) and slightly longer process duration (here, τ_r = 2.1 s), which covers the S.S. *r*-region of the *R.E.E.*, the full third *r*-process peak at $A \simeq$ 195 and beyond, up to the actinides. This last n_n component has

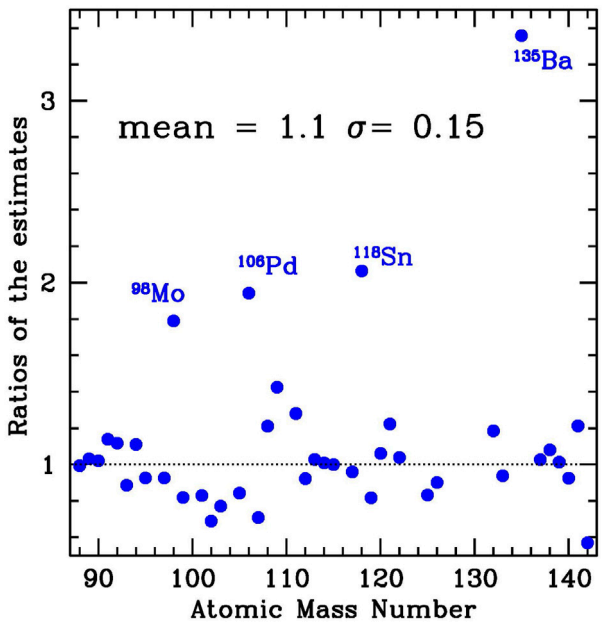

FIGURE 5
Ratios between the two sets of predictions for the *s*-fractions, as presented in Table 1. Despite the good agreement, with rather randomly distributed differences, a mean value close to unity, and a reasonable variance, a few outliers emerge and are shown here. The plot includes all nuclei predicted to derive from *s*-processing by a fraction larger than 10%. The mean value and variance are computed excluding nuclei that are off by more than a factor of 3, in this case only ^{135}Ba.

been normalized to the top of the peak with its *r*-only isotopes of Os, Ir, and Pt, formed in the back decay of their extremely neutron-rich, experimentally still unknown, $N \simeq 126$ precursor isotopes of the nuclei from $Z = 68$ (Er) to $Z = 72$ (Hf). Presently, we know that this kind of a *main* or even *strong r*-process pattern "mimics" the elemental abundances of the so-called *r*-enriched metal-poor halo stars with [Eu/Fe] $\geq +0.8$. Typical examples for this class of stars are the normal *r-II Sneden star* (CS22892-052, see Sneden et al., 2003) and the so-called *actinide-boost Cayrel-star* (CS31082-001, see Hill et al., 2002), attributed to different types of *NSM* (see Rosswog et al., 2018; Farouqi et al., 2022).

By simply adding up these three abundance patterns, we get a total abundance distribution which comes relatively close to the S.S. *r-blend*. In particular, our computed estimates for the *r*-process contributions to S.S. abundances, normalized to N(Si) = 10^6, and with updated nuclear inputs are presented in Figure 4.

In the simplest possible physical realization of the solar *r*-process distribution, stellar and *NSM* models would have to find where exactly the aforementioned "components" are produced by nucleosynthesis models. Quite obviously, this is a very naive view, as no astrophysical source can be imagined to host such simple neutron-capture processes at constant neutron density. The previous indications, and their descending suggestions for nuclear parameters, have instead to be looked at as first-order approximations, good for an assessment of the very complex nuclear problems related to the reaction paths of *r*-nuclei. As we shall see, even this simple approach already yields useful indications and a remarkable general consistency with Solar System data. Also attributing the aforementioned components to specific stellar sources is a difficult task in the cluster abundance patterns observed in galactic, mainly low-metallicity, stars. With these limits in mind, we comment, however, briefly on this point in Appendix 1.

4 Comparisons and discussion

A comparison of the results from the two neutron-capture approaches outlined so far (Figures 2, 4) is presented in Table 1. As mentioned, for what concerns the *r*-process model, here the original computations shown in Figure 3 have been updated, considering various different mass models with consistent *QRPA(GT + ff)* β-decay predictions by Farouqi et al. (2010) and the quoted recent deformed *FRDM12/QRPA* model combination by Kratz et al. (2014).

In Figure 5, we show the resulting ratios between the two sets of expectations for the *s*-process fractions of solar abundances. The agreement between these completely independent approaches is quite good. It is actually the best so far published, to our knowledge.

Despite this satisfactory outcome of our work, some discrepancies remain and require a more detailed analysis, as presented in the following subsections.

4.1 ^{98}Mo

The element Mo as measured in early S.S. materials provides important tools for understanding the contamination of the presolar nebula in heavy nuclei. On the one hand, its isotopic admixture in the *mainstream*-type of presolar SiC grains (Stephan et al., 2019) is quite typical of AGB star progenitors (Palmerini et al., 2021). On the other hand, Mo isotopes show very different anomalies in the so-called presolar *SiC – X*-grains (Pellin et al., 2006), whose origin has been attributed to *ccSNe* (Farouqi et al., 2009; Kratz et al., 2019).

Stephan and Davis (2021) inferred, from isotopic measurements in presolar SiC grains of AGB origins, estimates for the *r*- and *s*-process decoupling of Mo isotopes. In the specific case of ^{98}Mo, our estimates from the *waiting-point* approximation would suggest a lower *s*-process percentage (42.3%) than the one from the aforementioned authors (74.4%, very similar to the expectation from AGB models, 75.7%). In *s*-process scenarios, the synthesis of lighter Mo isotopes depends on several branching reactions at Nb isotopes, with contributions from isomeric states at ^{93}Nb,

^{94}Nb, and ^{95}Nb (see Figure 5 in Palmerini et al., 2021). All of them terminate before ^{96}Mo, which is an *s*-only nucleus whose abundance is very well reproduced by the models discussed in Section 2 (see Figure 2). We remember, however, that cross-sections in the Zr–Mo region are still very uncertain (for the unstable ^{95}Zr, experimental information is essentially missing), and new measurements are crucial here for any conclusion. Cross-sections for Mo isotopes are actually under measurement now by the n_TOF collaboration (Guerrero et al., 2013).

Concerning the *r*-process predictions, we compare the results from the old mass- and shell model combination *ETFSI-Q/QRPA* (as used e.g., in Kratz et al., 2000) with our most recent *FRDM/QRPA* computations (see e.g., Kratz et al., 2014). For both model combinations, the basic nuclear parameters are obtained from the mass model. They are the mass derivatives Q_β and S_n, in addition to the ground-state shape of the β-decay mother isotope, related to the *quadrupole deformation parameter*, ϵ_2, (for which positive values mean prolate shapes and negative values mean oblate shapes). With these parameters, the so-called *β-strength function* is calculated within the *QRPA* shell model, from which spins and parities (J^π), level schemes, β-feedings (log *ft* values), and finally the integral quantities, $T_{1/2}$ and β-delayed neutron-branchings P_{xn}, are deduced.

To summarize, for ^{98}Mo and the following cases ^{118}Pd, ^{118}Sn, and ^{135}Ba, we compare the respective hold-up points of the isotopic *r*-matter flow at $S_n \lesssim 2$ MeV for masses *A* and (*A*+ 1), which define the *r*-process progenitor isotopes with their β-decay parameters $T_{1/2}$ and P_{xn} and their resulting initial isotopic waiting-point abundances. After modulation by the β-delayed *n*-branchings during the freeze-out, the final abundance yields of the stable nuclei of interest are obtained.

For the specific case of ^{98}Mo ($Z = 42$, $N = 56$), in both mass/shell model combinations, the dominant progenitors at $A = 98$ are ^{98}Kr ($Z = 36$, $N = 62$) and ^{98}Se ($Z = 34$, $N = 64$). For the *ETFSI-Q/QRPA* version, they account for ≃ 81% and ≃19%, respectively. The S_n values for the dominant ^{98}Kr hold-up point are practically identical for both model combinations, and (to our relief) the β-decay properties $T_{1/2}$ and P_n are experimentally known for the whole isobaric decay chain to ^{98}Mo. Since the relevant nuclear data predictions for ^{98}Se are also quite similar, we can estimate the total effect for $A = 98$, which is negligible.

More substantially, instead, the effect from the single waiting-point progenitor isotope in the $A = 99$ mass chain ($Z = 35$, $N = 64$), i.e., ^{99}Br will feed the $A = 98$ mass chain *via* its predicted high P_n value. Here, relative to *ETFSI-Q*, in the *FRDM12* mass model, the decreasing S_n trend to the hold-up isotopes with $S_n \simeq 2$ MeV is shifted by two units to higher masses. As a consequence, with the *FRDM/QRPA* model combination, the calculated waiting-point abundance of ^{99}Br is reduced. In addition, taking into account the slightly different P_n predictions, the final S.S. *r*-fraction of the stable isotope ^{98}Mo would be reduced from 57.7%, as listed in Table 1, to about 45%, which would correspond to an increase of the S.S. *s*-fraction from 42.3% to about 55%, in better agreement with the AGB s-process model predictions, now being only a factor 1.38 lower than the S.S. *s*-values.

The aforementioned discussion is only an attempt of clarifying how the present numbers still have an unavoidable *local* dependence on the choice of nuclear input data. We underline that these difficulties cannot be overcome by referring to specific astrophysical sites, being rooted in the nuclear inputs; they will affect equally any nucleosynthesis model, as all such models require nuclear input parameters. Our estimates represent, therefore, a *reasonable* approximation to the present state-of-the art. Although a "universal" set of inputs does not exist, we can, nevertheless, receive useful indications from comparisons like the ones discussed here.

4.2 ^{106}Pd and ^{118}Sn

A very complex situation characterizes the region from Pd to Sn, for which the rather intricated *s*-process branching points are illustrated in Figure 6.

In the past 15 years, this region was the subject of a hot debate on the possible existence of a *light element primary production* mechanism, or *LEPP* (Travaglio et al., 2004), just devised to explain abundance deficiencies in this mass region (Montes et al., 2007). Today little remains of that debate, with the understanding that a blend of different *r*-process components is required (see Figure 3 and Farouqi et al., 2009).

Even now, however, the outliers ^{106}Pd and ^{118}Sn certify the difficulties in this mass interval. From the *s*-process point of view, the cross-sections to the various (not always thermalized) isomeric states (Theis et al., 1998) shown in Figure 6 are almost unknown or very uncertain, as is the behavior of the branching β-decays in the stellar plasma. This is, therefore, an atomic mass zone where new experimental studies are needed, both for cross sections and decay rates, before the estimates of Table 1 can be improved significantly. Among the β-decay rates to measure in highly ionized environments, we underline, in particular, the cases of ^{113,115}Cd and ^{115}In, hosting possibly non-thermalized isomeric states (Takahashi and Yokoi, 1987).

From the *r*-process point of view, for the even–even nucleus ^{106}Pd ($Z = 46$, $N = 60$), the nuclear data analysis starts to become more difficult than the possible *r*-process progenitor isotopes of lighter elements. There are two main reasons for this. First, the strongly dominating, single *r*-process precursor isotope ($Z = 38$, $N = 68$) ^{106}Sr was not known when the *ETFSI-Q/QRPA* and *FRDM/QRPA* calculations were performed. Some β-decay properties were, however, already known from the neighboring Y to Nb isotopes, which could be used to check the reliability of the model predictions for ^{106}Sr, and second, these progenitor sites already have two neutrons beyond the $N = 66$ mid-shell, between the magic $N = 50$ and $N = 82$ shells, where

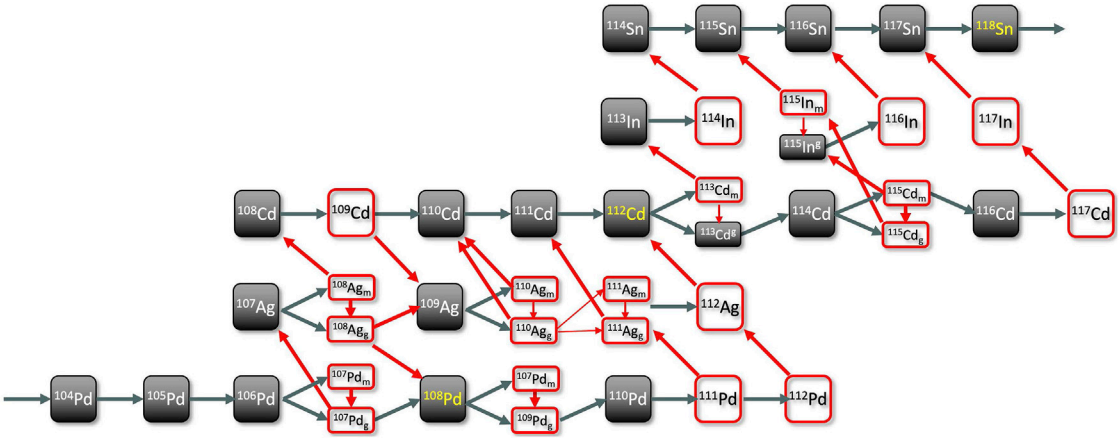

FIGURE 6
Section of the chart of the nuclei from Pd to Sn, including the isotopes ^{106}Pd and ^{118}Sn for which we have a discrepancy in the predictions from the two models discussed in the text. Crucial isomeric states are shown.

the transition between strongly deformed and spherical shapes is beginning. As expected for $N = 68$, both model combinations still predict a strong ground-state deformation of $\epsilon_2 \simeq 0.3$. Hence, the resulting patterns of the β-strength functions should also be quite similar. However, a first difference is already observed for the nuclear mass derivatives Q_β (energy output of the decay) and S_n (binding energy of the last neutron). The old mass formula *ETFSI-Q* predicts a 1.75-MeV larger Q_β value and a 230 keV lower S_n value relative to the more modern *FRDM* model. Consequently, the theoretical $T_{1/2,FRDM}$ is larger (by a factor $\simeq$ 2.3), and the $P_{n,FRDM}$ is reduced (by a factor $\simeq$ 1.5). By combining the possible effects of these two nuclear quantities, the final result on the S.S. *r*-fraction will be negligible.

For the predicted trends of the theoretical S_n values, the situation is, however, different. For the *FRDM* model, the hold-up point of the *r*-matter flow in the Sr isotopic chain at $S_n \simeq$ 2 MeV will again be slightly shifted to higher masses, as compared to the *ETFSI-Q* prediction. According to the nuclear Saha equation, this will distribute the initial waiting-point abundances to some extent to the progenitors ^{106}Sr and ^{108}Sr. A rough estimate of the likely effect on the final S.S. *r*-fraction would result in its reduction from $\simeq$ 74% from the *ETFSI-Q/QRPA* approach to values between $\simeq$ 67% and $\simeq$ 59%. This would reduce the present "discrepancy" in the latter case from a factor 1.5 to around 1.2.

Again, the ($Z = 50$, $N = 68$) even–even isotope ^{118}Sn has only a single, strongly dominating (but experimentally completely unknown) *r*-process progenitor ($Z = 42$, $N = 76$), i.e., ^{118}Mo. Furthermore, this isotope lies in the second part of the shape-transition region, only six neutrons below the spherical $N = 82$ shell, where practically all global mass models, not only *ETFSI-Q* and the different *FRDM* versions, have severe difficulties to predict reliable nuclear structure trends.

According to the aforementioned analysis presented, one can say that, in this mass range, future improvements of the agreement between the *r*-process and *s*-process models can possibly come from revisions of the nuclear parameters (cross sections and, probably more important, β-decay rates) for the slow neutron captures. Concerning the *r*-process, because of its "exponential sensitivity" (Saha equation), we would primarily request new S_n (nuclear mass) revisions and only as a second priority estimates of β-decays far from stability.

4.3 ^{135}Ba

The *s*-process production of ^{135}Ba remains very uncertain today, as a consequence of the evidence that the decay rates of Cs isotopes adopted for decades (Takahashi and Yokoi, 1987) are not accurate enough. Revisions have been recently presented (Li et al., 2021; Taioli et al., 2021) and thanks to them, it was shown that it is now possible to improve considerably both the reproduction of solar abundances for the *s*-only nuclei ^{134,136}Ba (see Busso et al., 2021; Taioli et al., 2021) and the isotopic admixture of Ba isotopes in presolar SiC grains (Li et al., 2021; Palmerini et al., 2021). However, our estimate for the *s*-contribution to ^{135}Ba still depends remarkably on other issues. This includes, primarily, the cross sections of the same Ba isotopes and of ^{133}Cs, then also the details on how the ^{134}Cs($\beta^+\nu$)^{134}Ba and ^{135}Cs($\beta^+\nu$)^{135}Ba operate in stars, which require the precise knowledge of the temperature evolution in the layers where ^{135}Ba is produced, i.e., the convective *thermal instabilities* of the He-shell in AGB stars (Busso et al., 1999). Ultimately, this is linked to how we model convection; hence, here we cannot absolutely mention that the remaining uncertainties are purely nuclear in origin. As shown in

Figure 13a of Palmerini et al. (2021), even the most precise constraints available currently (i.e., those from the isotopic Ba admixture in mainstream presolar SiC grains) still offer ample space for a possible lower *s*-process contribution to this nucleus, which would fit better with the *r*-process predictions (see Table 1, column 6, and Figure 5. See also the following discussion).

Let us then see whether the origin of the discrepancy in Table 1 and in Figure 5 for ^{135}Ba can come from uncertainties in the *r*-process approach. The potential progenitor isotopes at Z = 49 (In) and up to Z = 51 (Sb) are situated in a shape transition region, in this case between the spherical N = 82 shell closure and the well-known strongly deformed *R.E.E.* region beyond $N \simeq 90$.

According to our two model combinations, the three dominating precursor isotopes that may contribute to the abundance of ^{135}Ba are ^{135}In (Z = 49, N = 86), ^{136}Sn (Z = 50, N = 86), and ^{138}Sn (Z = 50, N = 88). Since these isotopes are predicted to have still spherical ground-state shapes ($\epsilon_2 \lesssim 0.1$), they should have quite similar nuclear mass and β-decay rate values. However, since the *r*-progenitor nuclei lie already quite far from β-stability, their β-delayed neutron-branchings of one to three neutrons play an important role. This is, indeed, confirmed by the available experimental data (Audi et al., 2012), which indicate a clear preference for the *FRDM12/QRPA* model predictions as compared to the older *ETFSI-Q/QRPA* approach.

In any case, both model combinations agree on the fact that, in the rather complex β-delayed neutron-branchings during the decay back to stability of both progenitor nuclei ^{135}In and ^{138}Sn, only negligible fractions of the initial abundances reach ^{135}Ba. Hence, only the β-delayed neutron decay of the progenitor ^{136}Sn finally populates ^{135}Ba, with about 40% of its initial abundance. Due to the complex β-delayed neutron decay pattern far from stability, the resulting effect of only a slight reduction in the final S.S. *r*-fraction of ^{135}Ba (maybe by $\simeq$ 10%) can be inferred.

An indication of what should be obtained here for ^{135}Ba can be obtained from observations of *r*-II metal-poor stars, through the Ba – f_{odd} parameter. In the isotopic composition of Ba of a certain environment, Ba – f_{odd} expresses the abundance ratio of odd isotopes to the total abundance of the element. Under *r*-process conditions, this last can be approximated by excluding the even isotopes, except for the dominant ^{138}Ba so that

$$Ba - f_{odd} \simeq \frac{^{135}Ba + ^{137}Ba}{^{135}Ba + ^{137}Ba + ^{138}Ba}. \quad (2)$$

Ba – f_{odd} can be measured by high-resolution spectroscopy in a number of metal-poor halo stars (see Mashonkina and Christlieb, 2014; Mashonkina and Belyaev, 2019, and Mashonkina et al., 2017, private communication) by a careful analysis of the hyperfine splitting. From these observations, a mean value of Ba – f_{odd} = 0.4 ± 0.10 was obtained.

This result can now be compared to that of our model predictions. From the data of *ETFSI-Q/QRPA* (Kratz et al., 2007), a mean value of 0.49 ± 0.03 could be derived, while from the more recent *FRDM12/QRPA* version (Kratz et al., 2014), a somewhat lower mean value of 0.43 ± 0.03 was obtained. From Table 1, we would now get $\simeq$ 0.45. These results are all in good agreement with the *Ba* – f_{odd} measurements in halo stars. On the contrary, from our AGB *s*-process estimates shown in Table 1, the resulting value is Ba – $f_{odd} \lesssim 0.3$, dominated by the estimate for ^{135}Ba.

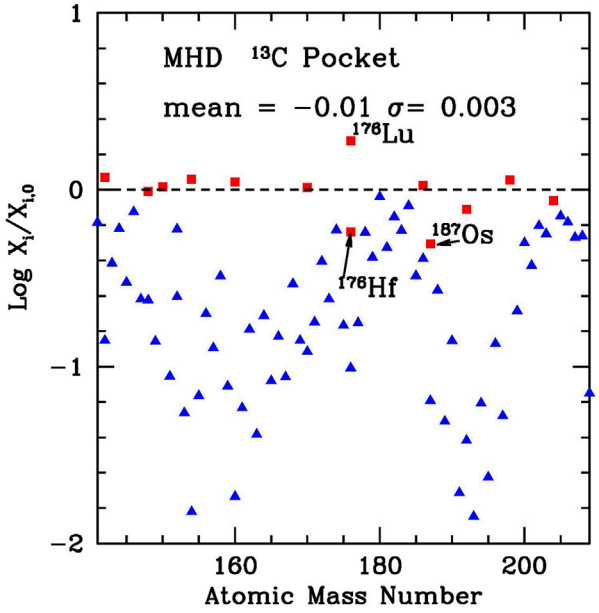

FIGURE 7
Distribution of *s*-process fractional abundances in the mass range 142 $\lesssim A \lesssim$ 208, as obtained with the procedure described in Busso et al. (2021) and Palmerini et al. (2021). Red symbols refer to the so-called *s – only* nuclei, which are shielded by stable isotopes against contributions from the *r*-process.

These facts suggest that in this case, it is the *s*-process computation that might be improved by new nuclear data on cross sections and decay rates. For the weak interactions, in particular, experimental measurements in ionized plasmas on the rates for the β^- decays of ^{134,135}Cs would be highly needed.

4.4 Nuclei heavier than A = 142

Our estimates for S.S. abundances of heavy nuclei ($A \geq 142$) as descending from the AGB models adopted in the present study are shown in Figure 7. As is clear from the plot, over a general trend characterized by a good reproduction of the solar abundances for *s*-only nuclei (red dots), with a small dispersion, three very remarkable outliers appear, at ^{176}Lu, ^{176}Hf, and ^{187}Os, which are among the reasons why we did not attempt a complete comparison in this mass range.

The outliers of Figure 7 are related to nuclear problems known since a long time and for which only new measurements of decay rates under partial ionization conditions would help. For the isotopes ^{176}Lu and ^{176}Hf, a thorough analysis was performed by Wisshak et al. (2006a); Wisshak et al. (2006b), to which we address interested readers. Here, isomeric states at ^{175}Yb, ^{176}Lu, and ^{177}Hf are involved in the reaction chain. While for ^{175}Yb and ^{177}Hf, the isomers are depopulated, and the nuclei are in their ground states under *s*-process conditions, this is not so for ^{176}Lu. Its ground state is essentially stable ($T_{1/2} \simeq 3.8 \times 10^{10}$ yr) and was considered for a long time as a clock for cosmo-chronology (Audouze et al., 1972). Instead, it is now known that the isomer is partially thermalized at the temperature ($T \simeq 23$–$25\ keV$) of AGB thermal pulses. This induces a sharp reduction of the half-life due to the high-energy thermal photons. As a consequence, ^{176}Lu becomes, in principle, a sensitive thermometer of the environment. For this to occur, however, all the pertinent cross sections and decay rates should be well-known. On the contrary, for the parent ^{175}Yb, only theoretical estimates exist, for both parameters, and measurements for ^{176}Lu itself were carried out in Karlsruhe (Wisshak et al., 2006a) and are waiting for more modern confirmations. Also, the ^{176}Hf destruction, through neutron captures either to ^{177}Hf^{g} or to ^{177}Hf^{m} should in this context be verified. High accuracy is required to settle this problem, as the decay of ^{176}Lu was traditionally assumed to control the ^{176}Hf abundance (Prantzos, 2019), which is, in general, difficult to achieve, as the solar abundance of Hf is larger than that of Lu.

Another crucial issue concerns ^{187}Os. Its parent ^{187}Re is a very long-lived nucleus at low temperatures ($T_{1/2} \simeq 43.5$ Gyr). However, it is known that under stellar conditions, this isotope, like, e.g., ^{207}Tl and ^{163}Dy (which is stable at laboratory temperatures), can undergo *bound* state decays, i.e., decays where the electron is not emitted as a free particle but is captured by the daughter nucleus (^{187}Os in this case) to form a hydrogenoid bound state. This significantly increases the decay rate, (by nine orders of magnitudes for completely stripped ^{187}Re), as verified, e.g., by works at the ESR storage ring in Darmstadt (Bosch, 2006; Litvinov and Bosch, 2011). Plasma traps like the future *PANDORA* experiment (Mascali et al., 2020) will soon offer a place where to mimic the partial ionization conditions prevailing in AGB stars, providing new information on several uncertain β-decay rates mentioned in this article for the *s*-process.

5 Preliminary conclusions and expected improvements

In this study, we present predictions for the contributions to solar abundances of trans-Fe nuclei synthesized by neutron captures. Both the *r*-process estimates and the complementary *s*-process ones are shown, in the aim of clarifying the problems that are still affecting their respective nuclear inputs. We limited our analysis to the atomic mass range between Sr and Pr because for heavier nuclei, both models are affected by rather large uncertainties, making such a comparison difficult. In the two independent views, we adopted approaches that are already satisfying basic, universally recognized constraints so that we can trust that the remaining inconsistencies do not come from astrophysical model details but can be traced back to limits in the available nuclear ingredients.

The results are shown in terms of independent predictions for the *s*-process fraction of solar abundances and demonstrate an unprecedented agreement, where in the majority of cases, the ratios of the two estimates are $\lesssim 1.20$ (a 20% scatter), not far from the uncertainty of the experimental σN curve. For four nuclei (^{108}Mo, ^{106}Pd, ^{118}Sn, and ^{135}Ba), there is a clear disagreement that requires a critical analysis. From the ensuing discussion, it has been suggested that decay rates crucial for the *s*-process (in particular at ^{113,115}Cd, ^{115}In, and ^{134,135}Cs) be verified experimentally, especially in ionized plasma environments. Although, as mentioned, we did not perform a detailed comparison for the *R.E.E.*, from a simple inspection of the existing problems in reproducing *s*-only nuclei, the same conclusion emerges for some heavy nuclei that are very long-lived in the laboratory but display a different behavior in the high-temperature and high-ionization conditions of a stellar plasma (these are e.g., the cases of ^{176}Lu and ^{187}Re).

From the *r*-process point of view, of course, the situation is much more difficult. In the ideal case, one would request experimental data for *r*-process progenitor isotopes related to nuclear masses (in particular neutron-separation energies, S_n and β-decay properties, $T_{1/2}$, and P_{xn}). Ionic traps like *Pandora* will have, however, no access to this data region because of significantly short terrestrial half-lives (for the most important neutron magic isotopes, except ^{80}Zn, $T_{1/2} \lesssim 200$ ms).

For the *R.E.E.* nuclei and the Pt-peak, actually, progenitor isotopes lie very far from stability and are in most cases out of any experimental reach, even for facilities like *RIKEN* or *CERN/ISOLDE*. We should then focus on the nuclear structure development within isobaric chains, from stability toward the progenitor nuclei, in order to derive more reliable, local, and short-range extrapolations.

For lighter nuclei, whenever possible, detailed $1n$- to $3n$-branchings should be measured, for isotopes involved in the β-decay back to stability. Of particular interest, in this case, are nuclides at magic and semi-magic neutron shells (which act as bottlenecks for the *r*-process matter flow), as well as isotope sequences in the different shape-transition regions, where practically all global models have large uncertainties.

Data availability statement

The original contributions presented in the study are included in the article/Supplementary Material; further inquiries can be directed to the corresponding author.

Author contributions

MB: conceptualization, computations, and text writing. K-LK: conceptualization, computations, and text writing. VA-D: conceptualization and computations. SP: conceptualization and computations. WA: conceptualization and computations.

Funding

This research was supported by the Italian National Institute for Nuclear Physics (INFN), through the PANDORA and n_TOF projects, inside the National Scientific Commission 3.

Acknowledgments

We are grateful to two unknown referees (expert in nuclear physics and in stellar models), for greatly helping us in improving the clarity and completeness of the manuscript. MB is indebted to the colleagues who helped in building our knowledge of AGB star nucleosynthesis, R. Gallino above the others, for decades of friendship and collaboration. K-LK wants to thank B. Pfeiffer, G. Lhersonneau, P. Möller, and W.B. Walters for many years of pleasant collaboration in experimental and theoretical nuclear physics. We are also indebted to S. Taioli, S. Simonucci, D. Vescovi, and S. Cristallo for useful suggestions.

Conflict of interest

The authors declare that the research was conducted in the absence of any commercial or financial relationships that could be construed as a potential conflict of interest.

Publisher's note

References

Abbott, B. P., Abbott, R., Abbott, T. D., Acernese, F., Ackley, K., Adams, C., et al. (2017). GW170817: Observation of gravitational waves from a binary neutron star inspiral. *Phys. Rev. Lett.* 119, 161101. doi:10.1103/PhysRevLett.119.161101

Antonuccio-Delogu, V., Busso, M., and Palmerini, S. (2022). Beyond Iron: Numerical models of s- and r-process element distributions. *Universe* (in press).

Audi, G., Kondev, F. G., Wang, M., Pfeiffer, B., Sun, X., Blachot, J., et al. (2012). The Nubase2012 evaluation of nuclear properties. *Chin. Phys. C* 36, 1157–1286. doi:10.1088/1674-1137/36/12/001

Audouze, J., Fowler, W. A., and Schramm, D. N. (1972). ^{176}Lu and s-Process Nucleosynthesis. *Nat. Phys. Sci.* 238, 8–11. doi:10.1038/physci238008a0

Battino, U., Pignatari, M., Ritter, C., Herwig, F., Denisenkov, P., Den Hartogh, J. W., et al. (2016). Application of a theory and simulation-based convective boundary mixing model for AGB star evolution and nucleosynthesis. *Astrophys. J.* 827, 30. doi:10.3847/0004-637X/827/1/30

Battino, U., Tattersall, A., Lederer-Woods, C., Herwig, F., Denissenkov, P., Hirschi, R., et al. (2019). NuGrid stellar data set - III. Updated low-mass AGB models and s-process nucleosynthesis with metallicities Z= 0.01, Z = 0.02, and Z = 0.03. *Mon. Not. R. Astron. Soc.* 489, 1082–1098. doi:10.1093/mnras/stz2158

Bisterzo, S., Gallino, R., Käppeler, F., Wiescher, M., Imbriani, G., Straniero, O., et al. (2015). The branchings of the main s-process: Their sensitivity to α-induced reactions on ^{13}C and ^{22}Ne and to the uncertainties of the nuclear network. *Mon. Not. R. Astron. Soc.* 449, 506–527. doi:10.1093/mnras/stv271

Bisterzo, S., Gallino, R., Straniero, O., Cristallo, S., and Käppeler, F. (2012). The s-process in low-metallicity stars - III. Individual analysis of CEMP-s and CEMP-s/r with asymptotic giant branch models. *Mon. Not. R. Astron. Soc.* 422, 849–884. doi:10.1111/j.1365-2966.2012.20670.x

Bisterzo, S., Travaglio, C., Gallino, R., Wiescher, M., and Käppeler, F. (2014). Galactic chemical evolution and solar *s*-process abundances: Dependence on the^{13}c-pocket structure. *Astrophys. J.* 787, 10. doi:10.1088/0004-637X/787/1/10

Bosch, F. (2006). Beta decay of highly charged ions. *Hyperfine Interact.* 173, 1–11. doi:10.1007/s10751-007-9535-2

Burbidge, E. M., Burbidge, G. R., Fowler, W. A., and Hoyle, F. (1957). Synthesis of the elements in stars. *Rev. Mod. Phys.* 29, 547–650. doi:10.1103/RevModPhys.29.547

Busso, M., Picchio, G., Gallino, R., and Chieffi, A. (1988). Are s-elements really produced during thermal pulses in intermediate-mass stars?. *Astrophys. J.*, 196. doi:10.1086/166081

Busso, M., Gallino, R., and Wasserburg, G. J. (1999). Nucleosynthesis in asymptotic giant branch stars: Relevance for galactic enrichment and solar system formation. *Annu. Rev. Astron. Astrophys.* 37, 239–309. doi:10.1146/annurev.astro.37.1.239

Busso, M., Vescovi, D., Palmerini, S., Cristallo, S., and Antonuccio-Delogu, V. (2021). s-Processing in AGB stars revisited. III. Neutron captures from MHD mixing at different metallicities and observational constraints. *Astrophys. J.* 908, 55. doi:10.3847/1538-4357/abca8e

Busso, M., Wasserburg, G. J., Nollett, K. M., and Calandra, A. (2007). Can extra mixing in RGB and AGB stars Be attributed to magnetic mechanisms? *Astrophys. J.* 671, 802–810. doi:10.1086/522616

Cameron, A. G. W. (1957). Nuclear reactions in stars and nucleogenesis. *Publ. Astron. Soc. Pac.* 69, 201. doi:10.1086/127051

Coryell, C. D. (1956). *MITL.N.S. Prog. Rep. AECU-3423.*

Coryell, C. D. (1961). The chemistry of creation of the heavy elements. *J. Chem. Educ.* 38, 67. doi:10.1021/ed038p67

Cowan, J. J., Thielemann, F.-K., and Truran, J. W. (1991). The R-process and nucleochronology. *Phys. Rep.* 208, 267–394. doi:10.1016/0370-1573(91)90070-3

Cristallo, S., Piersanti, L., Straniero, O., Gallino, R., Domínguez, I., Abia, C., et al. (2011). Evolution, nucleosynthesis, and yields of low-mass asymptotic giant branch stars at different metallicities. II. The FRUITY database. *Astrophys. J. Suppl. Ser.* 197, 17. doi:10.1088/0067-0049/197/2/17

Cristallo, S., Straniero, O., Piersanti, L., and Gobrecht, D. (2015). Evolution, nucleosynthesis, and yields of AGB stars at different metallicities. III. Intermediate-Mass models, revised low-mass models, and the ph-FRUITY interface. *Astrophys. J. Suppl. Ser.* 219, 40. doi:10.1088/0067-0049/219/2/40

Denissenkov, P. A., Pinsonneault, M., and MacGregor, K. B. (2009). Magneto-thermohaline mixing in red giants. *Astrophys. J.* 696, 1823–1833. doi:10.1088/0004-637X/696/2/1823

Denissenkov, P. A., and Tout, C. A. (2003). Partial mixing and formation of the ^{13}C pocket by internal gravity waves in asymptotic giant branch stars. *Mon. Not. R. Astron. Soc.* 340, 722–732. doi:10.1046/j.1365-8711.2003.06284.x

Dillmann, I., Heil, M., Käppeler, F., Plag, R., Rauscher, T., and Thielemann, F. K. (2006). "KADoNiS- the Karlsruhe astrophysical database of nucleosynthesis in stars," in *Capture gamma-ray spectroscopy and related topics. Vol. 819 of American Institute of physics conference series*. Editors A. Woehr and A. Aprahamian, 123–127. doi:10.1063/1.2187846

Dillmann, I. (2014). "The new KADoNiS v1.0 and its influence on the s-process," in *XIII nuclei in the cosmos (NIC XIII)*, 57.

Evans, P. A., Cenko, S. B., Kennea, J. A., Emery, S. W. K., Kuin, N. P. M., Korobkin, O., et al. (2017). Swift and NuSTAR observations of GW170817: Detection of a blue kilonova. *Science* 358, 1565–1570. doi:10.1126/science.aap9580

Farouqi, K., Kratz, K. L., and Pfeiffer, B. (2009). Co-production of light p-s- and r-process isotopes in the high-entropy wind of type II supernovae. *Publ. Astron. Soc. Aust.* 26, 194–202. doi:10.1071/AS08075

Farouqi, K., Kratz, K. L., Pfeiffer, B., Rauscher, T., Thielemann, F. K., and Truran, J. W. (2010). Charged-particle and neutron-capture processes in the high-entropy wind of core-collapse supernovae. *Astrophys. J.* 712, 1359–1377. doi:10.1088/0004-637X/712/2/1359

Farouqi, K., Thielemann, F.-K., Rosswog, S., and Kratz, K.-L. (2022). Correlations of *r*-process elements in very metal-poor stars as clues to their nucleosynthesis sites. *Astron. Astrophys.* 663, A70. in press. doi:10.1051/0004-6361/202141038

Freiburghaus, C., Rembges, J. F., Rauscher, T., Kolbe, E., Thielemann, F. K., Kratz, K. L., et al. (1999a). The astrophysical r-process: A comparison of calculations following adiabatic expansion with classical calculations based on neutron densities and temperatures. *Astrophys. J.* 516, 381–398. doi:10.1086/307072

Freiburghaus, C., Rosswog, S., and Thielemann, F. K. (1999b). [CLC] [ITAL]r [/ITAL] [/CLC]-Process in neutron star mergers. *Astrophys. J.* 525, L121–L124. doi:10.1086/312343

Gallino, R., Busso, M., Picchio, G., Raiteri, C. M., and Renzini, A. (1988). On the role of low-mass asymptotic giant branch stars in producing a solar system distribution of s-process isotopes. *Astrophys. J.* 334, L45. doi:10.1086/185309

Guerrero, C., Boccone, V., Brugger, M., Calviani, M., Cerutti, F., Chiaveri, E., et al. (2013). "The latest on neutron-induced capture and fission measurements at the CERN n_TOF facility," in *Capture gamma-ray spectroscopy and related topics*. Editor P. E. Garrett, 354–364. doi:10.1142/9789814383646_0047

Herwig, F. (2005). Evolution of asymptotic giant branch stars. *Annu. Rev. Astron. Astrophys.* 43, 435–479. doi:10.1146/annurev.astro.43.072103.150600

Hill, V., Plez, B., Cayrel, R., Beers, T. C., Nordström, B., Andersen, J., et al. (2002). First stars. I. The extreme r-element rich, iron-poor halo giant CS 31082-001. Implications for the r-process site(s) and radioactive cosmochronology. *Astron. Astrophys.* 387, 560–579. doi:10.1051/0004-6361:20020434

Hillebrandt, W. (1978). The rapid neutron-capture process and the synthesis of heavy and neutron-rich elements. *Space Sci. Rev.* 21, 639–702. doi:10.1007/BF00186236

Honda, S., Aoki, W., Ishimaru, Y., and Wanajo, S. (2007). Neutron-capture elements in the very metal-poor star HD 88609: Another star with excesses of light neutron-capture elements. *Astrophys. J.* 666, 1189–1197. doi:10.1086/520034

Iben, J. I., and Renzini, A. (1982). On the formation of carbon star characteristics and the production of neutron-rich isotopes in asymptotic giant branch stars of small core mass. *Astrophys. J.* 263, L23–L27. doi:10.1086/183916

Iben, J. I., and Truran, J. W. (1978). On the surface composition of thermally pulsing stars of high luminosity and on the contribution of such stars to the element enrichment of the interstellar medium. *Astrophys. J.* 220, 980–995. doi:10.1086/155986

Ji, A. P., Drout, M. R., and Hansen, T. T. (2019). The lanthanide fraction distribution in metal-poor stars: A test of neutron star mergers as the dominant r-process site. *Astrophys. J.* 882, 40. doi:10.3847/1538-4357/ab3291

Kaeppeler, F., Gallino, R., Busso, M., Picchio, G., and Raiteri, C. M. (1990). S-process nucleosynthesis: Classical approach and asymptotic giant branch models for low-mass stars. *Astrophys. J.* 354, 630. doi:10.1086/168720

Käppeler, F., Gallino, R., Bisterzo, S., and Aoki, W. (2011). Thesprocess: Nuclear physics, stellar models, and observations. *Rev. Mod. Phys.* 83, 157–193. doi:10.1103/RevModPhys.83.157

Karakas, A. I., and Lattanzio, J. C. (2014). The dawes review 2: Nucleosynthesis and stellar yields of low- and intermediate-mass single stars. *Publ. Astron. Soc. Aust.* 31, e030. doi:10.1017/pasa.2014.21

Kratz, K.-L., Akram, W., Farouqi, K., and Hallmann, O. (2019). "Production of light trans-Fe elements in core collapse-supernovae: Implications from presolar SiC-X grains," in *Exotic nuclei and nuclear/particle AstroPhysics (VII). Physics with small accelerators. Vol. 2076 of American Institute of physics conference series*, 030002. doi:10.1063/1.5091628

Kratz, K.-L., Bitouzet, J.-P., Thielemann, F.-K., Moeller, P., and Pfeiffer, B. (1993). Isotopic r-process abundances and nuclear structure far from stability: Implications for the r-process mechanism. *Astrophys. J.* 403, 216. doi:10.1086/172196

Kratz, K.-L., Farouqi, K., and Möller, P. (2014). A high-entropy-wind r-process study based on nuclear-structure quantities from the new finite-range droplet model frdm(2012). *Astrophys. J.* 792, 6. doi:10.1088/0004-637X/792/1/6

Kratz, K.-L., Farouqi, K., Pfeiffer, B., Truran, J. W., Sneden, C., and Cowan, J. J. (2007). Explorations of the r-processes: Comparisons between calculations and observations of low-metallicity stars. *Astrophys. J.* 662, 39–52. doi:10.1086/517495

Kratz, K.-L., Pfeiffer, B., Thielemann, F.-K., and Walters, W. B. (2000). Nuclear structure studies at ISOLDE and their impact on the astrophysical r-process. *Hyperfine Interact.* 129, 185–221. doi:10.1023/A:1012694723985

Kratz, K. L., Böhmer, W., Freiburghaus, C., Möller, P., Pfeiffer, B., Rauscher, T., et al. (2001). On the origin of the Ca-Ti-Cr isotopic anomalies in the inclusion EK-1-4-1 of the Allende-meteorite. *Mem. Soc. Astron. It.* 72, 453–466.

Kratz, K. L., Farouqi, K., Mashonkina, L. I., and Pfeiffer, B. (2008). Nucleosynthesis modes in the high-entropy-wind of type II supernovae. *New Astron. Rev.* 52, 390–395. doi:10.1016/j.newar.2008.06.015

Kratz, K. L., Gabelmann, H., Möller, P., Pfeiffer, B., Ravn, H. L., and Wöhr, A. (1991). Neutron-rich isotopes around the r-process "waiting-point" nuclei {$\mmultiscripts{\mathrm{/}}{\postscript{}{79}}{\prescript{29}{}}{}}$}$Cu_{50}$ and {$\mmultiscripts{\mathrm{/}}{\postscript{}{80}}{\prescript{30}{}}{}}$}$Zn_{50}$. *Zeitschrift fur Physik A Hadrons Nucl.* 340, 419–420. doi:10.1007/BF01290331

Kratz, K. L. (1988). Nuclear physics constraints to bring the astrophysical R-process to the "waiting point". *Rev. Mod. Astronomy* 1, 184–209. doi:10.1007/978-3-642-74188-3_9

Kratz, K. L., Ziegert, W., Hillebrandt, W., and Thielemann, F. K. (1983a). Determination of stellar neutron-capture rates for radioactive nuclei with the aid of beta-delayed neutron emission. *Astron. & Astrophys.* 125, 381–387.

Kratz, K. L., Ziegert, W., Thielemann, F. K., and Hillebrandt, W. (1983b). Beta-delayed neutron emission as the inverse process to neutron-capture on radioactive isotopes. *Max Planck Inst. fur Astrophys. Rep.* 90, 111–112.

Lattimer, J. M., Mackie, F., Ravenhall, D. G., and Schramm, D. N. (1977). The decompression of cold neutron star matter. *Astrophys. J.* 213, 225–233. doi:10.1086/155148

Lhersonneau, G., Pfeiffer, B., Kratz, K. L., Enqvist, T., Jauho, P. P., Jokinen, A., et al. (1994). Evolution of deformation in the neutron-rich Zr region from excited intruder state to the ground state. *Phys. Rev. C* 49, 1379–1390. doi:10.1103/PhysRevC.49.1379

Li, K.-A., Qi, C., Lugaro, M., Yagüe López, A., Karakas, A. I., den Hartogh, J., et al. (2021). The stellar β-decay rate of ^{134}Cs and its impact on the barium nucleosynthesis in the s-process. *Astrophys. J. Lett.* 919, L19. doi:10.3847/2041-8213/ac260f

Litvinov, Y. A., and Bosch, F. (2011). Beta decay of highly charged ions. *Rep. Prog. Phys.* 74, 016301. doi:10.1088/0034-4885/74/1/016301

Liu, N., Savina, M. R., Davis, A. M., Gallino, R., Straniero, O., Gyngard, F., et al. (2014). Barium isotopic composition of mainstream silicon carbides from murchison: Constraints for s-process nucleosynthesis in asymptotic giant branch stars. *Astrophys. J.* 786, 66. doi:10.1088/0004-637X/786/1/66

Liu, N., Savina, M. R., Gallino, R., Davis, A. M., Bisterzo, S., Gyngard, F., et al. (2015). Correlated strontium and barium isotopic compositions of acid-cleaned single mainstream silicon carbides from murchison. *Astrophys. J.* 803, 12. doi:10.1088/0004-637X/803/1/12

Lodders, K. (2021). Relative atomic solar system Abundances, mass fractions, and atomic masses of the elements and their isotopes, composition of the solar photosphere, and compositions of the major chondritic meteorite groups. *Space Sci. Rev.* 217, 44. doi:10.1007/s11214-021-00825-8

Lugaro, M., Karakas, A. I., Stancliffe, R. J., and Rijs, C. (2012). The s-process in asymptotic giant branch stars of low metallicity and the composition of carbon-enhanced metal-poor stars. *Astrophys. J.* 747, 2. doi:10.1088/0004-637X/747/1/2

Maiorca, E., Magrini, L., Busso, M., Randich, S., Palmerini, S., and Trippella, O. (2012). News on the s process from young open clusters. *Astrophys. J.* 747, 53. doi:10.1088/0004-637X/747/1/53

Mascali, D., Busso, M., Mengoni, A., Amaducci, S., Giuseppe, C., Celona, L., et al. (2020). "The PANDORA project: An experimental setup for measuring in-plasma β-decays of astrophysical interest," in *European physical journal web of conferences. Vol. 227 of European physical journal web of conferences*, 01013. doi:10.1051/epjconf/202022701013

Mashonkina, L., and Christlieb, N. (2014). The Hamburg/ESO R-process Enhanced Star survey (HERES). IX. Constraining pure r-process Ba/Eu abundance ratio from observations of r-II stars. *Astron. Astrophys.* 565, A123. doi:10.1051/0004-6361/201423651

Mashonkina, L. I., and Belyaev, A. K. (2019). Even-to-Odd barium isotope ratio in selected galactic halo stars. *Astron. Lett.* 45, 341–352. doi:10.1134/S1063773719060033

Mashonkina, L. I., Vinogradova, A. B., Ptitsyn, D. A., Khokhlova, V. S., and Chernetsova, T. A. (2007). Neutron-capture elements in halo, thick-disk, and thin-disk stars. Strontium, yttrium, zirconium, cerium. *Astron. Rep.* 51, 903–919. doi:10.1134/S1063772907110042

Merrill, P. W. (1952). Spectroscopic observations of stars of class. *Astrophys. J.* 116, 21. doi:10.1086/145589

Möller, P., Pfeiffer, B., and Kratz, K.-L. (2003). New calculations of gross β-decay properties for astrophysical applications: Speeding-up the classical r process. *Phys. Rev. C* 67, 055802. doi:10.1103/PhysRevC.67.055802

Montes, F., Beers, T. C., Cowan, J., Elliot, T., Farouqi, K., Gallino, R., et al. (2007). Nucleosynthesis in the early Galaxy. *Astrophys. J.* 671, 1685–1695. doi:10.1086/523084

Niederer, F. R., Papanastassiou, D. A., and Wasserburg, G. J. (1980). Endemic isotopic anomalies in titanium. *Astrophys. J.* 240, L73–L77. doi:10.1086/183326

Nishimura, N., Sawai, H., Takiwaki, T., Yamada, S., and Thielemann, F. K. (2017). The intermediate r-process in core-collapse supernovae driven by the magneto-rotational instability. *Astrophys. J.* 836, L21. doi:10.3847/2041-8213/aa5dee

Nordhaus, J., Busso, M., Wasserburg, G. J., Blackman, E. G., and Palmerini, S. (2008). Magnetic mixing in red giant and asymptotic giant branch stars. *Astrophys. J.* 684, L29–L32. doi:10.1086/591963

Nucci, M. C., and Busso, M. (2014). Magnetohydrodynamics and deep mixing in evolved stars. I. Two- and three-dimensional analytical models for the asymptotic giant branch. *Astrophys. J.* 787, 141. doi:10.1088/0004-637X/787/2/141

Palmerini, S., Busso, M., Vescovi, D., Naselli, E., Pidatella, A., Mucciola, R., et al. (2021). Presolar grain isotopic ratios as constraints to nuclear and stellar parameters of asymptotic giant branch star nucleosynthesis. *Astrophys. J.* 921, 7. doi:10.3847/1538-4357/ac1786

Pearson, C., Krueger, M., and Ganz, E. (1996). Direct tests of microscopic growth models using hot scanning tunneling microscopy movies. *Phys. Rev. Lett.* 76, 2306–2309. doi:10.1103/PhysRevLett.76.2306

Pellin, M. J., Savina, M. R., Calaway, W. F., Tripa, C. E., Barzyk, J. G., Davis, A. M., et al. (2006). "Heavy metal isotopic anomalies in supernovae presolar grains," in *37th annual lunar and planetary science conference. Lunar and planetary science conference*. Editors S. Mackwell and E. Stansbery, 2041.

Pfeiffer, B., Kratz, K. L., and Thielemann, F. K. (1997). Analysis of the solar-system r-process abundance pattern with the new ETFSI-Q mass formula. *Z. Phys. A -. Part. Fields.* 357, 235–238. doi:10.1007/s002180050237

Pfeiffer, B., Lhersonneau, G., Gabelmann, H., and Kratz, K. L.the ISOLDE-Collaboration (2002). *A tentative 4- isomeric state in Sr-98. arXiv e-prints* , nucl-ex/0202025.

Prantzos, N. (2019). Galactic chemical evolution with rotating massive star yields. *Nucl. Cosmos XV* 219, 83–89. doi:10.1007/978-3-030-13876-9_1

Reifarth, R., Erbacher, P., Fiebiger, S., Göbel, K., Heftrich, T., Heil, M., et al. (2018). Neutron-induced cross sections. From raw data to astrophysical rates. *Eur. Phys. J. Plus* 133, 424. doi:10.1140/epjp/i2018-12295-3

Rosswog, S., Liebendörfer, M., Thielemann, F. K., Davies, M. B., Benz, W., and Piran, T. (1999). Mass ejection in neutron star mergers. *Astron. & Astrophys.* 341, 499–526.

Rosswog, S., Sollerman, J., Feindt, U., Goobar, A., Korobkin, O., Wollaeger, R., et al. (2018). The first direct double neutron star merger detection: Implications for cosmic nucleosynthesis. *Astron. Astrophys.* 615, A132. doi:10.1051/0004-6361/201732117

Salpeter, E. E. (1955). The luminosity function and stellar evolution. *Astrophys. J.* 121, 161. doi:10.1086/145971

Seeger, P. A., Fowler, W. A., and Clayton, D. D. (1965). Nucleosynthesis of heavy elements by neutron capture. *Astrophys. J. Suppl. Ser.* 11, 121. doi:10.1086/190111

Shibata, K., Iwamoto, O., Nakagawa, T., Iwamoto, N., Ichihara, A., Kunieda, S., et al. (2011). JENDL-4.0: A new library for innovative nuclear energy systems. *J. Korean Phys. Soc.* 59, 1046–1051. doi:10.3938/jkps.59.1046

Sneden, C., Cowan, J. J., Lawler, J. E., Ivans, I. I., Burles, S., Beers, T. C., et al. (2003). The extremely metal-poor, neutron capture-rich star CS 22892-052: A comprehensive abundance analysis. *Astrophys. J.* 591, 936–953. doi:10.1086/375491

Sneden, C., McWilliam, A., Preston, G. W., Cowan, J. J., Burris, D. L., and Armosky, B. J. (1996). The ultra–metal-poor, neutron-capture–rich giant star CS 22892-052. *Astrophys. J.* 467, 819. doi:10.1086/177656

Stephan, T., and Davis, A. M. (2021). Molybdenum isotope dichotomy in meteorites caused by s-process variability. *Astrophys. J.* 909, 8. doi:10.3847/1538-4357/abd725

Stephan, T., Trappitsch, R., Davis, A. M., Pellin, M. J., Rost, D., Savina, M. R., et al. (2018). Strontium and barium isotopes in presolar silicon carbide grains measured with CHILI-two types of X grains. *Geochim. Cosmochim. Acta* 221, 109–126. doi:10.1016/j.gca.2017.05.001

Stephan, T., Trappitsch, R., Hoppe, P., Davis, A. M., Pellin, M. J., and Pardo, O. S. (2019). Molybdenum isotopes in presolar silicon carbide grains: Details of s-process nucleosynthesis in parent stars and implications for r- and p-processes. *Astrophys. J.* 877, 101. doi:10.3847/1538-4357/ab1c60

Suess, H. E., and Urey, H. C. (1956). Abundances of the elements. *Rev. Mod. Phys.* 28, 53–74. doi:10.1103/RevModPhys.28.53

Taioli, S., Vescovi, D., Busso, M., Palmerini, S., Cristallo, S., Mengoni, A., et al. (2021). Theoretical estimate of the half-life for the radioactive ^{134}Cs and ^{135}Cs in astrophysical scenarios. *arXiv e-prints, Ap.J* 2022. *in press*, arXiv:2109.14230.

Takahashi, K., Witti, J., and Janka, H. T. (1994). Nucleosynthesis in neutrino-driven winds from protoneutron stars II. The r-process. *Astron. & Astrophys.* 286, 857–869.

Takahashi, K., and Yokoi, K. (1987). Beta-decay rates of highly ionized heavy atoms in stellar interiors. *Atomic Data Nucl. Data Tables* 36, 375–409. doi:10.1016/0092-640X(87)90010-6

Theis, C., Käppeler, F., Wisshak, K., and Voss, F. (1998). On the puzzling origin of the rare in and SN isotopes. *Astrophys. J.* 500, 1039–1048. doi:10.1086/305777

Travaglio, C., Gallino, R., Arnone, E., Cowan, J., Jordan, F., and Sneden, C. (2004). Galactic evolution of Sr, Y, and Zr: A multiplicity of nucleosynthetic processes. *Astrophys. J.* 601, 864–884. doi:10.1086/380507

Trippella, O., Busso, M., Palmerini, S., Maiorca, E., and Nucci, M. C. (2016). s-Processing in AGB stars revisited. II. Enhanced 13C production through MHD-induced mixing. *Astrophys. J.* 818, 125. doi:10.3847/0004-637X/818/2/125

Vescovi, D., Cristallo, S., Busso, M., and Liu, N. (2020). Magnetic-buoyancy-induced mixing in AGB stars: Presolar SiC grains. *Astrophys. J.* 897, L25. doi:10.3847/2041-8213/ab9fa1

Vescovi, D., Cristallo, S., Palmerini, S., Abia, C., and Busso, M. (2021). Magnetic-buoyancy-induced mixing in AGB stars: Fluorine nucleosynthesis at different metallicities. *Astron. Astrophys.* 652, A100. doi:10.1051/0004-6361/202141173

Vescovi, D. (2021). Mixing and magnetic fields in asymptotic giant branch stars in the framework of FRUITY models. *Universe* 8, 16. doi:10.3390/universe8010016

Vescovi, D., and Reifarth, R. (2021). s-Processing in asymptotic giant branch stars in the light of revised neutron-capture cross sections. *Universe* 7, 239. doi:10.3390/universe7070239

Wasserburg, G. J., Lee, T., and Papanastassiou, D. A. (1977). Correlated O And Mg isotopic anomalies in Allende Inclusions: II. Magnesium. *Geophys. Res. Lett.* 4, 299–302. doi:10.1029/GL004i007p00299

Wisshak, K., Voss, F., Käppeler, F., Kazakov, L., Bečvář, F., Krtička, M., et al. (2006b). Fast neutron capture on the Hf isotopes: Cross sections, isomer production, and stellar aspects. *Phys. Rev. C* 73, 045807. doi:10.1103/PhysRevC.73.045807

Wisshak, K., Voss, F., Käppeler, F., and Kazakov, L. (2006a). Stellar neutron capture cross sections of the Lu isotopes. *Phys. Rev. C* 73, 015807. doi:10.1103/PhysRevC.73.015807

Woosley, S. E., Wilson, J. R., Mathews, G. J., Hoffman, R. D., and Meyer, B. S. (1994). The r-process and neutrino-heated supernova ejecta. *Astrophys. J.* 433, 229. doi:10.1086/174638

Appendix 1: Some comments on stellar models

A general, synthetic outline of the stellar parents of neutron-rich elements beyond iron can be found in El Eid (2018). We briefly comment on these astrophysical sources below, believing that this brief summary can be sufficient for an article, which is mainly devoted to nuclear, not stellar, effects.

Stellar models for the *s*-process

Beyond the *main* *s*-process component discussed in this study, it is well-known that another, less effective, slow neutron capture process exists, where massive stars ($M \geq 10\,M_{\odot}$) contribute to the production of heavy elements between $A = 60$ and $A = 90$, in what is called the *weak* *s*-process (occurring during core-He and shell-C burning phases, mainly thanks to the activation of the $^{22}Ne(\alpha,n)^{25}Mg$ reaction). Rotation can also boost this *s*-process component in massive star models of low metallicity, letting it reach higher atomic masses. While we do not address these issues here, interested readers can find details in Pignatari et al. (2010) and Nishimura et al. (2017).

Rather, some words must be spent on the mixing mechanisms driving the formation of the neutron source $^{13}C(\alpha,n)^{16}O$ in AGB stars, generating the main component discussed in the previous sections. The general characteristics that these mixing phenomena must have were outlined a few years ago in Busso et al. (2011) and further specified in Nucci and Busso (2014). In the first of these contributions, it was shown that the most common extra-mixing mechanisms explored in stellar evolution (like thermohaline diffusion and various types of rotationally-induced mass transport) would be too slow and ineffective to produce adequate circulation at the H–He interface. It was also argued that a faster process, like magnetic buoyancy, might instead provide the required effects.

While this last mechanism was, indeed, explored by us in recent years and used also in the present study, other physical processes might obtain the same effects. In particular, in Nucci and Busso (2014) it was shown that the geometrical simplifications adopted in our MHD model are equivalent to establish buoyancy with a velocity growing at least quadratically with radius. Any mechanism performing this might then be used, as well. Among promising physical phenomena certainly occurring in stars, but not explored sufficiently so far, we can mention gravity waves (Battino et al., 2016, 2019), and in general any wave-like propagation including some transport of mass. We believe looking for such possible alternatives to MHD mixing would be very important and probably highly rewarding. The first thing to be verified would be the ability of such transport mechanisms to provide the extended pockets with *flat* ^{13}C distributions, which were shown to be necessary by Liu et al. (2015). They would also imply the same reduction in ^{14}N and the same low values of the neutron density discussed in the present article.

Stellar models for the *r*-process

Rather recently (2017), the *White paper on Nuclear Astrophysics* recognized (Arcones et al., 2017), among the main open problems in our understanding of the origin of the elements, some crucial issues concerning the fast neutron captures. Among other things, there were questions like 1) "where are the 54 elements beyond iron created that are traditionally attributed to a rapid neutron capture process (*r*-process)?" and 2) "what is the contribution of neutrino-driven winds in core collapse supernovae (ccSNe) to nucleosynthesis and what role do neutrino properties play?" Despite the fact that, in the same year, observations from the kilonova associated to the gravitational wave source GW170817 became available, the same questions remain unanswered now. Indeed, while it seems clear that in the kilonova ejecta there were regions whose high opacities are in line with lanthanide-rich materials (Stratta, 2019) and while also lines of Sr and Y have been observed (Vieira 586 et al., 2022), it appears that the kilonova did not produce a typical solar-like *r*-process distribution (Ji et al., 2019). Other sources, like collapsars (Siegel et al., 2019) and *ccSNe* (Suzuki et al., 2019) remain on the stage, in this last case with results remarkably dependent on the nuclear mass model adopted for determining β decays for waiting-point nuclei.

In the present, still uncertain, situation, we remind what has been said in Section 3, commenting Figure 3. The heavier nuclei of the third panel in the figure are today commonly attributed to *NSM* of various types, while the lighter isotopes of panel 1 can still be safely ascribed to *ccSNe* (Yamazaki et al., 2022). For the intermediate distribution of panel 2 (corresponding to a *weak* or *incomplete* *r*-process) best candidates remain jet-like magneto-rotational supernovae (Nishimura et al., 2017; Farouqi et al., 2022). Contributions might come also from jet-like emissions in *NSM* (Yamazaki et al., 2022) and from collapsars (Siegel et al., 2019).

Frontiers in Physics

Investigates complex questions in physics to understand the nature of the physical world

Addresses the biggest questions in physics, from macro to micro, and from theoretical to experimental and applied physics.

Discover the latest Research Topics

See more →

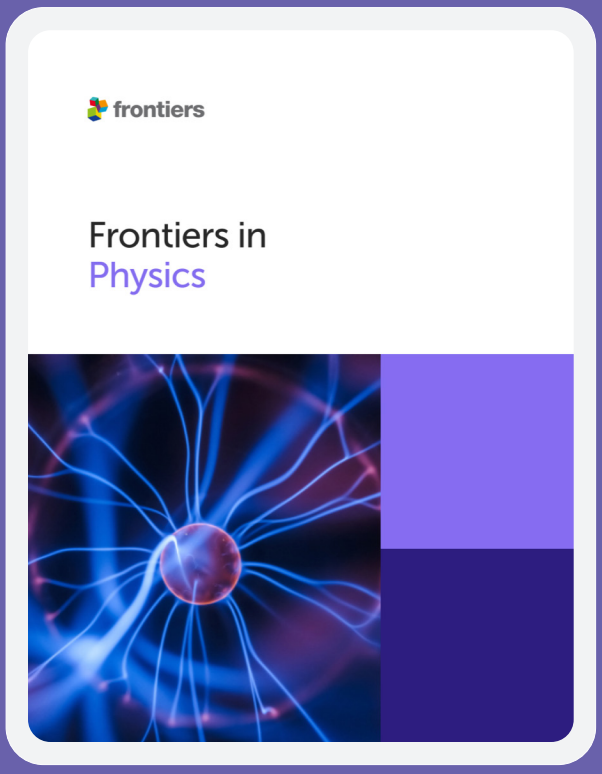

Frontiers

Avenue du Tribunal-Fédéral 34
1005 Lausanne, Switzerland
frontiersin.org

Contact us

+41 (0)21 510 17 00
frontiersin.org/about/contact